Future Changes in Extratropical Cyclones over Eastern North America and the Western Atlantic in Climate Models and a Downscaled Mesoscale Model

A Dissertation Presented

by

Zhenhai Zhang

to

The Graduate School

in Partial Fulfillment of the

Requirements

for the Degree of

Doctor of Philosophy

in

Marine and Atmospheric Science

Stony Brook University

December 2016

Stony Brook University

The Graduate School

Zhenhai Zhang

We, the dissertation committee for the above candidate for the

Doctor of Philosophy degree, hereby recommend

acceptance of this dissertation.

Brian A. Colle, Professor and Dissertation Advisor
School of Marine and Atmospheric Sciences, Stony Brook University

Edmund K.M. Chang, Professor and Chair of Defense
School of Marine and Atmospheric Sciences, Stony Brook University

Malcolm J. Bowman, Professor and Committee Member
School of Marine and Atmospheric Sciences, Stony Brook University

Minghua Zhang, Professor and Committee Member
School of Marine and Atmospheric Sciences, Stony Brook University

Gary M. Lackmann, Professor and Outside Committee Member
Department of Marine, Earth, and Atmospheric Sciences, North Carolina State University

This dissertation is accepted by the Graduate School

Nancy Goroff
Interim Dean of the Graduate School

Abstract of the Dissertation

Future Changes in Extratropical Cyclones over Eastern North America and the Western Atlantic in Climate Models and a Downscaled Mesoscale Model

by

Zhenhai Zhang

Doctor of Philosophy

in

Marine and Atmospheric Science

Stony Brook University

2016

Extratropical cyclones are one of the main drivers of regional climate, and they play a dominant role in both the day-to-day weather and extreme events during cool season (November-March) over eastern North America and western Atlantic. A better understanding of the regional changes of extratropical cyclones under climate change is vital important for decision makers and the public to prepare for these changes and minimize the associated risks. This thesis provides a comprehensive study in the ability of climate and weather prediction models in simulating the variability of extratropical cyclones, the regional future changes of the extratropical cyclones, and their associated regional climate and extreme weather during cool season over eastern North America and western Atlantic.

An automated tracking algorithm is employed to identify extratropical cyclones during cool seasons for 15 Coupled Model Intercomparison Project Phase 5 (CMIP5) models and reanalysis products. The model's performance in simulating cyclones during the historical period is evaluated with respect to the results from reanalysis. The future changes in cyclone activities through 21st century are investigated for the high-emission future experiment of CMIP5 models forced by Representative Concentration Pathway 8.5 (RCP8.5) scenario. Although cyclone frequency along the storm track over eastern North America and western Atlantic decreases significantly in the future, intense cyclones along the U.S. East Coast have a slight increase, with more rapid deepening cases in the models.

In addition to the frequency and intensity of extratropical cyclones, a cyclone relative approach is developed to explore the structure and intensity of precipitation within synoptic-scale cyclone systems in CMIP5 models. There is a large increase trend of precipitation associated with cyclones over eastern North America and western Atlantic through 21st century due to the significant increase in available moisture under global warming. The increase of precipitation mainly comes from relatively strong cyclones, while the increase from weak cyclones is inhibited by the decrease of cyclone frequency. Although the baroclinicity is decreasing under global warming, more cyclone cases are accompanied with more extreme precipitation events due to the positive feedback between latent heat release from precipitation and cyclone deepening over U.S. East Coast region.

The coarse-resolution CMIP5 GCMs are able to simulate the large-scale structure of cyclones. However, they cannot resolve many terrain specific features and the high-impact mesoscale physical processes. To better understand the future changes in extratropical cyclone activities for regional applications, the global simulations of selected CMIP5 models are dynamically downscaled to develop high-resolution climate simulations over eastern North America and western Atlantic using Weather Research and Forecasting model (WRF). Although the cyclone frequency in WRF is dominated by the corresponding GCM, the high-resolution WRF can simulate cyclone intensity more realistically, while the cyclone intensity in the low-resolution WRF is closer to the GCM. During the future period, the low-level diabatic potential vorticity (DPV) becomes stronger while the baroclinicity is weaker in WRF, indicating that the enhanced latent heat release becomes more important to cyclone developing than the historical period. Meanwhile, the increase of extreme precipitation in WRF is much larger than the increase in GCM, although WRF overestimates the seasonal mean precipitation in the historical period.

Table of Contents

List of Tables

List of Figures

Chapter 2

Chapter 3

Chapter 4

Chapter 5

List of Abbreviations

Best7: the 7 CMIP5 models with better historical performance

CCSM4: Community Climate System Model version 4

CESM: Community Earth System Model

CFSR: Climate Forecast System Reanalysis

CMAP: Climate Prediction Center Merged Analysis of Precipitation

CMIP5: Coupled Model Intercomparison Project Phase 5

C-WRF-HR: high resolution (~20km) WRF forced by CCSM4

C-WRF-LR: low resolution (~100km) WRF forced by CCSM4

DPV: diabatic potential vorticity

EC: East Coast of North America

ECL: East Coast Land

ECW: East Coast Water

ECWA: East Coast and Western Atlantic

ECMWF: European Centre for Medium-Range Weather Forecasts

ERA-Interim: ECMWF Re-Analysis Interim

ENSO: El Nino and Southern Oscillation

GCM: general circulation model

GPCP: Global Precipitation Climate Project

G-WRF-HR: high resolution (~20km) WRF forced by GFDL-ESM2M

G-WRF-LR: low resolution (~100km) WRF forced by GFDL-ESM2M

IPCC: Intergovernmental Panel on Climate Change

M-Center: Moderate (990-1005hPa) Cyclone Center

PD: absolute difference for cyclone central pressure

PGW: pseudo global warming

PMAX: precipitation maximum

PR: spatial correlation for cyclone central pressure

PS: Surface Pressure

RCP8.5: Representative Concentration Pathway 8.5

RH: Relative Humidity

SLP: Sea Level Pressure

SST: Sea Surface Temperature

S-Center: Strong (< 990hPa) Cyclone Center

TD: absolute difference for cyclone track density

TR: spatial correlation for cyclone track density

WA: Western Atlantic

Worst7: the 7 CMIP5 models with worse historical performance

WRF: Weather Research and Forecasting model

WRF-HR: high resolution (~20km) WRF

WRF-LR: low resolution (~100km) WRF

WPS: WRF Preprocessing System

W-Center: Weak (>1005hPa) Cyclone Center

Acknowledgments

I would like to thank my advisor Dr. Brian Colle for all of his guidance, supports, and patience through my PhD project. I would also like to thank my dissertation committee, including Dr. Edmund Chang, Dr. Minghua Zhang, Dr. Gary Lackmann, and Dr. Malcolm Bowman, for their comments and feedbacks through my dissertation.

A special thanks goes to the SOMAS faculty and colleagues, you make the SOMAS being a wonderful and unique place to study and work.

Finally, I would like to thank my wife for her tremendous support, courage and love; thank my daughter, she is the source of my happiness; and thank my parents for their great help and support.

Chapter 1: Introduction

Extratropical cyclones are one of the main drivers of regional climate, and they play a dominant role in both the day-to-day weather and extreme events during cool season in midlatitude. The strong winds, heavy precipitation, rapid temperature change, and coastal flooding from extratropical cyclones have serious environmental, societal, and economic impacts, especially for the densely populated regions, such as eastern North America. Therefore, a better understanding of extratropical cyclone variability and its future changes is of great importance. The goal of this thesis is to contribute to improve the understanding to the capability of numerical models in simulating extratropical cyclones, quantify the future changes of the extratropical cyclones during cool season over eastern North America and western Atlantic, and to explore some of the physical mechanisms associated with these changes. In the following sections, a brief overview is given on the background of extratropical cyclones, the high-impact weather associated with cyclones, and the other studies investigating the future changes of the cyclones. Then, the main goals of this thesis will be briefly outlined.

1.1. Background

Midlatitude storm tracks are the most frequent paths of extratropical cyclone activity, which have been quantified as standard deviation of 500 hPa geopotential height, Eady growth rate, and cyclone count (Hoskins and Hodges, 2002; Paciorek et al. 2002; Hodges et al. 2003; Wernli and Sprenger, 2007; Chang 2009; Hodges et al. 2011). In all of these studies there are two most prominent storm tracks across the northern hemisphere: one from eastern North America across the North Atlantic and another from near Japan across the North Pacific. Chang et al. (2002) concluded that the preexisting, finite amplitude baroclinic eddies are modulated by the longitudinal variation in both the baroclinic and barotropic components of basic state flows, and this modulation leads to the observed storm tracks. Other physical processes, especially diabatic heating from latent heat release in rising air over the cyclone comma head provides an additional energy source to the development of these eddies (Hoskins and Valdes 1990; Chang et al. 2002; Black 1998).

There has been a large inter-decadal variability in extratropical cyclones during the past several decades (Chang et al. 2002; Wang et al. 2006; Feser et al 2014; Colle et al. 2015). Geng and Sugi (2001) found that the frequency and intensity of extreme extratropical cyclones (with stronger pressure gradient, faster moving speed, and stronger deepening rate) over North Atlantic increased from 1950s to the end of 20th century. On inter-annual timescales, storm tracks change in response to the El Nino and Southern Oscillation (ENSO) cycle, storm track shifts equatorward during El Nino years in response to local enhancement of the Hadley circulation (Chang et al. 2002; Straus and Shukla 1997). Hirsch et al. (2001) completed a winter storm climatology (from 1951-1997) over East Coast of US using the NCEP reanalysis, indicating the similar inter-annual variations associated with ENSO (more storms in El Nino winter) and relatively large inter-decadal variations over East Coast, but no significant long term trend during the late 20th Century. Their results also showed that the winter storms occurred most often in January and February. Associated with midlatitude baroclinic zone, the extratropical cyclones have significant seasonal variability. Similar with pole-to-equator temperature gradient, which is strongest during winter, the extratropical cyclones are most active during winter with a single maximum in January over the North Atlantic (Nakamura 1992). Different from Atlantic, over the Pacific the cyclone activities are strongest during late fall and early spring with a significant weakening in midwinter because the strength of the upper tropospheric jet excesses the optimal range (up to ~45 m/s) for baroclinic wave activity (Nakamura 1992), and the diabatic contribution due to latent heat release has a maximum in fall with a relative minimum in midwinter (Chang and Song 2006).

1.2. High-impact weather associated with extratropical cyclones

Extratropical cyclones are often accompanied by heavy precipitation, with the maximum located immediately to the northeast of the center, where there is strong upward vertical motion and moisture flux (Field and Wood 2007; Naud et al. 2012). Field and Wood (2007) suggested that the precipitation rate is positively correlated with not only integrated atmosphere moisture, but also the cyclone strength, since the vertical motions typically increase with cyclone strength. Similar with the cyclones activity, the precipitation associated with Atlantic extratropical cyclones also has the maximum in winter (Chang and Song 2006). During the winter extratropical cyclones contribute over 80% of the total cool season precipitation over the eastern North America (Hawcroft et al. 2012). Meanwhile, they are responsible for 93-100% of extreme precipitation over Northeast United States from November to May (Agel et al. 2015), including blizzards (Novak et al. 2008), which have major economic and societal impacts in winter over this heavily populated Northeast United States. For example, a federal state of emergency was declared for Connecticut after the 8-9 February 2013 extratropical cyclone produced more than 1 m of snow in central Connecticut, and more than 0.6 m in part of Long Island during the evening rush hour (Picca et al. 2014).

Extratropical cyclones contribute vast majority of non-convective high wind events in many parts of the world, including the east coast of North America (Knox et al. 2011); and the non-convective high wind events caused 616 fatalities from 1980-2005 in United States (Ashley and Black 2008).

Storm surge is another major hazard due to the strong surface wind and low surface pressure when the coastal areas are impacted by extratropical cyclones (Colle et al. 2008; DiLiberto et al. 2011). For example, New York City is extremely vulnerable to the storm surge produced by extratropical cyclones (Colle et al. 2008; Colle et al. 2010; Sweet and Zervas 2011; Colle et al. 2015).

1.3. Extratropical cyclones in climate models

Global climate models are widely used in the investigation to the historical extratropical cyclones and the future change of these storms. However, to have confidence for utilizing these models it is important to understand their performance in the simulation of extratropical cyclones, from the spatial distribution of storm track to the structure, intensity, and physical processes of individual cyclones.

Bauer and Genio (2006) found that the coarse-resolution Goddard Institute for Space Studies (GISS) global climate model (GCM) produced fewer, generally weaker, and slower-moving cyclones than the reanalysis, and the cyclones in model were shallower and drier aloft producing less storm precipitation because of the weaker ageostrophic circulation. Catto et al. (2010) compared the 100 most intense extratropical cyclones in the North Hemisphere winter from a high-resolution (around 1°) GCM and reanalysis; they demonstrated that the climate models can capture the structural features (wind speeds, equivalent potential temperature, mean sea level pressure, vertical velocity, and relative humidity) of extratropical cyclones, but there was uncertainties in some mesoscale processes due to parameterizations of diabatic processes.

However, the evaluation of multiple models is needed to get a more complete picture of how well extratropical cyclones are represented in models.

Chang et al (2013) investigated the storm track activities in 17 Coupled Model Intercomparison Project phase 3 (CMIP3) models and found an equatorward bias for the storm-track distribution, and they also found that most of the models had significant biases in storm-track amplitude which is highly correlated with the biases of mean available potential energy due to the biases of mid-tropospheric temperature gradients. Zappa et al. (2013) showed that Coupled Model Intercomparison Project Phase 5 (CMIP5) models had improved ability than CMIP3 to simulate the extratropical cyclones in the North Hemisphere, but still had biases in the distribution of storm track and underestimated the intensity of cyclones which in part directly depended on the parameterizations of GCMs.

There are many challenges using GCMs to simulate extratropical cyclones. Models' performance is negatively correlated with model resolution; high-resolution models are more likely to have smaller biases (Jung et al. 2006; Chang et al. 2013). Current GCMs are typically at the grid spacing on the order of 100-200 km, which is too coarse to resolving the strong baroclinicity, sea surface temperature (SST), and latent heating (Willison et al. 2013). Meanwhile, horizontal resolution is not the only factor controlling the models' performance in extratropical cyclone simulation (Chang et al. 2013; Colle et al. 2013). The parameterizations of the model and the simulations of the complex interactions between multi-scale dynamic processes also have large impact on the cyclone simulation (Zappa et al. 2013). Dynamical downscaling with high-resolution regional model provides an alternative to the extratropical cyclone modeling. He et al. (2013) illustrated a downscaling approach to improve the simulation of a central U.S. cyclone, in which Weather Research and Forecasting model (WRF) was oneway nested within the Community Earth System Model (CESM). Another downscaling approach used for cyclone was known as pseudo-global-warming (PGW) in which the thermodynamic changes derived from the GCM (future minus historical) were added to the reanalysis-derived initial and boundary conditions for the future simulations (Sato et al. 2007; Rasmussen et al. 2011; Lackmann 2013; Marciano et al. 2015).

1.4. Future changes in extratropical cyclone

Many studies (Geng and Sugi 2003; Lambert and Fyfe 2006; Bengtsson et al. 2009; Chang 2013, Zappa et al. 2013) have shown a decrease in the frequency of the extratropical cyclones over North Hemisphere under global warming due to the polar warming amplification, which in turn reduces the temperature gradient in the lower troposphere. However, there are uncertainties in the future changes in cyclone intensity (Geng and Sugi 2003; Lambert and Fyfe 2006; Catto et al. 2011). Increases in cyclone intensity were found in some regional areas. An increase of cyclone intensity was detected near Great Britain and Aleutian Isles in an ensemble of ECHAM5/MPIOM1 simulations for SRES A1B and A2 forcing scenarios (Pinto et al. 2007). In the simulations of 10 strongly developing extratropical cyclones in present and future thermodynamic environments, Marciano et al. (2015) demonstrated that the enhanced latent heat release was responsible for the intensity increase in both of sea level pressure (SLP) and 10 m wind speed of those cyclones in the future over U.S. East Coast.

Meanwhile, over eastern North America the precipitation associated with extratropical cyclones has a significant increase (Zappa et al. 2013; Lombardo et al. 2015; Marciano et al. 2015). However, for different regions, the relationship between the cyclone change and precipitation change is different. Zappa et al. (2015) found that there is a reduction in the total winter precipitation over Mediterranean due to the decrease of cyclone frequency in the CMIP5 models; and that reduction in total precipitation is amplified by the decrease in the average precipitation of each cyclone over the East Mediterranean, but compensated by the increase in the average precipitation of each cyclone over the North Mediterranean.

1.5. Motivation

CMIP5 models provide a unique multi-model framework for assessing the capability of GCMs in extratropical cyclone simulation and the future changes of these cyclones. More importantly, CMIP5 models provide high-frequency (6-hourly) model output data that allows for cyclone tracking using this multi-model ensemble for the first time. There are some studies investigating the future changes of the extratropical cyclone in CMIP5 models. Zappa et al. (2013) found a ~3.6% reduction in the total cyclone number in winter over North Atlantic and Europe in CMIP5 forced by the midrange Representative Concentration Pathway (RCP4.5) emission scenario. Chang (2013) suggested that there is a significant decrease in extratropical cyclones over North America, with the largest decrease (32.6%) in summer in CMIP5 models. However, more studies are needed to focus on the regional details in some particular regions, such as eastern North America, which is heavily populated and vulnerable to the extreme events associated with extratropical cyclones.

In addition to the frequency, intensity, and the distribution of extratropical cyclones, the direct impacts of heavy precipitation and strong winds are important. And under global warming, a pronounced increase was found in the surface precipitation over the North Atlantic and North America in some studies (Zappa et al. 2013; Lombardo et al. 2015; Marciano et al. 2015).

However, the regional changes in cyclone associated precipitation and the linkage to synoptic-scale cyclone systems over eastern North America are still unclear.

There are many challenges using GCMs to simulate extratropical cyclones. The coarse-resolution (100-200 km) CMIP5 GCMs are able to simulate the large-scale structure of cyclones; but they cannot resolve many of the high-impact mesoscale physical processes, such as heavy frontal precipitation. Dynamical downscaling is need to investigate the future regional changes and to better understand the physical processes responsible for the future changes of extratropical cyclones over eastern North America and western Atlantic. The study from Marciano et al. (2015) focused on only ten strongly developing Miller-A cyclones. But the potential changes for many other kinds of cyclones are unclear.

This thesis focuses on the extratropical cyclones over eastern North America and western Atlantic during cool season and aims to address the following questions:

1) How well can the global climate models simulate the extratropical cyclone activities over eastern North America and western Atlantic?
2) How will extratropical cyclones frequency, intensity and distribution change during the next several decades based on the simulations of global climate models?
3) How will the precipitation associated with extratropical cyclones change over eastern North America and western Atlantic under climate change?
4) What are some of the physical reasons for the future change in cyclone activity?
5) Can the high-resolution regional model tell us more details concerning the future changes of extratropical cyclones, and improve our understanding to these changes?

Chapter 2 describes the data and methods used in this thesis. Chapter 3 focuses this historical evaluation and future prediction of extratropical cyclones over eastern North America and western Atlantic during cool season in CMIP5 models. Chapter 4 examines the future changes in precipitation associated with extratropical cyclones and explores the potential reasons for the cyclone changes in CMIP5. Chapter 5 demonstrates the dynamical downscaling of extratropical cyclones and their future changes using WRF, and investigates the impacts of high-resolution dynamical downscaling and the physical processes associated with the future cyclone changes. Chapter 6 provides the conclusions and discusses potential future work.

Chapter 2: Data and Methods

2.1. CMIP5 and reanalysis datasets

A few domains are used in this study to investigate the historical and future changes in extratropical cyclones over eastern North America and western Atlantic (Fig. 2.1): East Coast Land (ECL), East Coast Water (ECW), East Coast (EC), Western Atlantic (WA), and East Coast and Western Atlantic (ECWA). The cool season period for the analysis is defined from November to March. The historical period is defined as the 1979-2004 cool seasons, while three future periods in 21st century are defined as early (2009-2038), middle (2039-2069), and late (2069-2098) 21st century.

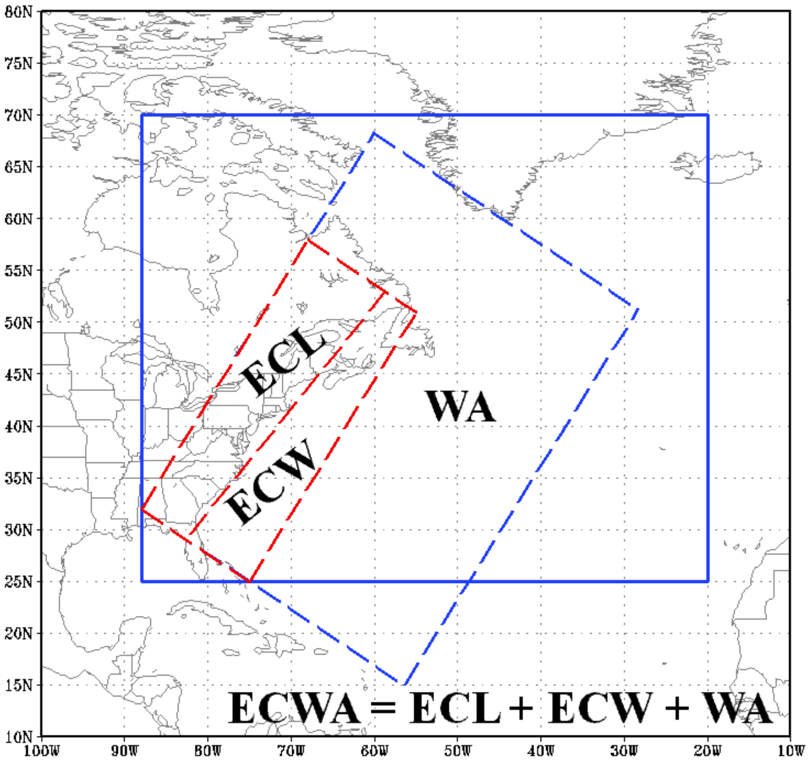

Fig. 2.1: The domains used in this study. The solid blue box is the region used for the cyclone track density evaluation; the dashed boxes are East Coast Land (ECL), East Coast Water (ECW), Western Atlantic (WA), and East Coast Western Atlantic (ECWA), respectively.

The Climate Forecast System Reanalysis (CFSR; Saha et al. 2010) at ~38-km grid spacing and the Interim Re-Analysis (ERA-Interim; Dee et al. 2011) at ~58-km grid spacing were analyzed and compared for the extratropical cyclone properties. Consistent with the other study (Hodges et al. 2011; Wang et al. 2016), the results from the CFSR and ERA-Interim are very close. For example, Fig. 2.2 shows the intensity distribution of the cyclones within EC region in Fig. 2.1 using the cyclone tracker outlined in the next section. There are 64.4 (63.5) cyclone tracks per cool season during the historical period in CFSR (ERA-Interim), the distributions of relative intense cyclones (< 1000 hPa) are almost the same.

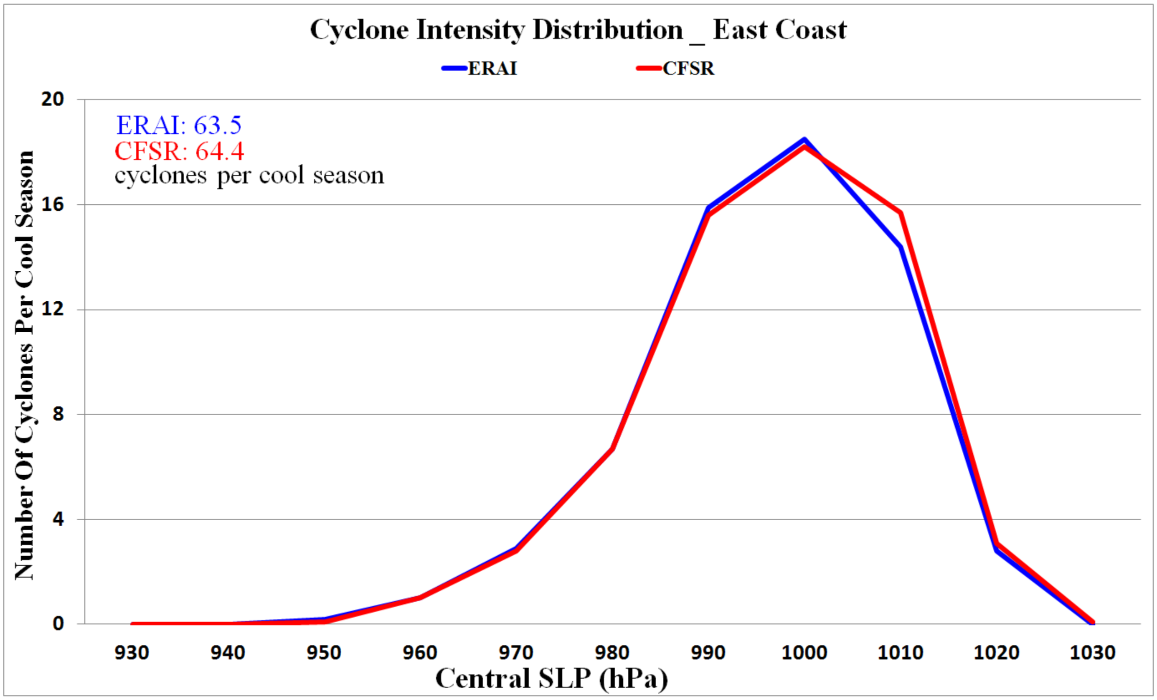

Fig. 2.2: Intensity distribution of cyclones within EC region for CFSR (red) and ERA-Interim (blue). The intensity is defined as the minimum SLP along each cyclone track within EC region.

However, Wang et al. (2016) found there are larger spreads for the extratropical cyclone counts and intensity among 9 reanalysis datasets. They also showed that the agreement in the relatively deep cyclone count is generally better in winter than in summer and better in the North Hemisphere than in the South Hemisphere, with nearly perfect agreement for the counts of North

Hemisphere winter deep cyclones. Therefore, only the CFSR is used to verify and compare the extratropical cyclone properties with the CMIP5 models over eastern North America and western Atlantic during cool season.

The Climate Model Intercomparison Project phase 5 (CMIP5, Taylor et al. 2012) provides a unique state-of-the-art multi-model dataset to advance our knowledge of climate variability and climate change. The model output from CMIP5 historical experiment and high-emission future experiment forced by the Representative Concentration Pathway 8.5 (RCP8.5) scenario were used for historical and future periods respectively. In the CMIP5 historical experiment (20th century), the models were forced by the observed greenhouse gas concentrations, ozone, solar forcing, land use, and aerosols. In RCP8.5 experiment, the models were forced by high greenhouse gas emissions, which raised the radiative forcing pathway to 8.5 W/m^2 by the end of 21st century. Six-hourly sea-level pressure (SLP) from the 15 CMIP5 models in Table 2.1 was used for the cyclone tracking.

Two precipitation products were used to verify and compare the seasonal mean precipitation with CMIP5 models: Global Precipitation Climate Project (GPCP; Adler et al. 2003) V2.2 monthly mean precipitation data (2.5°×2.5° resolution) from National Oceanic and Atmospheric Administration (NOAA), and Climate Prediction Center Merged Analysis of Precipitation (CMAP; Xie and Arkin 1997) monthly mean data (2.5°×2.5° resolution) from National Center for Atmospheric Research (NCAR). The GPCP data combines the precipitation information available from several different sources, including rain gauge stations, satellites, and sounding observations. The CMAP data were obtained from 5 kinds of satellite estimates (GPI, OPI, SSM/I scattering, SSM/I emission and MSU).

Table 2.1: The CMIP5 models used for historical evaluation and future prediction of the extratropical cyclones, and their attributes. Red indicates the high-resolution models.

Model	Center	Horiz. Resolution (lon. × lat.)	Number of model levels	Reference
CCSM4*	National Center for Atmospheric Research, USA	1.25×0.94	26	Gent et al. (2011)
EC-Earth	EC-Earth Consortium	1.125×1.12	62	Hazeleger et al. (2010)
MRI-CGCM3*	Meteorological Research Institute, Japan	1.125×1.12	48	Yukimoto et al. (2011)
CNRM-CM5.1*	National Centre for Meteorological Research, France	1.4×1.4	31	Michou et al. (2011)
MIROC5	Atmosphere and Ocean Research Institute (University of Tokyo), National Institute for Environmental Studies, and Japan Agency for Marine-Earth Science and Technology, Japan	1.4×1.4	40	Watanabe et al. (2010)
HADGEM2-ES	Met Office Hadley Centre, UK	1.875×1.25	38	Jones et al. (2011)
HADGEM2-CC*	Met Office Hadley Centre, UK (Chemistry-coupled version)	1.875×1.25	60	Jones et al. (2011)
INMCM4*	Institute for Numerical Mathematics, Russia	2.0×1.5	21	Volodin et al. (2010)
IPSL-CM5A-MR*	Institut Pierre Simon Laplace, France	2.50×1.25	39	Dufresne et al. (2012)
MPI-ESM-LR*	Max Planck Institute for Meteorology, Germany	1.9×1.9	47	Jungclaus et al. (2006); Zanchettin et al. (2011)
NorESM1-M	Norwegian Climate Center, Norway	2.5×1.9	26	Zhang et al. (2012)
GFDL-ESM2M*	NOAA Geophysical Fluid Dynamics Laboratory, USA	2.5×2.0	24	Donner et al. (2011)
IPSL-CM5A-LR*	Institut Pierre Simon Laplace, France	3.75×1.8	39	Dufresne et al. (2012)
BCC-CSM1.1	Beijing Climate Center, China Meteorological Administration, China	2.8×2.8	26	Wu et al. (2011)
MIROC-ESM-CHEM*	Japan Agency for Marine-Earth Science and Technology, Atmosphere and Ocean Research Institute.	2.8×2.8	80	Wantanbe et al. (2011)

For CMIP5 models, the daily precipitation, surface temperature, and air temperature, relative humidity, wind speed, vertical motion (omega) on pressure levels from 10 models (with * in Table 2.1) were used to explore the precipitation changes and the related physical processes. The 10 CMIP5 models were used because those daily data were available only for these 10 models at the time of this work. The ten models have different horizontal resolution, varying from 1.25°×0.94° to 2.8°×2.8°, so all of these model data and the two precipitation products were interpolated onto a common 1°×1° longitude-latitude grid.

2.2. Cyclone tracking approach

The cyclone tracking scheme employed in this thesis is developed by Hodges (1994; 1995). This scheme has been widely used (Hoskins et al. 2002, 2005; Zappa et al. 2013; etc.). Different from some other cyclone studies, which used 850-hPa vorticity for Hodges tracking approach, this thesis only uses SLP every 6-h to track the cyclones. Although the vorticity tracking is better at describing some smaller-scale systems (Hoskins et al. 2002), it also tends to flag some small-scale surface troughs (non-cyclones with a vorticity maximum) as cyclone centers. An example at 0600 UTC 10 January 2001 is shown in Fig. 2.3. This thesis focuses on the extratropical cyclones with closed SLP circulations.

The SLP disturbances needed for tracking can be strongly influenced by large spatial scales and strong background flows. For example, during an enhancement of the subtropical jet the weak and fast moving cyclones can be masked by the background flow until it significantly developed. Therefore, a spectral bandpass filter was used to pre-process the data. The planetary scales (total wavenumber equal or less than 5) are removed. The data are also truncated to remove small scales (total wavenumber larger than 70). The lower end of spectral filter band was set as wavenumber 70 in order to retain the small scale systems as well as remove too small scale noise.

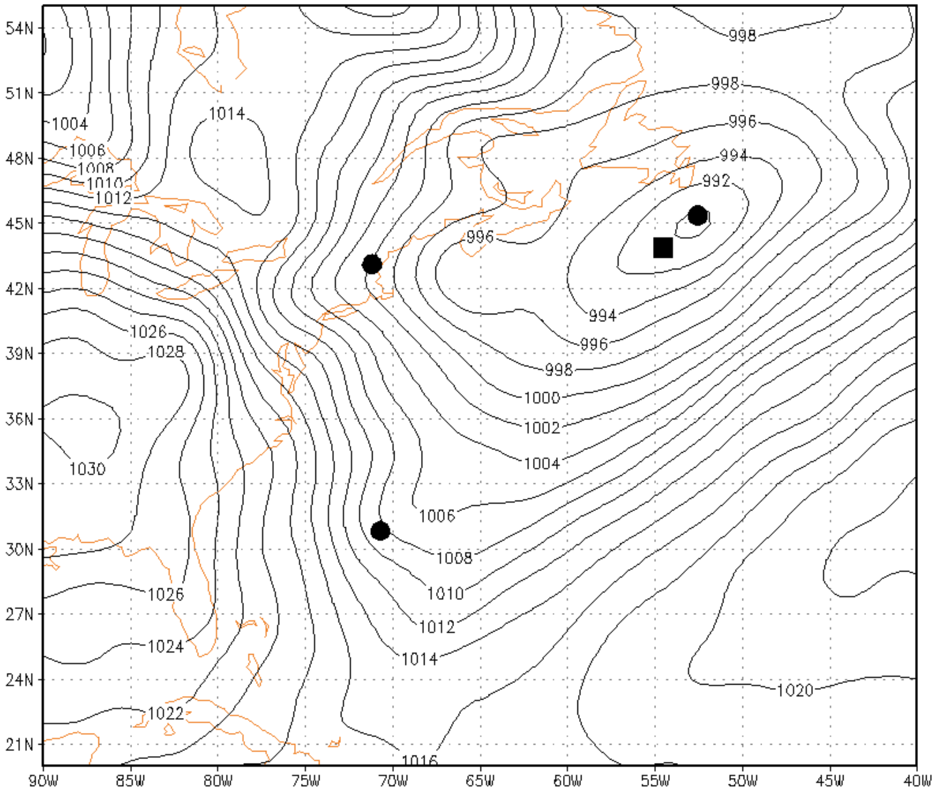

Fig. 2.3: SLP from CFSR at 0600 UTC 10 January 2001. The dots and square represent where the 850hPa vorticity and SLP tracking approaches identified cyclone centers, respectively, using the 24-h minimum lifetime and 1000 km minimum moving distance thresholds. The SLP tracking is based on the anomaly of pressure, and therefore it does not necessarily lie exactly at the low center.

The cyclone tracking involves four steps. (1) Segmentation identifies the objects in the MSLP fields. The objects are the regions around minima in the MSLP field. This entails thresholding the data into object and background points and then the partitioning of the object points into distinct objects, which alone are stored for further processing to find feature points. (2) Feature detection part identifies suitable points, like local minimum in MSLP field, within each object. The extrema are easy to find, simply by comparing each object point with its neighbors. If clusters of local extrema occur with points having the same local extreme value, the centroid of these points is found for each cluster so that each cluster is represented by a single feature point. (3) Tracking using a constrained optimization of a cost function is used (based on the algorithm of Salari and Sethi 1990). Those feature points connected as one cyclone are labeled with a unique storm ID. All of these feature points are stored in records that have four indices for a 2D domain: two for the coordinates (latitude and longitude), one for the strength of the feature point, and one for the track number on which the feature point lies. (4) Filtering identifies storms filtered to retain only those that last at least 24 h (following Neu et al. 2013) and move farther than 1000 km. The minimum lifetime and minimum moving distance are set to remove the feature points exist for too short time or remain too stationary.

This automated cyclone tracking approach was evaluated manually for 11 Januaries every other year from 1980 to 2000, from 20° to 60°N and from 40° to 90° W. Totally 2286 cyclone centers were identified with 181 cyclone centers missed (7.9%) and 103 false alarmed (4.5%) by the tracker. Therefore, the uncertainty of the automated cyclone tracking results is 5%-10%.

2.3. Evaluation of model performance

Each CMIP5 model was evaluated for cyclone track density and cyclone central pressure with respect to the CFSR. For cyclone track density, a spatial correlation (TR) between individual models and the CFSR is computed over the ECWA region in Fig. 2.1:

$$\mathrm{TR} = \frac{\sum_{i=0}^{N}(\mathrm{M_i} - \overline{\mathrm{M}})(\mathrm{C_i} - \overline{\mathrm{C}})}{\sqrt{\sum_{i=0}^{N}(\mathrm{M_i} - \overline{\mathrm{M}})^2}\sqrt{\sum_{i=0}^{N}(\mathrm{C_i} - \overline{\mathrm{C}})^2}} \quad , \qquad (2.1)$$

in which: Mi is the model track density for grid I, $\overline{\mathrm{M}}$ is the model average track density of all grids, Ci is the CFSR track density in grid i., $\overline{\mathrm{C}}$ is the CFSR average track density of all grids, and N is the number of total grids. A similar spatial correlation was also calculated for the distribution of cyclone central pressures (PR), in which: Mi: is model cyclone number in pressure bin I, $\overline{\mathrm{M}}$ is the model average cyclone number of all bins, Ci is the CFSR cyclone number in bin i, $\overline{\mathrm{C}}$ is the CFSR average cyclone number of all bins, and N is the number of total bins (N = 11: < 935 hPa, 935-945, 945-955 … 1015-1025, > 1025).

An absolute difference was calculated for the cyclone track density (TD) within the ECWA region in Fig. 2.1:

$$\mathrm{TD} = \frac{1}{N}\sum_{i=0}^{N}(|\mathrm{M_i} - \mathrm{C_i}|) \quad , \qquad (2.2)$$

in which Mi: is the model track density in grid box i, Ci is the CFSR track density in grid i, and N is the total number of grids. A mean absolute difference of cyclone number for three pressure bins (PD) was also calculated using equation 2, in which Mi is the model cyclone number in bin i, Ci is the CFSR cyclone number in bin i, and N is the total number of total bins (N = 3; < 975 hPa, 975-1005 hPa, and > 1005hPa).

2.4. Cyclone relative approach

In order to extract the information associated with extratropical cyclones accurately, a cyclone relative approach is applied as in some other studies (Chang and Song 2006; Field and Wood, 2007; Naud et al. 2012; Naud et al. 2013; Marciano et al. 2015).

Using the cyclone data (the time, longitude and latitude for each cyclone center), each cyclone center is located on the map, and then a cyclone relative box is defined around the cyclone center. The cyclone relative box uses the cyclone center as the origin and is in X-Y coordinate instead of the geographic longitude-latitude coordinate from the models, so that each cyclone relative box can cover the same area avoiding the impact of latitude change. Otherwise, if we use the fixed degrees in longitude/latitude to define the cyclone-relative box, the area of a box at 30°N will be about twice large as the area of a box around 65°N.

Fig. 2.4 shows an example of cyclone relative approach: a cyclone relative box (red box in Fig. 2.4a) is defined around the cyclone center (black dot in Fig. 2.4a), and the SLP and precipitation within the box is extracted and interpolated to the cyclone-related X-Y (4000km×4000km) coordinate (the coordinate in Fig. 2.4b). The cyclone relative box is relatively large (4000km×4000km) at first, and will be modified for different purposes. Any fields within the cyclone relative box which contains the important information around the cyclone center can be extracted and stored for further use.

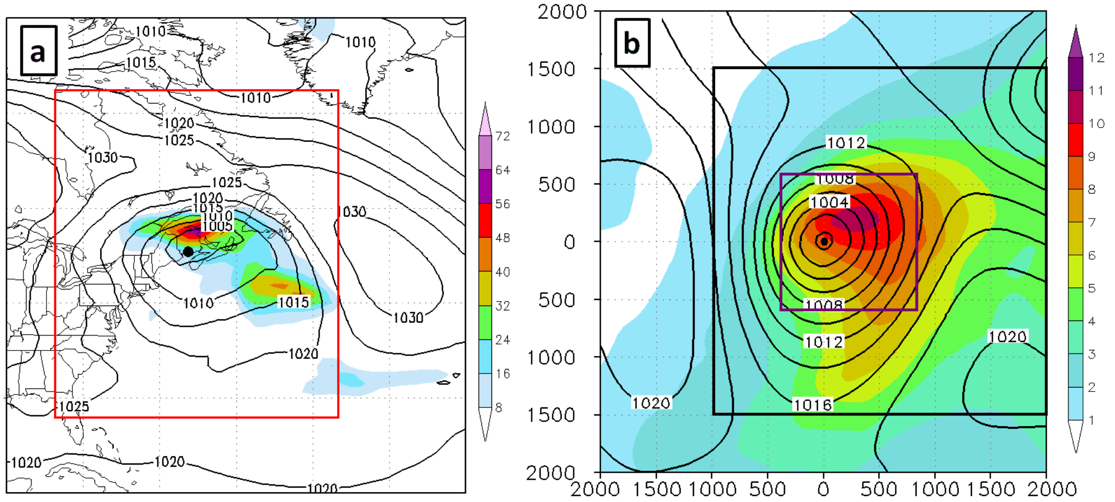

Fig. 2.4: An example of cyclone relative approach. (a) The precipitation (colors, mm/day) and SLP (contours, hPa) on the map; the red box is a cyclone relative box. (b) The composite of cyclone SLP (contours, hPa) and precipitation rate (colors, mm/day).

The cyclone relative fields can be used to generate the cyclone-related composite fields around the cyclone center, This kind of cyclone-related composite can reproduce the amplitude and structure of the important fields within the synoptic-scale cyclone systems for any kind of cyclones (e.g. for a particular cyclone intensity category, or over a particular region). Fig. 2.4b shows the mean composite cyclone relative precipitation (colors, mm day^{-1}) and SLP (black contours, hPa) for cyclone centers within ECL region during historical period from CFSR. The structure of the composite precipitation with a maximum just located immediately to the northeast of the cyclone center is consistent with previous studies (Chang and Song 2006; Field and Wood 2007; Naud et al. 2012), and the precipitation rate is comparable to the results in those studies.

The cyclone relative fields can also be put back onto the geographic map according to their original positions to create the earth-related cyclone relative fields. This kind of earth-related cyclone relative fields provides more accurate estimates of the fields associated with cyclones over the geographic map than simply averaging or summing the data. For example, the earth-related cyclone relative precipitation over the geographic map is calculated using the precipitation within a 3000 km × 3000 km cyclone relative box (black box in Fig. 2.4b), which was sized to cover most of the precipitation around the cyclone center. The sensitivity of the results to the size of the cyclone relative box (3000 km × 3000 km) for precipitation has been tested using a smaller box (2000 km × 2000 km); the contribution of cyclone relative precipitation amount to total amount decreases slightly and there is no significant impact on the results of future changes in cyclone relative precipitation.

2.5. Dynamical downscaling using WRF

a. <u>Data pre-processing</u>

Weather Research and Forecasting model (WRF, Version 3.6.1) using the Advanced Research WRF (ARW) dynamical core from National Center for Atmospheric Research (NCAR) is employed to dynamically downscale two CMIP5 models, CCSM4 and GFDL-ESM2M. The two models were selected because the high resolution (0.94°×1.25°) CCSM4 has relatively better performance in cyclone simulations and the low resolution (2.0°×2.5°) GFDL-ESM2M has large biases. The output data from the CMIP5 historical and RCP8.5 experiments are used to create the initial and boundary conditions for WRF historical and future runs respectively. The data includes 6-hourly one-level surface pressure (PS) and sea level pressure (SLP); 6-hourly air temperature (T), wind (U&V), and relative humidity (RH) on GCM model levels (26 levels for CCSM4 and 24 levels for GFDL-ESM2M); daily surface snow amount (SNW, if not available, monthly mean snow amount is used instead); monthly mean soil temperature (TSL) and soil moisture (MRLSL); and daily sea surface temperature (SST) from CCSM4 and GFDL-ESM2M ocean models.

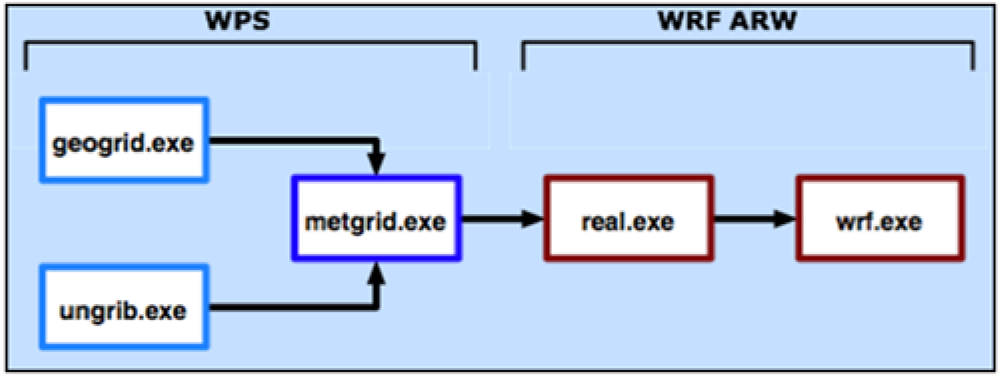

Fig. 2.5: Basic steps for regular WRF runs (from WRF ARW online tutorial).

A pre-processing step is needed to convert the CMIP5 model output data to what can be read and used by WRF. WRF Preprocessing System (WPS) is a set of three programs (shown in Fig. 2.5) to prepare input data for WRF. The “geogrid” interpolates static geographical data to the WRF grids. The “ungrib” extracts GRIB-formatted meteorological data from external data source and packs the data into a WPS intermediate file format. In this thesis, a new data pre-processing program is developed to convert the CMIP5 model output data to WPS intermediate file format, instead of “ungrib” in WPS. It includes 4 steps. (1) Extracting data: extract the data within a regional domain (10-70°N, 120-30°W) and for winter period (from 29th December to 2nd April). (2) Vertical interpolation: interpolate T, RH, U and V from CMIP5 GCM model levels (such as hybrid sigma pressure coordinate) to 22 pressure levels (1000, 975, 950, 925, 900, 850, 800, 750, 700, 650, 600, 550, 500, 450, 400, 350, 300, 250, 200, 150, 100, 50 hPa), which are the same with the vertical levels of many typical WRF input data. (3) Horizontal interpolation: interpolate SST from the ocean model coordinate (i.e. rotated polar coordinate) to regular latitude-longitude coordinate. (4) Converting data: convert the prepared data from NetCDF format to WPS intermediate file format. After these 4 steps, WPS can read the pre-processed CMIP5 data and use it to prepare the input data for WRF.

b. *Model configuration*

In the dynamical downscaling, there are two sets of WRF runs using the same initial and boundary conditions but different horizontal resolution: 0.2 degree (~20km, WRF-HR) and 1.0 degree (~100km, WRF-LR). These two sets of WRF runs with different resolution are used to demonstrate the impacts of model resolution on the simulation of extratropical cyclones, since the resolving of some mesoscale physical processes is very sensitive to the model resolution (Willison et al. 2013).

The domain (blue box in Fig. 2.6) for WRF run is from 24°N to 60°N and from 103°W to 45°W. This domain covers the major part of the storm track over Eastern U.S. and Western Atlantic. For the WRF runs, the historical period is from 1986 to 2005, which is the last 20 years of CMIP5 historical experiment; and the future period is from 2080 to 2099, which is the last 20 years of CMIP5 21st century RCP8.5 experiment. For each winter, WRF is initialized at 29th

December and stopped at 2nd April. Only the output of January, February and March was used for the analysis.

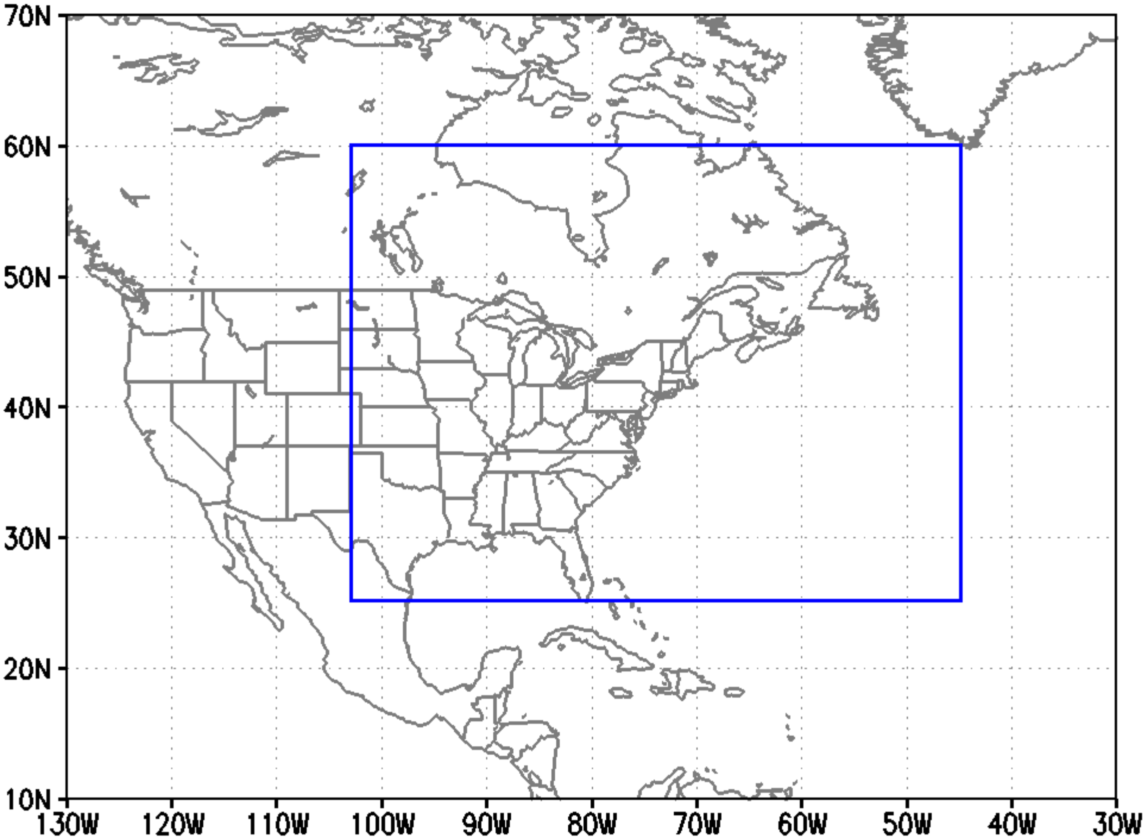

Fig. 2.6: The domain for WRF runs, from 24°N to 60°N and from 103°W to 45°W.

These physical schemes for WRF were selected based on results of an 8-member WRF ensemble of historical (1985-2004 winters) simulations performed by Kelly Lombardo. These WRF simulations were forced by the same NCEP Reanalysis 2 data (2.5°×2.5° resolution) for initial and boundary conditions, SST, and snow cover, but using 8 different sets of physical schemes. Comparing with the CFSR, member 3 has the smallest biases in cyclone track density and intensity distribution (not shown). Therefore, the physical schemes of member 3 were selected for the WRF simulations in this study. Those physics schemes include: Morrison microphysics, Betts-Miller cumulus parameterization, RRTM long-wave radiation, Goddard short-wave radiation, Mellor-Yamada-Janjic boundary layer physics, Noah land surface physics. Since our future simulations are forced by the data from CMIP5 RCP8.5 experiment, the CO2 concentration in the long-wave radiation scheme (RRTM) for future runs is modified to 936 PPMV, which is the value at the end of 21st century in CMIP5 RCP8.5 scenario, to keep consistent with the input from CMIP5 RCP8.5 experiment.

Chapter 3:

Historical Evaluations and Future Predictions of Extratropical Cyclones

3.1. Historical evaluation of extratropical cyclones in the CMIP5 models

A historical evaluation of the extratropical cyclones in these models is needed to investigate the capability of the CMIP5 models for cyclone simulation. This section provides a comprehensive historical evaluation of cyclone track density, intensity distribution, genesis density, and deepening rate over eastern North America and western Atlantic in CMIP5 models.

3.1.1 Cyclone track density

The cyclone track density for the CMIP5 models are compared with the CFSR for the historical (1979-2004) cool seasons. The cyclone track density for CFSR (Fig. 3.1a), illustrates three regions of high cyclone track density (>5 cyclones per cool season per 50,000 km^2): Over the Great Lakes, along the East Coast of North America and western Atlantic, and the east of southeast Greenland.

The ensemble mean of the 15 CMIP5 models is able to reproduce three similar high track densities, but the amplitude is 10-25% smaller than CFSR (Fig. 3.1b). Meanwhile, the spread (one standard deviation value from the mean) of the CMIP5 models is large over those three regions, ranging from ~1.0 (cyclone per cool season per 50,000 km^2) over the Great Lakes, ~1.2 over east of southeast Greenland, and 0.5-1.0 along the U. S. East Coast. The large spread (> 0.6) over East Coast and western Atlantic is located near the entrance (southwestern) and the two sides (northwestern and southeastern) of the high track density region, which illustrates that there are large uncertainties among these models for the cyclone genesis and the position of the tracks (more onshore of offshore).

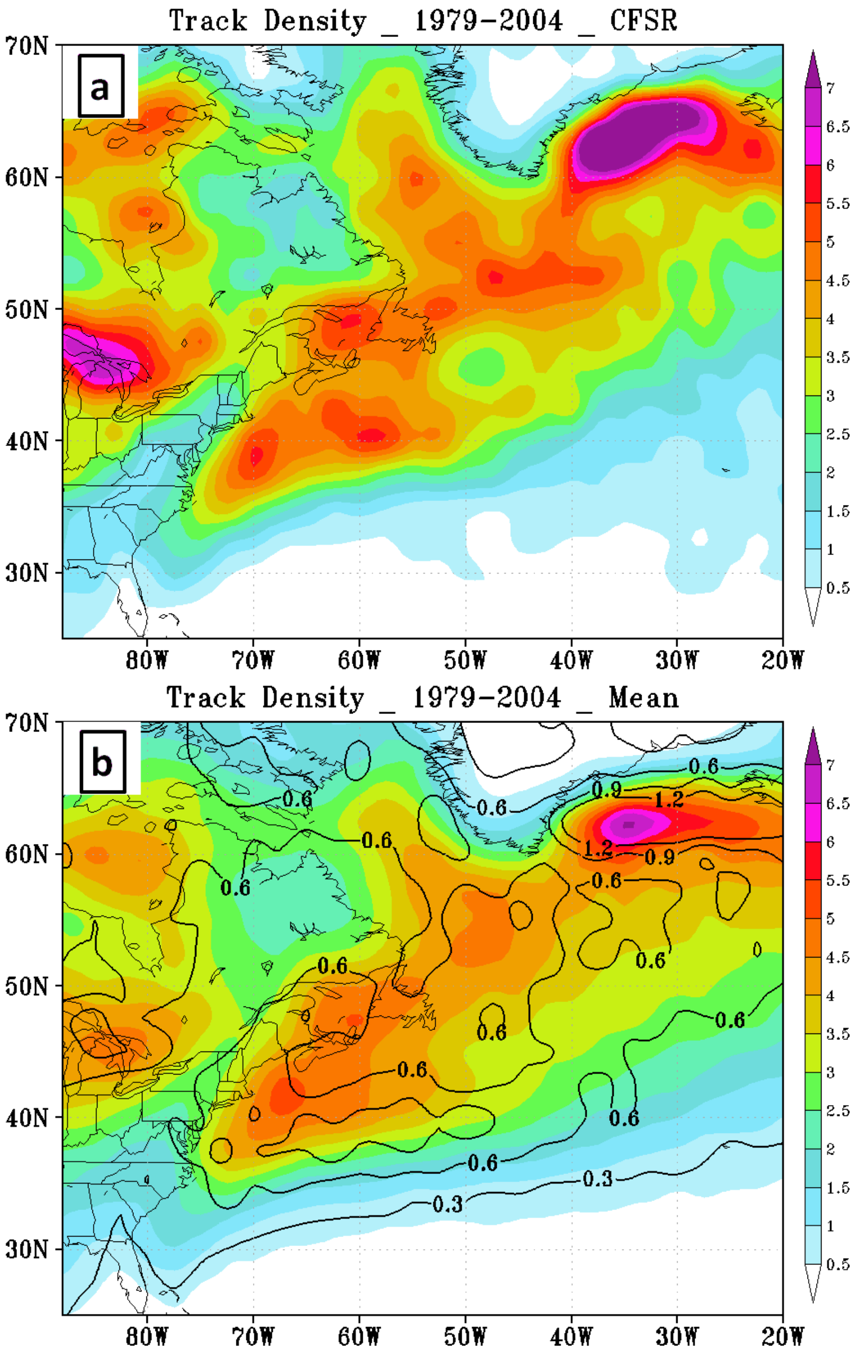

Fig. 3.1: Mean cyclone track density (cyclone per cool season per 50,000 km^2) for the historical period (1979-2004 cool seasons) for (a) CFSR and (b) ensemble mean of the 15 CMIP5 models, contours are the spread (one standard deviation) among models.

The mean track density for the 7 high resolution models (red in Table 2.1) and the 8 lower resolution models are compared to highlight the impacts of model resolution (Fig. 3.2). The mean track density of high resolution models (Fig. 3.2a) has a more well-defined maximum to the north of Gulf Stream along East Coast and to the east of southern Greenland, with the maximum located more offshore of the East Coast and extending to east and northeast. This structure is more similar to the track density of CFSR than the lower resolution models. Although the mean track density of low resolution models (Fig. 3.2b) is also able to produce the track density maximum from east coast to the east of southern Greenland, the track density maximum along East Coast was too far north and too close to the coast of Northeast U.S., and with a larger spread (0.6-1.0 cyclone per cool season per 50,000 km^2) than the higher resolution models. The mean of low resolution models also significantly underestimates the track density maximum around the southeastern Greenland.

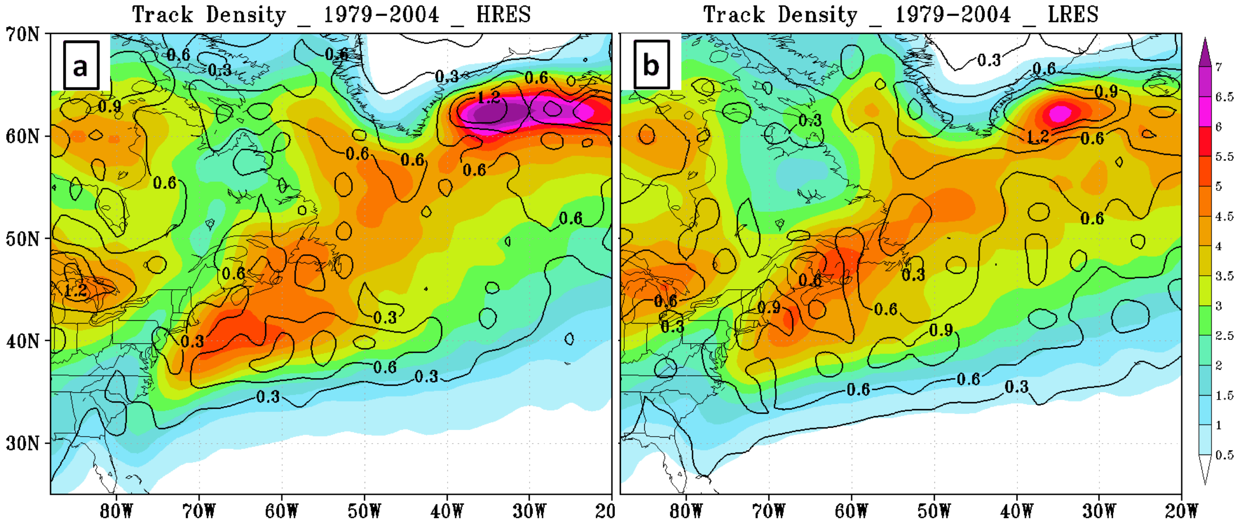

Fig. 3.2: Same as Fig. 3.1, but for (a) the mean of 7 high resolution models (red in Table 2.1) and (b) the mean of 8 low resolution models (black in Table 2.1).

The comparison between IPSL-CM5A-MR (2.5°×1.25°) and IPSL-CM5A-LR (3.75°×1.8°) provides a more accurate estimate for the impacts of model resolution, since the only difference between the two models is resolution, although both of them are relatively low resolution. The track density of IPSL-CM5A-LR (Fig. 3.3a) is concentrated along the East Coast and the density maximum is overestimated. Meanwhile, the IPSL-CM5A-MR (Fig. 3.3b), which has ~50% greater horizontal resolution, reduces the maximum of track density along east coast and extends the track density farther eastward and southward along the U.S. East Coast, which is closer to the CFSR. This result is consistent with Woollings et al. (2010), who found that the storm track shifted southward toward the Gulf Stream when a higher resolution SST is used.

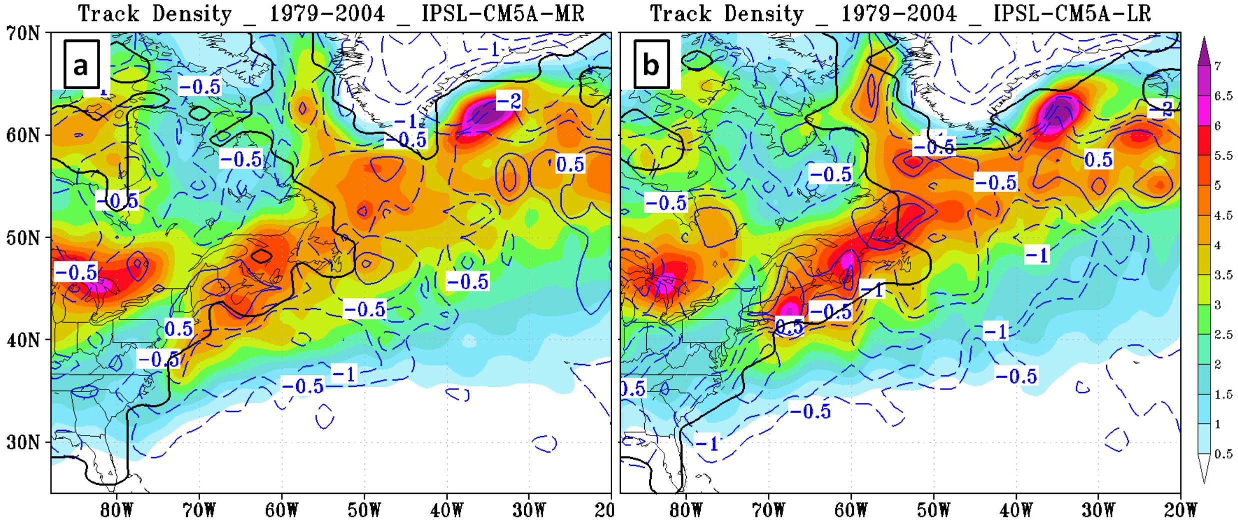

Fig. 3.3: Same as Fig. 3.1, but for (a) IPSL-CM5A-MR and (b) IPSL-CM5A-LR. The bold black solid lines are the coastline in the model. The blue contours are the difference between the model and the CFSR (model minus CFSR).

Fig. 3.4 shows the track density for selected models, including high resolution CCSM4, HadGEM2-ES, and MIROC5, and low resolution INMCM4, NorESM, and MPI-ESM-LR. CCSM4 (Fig. 3.4a) and HadGEM2 (Fig. 3.4c) have a well-defined track density maximum along East Coast just north of the Gulf Stream, starting from ~35°N and extending to east and northeast, which is very close the CFSR.

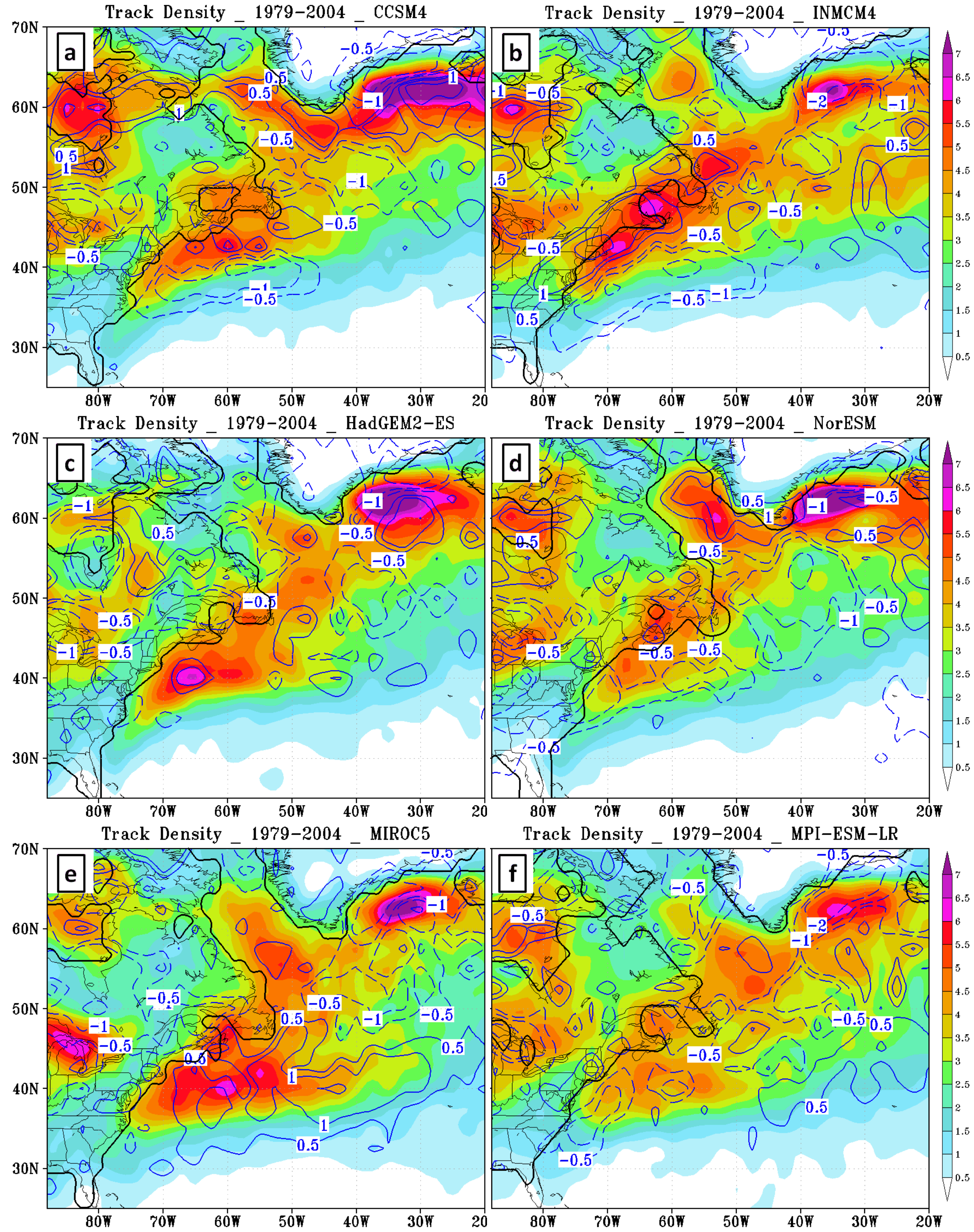

Fig. 3.4: Same as Fig. 3.3, but for the selected high resolution (a) CCSM4, (c) HadGEM2-ES, and (e) MIROC5, and the low resolution (b) INMCM4, (d) NorESM, and (f) MPI-ESM-LR.

The track density of low resolution INMCM4 (Fig. 3.4b) and NorESM (Fig. 3.4d) are similar to IPSL-CM5A-LR (Fig. 3.3b), with a high track density too far north and close to the coast of U.S. Northeast. However, the high resolution MRIOC5 (Fig. 3.4e) overestimates the cyclone track density around East Coast and the eastward extension of the maximum over this region. Meanwhile, different from the other low resolution models, MPI-ESM-LR (Fig. 3.4f) has a cyclone track density more offshore, which is similar to the CFSR. Those differences indicate that the resolution is not the only thing controlling the performance of models, thus other factors (such as physics) are also important.

3.1.2 Cyclone intensity distribution

The cyclone intensity distribution for the CMIP5 models is also compared with the CFSR. The cyclone intensity was evaluated with the minimum central SLP along cyclone track within a specific domain, such as the ECL and ECW. Fig. 3.5 shows the mean cyclone intensity distribution for the CFSR and CMIP5 models within the ECWA region (see Fig. 2.1) for the historical period (1979-2004 cool seasons). The maximum (about 21 cyclones per cool season) for the CFSR (black in Fig. 3.5) is in the 995-1005hPa bin.

Similar with the cyclone track density, the CMIP5 models were divided into two groups to highlight the differences between high resolution and low resolution models for the cyclone intensity distribution of ECWA region. The mean of the 8 low resolution models (red line in Fig. 3.5b) has the maximum in the 985-995hPa bin, with 21.1 cyclones per cool season, which is almost the same as the CFSR (20.7). However, the low resolution models underestimate the number of the weaker (> 995 hPa) and the stronger (< 985 hPa) cyclones. For example, the CFSR has 13.9 cyclones per cool season for the 965-975hPa bin, while low resolution model mean is ~9.7. Meanwhile, the 8 low resolution models have large spread (±1 standard deviation, the red vertical bars in Fig. 3.5a). Even though the mean of those models (21.1 cyclones per cool season) is close to the CFSR for the 985-995hPa bin, the IPSL-CM5A-MR (red dashed line in Fig. 3.5a) has 16.4 and MIROC-ESM-CHEM (blue dashed line in Fig. 3.5a) has 27.5 in this bin.

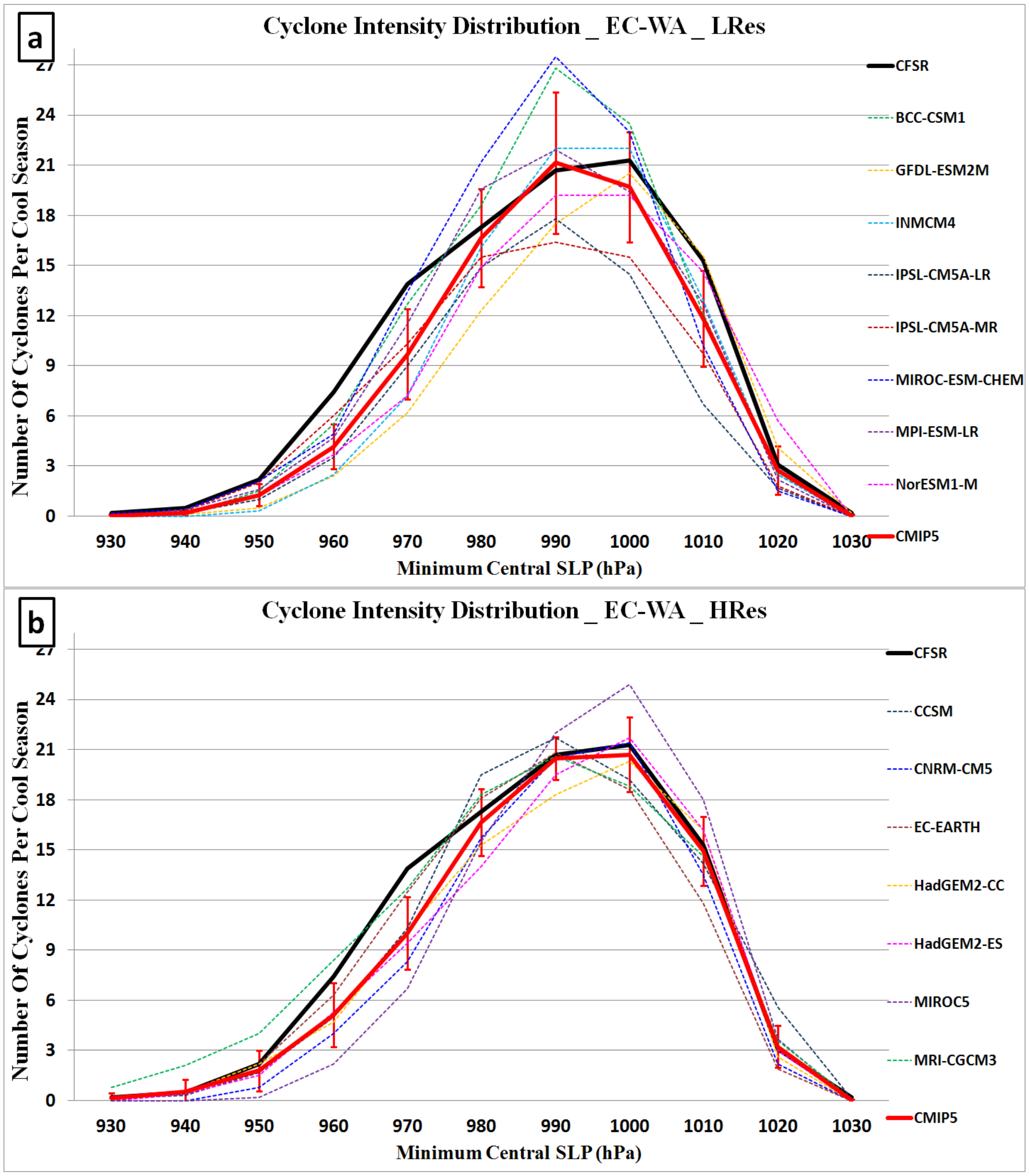

Fig. 3.5: The distribution of cyclone minimum central SLP along the track within ECWA region in Fig. 2.1 for historical period (1979-2004 cool seasons) for (a) CFSR (black line), 8 low resolution CMIP5 models (dashed lines), and the mean of the 8 models (red line); (b) CFSR (black line), 7 high resolution CMIP5 models (dashed lines), and the mean of the 7 models (red line). The red vertical bars are the spread (±1 standard deviation) of the models.

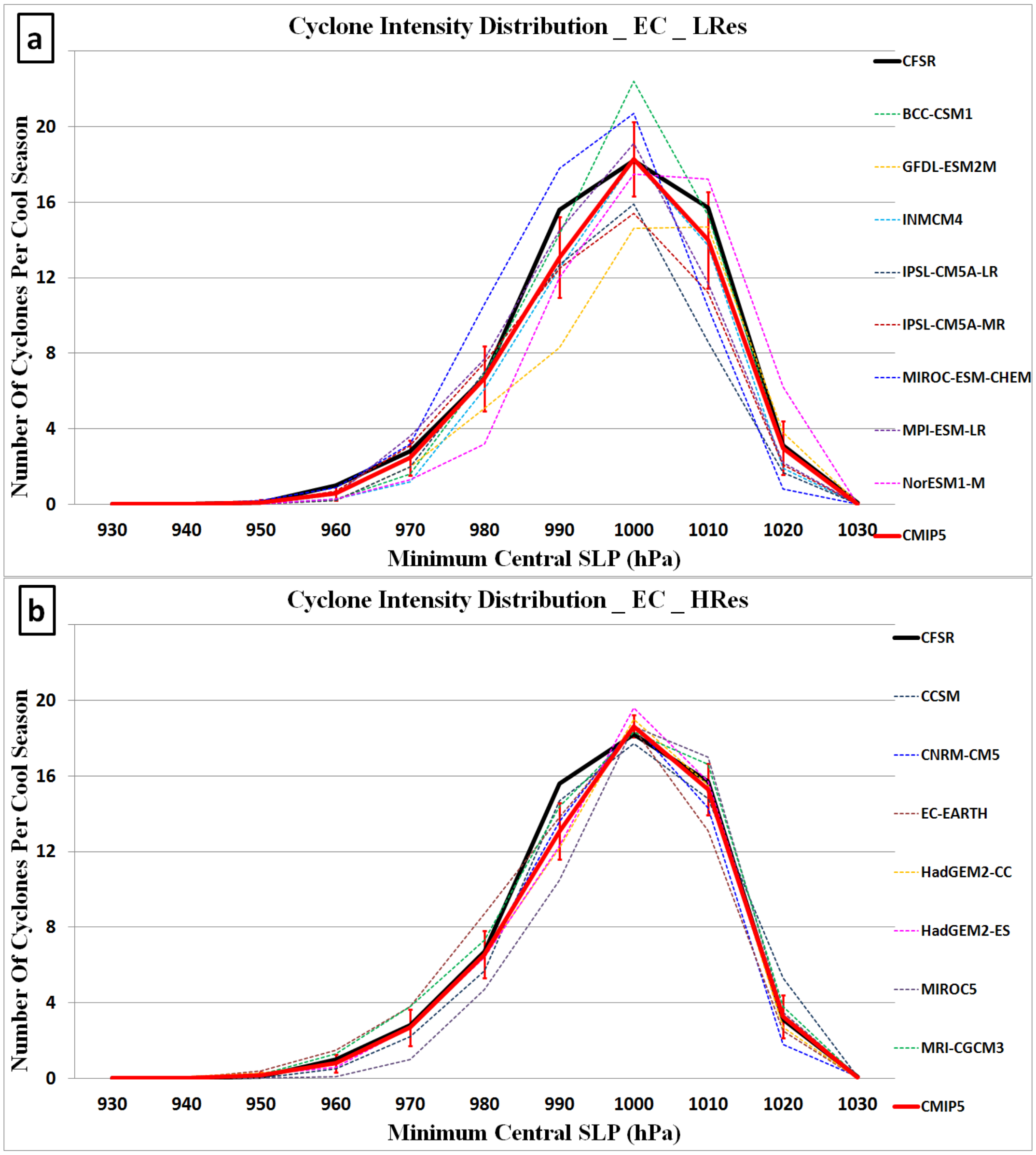

Fig. 3.6: Same as Fig. 3.5, but for the EC (ECL+ECW in Fig. 2.1) region.

The 7 high resolution (1°-1.5°) models have better performance for the cyclone intensity distribution within the ECWA region than the lower resolution models. The mean of these models (red line in Fig. 3.5b) represents most of the cyclones with minimum central SLP > 985 hPa, and the spread for those cyclones is much smaller than the low resolution models. The high resolution models, including the mean and most of the models, still underestimate the number of intense cyclones (< 985 hPa). Only MRI-CGCM3 (green dashed line in Fig. 3.5b) overestimating the more intense cyclones (< 965 hPa). The individual high resolution model may also have large bias, such as MIROC5 (purple dashed line Fig. 3.5b), whose intensity distribution is shifted towards to the weak part, and overestimates the number of cyclones with minimum central SLP > 985 hPa and underestimates the cyclones < 985 hPa significantly.

The intensity distribution for cyclones within the EC (ECL+ECW in Fig. 2.1) region was also calculated and compared with the CFSR (Fig. 3.6). The intensity distribution from CFSR for this EC region is narrower than the larger ECWA region. The mean intensity distribution of the 7 high resolution CMIP5 models is close to the CFSR with small spread (< 1.5 cyclones per cool season), only underestimates the cyclone number for the 985-995hPa bin by about 15% (Fig. 3.6b). However, the intensity distribution of low resolution models is too narrow, underestimating both weak and intense cyclones with large spread (Fig. 3.6a).

3.1.3 Cyclogenesis

As mentioned in Section 3.1.1, there are large uncertainties in track density at the North Atlantic storm track entrance around the middle of the U.S. East Coast, which indicates large variability of cyclogenesis over that region among these CMIP5 models. Therefore, the genesis (defined as the first center of each cyclone track) density was calculated for the CFSR and the 15 CMIP5 models to explore the cyclogenesis in these models.

There are two maxima (> 4 cyclones per 5 cool seasons per 50,000 km^2) for the cyclogenesis density in the CFSR, one along the U.S. East Coast and another to the east of the southeast Greenland (Fig. 3.7a). Along the U.S. East Coast, the high genesis density extends northward from just east of Florida to the east of southern New England (Fig. 3.7a). The mean cyclone genesis density for the 15 CMIP5 models (Fig. 3.7b) has the two similar genesis maxima;

however, the amplitude is weaker. Along the U.S. East Coast, the CMIP5 mean underestimates the cyclogenesis density by 40-50% to the south and 10-20% to the north, with large spread (> 0.6 cyclones per 5 cool seasons per 50,000 km^2) over that region.

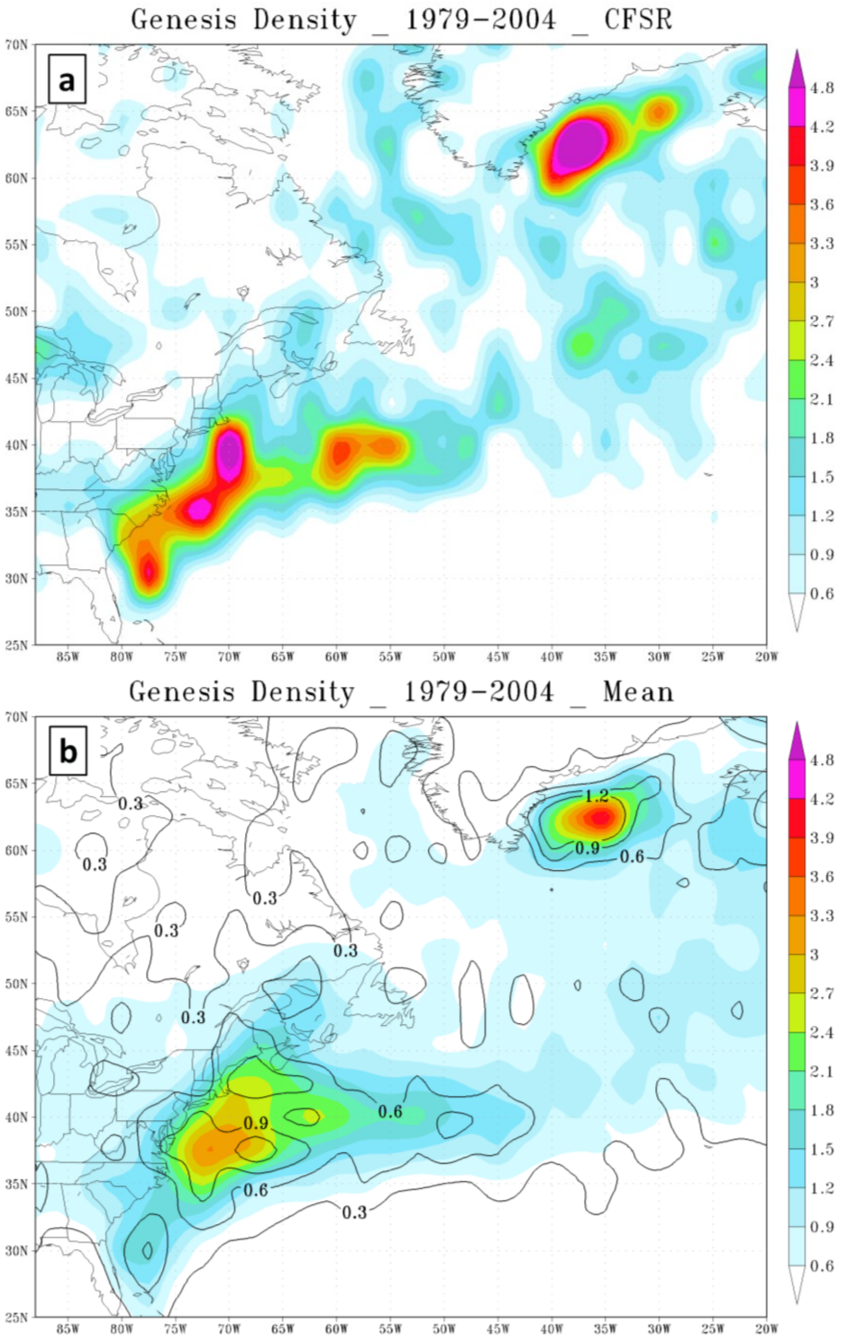

Fig. 3.7: Mean cyclone genesis density (cyclone per 5 cool seasons per 50000 km^2) for the historical period (1979-2004 cool seasons) for (a) CFSR and (b) the ensemble mean of the 15 CMIP5 models, contours are the spread (1 standard deviation) among models.

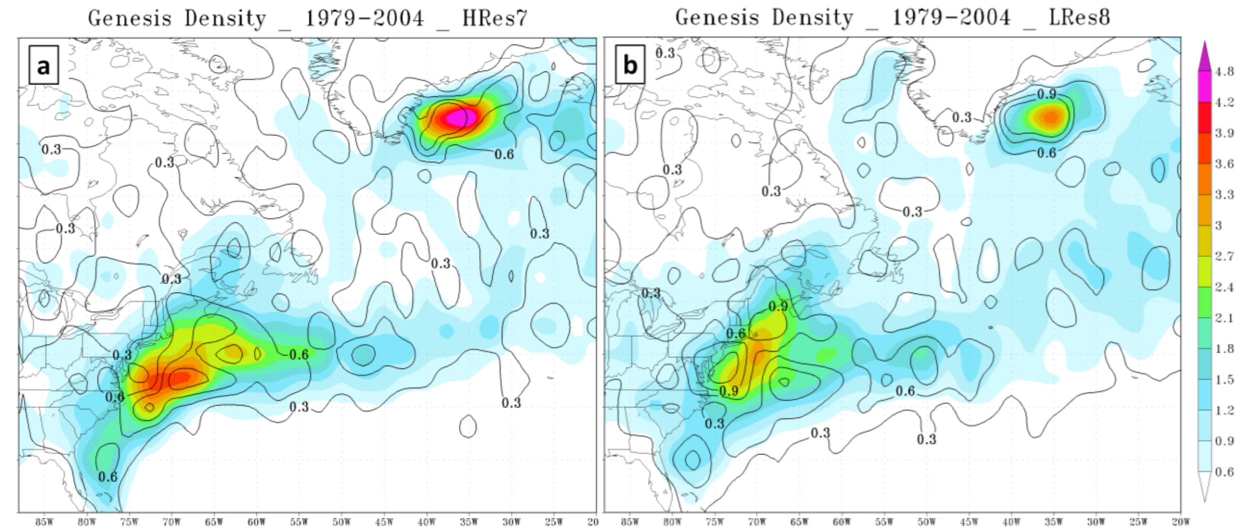

Fig. 3.8: Same as Fig. 3.7, but for (a) the mean of 7 high resolution models (red in Table 2.1) and (b) the mean of 8 low resolution models (black in Table 2.1).

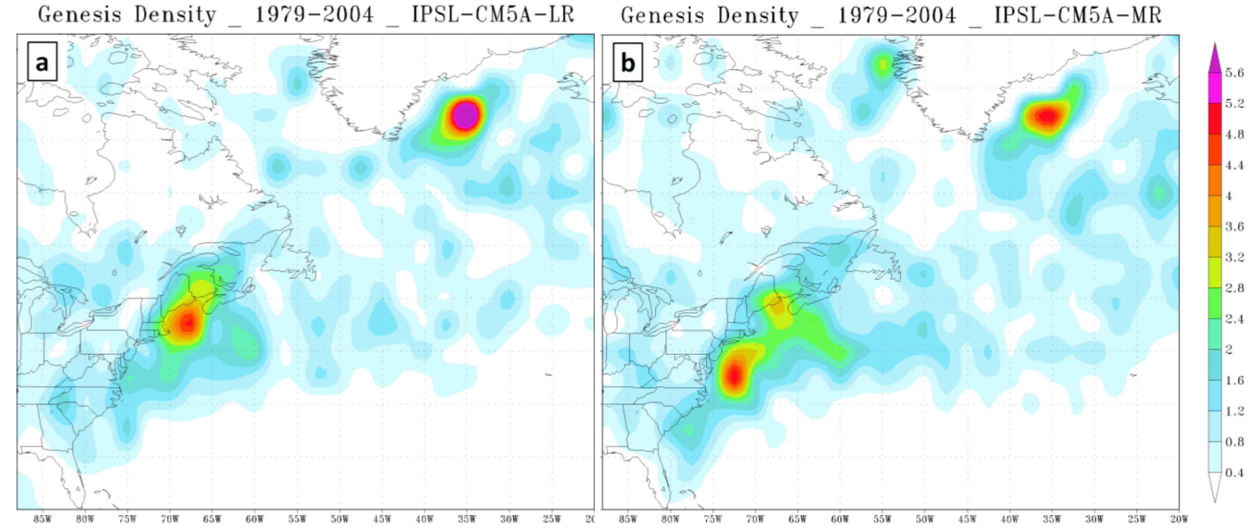

Fig. 3.9: Same as Fig. 3.7, but for (a) IPSL-CM5A-MR and (b) IPSL-CM5A-LR.

The cyclogenesis density for the mean of 7 high-resolution (red in Table 2.1) models and 8 low resolution models (black in Table 2.1) were compared to highlight the impacts of model resolution. The mean genesis density of the 7 high resolution models (Fig. 3.8a) is better than the mean of all 15 CMIP5 models. The mean of high resolution models has a larger genesis density (> 3.6 cyclones per 5 cool seasons per 50,000 km^2) along U.S. East Coast, which is closer to the

CFSR. The mean of low resolution models (Fig. 3.8b) underestimates the genesis density significantly, with a maximum of about 3.0 located to the north of U.S. East Coast.

Similar with the cyclone track density, the comparison of genesis density between IPSL-CM5A-MR and IPSL-CM5A-LR provides another estimate for the impacts of model resolution. The maximum center of cyclone genesis density along U.S. East Coast for IPSL-CM5A-LR (Fig. 3.9b) is shifted too far north and close to the Northeast U.S. coast, while the genesis density maximum along U.S. East Coast of IPSL-CM5A-MR (Fig. 3.9a) is closer to the CFSR.

3.1.4 Cyclone deepening

The comparison of cyclone intensity distribution for the CMIP5 models and the CFSR suggests that the cyclones in CMIP5 models tend to be weaker than the CFSR. It indicates that the cyclone deepening in CMIP5 models is likely slower than the deepening in the CFSR. To explore this, the distribution of cyclone deepening rates in the CMIP5 models, which was defined as the change of cyclone central SLP per 6 hours, was compared with that in the CFSR. The spatial density for the rapid deepening (deepening > 5 hPa/6h) in CMIP5 models was also calculated and compared with the CFSR.

Fig. 3.10 shows the distribution of cyclone deepening rates for the ECWA region during historical period (1979-2004 cool seasons). The CFSR (black line in Fig. 3.10) has the maximum (> 160 cases per cool season) at the -2 and 0 hPa/6h bins. The distribution of deepening rates in the 8 low-resolution CMPI5 models (black in Table 2.1) is too narrow and too concentrated at the -2 and 0 hPa/6h (Fig. 3.10a), with a large negative bias for the more rapid deepening storms (deepening > 5 hPa/6h).

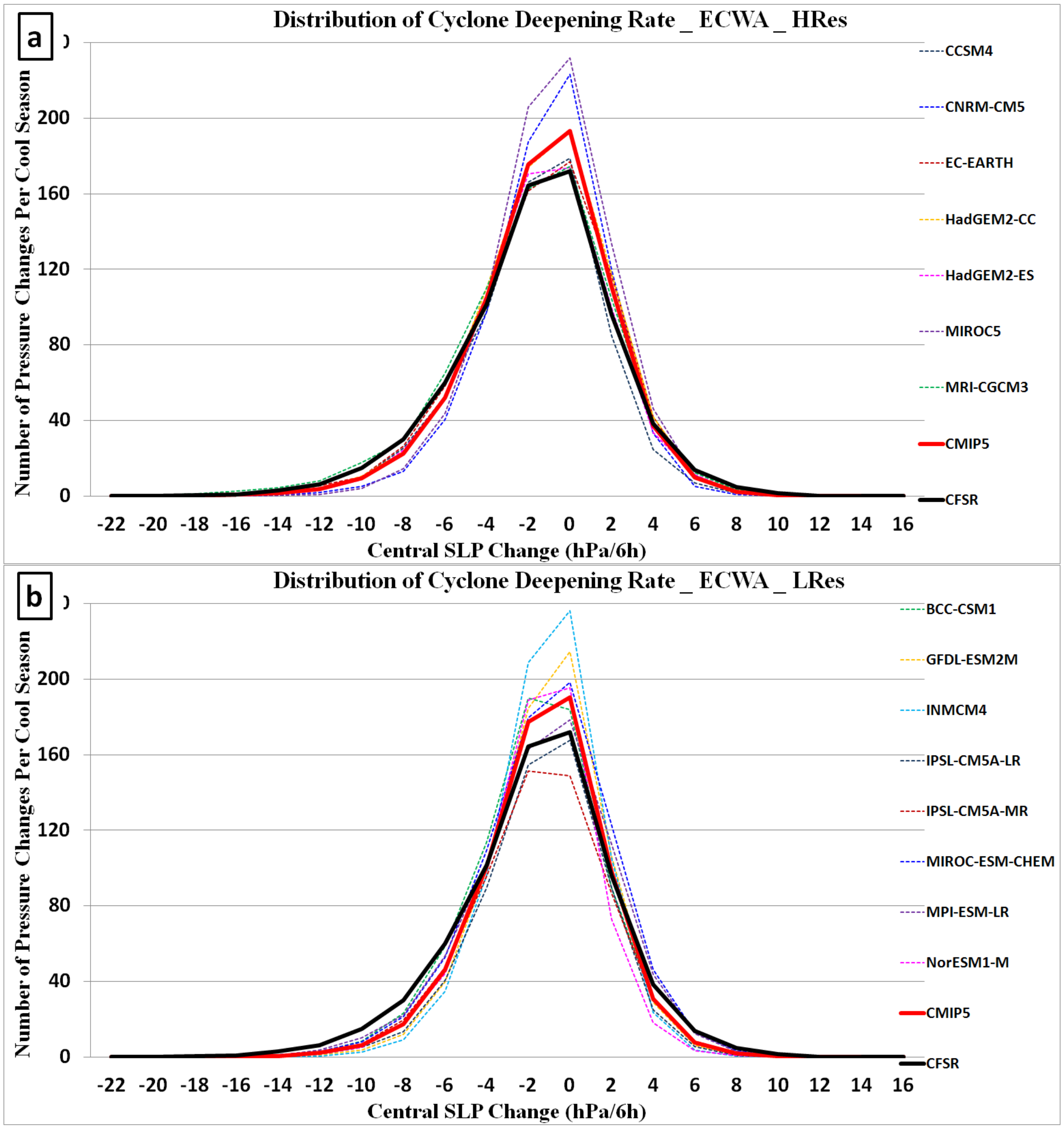

Fig. 3.10: The distribution of cyclone deepening rate within ECWA for historical period (1979-2004 cool seasons) for (a) CFSR (black line), 8 low resolution CMIP5 models (dashed lines), and the mean of the 8 models (red line); (b) CFSR (black line), 7 high resolution CMIP5 models (dashed lines), and the mean of the 7 models (red line).

The mean of the 7 high resolution models (red in Table 2.1) also overestimates for the frequency at the -2 and 0 hPa/6h bins by about 10% (Fig. 3.10b), and most of that positive bias is from two models, MIROC5 (dashed purple line) and CNRM-CM5 (dashed blue line). Those two models also have a large negative bias for the more rapid deepening storms (deepening > 5 hPa/6h). This is consistent with their cyclone intensity distribution (Fig. 3.5a), since the cyclones in those models are too weak. Meanwhile, the MRI-CGCM3 (dashed green line) overestimates the cyclone deepening rate slightly (Fig. 3.10a) and also overestimates the number of intense cyclones (Fig. 3.5a).

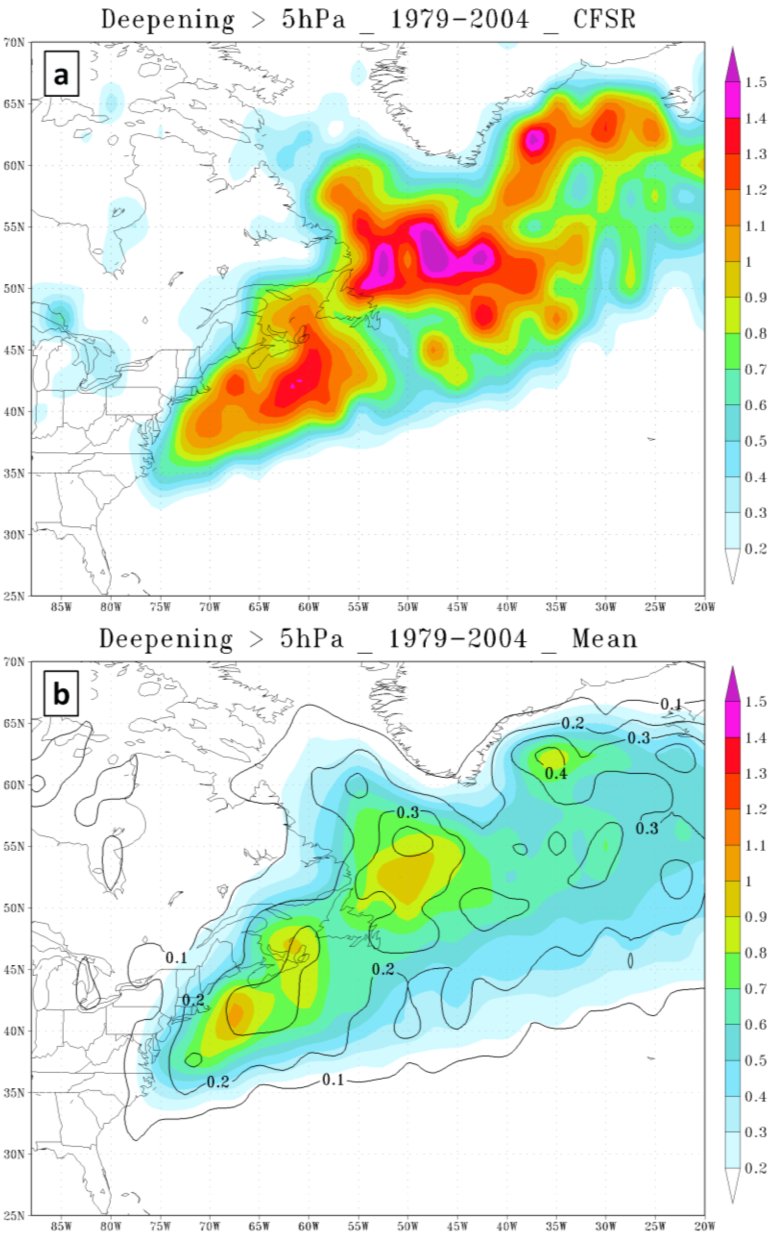

Fig. 3.11: Mean rapid deepening (> 5 hPa/6h) density (cyclone per cool season per 50,000 km^2) for the historical period (1979-2004) for (a) CFSR and (b) ensemble mean of the 15 CMIP5 models, contours are the spread (one standard deviation) among models.

Most of the rapid deepening (deepening > 5 hPa/6h) cases in the CFSR is located from just east of Northeast U.S. northeastward to the east of southeast Greenland (Fig. 3.11a). The mean of the 15 CMIP5 models has a very similar spatial distribution for the density of rapid deepening cases, but significantly underestimates the amount by 30-50% (Fig. 3.11b).

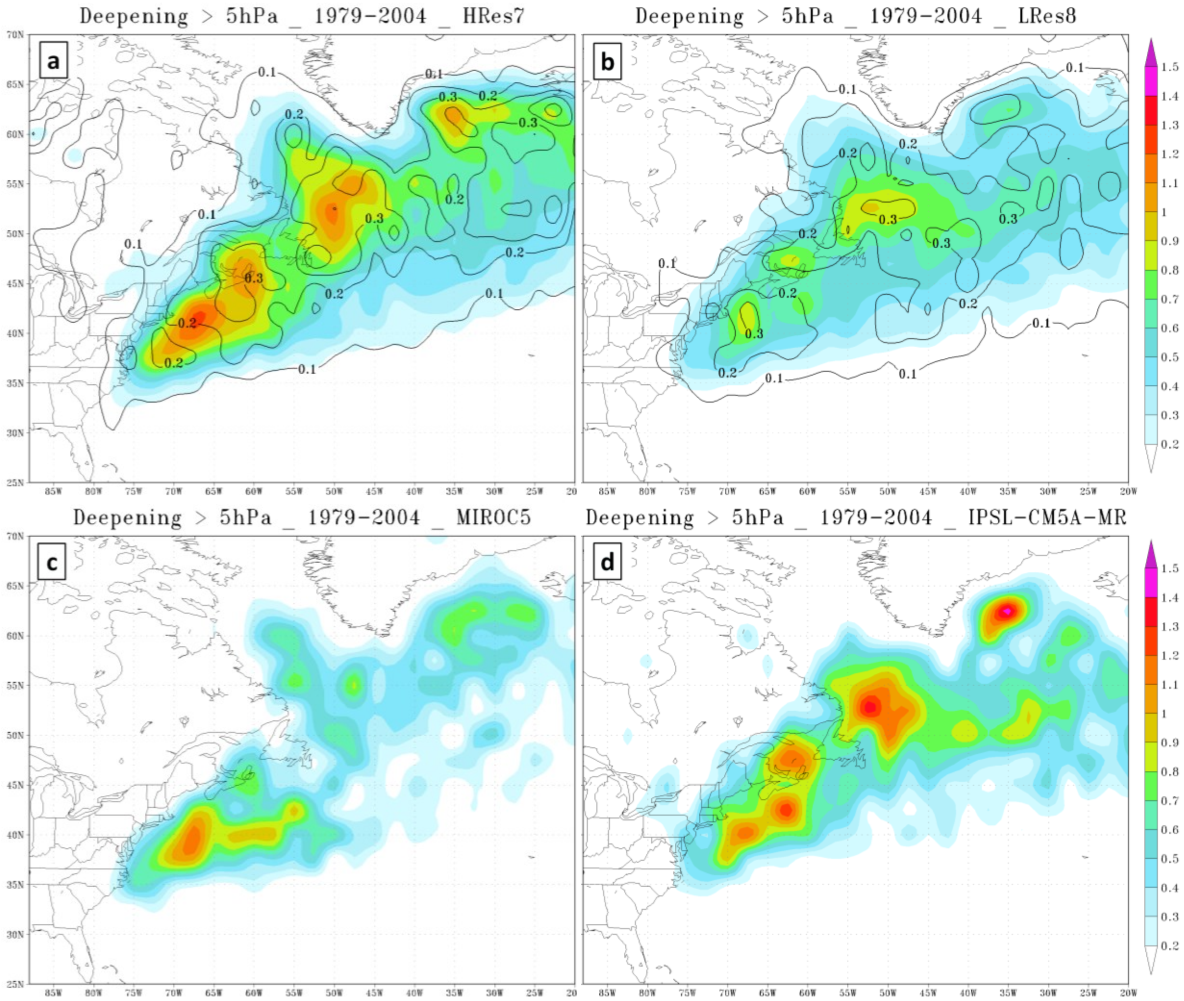

Fig. 3.12: Same with Fig. 3.11, but for (a) the mean of the 7 high resolution models; (b) the mean of the 8 low resolution model; (c) MIROC5; (d) IPSL-CM5A-MR.

The means of rapid deepening density for the high and low resolution models were also compared to explore the impact of model resolution. The high resolution models underestimate the rapid deepening density by 20-30% (Fig. 3.12a), while the low resolution models underestimate by nearly a factor of 2 (Fig. 3.12b). However, consistent with the results for cyclone track density and intensity distribution, the model resolution is not the only factor controlling the rapid deepening. The rapid deepening rate density of IPSL-CM5A-MR (2.5°×1.25°, Fig. 3.12d) is closer to the CFSR than the density of MIROC5 (1.4°×1.4°, Fig. 3.12c), not just for the amplitude but also for the spatial distribution.

3.1.5 Verification metrics

Section 3.1.1 – 3.1.4 provides the comparisons of cyclone track density, intensity distribution, genesis and deepening rate for the CFSR and the CMIP5 models, but a quantitative comparison is needed to evaluate the model performance. In this section, the model performance is evaluated using four indices for the cyclones within ECWA region (Fig. 2.1) with respect to the CFSR: the spatial correlation of cyclone track density (TR), the absolute difference of the cyclone track density (TD), the correction for the distribution of cyclone minimum SLP (PR), and the absolute difference for the distribution of cyclone minimum SLP (PD).

The evaluation is based only on the cyclone track density and intensity distribution. The calculation for the four indices is described in Section 2.3, and Table 3.1 shows the results for individual models, the mean of all 15 models (Mean), the mean of 7 high resolution models (HRes7), the mean of 8 low resolution models (LRes8), and the mean of the 7 best models (hereafter Best7). The models are ordered according to their final ranking, which is the average of their rankings for TR, TD, PR and PD. EC-EARTH has the best overall performance, since it has the best spatial distribution of cyclone track density (TR=0.949), and relatively good TD, PR and PD, all of these are in top 5. The low resolution IPSL-CM5A-LR (3.75°×1.8°) has the worst performance, since its track density is too concentrated and shifts to far north (Fig. 3.3b) and it significantly underestimates the number of cyclones in all intensity bins (Fig. 3.5b).

Table 3.1: The verification of the CMIP5 models for TR, TD, PR and PD. The CMIP5 member ranking is presented for each of these verification metrics, and the models are ordered according to their final ranking. The verification of the CMIP5 mean, Best7, high resolution seven (HRes7, in red), and low-resolution eight (LRes8) models is also presented. The Rk-TR, Rk-TD, Rk-PR and Rk-PD are the ranking for TR, TD, PR and PD respectively.

Models	**TR**	**TD**	**PR**	**PD**	***Rk-TR***	***Rk-TD***	***Rk-PR***	***Rk-PD***
EC-EARTH	0.9493	0.532	0.9889	3.13	1	4	2	3
MRI-CGCM3	0.9091	0.517	0.9920	1.90	9	2	1	1
CNRM-CM5	0.9415	0.513	0.9797	5.23	2	1	7	7
MPI-ESM-LR	0.9404	0.553	0.9831	3.77	3	6	5	4
HadGEM2-ES	0.9284	0.519	0.9812	4.10	6	3	6	6
HadGEM2-CC	0.9108	0.555	0.9873	4.03	8	7	4	5
CCSM4	0.9180	0.651	0.9759	3.07	7	11	9	2
IPSL-CM5A-MR	0.9325	0.708	0.9879	8.20	4	12	3	13
BCC-CSM1	0.9035	0.544	0.9764	5.97	12	5	8	8
INMCM4	0.9081	0.577	0.9631	6.07	11	8	10	9
GFDL-ESM2M	0.9307	0.588	0.9460	8.43	5	9	15	14
NorESM1	0.9089	0.747	0.9629	6.57	10	13	11	10
MIROC5	0.8884	0.640	0.9469	7.10	14	10	14	11
MIROC-ESM-CHEM	0.8839	0.783	0.9609	7.50	15	14	12	12
IPSL-CM5A-LR	0.8987	0.879	0.9594	10.93	13	15	13	15
Mean	**0.9667**	**0.340**	**0.9868**	**3.67**				
Best7	**0.9634**	**0.352**	**0.9932**	**2.80**				
HRes7	**0.9614**	**0.358**	**0.9899**	**2.82**				
LRes8	**0.9580**	**0.379**	**0.9828**	**4.89**				

Consistent with the results in previous sections, the mean of the 7 high resolution models (HRes7) tends to have better performance than the mean of the 8 low resolution models (LRes8). Six of the Best7 are high resolution models, with only the high resolution MIROC5 having a low ranking because of its large biases for both spatial track density and intensity distribution as described in Section 3.1.1 and 3.1.2. Although the mean of all 15 models (Mean) is slightly better than the Best7 for the spatial track density, the Best7 has lower errors than the Mean for cyclone intensity, especially for the PD. A seven worst models (Worst7) category, which includes the models that finished in the bottom seven of the verification ranking (Table 3.1), is also defined and compared with the Best7.

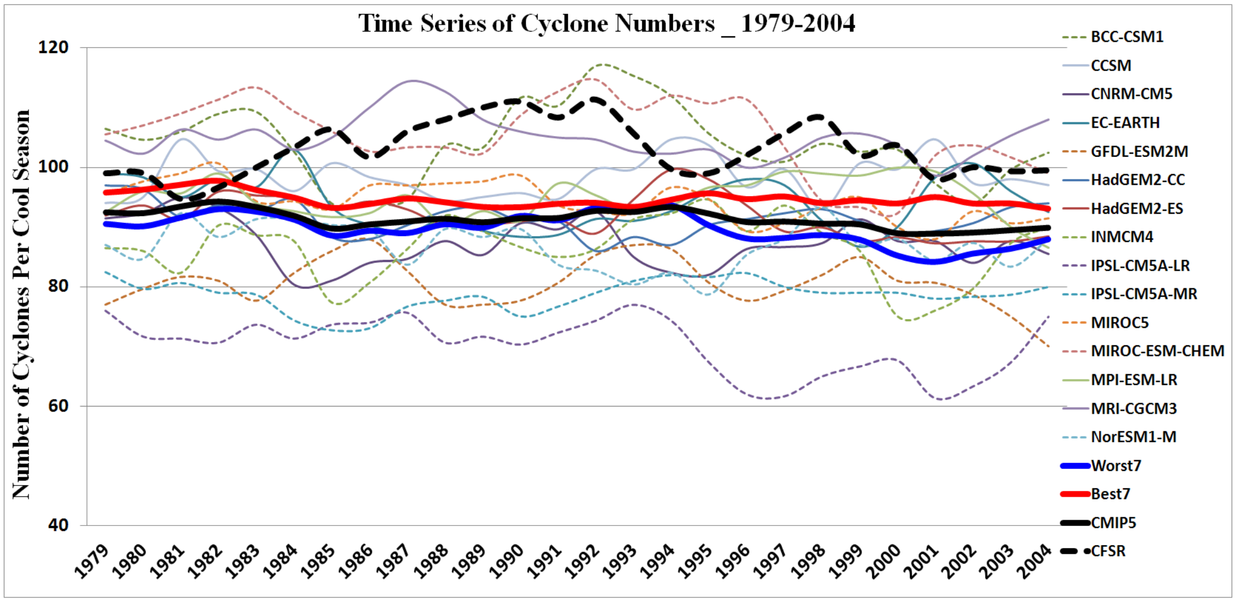

Fig. 3.13: Time series for the 1979-2004 cool seasons showing the numbers of cyclones per cool season within the ECWA region in Fig. 2.1 for the CFSR (black dashed line), mean of all CMIP5 members (black solid line), Best7 (red solid line), Worst7 (blue solid line), and the individual CMIP5 members (Best7 members solid lines and Worst7 dashed lines).

Fig. 3.13 shows a time series of the number of cyclones per cool season within the ECWA box in Fig. 2.1. There is a slight upward trend in cyclones in the CFSR from 1979 to 1991 (10-15% increase), but there has been a slight downward trend since the early 1990s (5-10%). Overall, the Best7 better simulates the number of cyclones compared to the CMIP5 and Worst7 means, but all means underestimate number of cyclones and there is relatively large (30-40%) spread among all of the models.

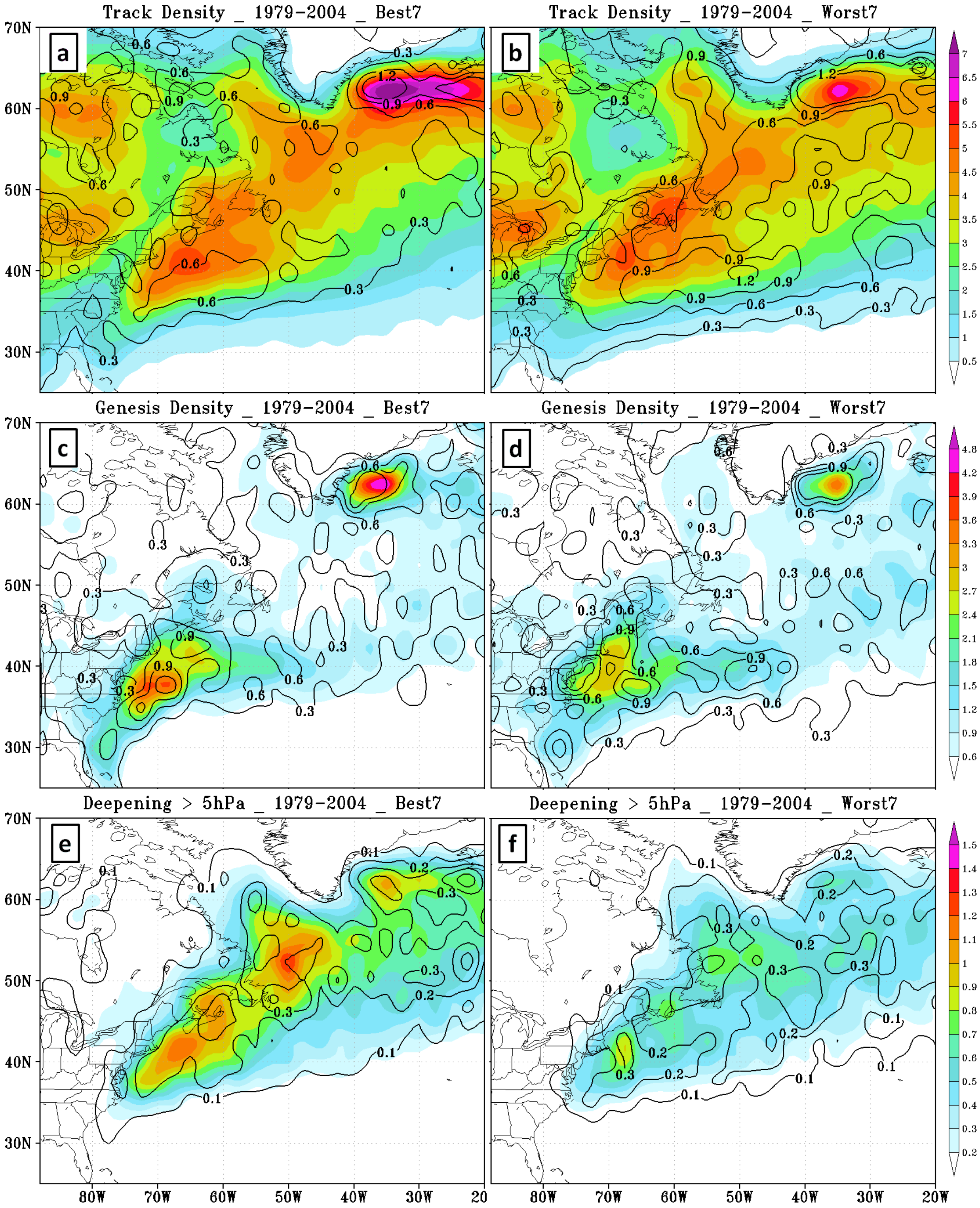

Fig. 3.14: From top to bottom: cyclone track density (cyclone per cool season per 50000 km^2), cyclone genesis density (cyclone per 5 cool seasons per 50,000 km^2), and cyclone rapid deepening rate density (cyclone per cool season per 50,000 km^2) for the historical period (1979-2004 cool seasons). The left panel is for the Best7 and the right panel is for the Worst7. The contours are the spread (one standard deviation) among models.

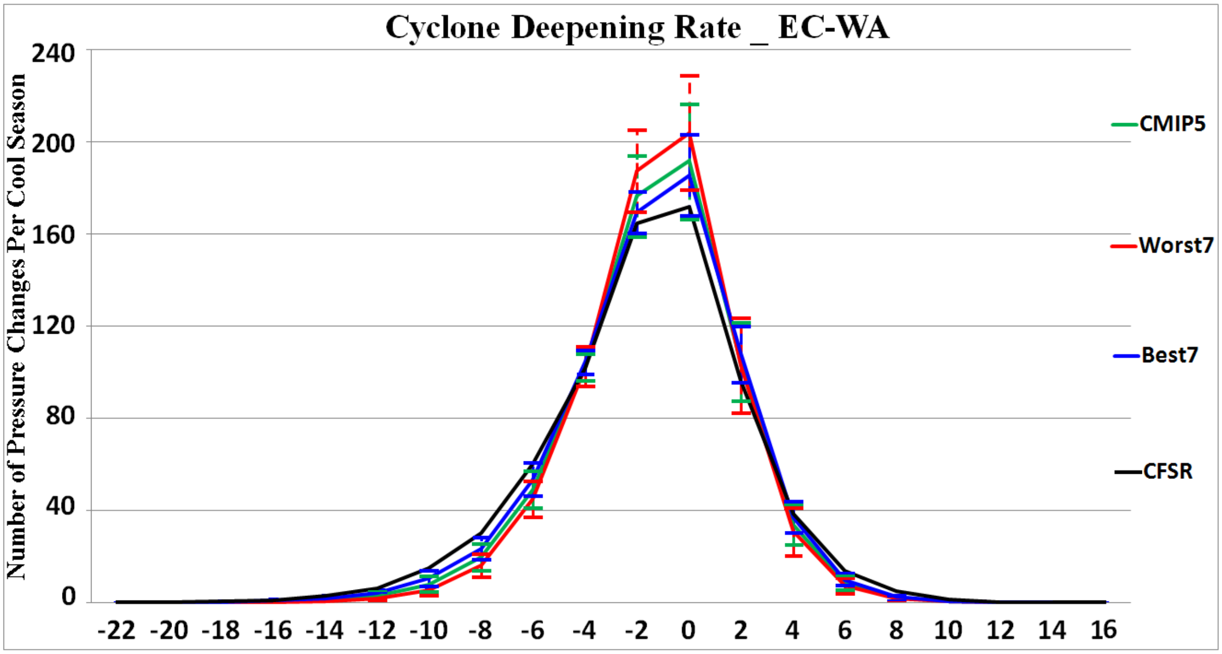

Fig. 3.15: Same as Fig. 3.10, but for the CFSR (black), the mean of all 15 CMIP5 models (green), the mean of Worst7 (red), and the mean of Best7 (blue). The vertical bars are the spread (±1 standard deviation) among the models.

Fig. 3.14 shows the comparison of cyclone track density, genesis density, and rapid deepening rate density between the Best7 and the Worst7. Overall, the Best7 has better performance than the Worst7. The track density maximum along east coast of North America in Worst7 is shifted to the north and it is too close to the U.S. Northeast. The amplitude in genesis density in the Best7 is closer to the CFSR, and the genesis maximum along East Coast in the Worst 7 is shifted too far north. The Worst7 underestimates the rapid deepening rate significantly, which is consistent with the distribution of the deepening rate (Fig. 3.15). The cyclone deepening rate distribution of Best7 (blue) is closer to the CFSR than the mean of all 15 models and the Worst7.

The Worst7 models underestimate the cyclone track density, intensity and rapid deepening rate significantly, and also have larger bias for the position of cyclone track and genesis density. Some of the important reasons, such as the baroclinicity and upper level jet, are explored for three of the Worst7 models in the following paragraphs.

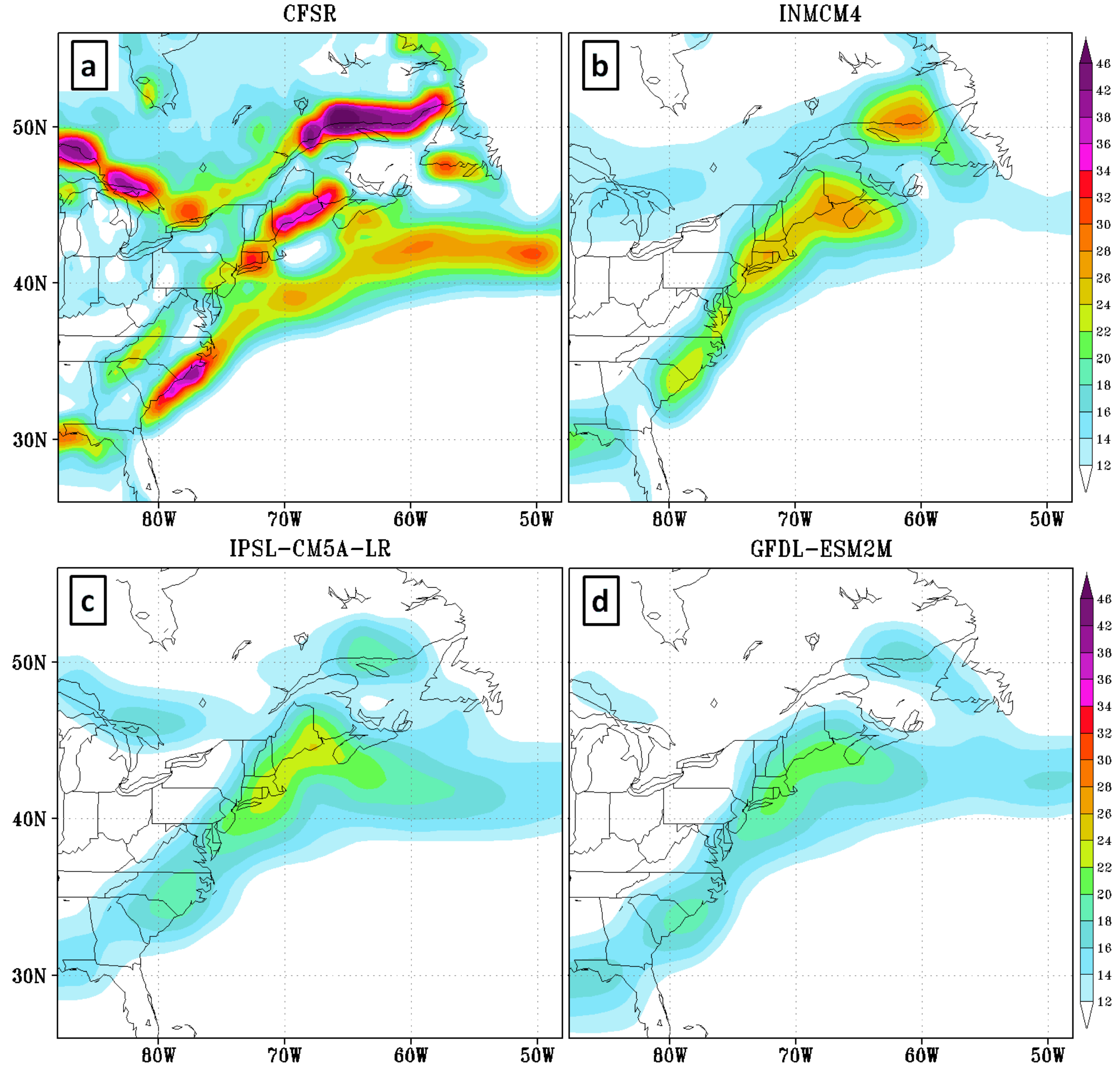

Fig. 3.16: The surface temperature gradient (K/1000km) for the (a) CFSR, (b) INMCM4, (c) IPSL-CM5A-LR, and (d) GFDL-ESM2M.

In the CFSR, there are four surface temperature gradient maxima (> 34 K/1000km) over eastern North America and western Atlantic: over the north coast of the Gulf of Saint Lawrence, over north side of Lake Superior and Lake Huron, at the southeastern of U.S. East Coast, and at the northeastern of U.S. East Coast during historical cool seasons (Fig. 3.16a). There is also a strong temperature gradient over the north of Gulf Stream, extending from the maximum at the southeastern of U.S. East Coast to the northeast. The CFSR has an Eady growth rate maximum (~0.95 day^{-1}) just east of the U.S. Northeast, and the upper level jet (42 m/s) over the middle latitudes (~40°N) of the U.S. East Coast (Fig. 3.17a).

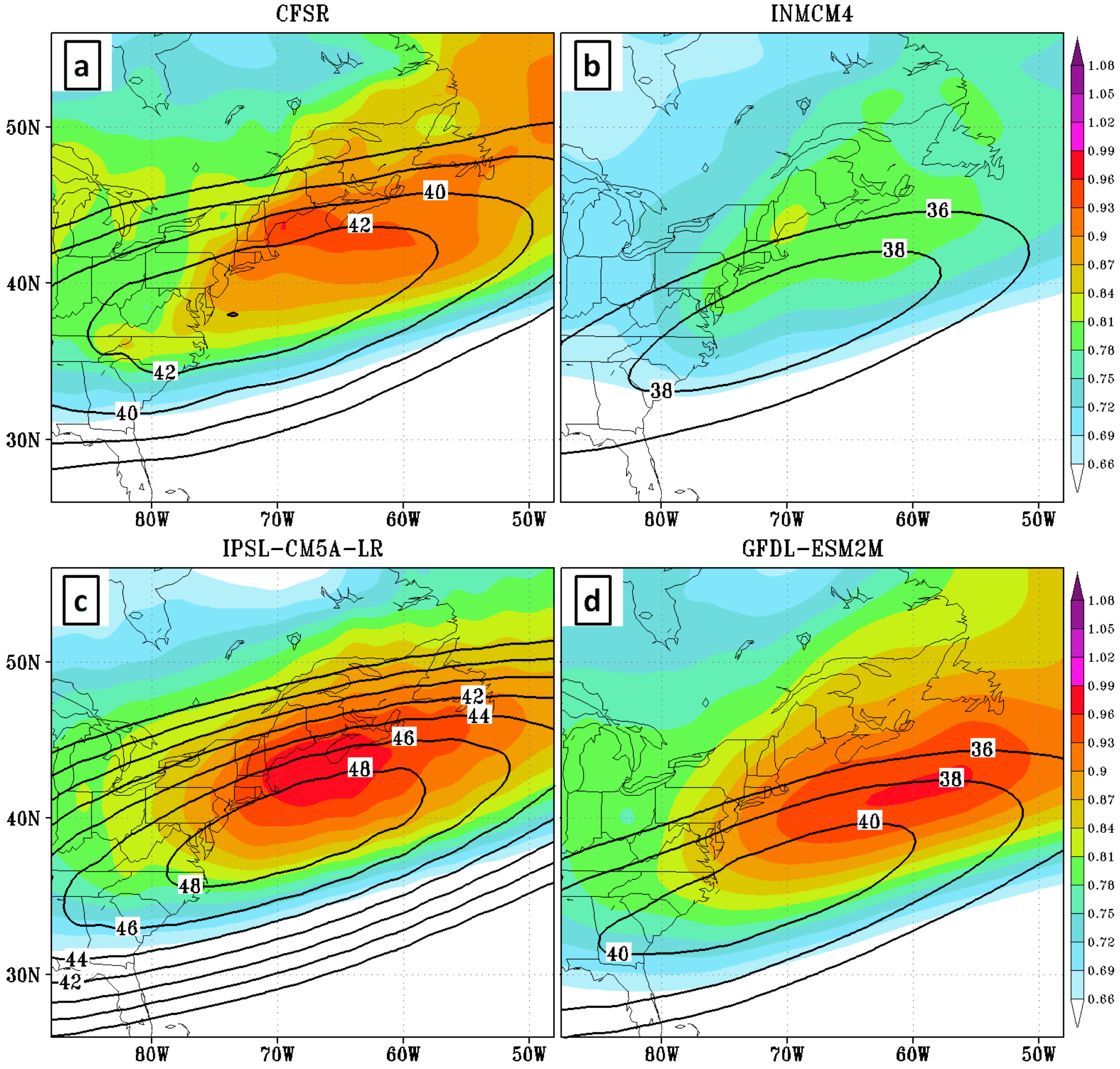

Fig. 3.17: Same as Fig. 3.16, but for the Eady growth rate at 850-500hPa (day^{-1}, colors) and the 250hPa wind speed (m/s, contours).

IPSL-CM5A-LR has only one surface temperature gradient maximum of ~22 K/1000km at the northeastern of U.S. East Coast (Fig. 3.16c) which is only about 60% of the CFSR at the same region. The surface temperature gradient in IPSL-CM5A-LR over the other regions is even weaker, < 50% of the CFSR. The cyclone track density maximum in IPSL-CM5A-LR (Fig. 3.3b) along east coast of North America is located at almost the same region of the temperature gradient maximum in this model. However, the maxima of the Eady growth rate (~1 day^{-1}) and the upper level jet (~48 m/s) in IPSL-CM5A-LR (Fig. 3.17) are stronger than the CFSR.

The surface temperature gradient in GFDL-ESM2M (Fig. 3.16d) is even weaker than IPSL-CM5A-LR, only 30-50% of the CFSR over those gradient maxima regions. The maximum of Eady growth rate (~1 day^{-1}) in GFDL-ESM2M is stronger than the CFSR, while the upper level jet maximum (~40 m/s) is slightly weaker than the CFSR (Fig. 3.17d). Meanwhile, both of the maxima for Eady growth rate and upper level jet are shifted to south by 300-500 km and more offshore than the CFSR. As a result, GFDL-ESM2M underestimates the cyclone frequency along the East Coast by 20-35%, but the track density maximum is not as concentrated as the IPSL-CM5A-LR and is more offshore (not shown).

The surface temperature gradient along the East Coast of U.S. in INMCM4 with a maximum of ~27 K/1000km is stronger than the previous two models, but still concentrated just along the coast of U.S. Northeast (Fig. 3.16b). Meanwhile, the maxima of the Eady growth rate (~0.82 day^{-1}) and upper level jet (~38 m/s) in INMCM4 (Fig. 3.17b) are too weak comparing to the CFSR. Hence, this model has the cyclone tracks concentrated just along the coast of U.S. Northeast (Fig. 3.4b) and underestimates the cyclone intensity significantly (Fig. 3.5a).

All of the Worst7 models significantly underestimate the surface temperature gradient, which is important to the cyclogenesis and developing. Some models, such as GFDL-ESM2M and IPSL-CM5A-LR, have too weak surface temperature gradient (only 30-60% of the CFSR) with only one maximum at the northeastern of U.S. East Coast. Some other models, such as INMCM4, have too weak baroclinicity at low troposphere and/or too weak upper level forcing, although they have slightly stronger surface temperature gradient than the other Worst7 models. More studies are needed to have a comprehensive understanding to the performance of these CMIP5 models in extratropical cyclones.

3.2. Future changes of the cyclones in CMIP5 models

The CMIP5 models are able to simulate the extratropical cyclone over eastern North America and western Atlantic for the cyclone track density, intensity distribution, genesis density and deepening rate, especially for the Best7 which has much smaller biases than the Worst7. Therefore, the results of Best7 are highlighted to explore the future changes of the extratropical cyclones over this region.

However, some studies (Stainforth et al. 2007; Reifen and Toumi 2009; Weigel et al. 2010) suggested that there is no evidence that any subset of models delivers significant improvement in prediction accuracy compared to the total ensemble and it is inappropriate to apply any calibrate or weight to models to produce forecast. Therefore, the results of Best 7 are highlighted, and the results for the mean of all 15 models and the Worst7 are also calculated and discussed. The future changes of extratropical cyclones are investigated for three future periods in 21st century, early (2009-2038), middle (2039-2069), and late (2069-2098) 21st century. The future changes are defined as the difference between future period and historical period (future minus historical, 1979-2004 cool seasons).

3.2.1 Future changes of cyclone track density and genesis density

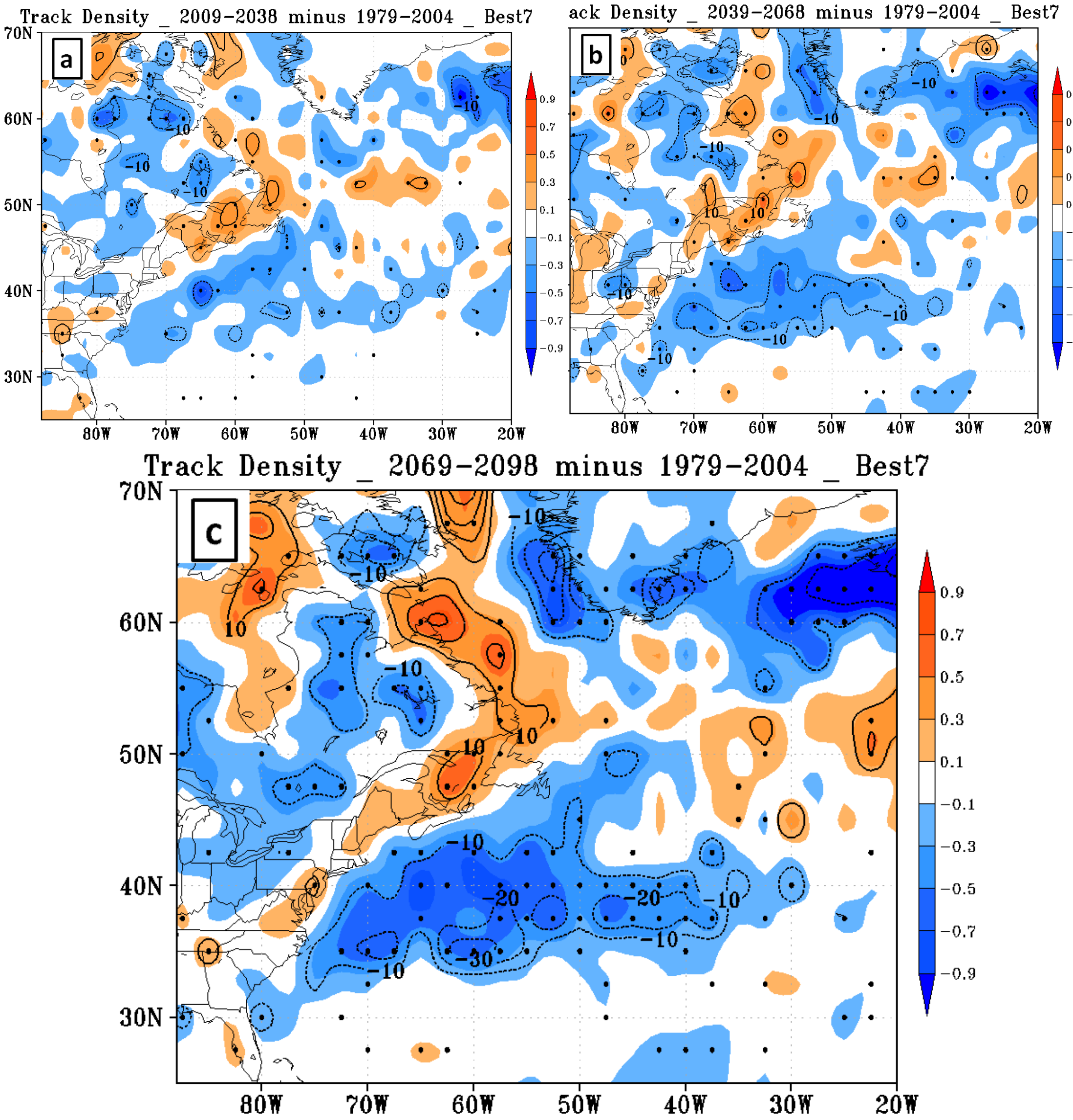

Fig. 3.18: The future changes of cyclone track density (shaded per cool season per 50,000km2) for the Best7 mean between the (a) 2009-2038, (b) 2039-2068, and (c) 2069-2098 cool seasons and the historical (1979-2004) and percent change (contoured every 10%). The dots are locations in which six of the seven Best7 models agree with the sign of the change.

Figure 3.16 shows the future changes of cyclone track density for the Best7. For the early 21st century (2009-2038 cool seasons), there is a 0.2-0.8 per season (5%-10%) reduction in cyclone track density over western Atlantic near the Gulf Stream (Fig. 3.18a). Meanwhile, there is a 5-10% increase in the track density around southeast Canada (Fig. 3.18a). During middle 21st century (2039-2068 cool seasons), the changes are larger (Fig. 3.18b), with a 10-15% reduction over the western Atlantic. By late 21st century, there are 10%-20% fewer extratropical cyclones over much of the western Atlantic storm track and the east of southeastern Greenland, with high model agreement (at least 6 of the seven Best7 models agree with the sign of the change) among models (Fig. 3.18c). Meanwhile, there are increases in the track density of 5-10% along the U.S. East Coast and 10-20% along the eastern Canadian coast, with high agreement among models for part of this region (Fig. 3.18c).

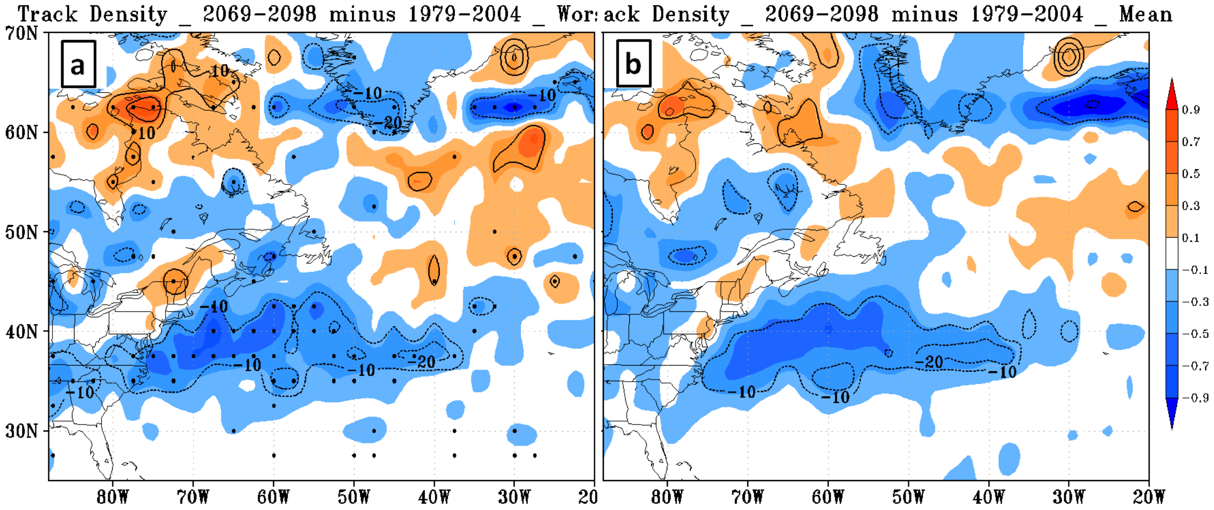

Fig. 3.19: Same as Fig. 3.18c (the future changes for 2069-2098), but for (a) the mean of Worst7; (b) the mean of all 15 CMIP5 models in Table 2.1.

For the same late 21st century period (2069-2098 cool seasons), the future change of the Worst7 relative to the historical period (1979-2004 cool seasons) is 5-10% less than the Best7 changes over the eastern North America and western Atlantic (Fig. 3.19a). There is also good agreement for the decrease over the western Atlantic, but the increase along the east coast of North America is very weak or near neutral from U.S. Northeast to the coast of eastern Canada (Fig. 3.19a). The result for mean of 15 models is smoother, with a decrease in cyclone track density over the continent of North America (5-10%) and the western Atlantic (10-20%), and a narrow neutral zone with a slight increase (around 5%) just along the East Coast of North America (Fig. 3.19b).

The future changes for cyclogenesis between Best7 and Worst7 is more consistent. There is a decrease (~5%) in the genesis density over the cyclogenesis maximum along the U.S. East Coast during early 21st century (not shown). This decrease becomes stronger through 21st century, reaching 20-25% by the end of 21st century for the Best7 (Fig. 3.20a). Meanwhile, there is an increase (~20%) over central Atlantic (Fig. 3.20a). For the Worst7, there is also a significant decrease in cyclogenesis at east of U.S. East Coast during early 21st century (Fig. 3.20b), but this decrease relative to the historical period is 5-10% smaller than the decrease in Best7, which is consistent with the smaller changes in track density.

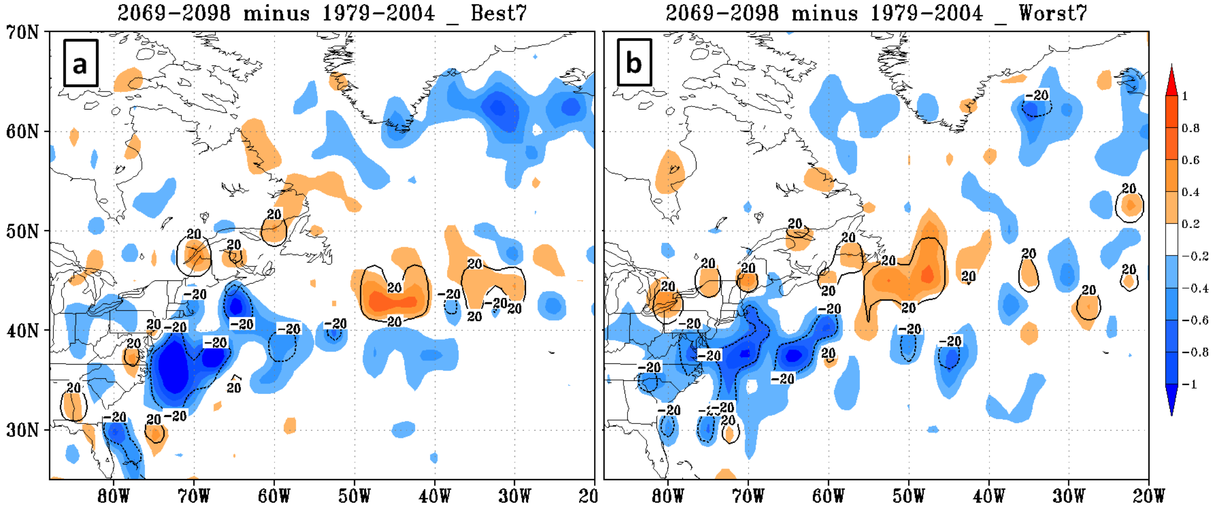

Fig. 3.20: The future changes of cyclone genesis density (shaded per 5 cool seasons per 50,000km^2) between late 21st century (2069-2098) and the historical (1979-2004) period and percent changes (contoured every 10%) for (a) mean of the Best7; (b) mean of the Worst7.

3.2.2 Future changes of cyclone intensity

The future changes of intensity distribution for those extratropical cyclones over eastern North America and western Atlantic were also examined. Within the ECWA region in Fig. 2.1, there is a decrease for the relatively weak cyclones (> 995 hPa) and this decrease nearly doubles from the early (3%-6%) to late (6%-12%) 21st century (Fig. 3.21) for the Best7. There is also a decrease in the relatively intense cyclones (< 985 hPa) during late 21st century (Fig. 3.21).

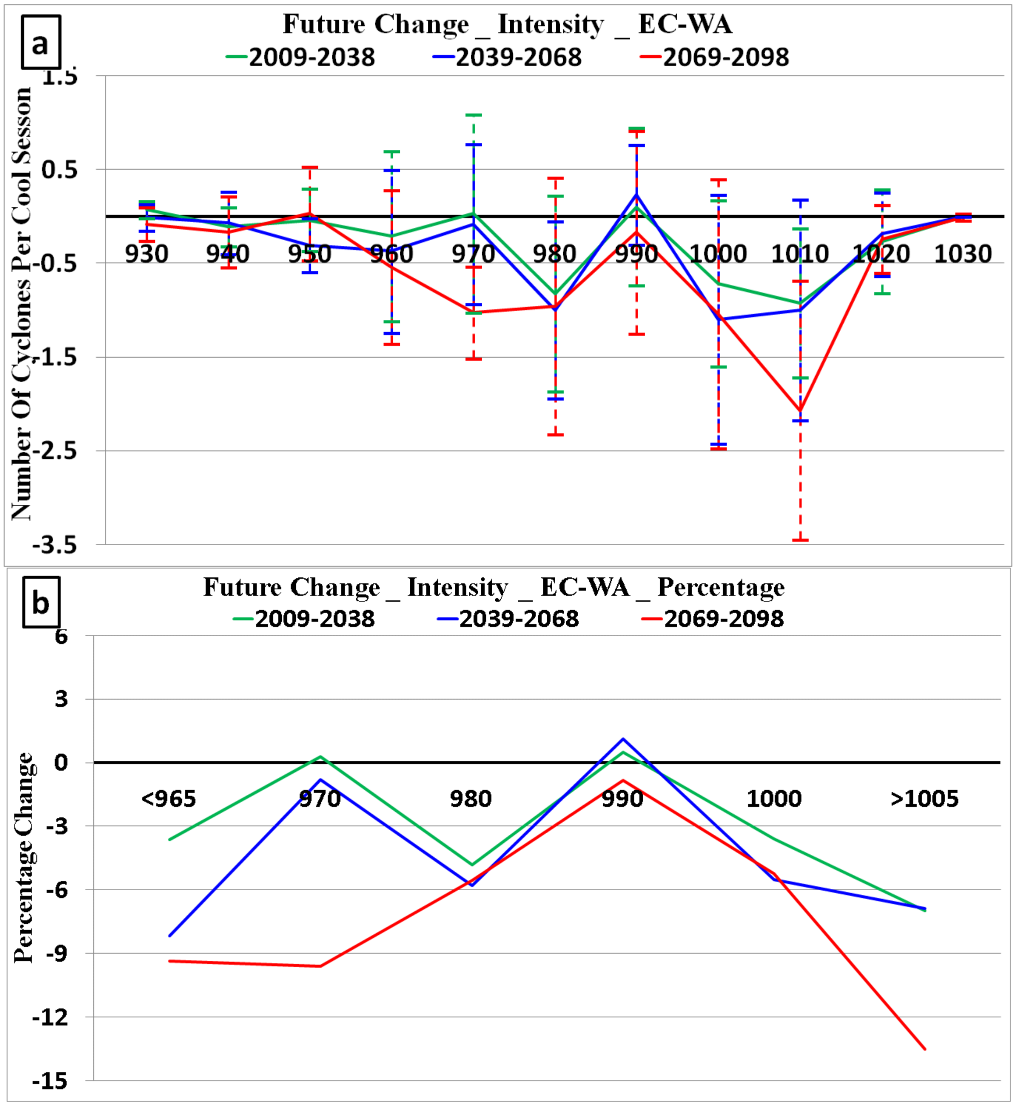

Fig. 3.21: (a) The future change of intensity (minimum central SLP) distribution for the cyclones within ECWA region from Best7; the vertical bars are the spread (±1 standard deviation) among models. (b) Same as (a), but for the percentage changes of intensity distribution.

There is an increase in the intense cyclones (< 985 hPa) within the ECL region for the Best7 models, especially for the middle 21st century (5-40%, blue line in Fig. 3.22a-b), which is even a slightly larger than the late 21st century (red line in Fig. 3.22a-b). The number of weak cyclones (> 995 hPa) within ECL decreases by about 6% for the early 21st century to about 12% by the late 21st century (Fig. 3.22a-b), which is similar with the ECWA. The future change in the number of intense cyclones (< 985 hPa) for the ECW region for the Best7 is just between the ECL and ECWA, nearly neutral (Fig. 3.22c-d). The number of weak cyclones (> 995 hPa) decreases by 3%-12% from early to late 21st century, which is similar with the decrease in the ECL and ECWA (Fig. 3.22c-d).

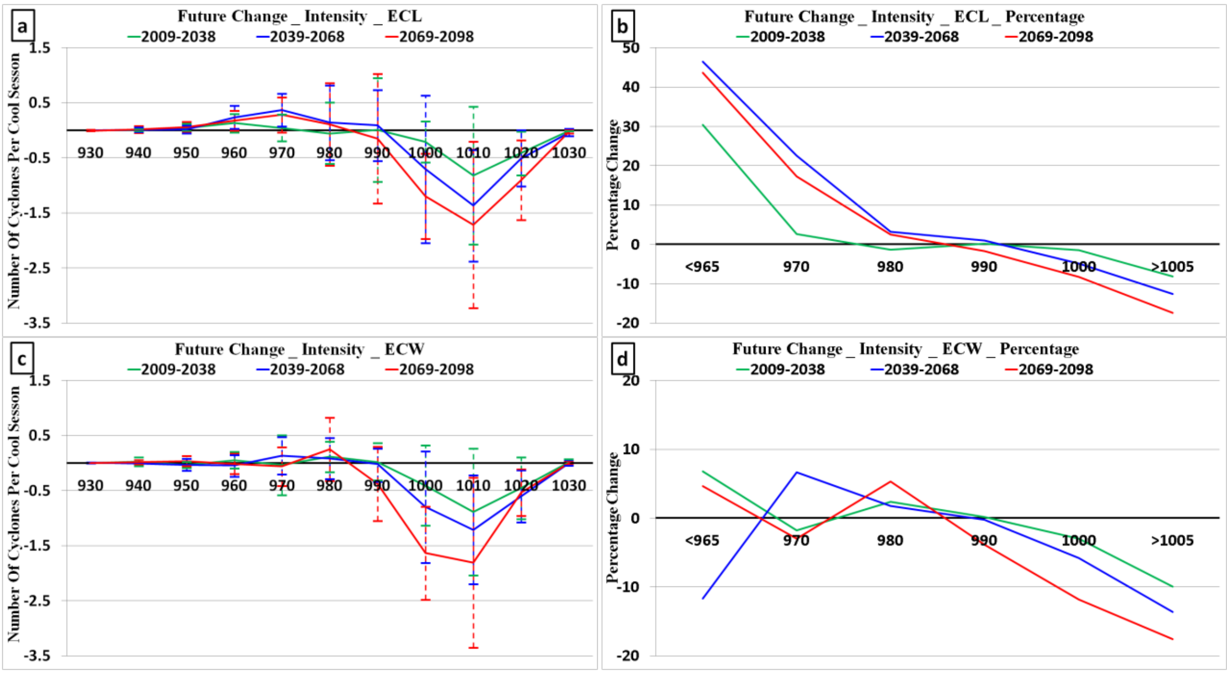

Fig. 3.22: Same as Fig. 3.21, but for (a) (b) the ECL region, and (c) (d) the ECW region.

Similar with the changes of cyclone track density within the ECL region, the future increase in the number of intense cyclones within the ECL almost disappears for the Worst7 (not shown). As a result, the mean of all 15 models has a smaller increase in the intense cyclone within ECL (Fig. 3.23) than the Best7. However, the decrease in the number of weak cyclones is robust, using the Best7 and the Worst7 models, and for the ECL to the ECWA regions. The mean of all 15 models also has a ~10% decrease in the number of weak cyclones for the ECL region (Fig. 3.23).

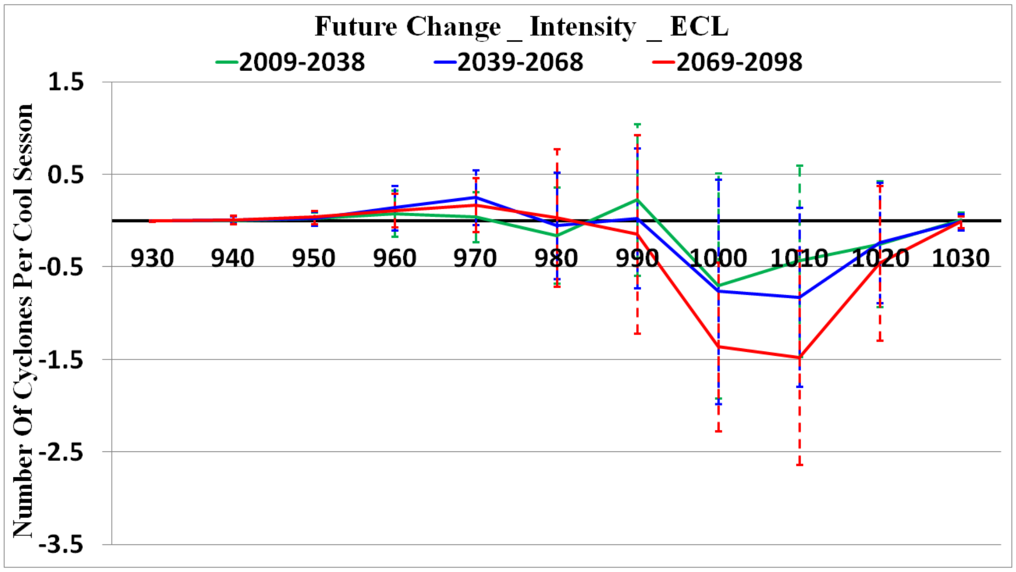

Fig. 3.23: Same with Fig. 3.22a, but for the mean of all 15 models in Table 2.1.

3.2.3 Future trends of cyclone frequency

The results in Section 3.2.1 and 3.2.2 suggest that the number of all cyclones within the ECWA region decreases through 21st century in CMIP5 RCP8.5 experiments, while there is an increase in the number of intense cyclones within the ECL region. To verify this, the time series of all and intense cyclone numbers within the ECWA, ECW and ECL regions through 21st century is calculated and compared.

Fig. 3.24 shows the time series for the number of all cyclones within the ECWA regions through 21st century. There is a near-linear decrease (~8% by the end of 21st century) in total cyclone number within the ECWA region for the mean of all 15 models (CMIP5, black in Fig. 3.24). Both of the trends for the Best7 (red in Fig. 3.24) and Worst7 (blue in Fig. 3.24) are similar to the mean of CMIP5. Although the spread among models is relatively large and the total number of cyclones ranged from 60-70 (IPSL-CM5A-LR) to 100-110 (MRI-CGCM3, BCC-CSM1, et al.), all decreasing trends in cyclone number within the ECWA region for CMIP5, Best7 and Worst7 mean have a nonzero trend that is significant at least at the 90% confidence level.

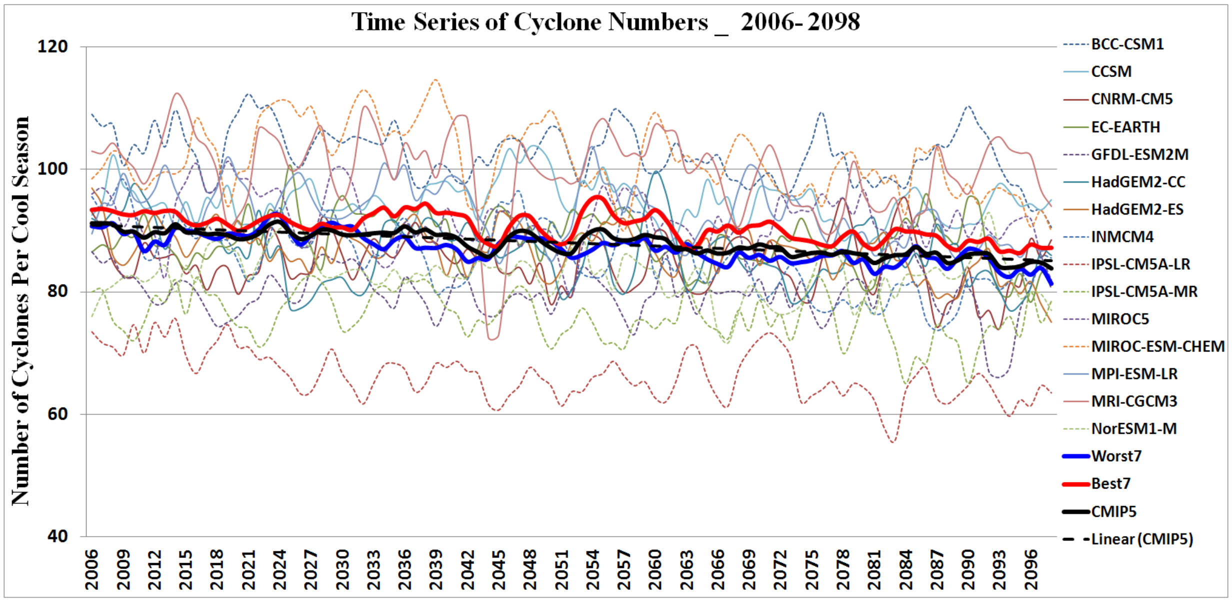

Fig. 3.24: The time series for the 2006-2098 cool seasons showing the numbers of total cyclone numbers per cool season within the ECWA region for the mean of all the 15 models (CMIP5, black), the Best7 (red), the Worst7 (blue), individual models, and a linear fit (dashed black) for the CMIP5 mean. The time series is 3-year running mean.

The total number of cyclones also has a decreasing trend through 21st century for the ECL (~3% by the end of 21st century) and ECW (~5%) regions for the Best7 (Fig. 3.25). The future change in the total cyclone numbers for the Worst7 (not shown) is similar to the Best7.

However, the future change in the relatively intense cyclones (< 980 hPa) for the ECL region is different from the ECWA and ECW. Within the ECL region, the number of relatively intense cyclones increases with a peak during 2050s (Fig. 3.26a). There is no upward trend in the number of relatively intense cyclones within the ECW region for the Best7 (Fig. 3.26b), although there is some interannual variability in the mean of the Best7 and large spread among these models. For the Worst7, there is also a downward trend for the total cyclone numbers within both the ECL and ECW region; but there is no significant change in the relatively intense cyclones within the ECL region (not shown).

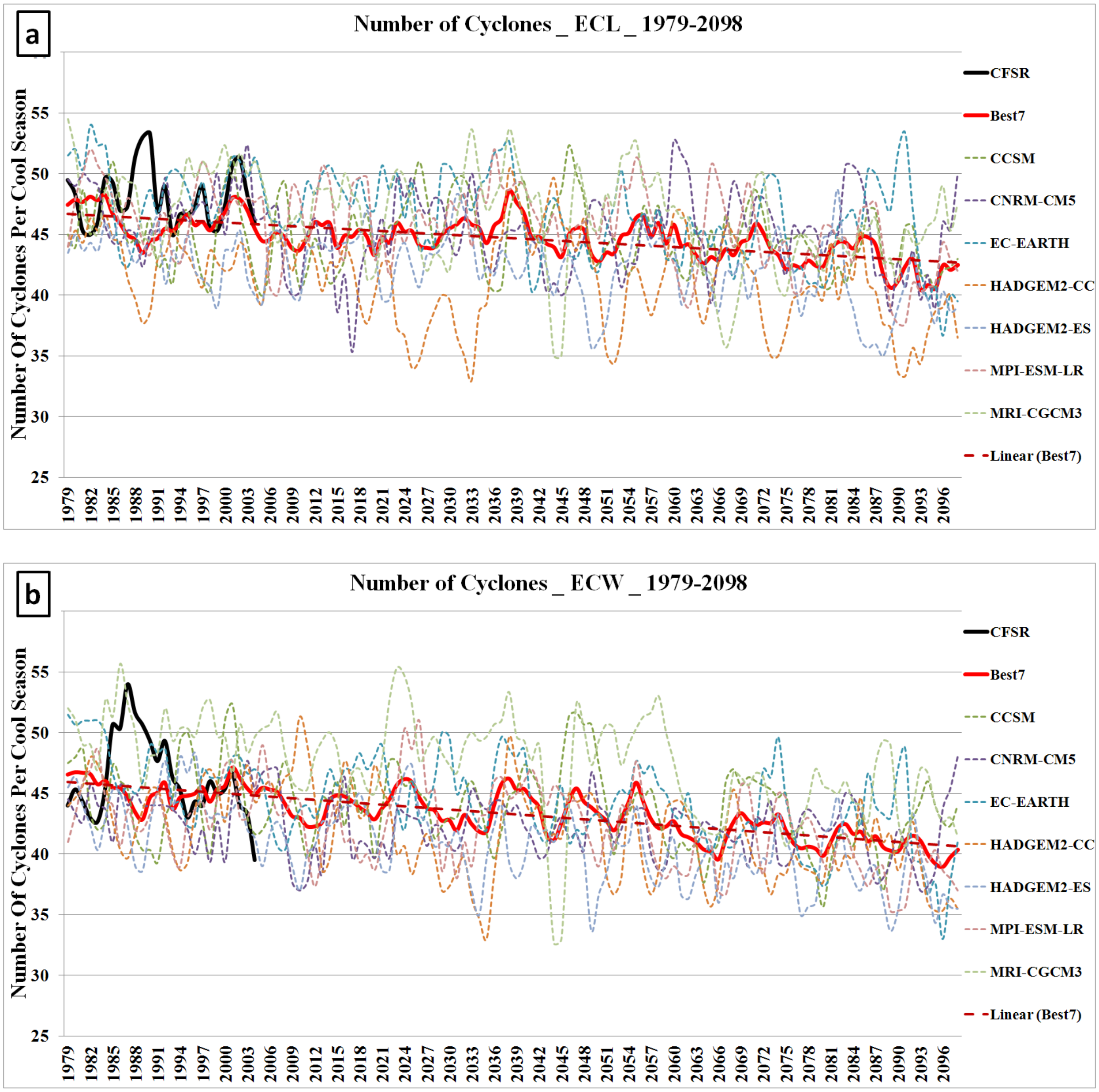

Fig. 3.25: The time series for the number of all cyclones within (a) the ECL region and (b) the ECW region, from 1979 to 2098 cool season for the CFSR (black), mean of the Best7 (red), the individual model (dashed), and a linear trend (dashed red) for the mean of the Best7.

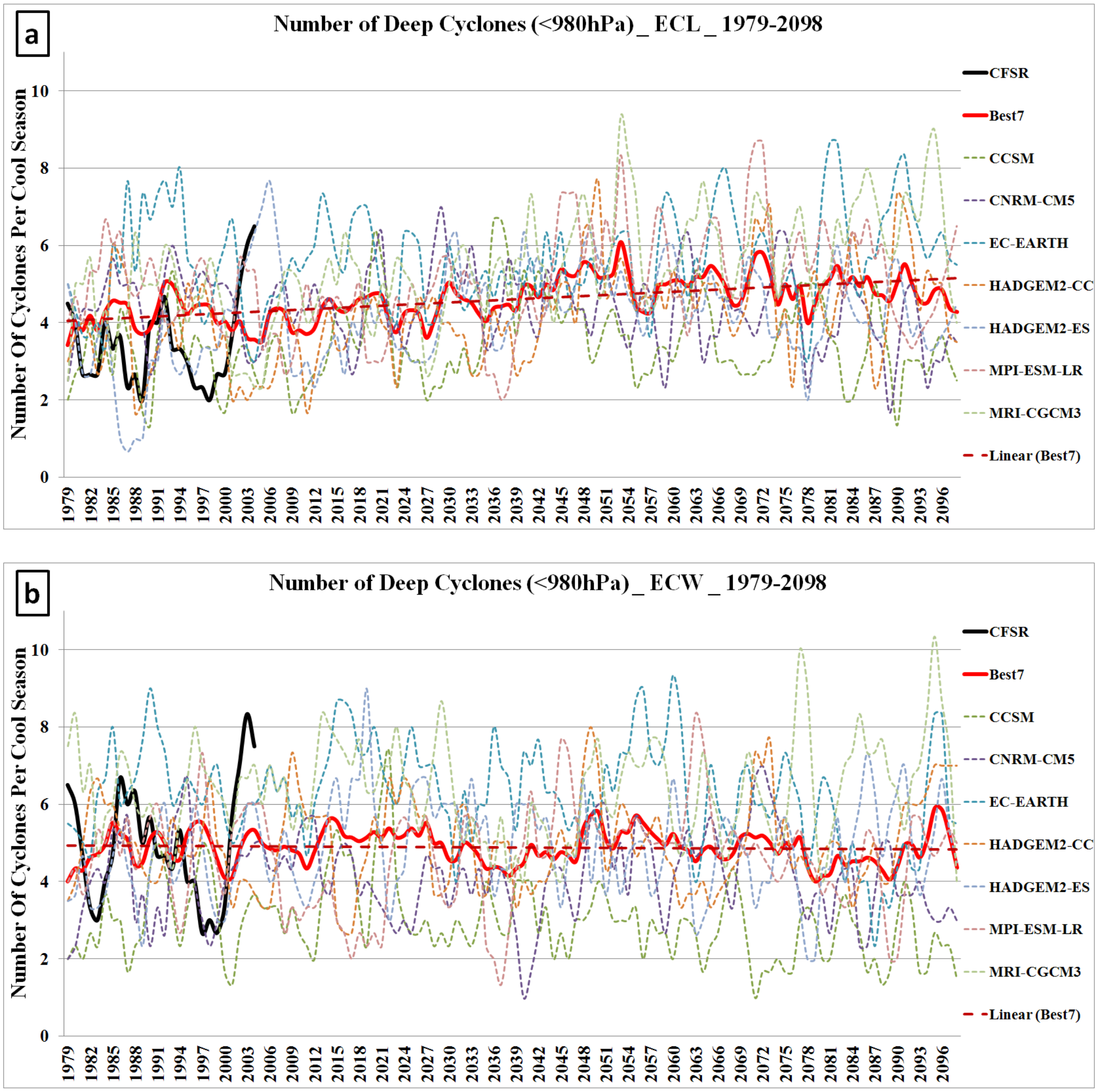

Fig. 3.26: Same as Fig. 3.25, but for the number of relatively intense cyclones (< 980 hPa).

3.2.4 Future changes of cyclone deepening rate

The future changes of spatial density of cyclone rapid deepening rate (> 5 hPa/6h) and the distribution of cyclone deepening rate for the ECL, ECW and ECWA regions are investigated in this section.

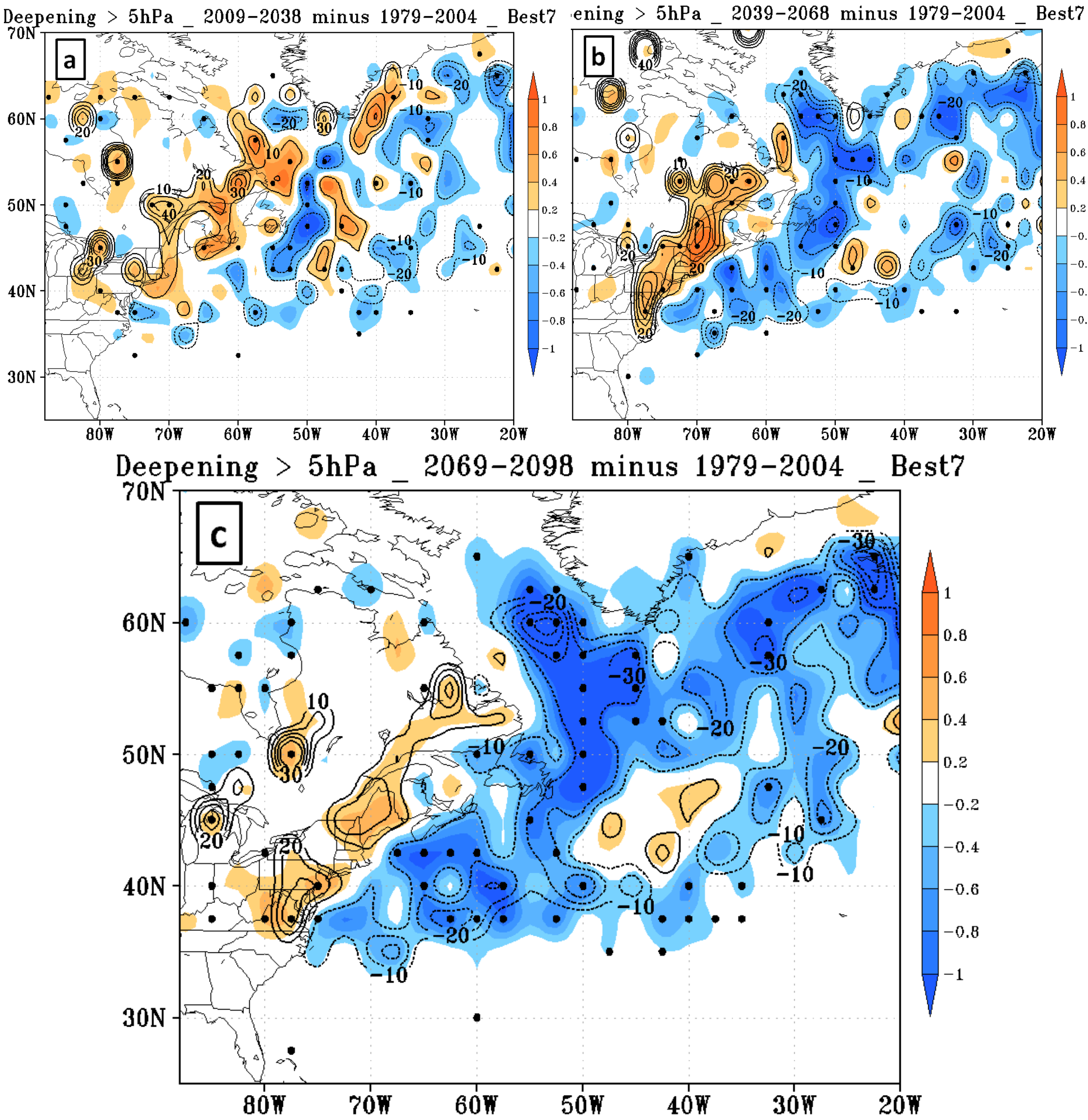

Fig. 3.27: The future changes of density for cyclone rapid deepening rate cases (shaded per 5 cool seasons per 50000km^2) for the Best7 mean between the (a) 2009-2038, (b) 2039-2068, and (c) 2069-2098 cool seasons and the historical (1979-2004) and percent change (contoured every 10%). The dots are locations in which six of the seven Best7 models agree with the sign of the change.

During early 21st century, there is an increase over the Great Lakes, Northeast of U.S. and southeastern Canada (5-40%) for the density of cyclone rapid deepening (Fig. 3.27a). Meanwhile, there is a small decrease (5-20%) along the storm track over western Atlantic (Fig. 3.27a). By the middle 21st century, both of these increasing and decreasing changes become stronger (Fig.

3.27b). The rapid deepening increase is concentrated over Northeast U.S. and southeastern Canada, reaching 10-40%. The decrease along the storm track over western Atlantic becomes more robust, increasing to 10-30% from the east of U.S. Northeast to the east of southeastern Greenland. By the late 21st century, the decrease over the storm track continues to be stronger and more widespread with very good model agreement (Fig. 3.27c); however, the increase along the Northeast U.S. coast and southeastern Canada is weaker (10-25%) than the increase in middle 21st century.

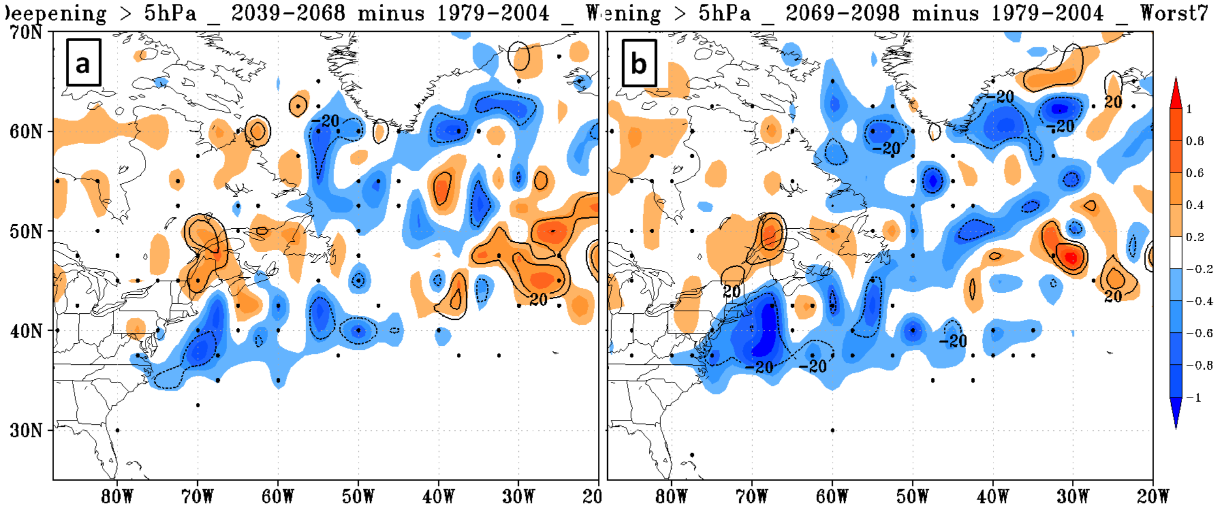

Fig. 3.28: Same as Fig. 3.27 (b) and (c), but for the mean of the Worst7.

The future increase and decrease in the density of cyclone rapid deepening rate is much weaker in the Worst7 (Fig. 3.28, only shown the middle and late 21st century). By the late 21st century, there is only a small and insignificant increase at the north of U.S. Northeast in the Worst7; and there is a decrease along the storm track over western Atlantic, with a maximum (20-25%) at the east of Northeast U.S. for the Worst7 (Fig. 3.28b).

In addition to the spatial density of rapid deepening cases, the distribution of deepening rate for all cyclones were also calculated to explore the future changes. Within the ECWA region, there is a significant decrease for all of the deepening (< -1 hPa/6h) bins through 21st century for the Best7 (Fig. 3.29). The decrease ranged from ~3% at the -2hPa/6h bin to ~20% at the <-9hPa/6h bin (Fig. 3.29b). Meanwhile, there are large uncertainties for the slow-developing part (-1 ~ 3 hPa/6h) among models, although there is a slight increase for the mean (Fig. 3.29a).

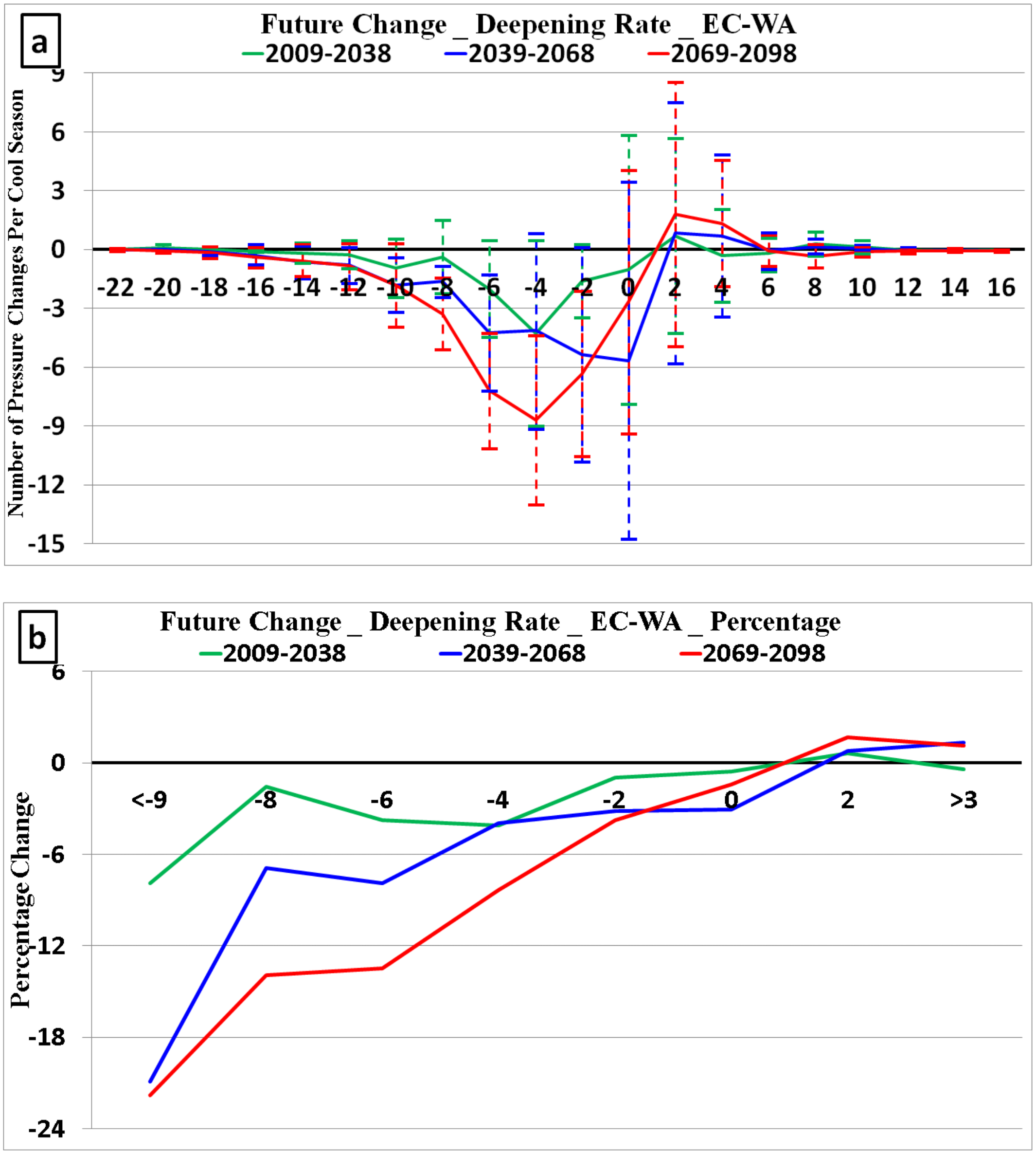

Fig. 3.29: (a) The future change in the distribution of deepening rate (hPa/6h) for the cyclones within the ECWA region (Fig. 2.1) from Best7; the vertical bars are the spread (±1 standard deviation) among models. (b) Same as (a), but for the percentage changes of intensity distribution.

There is an increase (5-40%) in the relatively rapid deepening (<-3 hPa/6h) for the cyclones within the ECL region through 21st century for the Best7, especially for the middle 21st century (Fig. 3.30a-b). Meanwhile in the ECW region there are large uncertainties among models for the changes and there is no significant change for the mean of the Best7 (Fig. 3.30c-d).

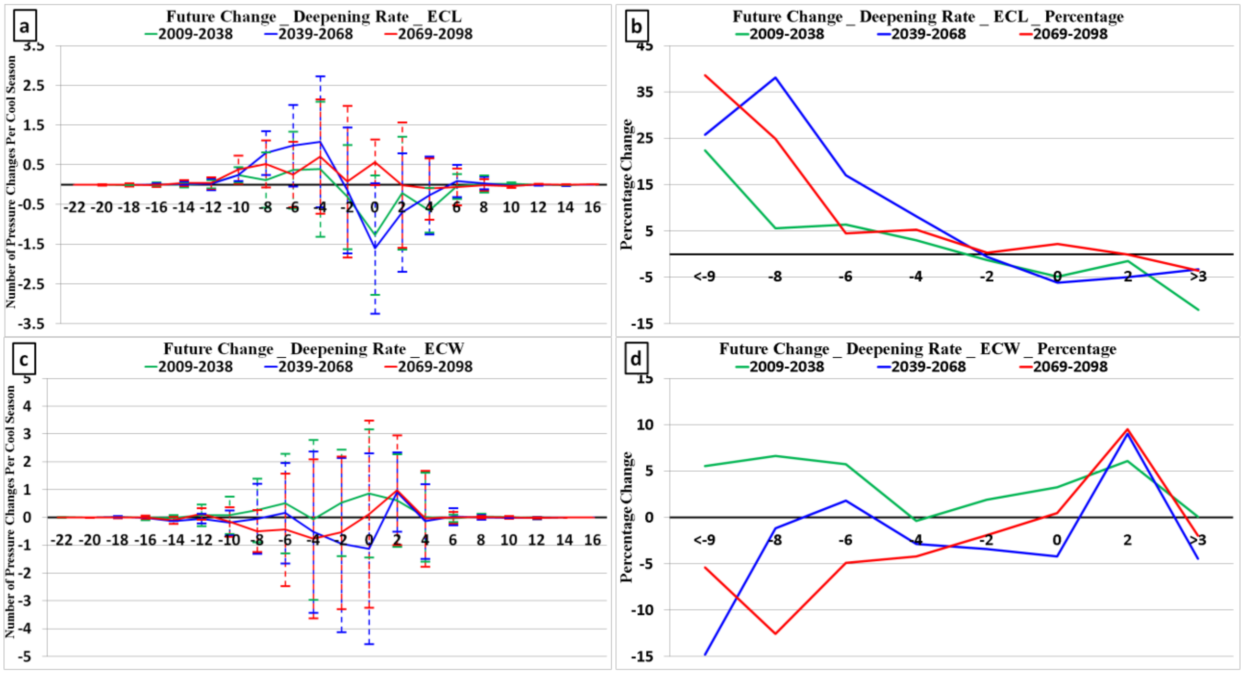

Fig. 3.30: Same as Fig. 3.29, but for (a-b) the ECL region and (c-d) the ECW region.

The distribution of cyclone deepening rates is also calculated for the Worst7. The decrease in the rapid deepening frequency for the ECWA region in the Worst7 is similar to the Best7. However, the increase in the rapid deepening frequency for the ECL region became much weak and near neutral in the Worst7 (not shown).

3.3. Summary

The extratropical cyclones over eastern North America and the western Atlantic in CMIP5 models for the historical period (1979-2004 cool seasons) were compared with the CFSR for cyclone track density, genesis density, intensity distribution, and deepening rate. The models were ranked based on their cyclone track density and intensity distribution.

The overall performance of the models is highly related to their resolution. Six of the top seven models (Best7) in the extratropical cyclone simulation are at relatively high resolution (< 2° at both longitude and latitude directions). Some high resolution models, such as CCSM4 and HadGEM2-ES, have well-defined cyclone track density maximum offshore along east coast of North America, which is close to the CFSR. Meanwhile, some low resolution models, such as IPSL-CM5A-LR and INMCM4, produce a cyclone track density maximum too far north and too close to the coast of U.S. Northeast. The comparison between high and low resolution models is consistent with the study from Woollings et al. (2010) suggesting that the storm track shifts southward toward the Gulf Stream when the higher resolution SST is used. However, there are exceptions, such as the low resolution MPI-ESM-LR, which has a number 3 overall ranking; and the high resolution MIROC5, which has large bias in the spatial distribution of cyclone track density and intensity distribution (Fig. 3.4e, TR in Table 3.1).

The intensity distribution of the low resolution models is too narrow, underestimating the number of both of the relatively strong and weak cyclones (Fig. 3.5b); and the high resolution models have better performance although they also underestimates the number of deep cyclones within the ECWA. The intensity distribution of the models is much closer to the CFSR for cyclones within the ECL region; the mean of high resolution models only underestimates the number of cyclones around 990hPa slightly. Meanwhile, the extratropical cyclones over the North Atlantic storm track in CMIP5 models deepen too slowly; the models underestimated the frequency of rapid deepening significantly, especially for the low resolution models (Fig. 3.11 and Fig. 3.12).

Overall, the model resolution is very important to the simulation of extratropical cyclones over eastern North America and western Atlantic, but the resolution is not the only factor controlling the model performance, which is consistent with the conclusion form Chang et al (2013). Although the individual CMIP5 model has biases more or less, the ensemble mean, especially for the mean of the Best7, has better performance than individual model. Therefore, the mean of the Best7 is primarily used to investigate the future changes of the extratropical cyclones over eastern North America and western Atlantic, and the mean of all 15 models is also discussed.

There is a decrease in cyclone track density over the western Atlantic storm track from 5%-10% in the early 21st century (2009-2038 cool seasons) to 10%-30% by the late 21st century (2069-2098 cool seasons) in the Best7 models, which is consistent with many other studies (Geng and Sugi 2003; Lambert and Fyfe 2006; Bengtsson et al. 2009; Chang 2013, Zappa et al. 2013) suggesting the decrease in extratropical cyclones over North America and western Atlantic. There is a weaker decrease (~10%) in cyclone track density over the inland continent of eastern North America in the late 21st century (Fig. 3.18c).

However, there is an increase (5%-20%) in the cyclone track density along the east coast of North America (Fig. 3.18) with more rapid deepening cases (Fig. 3.27) in the Best7 models. The frequency of intense cyclones (< 980 hPa) within the ECL region has an increase trend (Fig. 3.26a) through 21st century, while the frequency of all cyclones within the ECL region is decreasing (Fig. 3.25a) for the Best7. Thus, in the ECL there is a significant shift toward more intense cyclones by middle and late 21st century in the Best7 (Fig. 3.22a-b). In the ECW and ECWA regions, the frequency of all cyclones has a decrease trend (Fig. 3.24 and Fig. 3.25b) while the frequency of intense cyclones (< 980 hPa) has a neutral (Fig. 3.26b) and a weaker decrease (not shown) trend respectively.

The increase signals for cyclone frequency and rapid deepening are much weaker in the mean of all the 15 CMIP5 models; but even for the mean of all models, the future changes are neutral or slight increase in the track density and rapid deepening within the ECL, which indicates that the future changes in extratropical cyclones within the ECL are different from the western North Atlantic ocean.

Chapter 4:
Future Changes of Cyclone Relative Precipitation and the Associated Physical Processes

This chapter focuses on the future changes in precipitation associated with extratropical cyclones during cool season over eastern North America and western Atlantic. Using the cyclone relative approach described in Section 2.4, the future changes of cyclone relative precipitation on the earth-related map and within the synoptic-scale cyclone systems in the ten CMIP5 models (with * in Table 2.1) are examined. The physical processes responsible for the future precipitation changes and the impacts of precipitation changes on the extratropical cyclone developing are investigated to explore the relationship between future precipitation changes and cyclone changes.

4.1. Evaluation of the precipitation in CMIP5 models

Before examining the cyclone relative precipitation, the seasonal mean precipitation in the CMIP5 models (with * in Table 2.1) are compared with the GPCP and CMAP (described in Section 2.1) over eastern North America and western Atlantic during historical cool seasons. The historical seasonal mean precipitation amount for the CMIP5 ensemble mean has a maximum (over 1000 mm per cool season) over the east side of the storm track over 35-40°N (Fig. 4.1c); the location of the maximum is similar to the GPCP and CMAP (Fig. 4.1ab). The models have the largest spread of about 150 mm per cool season near the precipitation maximum (Fig. 4.1c). Comparing with the mean of the GPCP and CMAP (GPCP_CMAP), the CMIP5 ensemble mean underestimates the precipitation maximum by about 10% along the storm track, and the precipitation maximum in models is shifted south by 3-5°. The CMIP5 mean also underestimates precipitation amount (~20%) over the western part of the U.S. Gulf Coast. However, the CMIP5 mean overestimates the precipitation over the East Coast by 10-150 mm, especially over the storm track entrance region (>20%) at the east of U.S. Southeast (Fig. 4.1d).

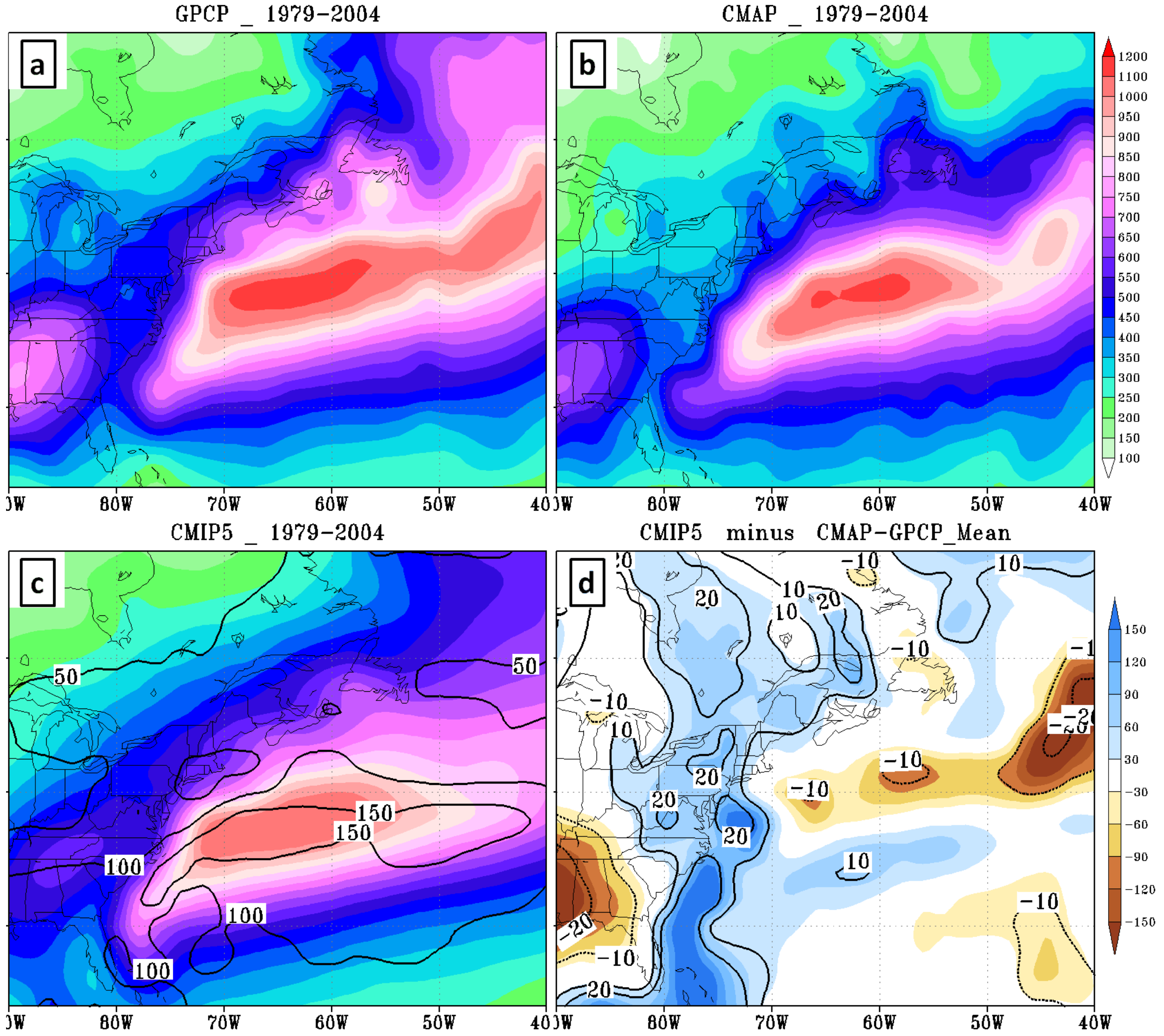

Fig. 4.1: The mean precipitation amount (mm per cool season) for GPCP, CMAP, the mean of 10 CMIP5 models (with * in Table 2.1), and the difference between the mean of CMIP5 models and the mean of GPCP and CMAP.

The performance of individual CMIP5 models and the CMIP5 ensemble mean were quantitatively evaluated with respect to the GPCP_CMAP. The Mean Absolute Error (MAE) and the normalized MAE were calculated at each grid within the eastern North America and western

North Atlantic domain (ECWA in Fig. 2.1), which covers the major part of the storm track as well as the precipitation maximum over that region.

Table 4.1: The Mean Absolute Error (MAE) and normalized MAE of seasonal mean precipitation amount over the eastern North America and western North Atlantic region (ECWA in Fig. 2.1) with respect to the mean of GPCP and CMAP for individual CMIP5 models and the ensemble mean of CMIP5, for the historical (1979-2004) cool seasons. The models in red are the models which have relatively better performance in the cyclone simulation in Section 3.1.5.

	Mean PCP (mm/season)	GPCP-CMAP MAE (mm/season)	Normalized MAE (%)
GFDL-ESM2M	559.2	53.3	11.1
CCSM4	547.0	71.0	13.7
CNRM-CM5	579.4	75.4	15.4
MPI-ESM-LR	550.8	85.8	18.5
MRI-CGCM3	546.7	82.9	18.9
IPSL-CM5A-LR	510.7	93.1	19.0
MIROC-ESM-CHEM	540.8	103.4	19.6
INMCM4	583.3	90.9	20.4
IPSL-CM5A-MR	517.5	106.6	22.3
HadGEM2-CC	632.9	119.2	23.0
CMIP5	**557.3**	**48.2**	**9.5**

The mean precipitation amount in this ECWA domain is 540 mm per cool season for GPCP_CMAP. For these ten models, five of them (red in Table 4.1) are the members of Best7 in Chapter 3, and thus have better performance than the other 5 for the cyclone simulations. Generally, the members with better cyclone simulation (CCSM4, CNRM-CM5, MPI-ESM-LR and MRI-CGCM3) tend to have relatively smaller MAE for precipitation amount. For example, CCSM4 has a well-defined precipitation maximum (Fig. 4.2a), which is close to GPCP and CMAP, while on the other hand IPSL-CM5A-MR (not a Best 7 member) has too much precipitation over U.S. Northeast (Fig. 4.2b).

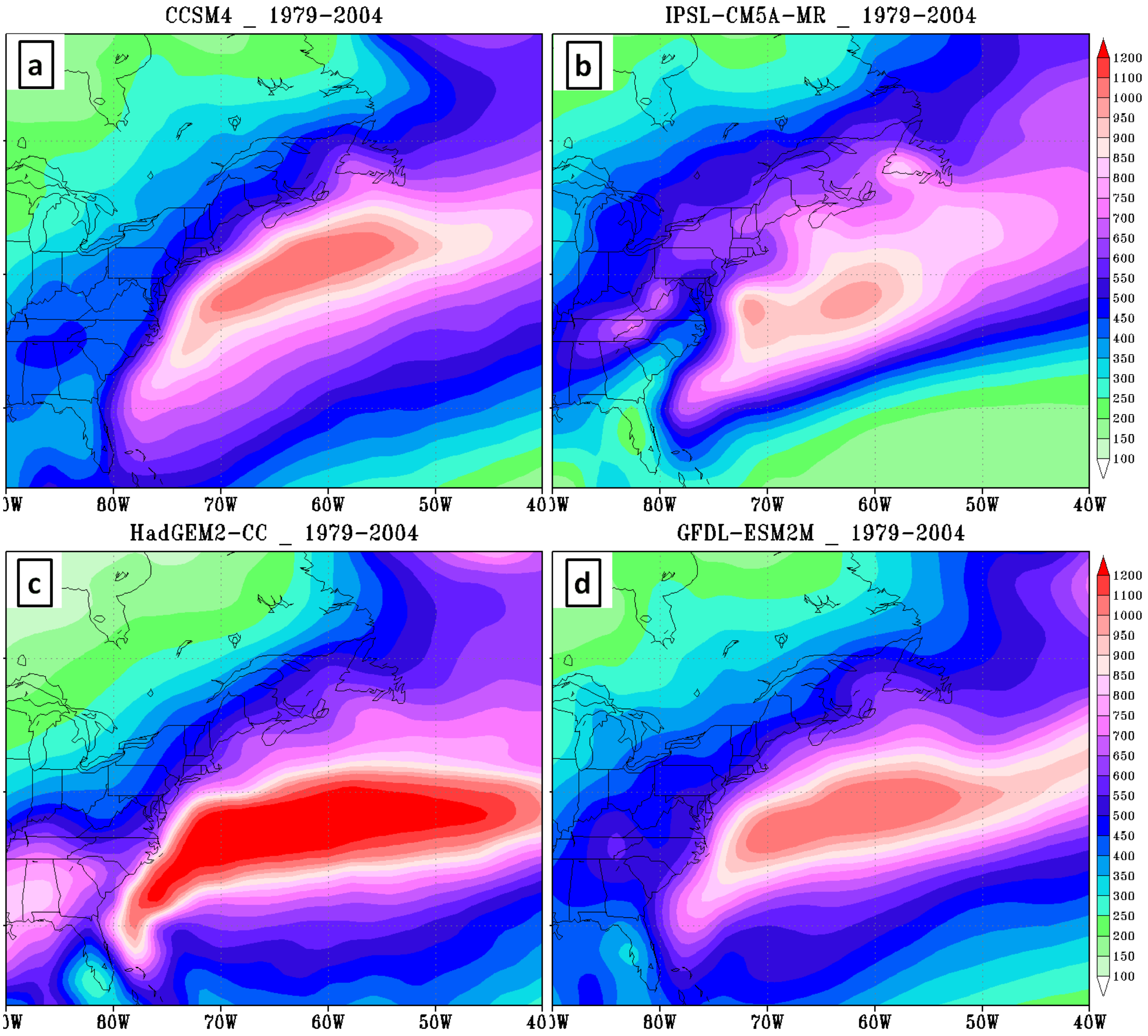

Fig. 4.2: Same as Fig. 4.1, but for (a) CCSM4, (b) IPSL-CM5A-MR, (c) HadGEM2-CC, and (d) GFDL-ESM2M.

However, there are exceptions, such as HadGEM2-CC and GFDL-ESM2M. HadGEM2-CC has a good performance for the cyclone simulations, but it has too much precipitation amount (~20%) over the North Atlantic storm track (Fig. 4.2c) than GPCP_CMAP because its average precipitation rate around each cyclone center over the ocean is significant (5-22%) larger than the other models (not shown). Meanwhile, the low-resolution (2.0°×2.5°) GFDL-ESM2M has the smallest MAE in precipitation amount (Fig. 4.2d). Although GFDL-ESM2M underestimates the cyclone frequency and intensity (Fig. 3.6a) over eastern North America and the western Atlantic, the cyclones in this model move the slowest (~ 42 km/h) in those ten CMIP5 models (~ 48 km/h for the mean of the ten models) bringing more precipitation amount along each cyclone track over this region.

The CMIP5 mean has smaller average error than each of the ten models, with the MAE of 48.2 mm per cool season and the normalized MAE of 9.5% in the ECWA region (Table 4.1), and more realistic spatial distribution (Fig. 4.1c). Although these CMIP5 models have different biases, the relatively smaller average error for the CMIP5 ensemble mean provides confidence to examine the future precipitation changes over eastern North America and the western Atlantic using the mean precipitation of these models.

4.2. Cyclone relative precipitation over eastern North America and western Atlantic

In order to examine the future changes of precipitation associated with extratropical cyclones over eastern North America and western Atlantic, the cyclone relative approach (Section 2.4) was employed to calculate the earth-related cyclone relative precipitation rate and amount over geophysical map. The cyclone relative precipitation rate was normalized to mm per day per cyclone center. The cyclone relative precipitation amount depends on two terms: the frequency of cyclones with precipitation impacting a region and the precipitation rate for each cyclone center.

The cyclone relative precipitation was calculated for all cyclone centers (here after ALL-Centers), the relatively strong cyclone centers (< 990 hPa, here after S-Centers), moderate centers (990-1005 hPa, here after M-Centers), and weak centers (> 1005 hPa, here after W-Centers). Those thresholds for different categories of intensity were selected to insure that each category had enough cyclone cases for different domains, such as the ECL, ECW and WA in Fig. 2.1, while also differentiating the relative intensity of the systems. The sensitivity of the results to the different thresholds was tested. For example, using < 985 hPa to define the S-Centers, it does not have a significant impact on the results for the S-Center; but there are larger uncertainties for the cyclone relative precipitation among models over the East Coast of U.S., since the sample size of the S-Centers will become too small for some models using a deeper cyclone threshold.

4.2.1 Cyclone relative precipitation in historical period

Over eastern North America and western North Atlantic, the ensemble mean cyclone center density of the 10 CMIP5 models used in this chapter is able to reproduce the storm track over the East Coast of North America and western North Atlantic. However, the cyclone center density maximum is shifted north and too close to the U.S. Northeast coast (Fig. 4.3a) comparing to the cyclone center density of CFSR (not shown).

The S-Centers, M-Centers, and W-Centers are mainly concentrated over the high (>50°N), middle (40-50°N) and low (<40°N) latitudes respectively. Meanwhile, the S-Centers, M-Centers and W-Centers contributing near 50% or more than 50% to the total cyclone center density over the corresponding regions along the storm track over western Atlantic (Fig. 4.3b-d). These spatial distributions of the S-Centers, M-Centers and W-Centers are similar to the CFSR (not shown).

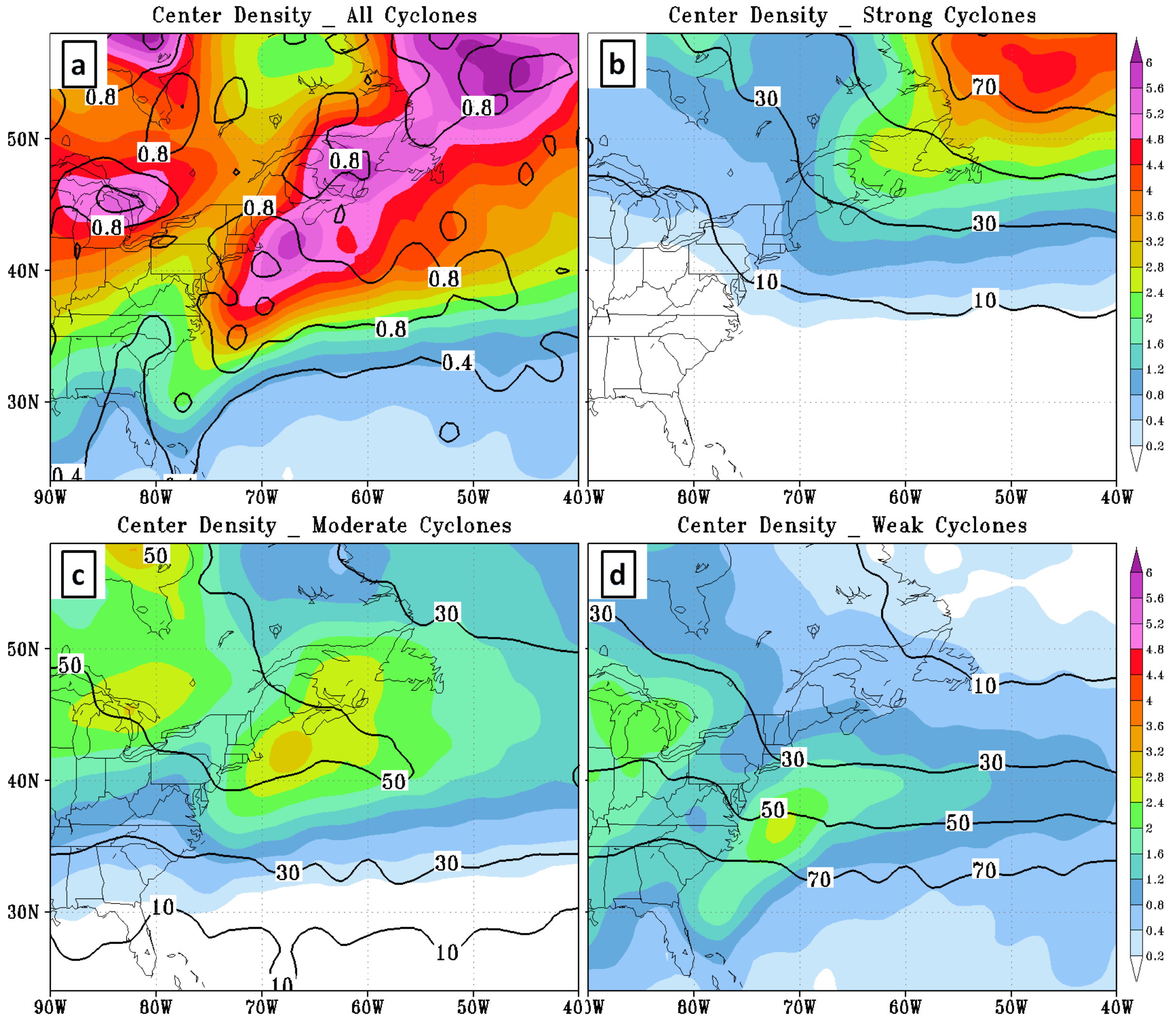

Fig. 4.3: The cyclone center density (colors, cyclone centers per cool season per 50,000 km^2) for the historical period (1979-2004 cool seasons) for mean of the 10 CMIP5 models (with * in Table 2.1) for (a) ALL-Centers (including all cyclone centers), (b) S-Centers (< 990 hPa), (c) M-Centers (990-1005 hPa), and (d) W-Centers (> 1005 hPa) cyclone centers. The contours in (a) are the spread (one standard deviation) among models, and the contours in (b)-(d) are the contribution (%) to the density of ALL-Centers.

The precipitation amount associated with those cyclone centers (the precipitation within the black box in Fig. 2.4b) contributes from 60% at relatively lower latitude (~25°N) to over 90% at relatively higher latitude (> 40°N) to the total precipitation amount in the mean of the ten CMIP5 models (contours in Fig. 4.4a), which is similar to the results of the GPCP and ERA-Interim from Hawcroft et al. (2012). The distribution of cyclone relative precipitation amount for

S-Centers, M-Centers, and W-Centers is controlled by the distributions of those cyclone centers (Fig. 4.4b-d). For example, from the south to the north part of U.S. Northeast, the S-Centers contribute 10-30%, the M-Centers contribute 40-50%, and the W-Centers contribute 20-40% of the total cool season precipitation amount (Fig. 4.4b-d), which is similar with their contributions to the total cyclone center density over this region (Fig. 4.3b-d).

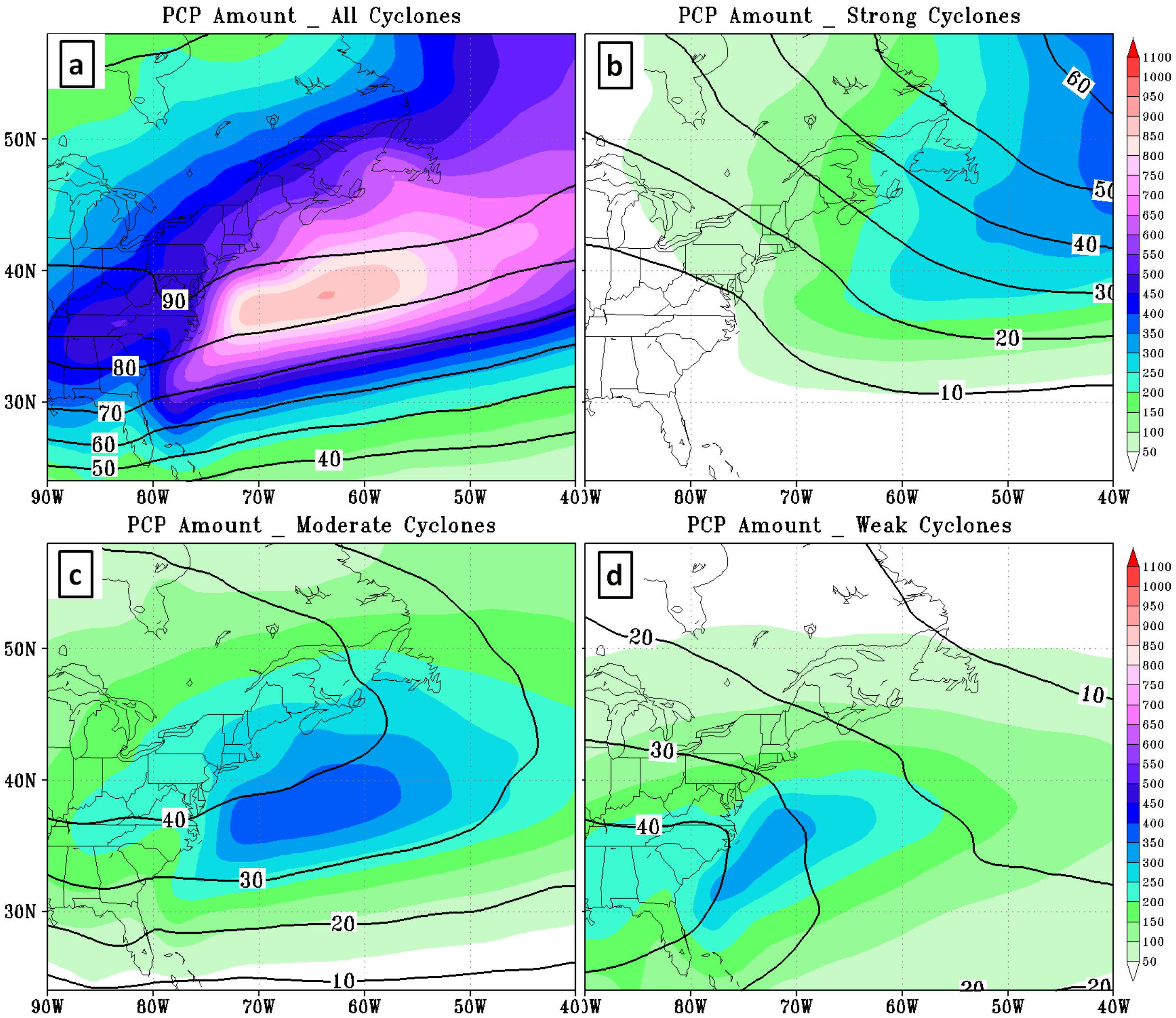

Fig. 4.4: Same as Fig. 4.3 but for the cyclone relative precipitation amount (colors, mm per cool season) and the contribution (contours, %) to the total precipitation during cool season (November-March).

The cyclone relative precipitation rate for ALL-Centers has the maximum (> 8 mm/day) over the western North Atlantic close to the coast between 33°N and 40°N (Fig. 4.5a), with the largest standard deviation (>1 mm/day) over the same region. The spatial pattern of cyclone relative precipitation rate for the S-Centers, M-Centers, and W-Centers is similar with the ALL-Centers. The S-Centers have largest precipitation rate (> 9 mm/day) located at the east of U.S. East Coast, with the largest spread of 1.5-2 mm/day (Fig. 4.5.b), while the precipitation rate for M-Centers (~ 8 mm/day) and W-Centers (~ 7 mm/day) is smaller (Fig. 4.5.cd).

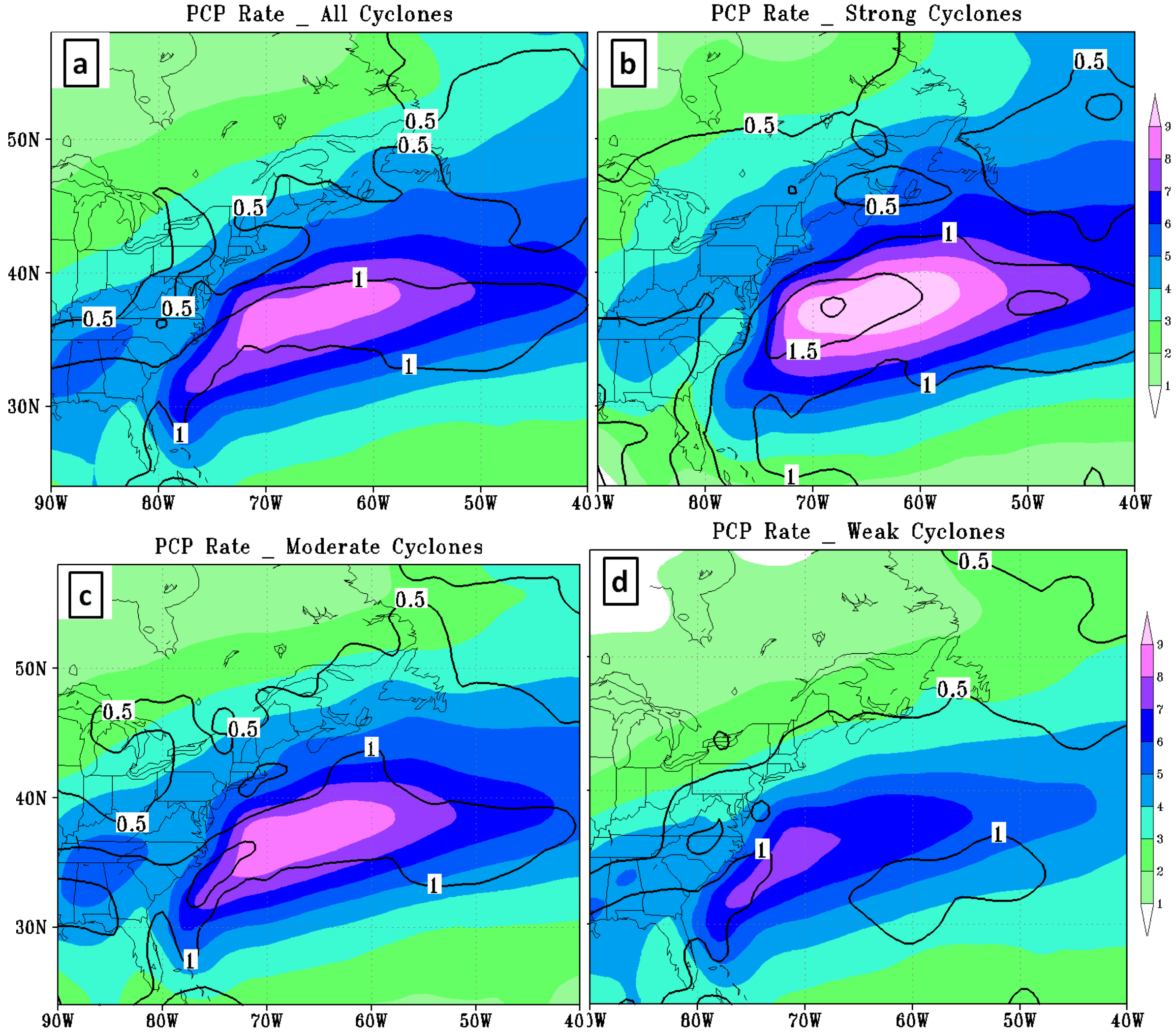

Fig. 4.5: Same as Fig. 4.3 but for the cyclone relative precipitation rate (mm/day) and the contours are the spread (one standard deviation) among models.

4.2.2 Future changes in cyclone relative precipitation

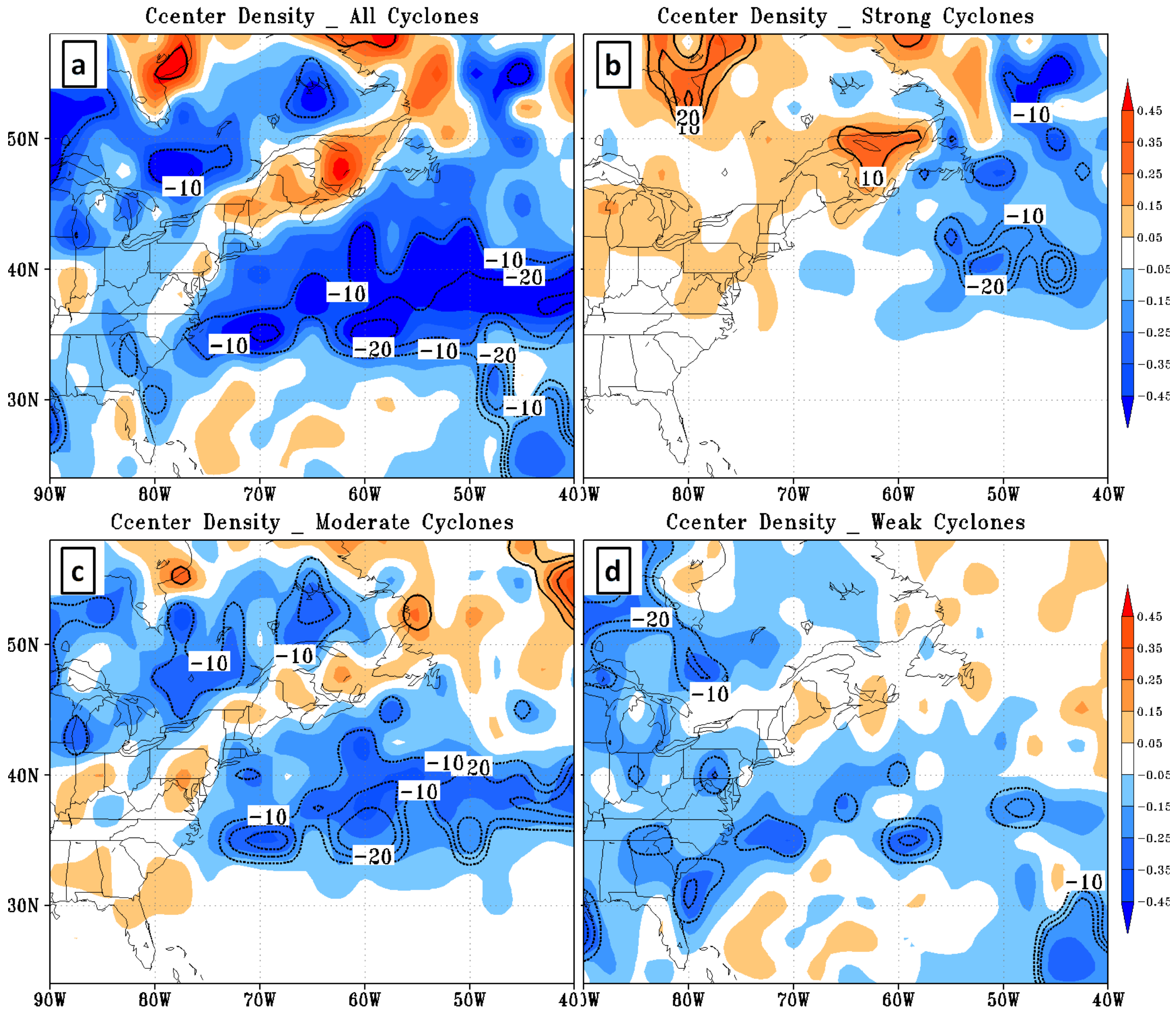

Fig. 4.6: Future change of cyclone center density (colors, cyclone center per cool season per 50,000 km^2) for late 21st century (2069-2098 cool seasons) for mean of the 10 CMIP5 models (with * in Table 2.1) for (a) ALL-Centers, (b) S-Centers, (c) M-Centers, and (d) W-Centers. The contours are the percentage of the future changes (every 10%).

The future changes of the cyclone center density, cyclone relative precipitation amount, and precipitation rate were calculated for the three future periods: early (2009-2038), middle (2039-2068), and late (2069-2098) 21st century cool seasons. The future changes become stronger from early to late 21st century, so only the results from this period are shown and discussed.

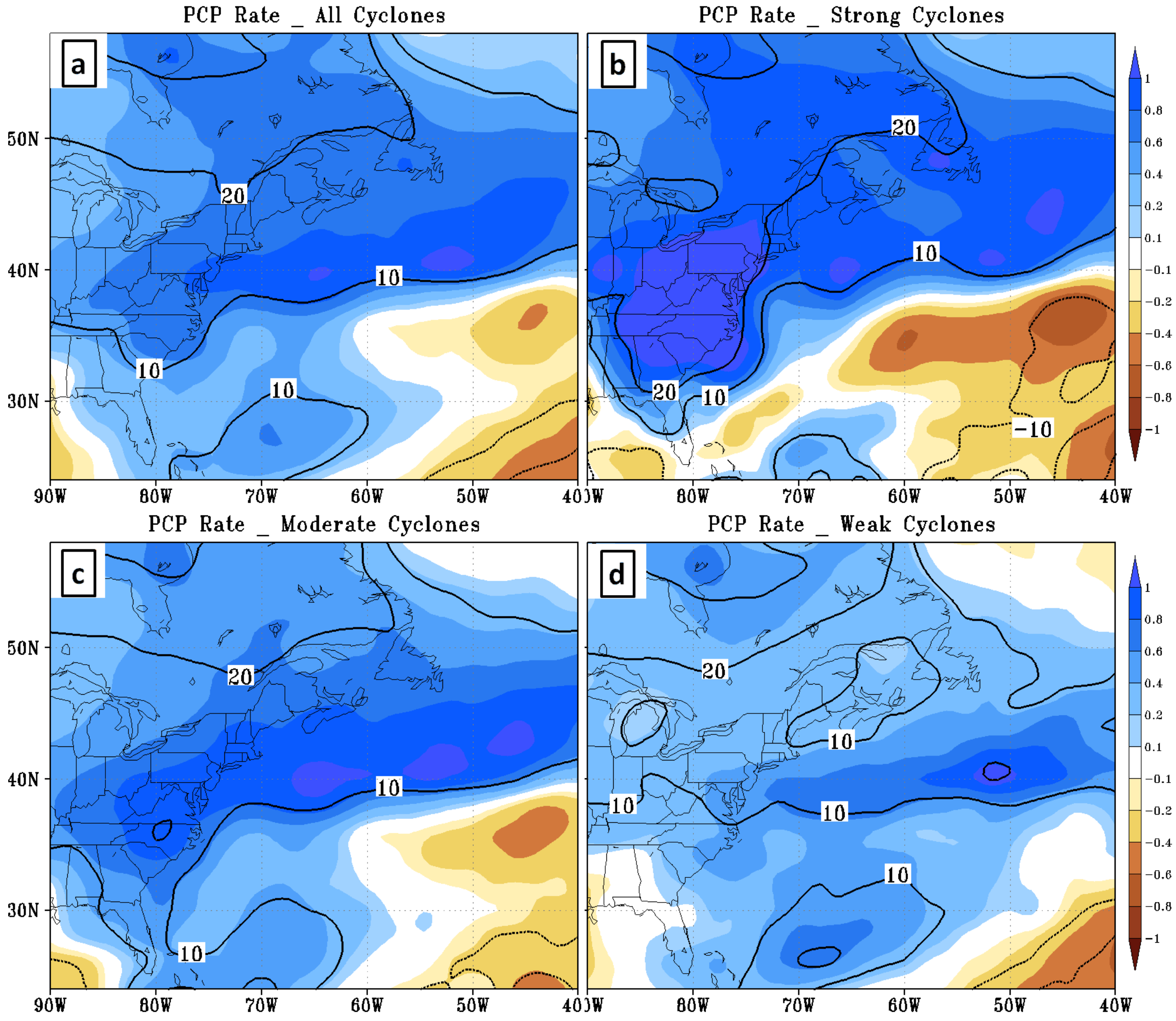

Fig. 4.7: Same as Fig. 4.6, but for the cyclone relative precipitation rate (mm/day).

As in Section 3.2.1, there is a decrease of cyclone center density in most areas of eastern North America and western North Atlantic, and the largest decrease (10-20%) is over the western North Atlantic (Fig. 4.6a). However, along the East Coast the change is neutral or slight increase (5-10%) onshore (Fig. 4.6a). The decrease over the western Atlantic is consistent for the S-Centers, M-Centers, and W-Centers (Fig. 4.6b-d). Meanwhile, there is a slight increase in the cyclone center density for S-Centers over the coast and the Great Lakes (Fig. 4.6b), a narrow neutral region along the East Coast between the decrease over the ocean and continent for the M-Centers (Fig. 4.6c), and a decrease almost everywhere for the W-Centers (Fig. 4.6d).

The normalized cyclone relative precipitation rate of ALL-Centers increases over 10-20% over the storm track region (Fig. 4.7a). Comparing with the ALL-Centers, the S-Centers have larger increase over the ECL region for both of the absolute value and the percentage, 20-30% with respect to the historical precipitation rate of the S-Centers (Fig. 4.7b). The increases of precipitation rate are smaller for M-Centers (10-20%) and W-Centers (around 10%) along the East Coast (Fig. 4.7c-d).

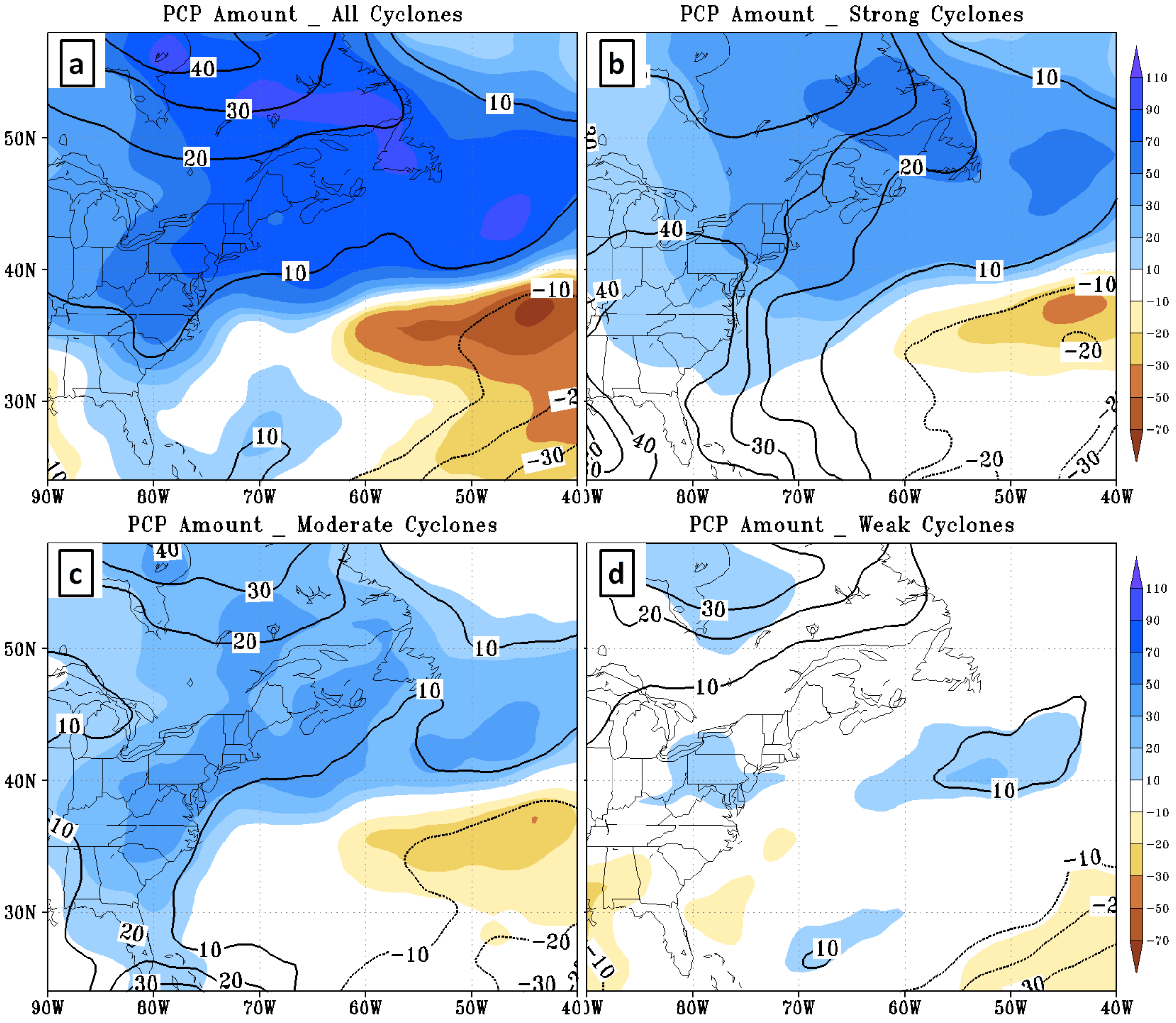

Fig. 4.8: Same as Fig. 4.6, but for the cyclone relative precipitation amount (mm per cool season).

The cyclone relative precipitation amount increases along the East Coast of North America from the south (~5%) to the north (20-30%), with most of the increase from the S-Centers and M-Centers. Meanwhile, the precipitation change from W-Centers is almost neutral along the East Coast (Fig. 4.8). There is a large increase (> 30%) in precipitation amount associated with S-Centers over most of the ECL region (Fig. 4.8b) given the 20-30% increase in S-Centers precipitation rate (Fig. 4.7b) and the slight increase (5-10%) in the frequency of the S-Centers over the ECL (Fig. 4.6b). The M-Centers have a smaller increase (10-20%) in the precipitation amount over the ECL (Fig. 4.8c). Meanwhile, the precipitation amount for the W-Centers does not have any significant change over the ECL (Fig. 4.8d); although the precipitation rate associated with the W-Centers is increasing (Fig. 4.7d), the W-Centers density is decreasing over most of the East Coast region (Fig. 4.6d), canceling the increase of precipitation rate.

Overall, in the ECL region the S-Centers have the largest increase in precipitation rate (Fig. 4.7), and the potential reasons for that will be explored in the Section 4.3.3. Meanwhile, most of the increase in cool season precipitation amount over eastern North America and western Atlantic is from the S-Centers and M-Centers (Fig. 4.8); although the W-Centers contributes over 30% to the total precipitation at relatively lower latitudes (< 40°N) and there is a ~10% increase in the precipitation rate, the frequency of W-Centers decreases by 5-15% over this region.

4.2.3 Cyclone relative precipitation extremes

In addition to the mean cyclone relative precipitation amount and rate, the extreme precipitation associated with cyclones was also examined over the geophysical map.

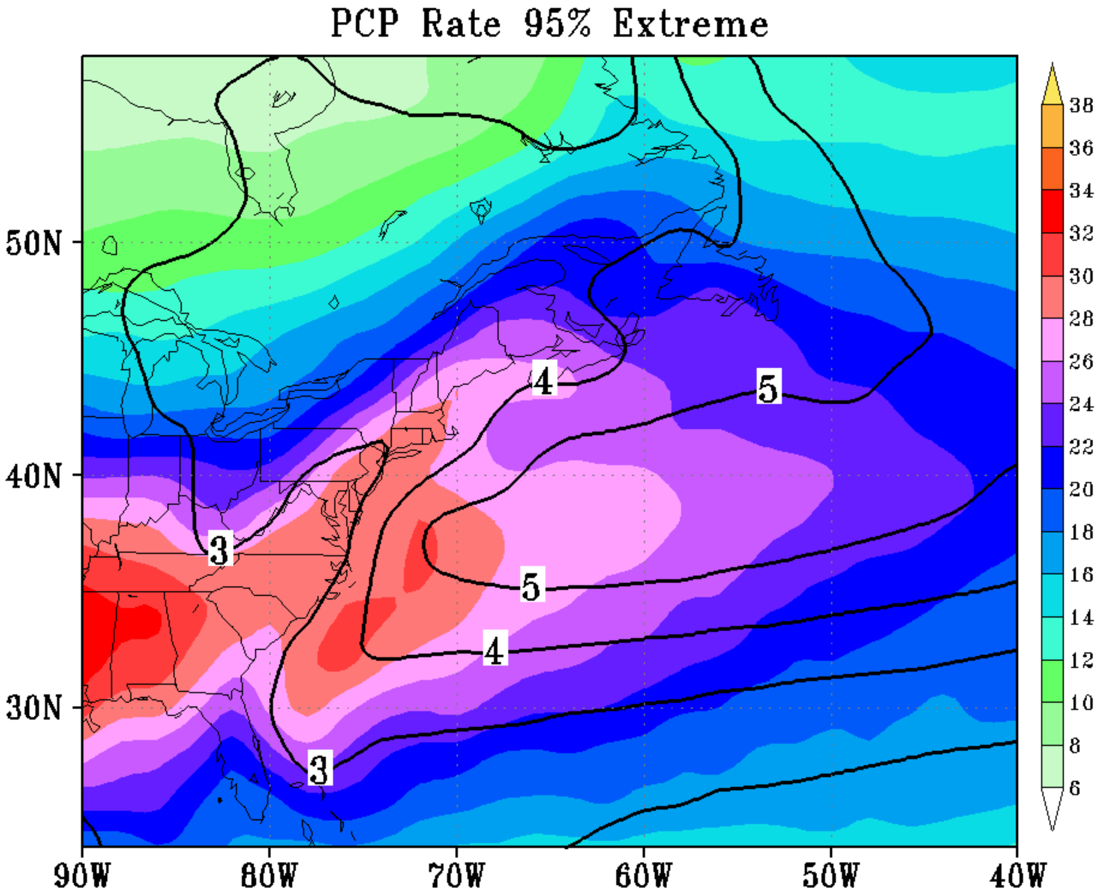

Fig. 4.9: The historical cyclone relative precipitation extreme (95% percentile) rate (colors, mm/day) and the frequency (contours, days per cool season) for the historical period (1979-2004 cool seasons) for the ensemble mean of the ten CMIP5 models.

The precipitation extreme at each grid point is defined using the 95% percentile for the historical and three future periods, respectively. At each grid point, the samples are recorded when it has at least 1 mm/day precipitation rate and is covered by a cyclone relative box. Although there are a few extreme precipitation cases (< 5% at latitudes < 30°N, not shown) out of the cyclone relative box, nearly all of the extreme precipitation is associated with extratropical cyclones (within the cyclone relative box) during cool season. Figure 4.9 shows the extreme events threshold at each grid for the historical period. There are two maxima (over 30 mm/day): one is at east of the U.S. East Coast and the other one is over the north of Mexico Gulf. The frequency along the East Coast is around 3 days per cool season. During late 21st century, the largest increase (> 5mm/day, about 20%) is just along the East Coast region (ECL and ECW), while the increase within the ECWA region is much smaller (Fig. 4.10). The increases of early and middle 21st century are smaller than the late 21st century (not shown).

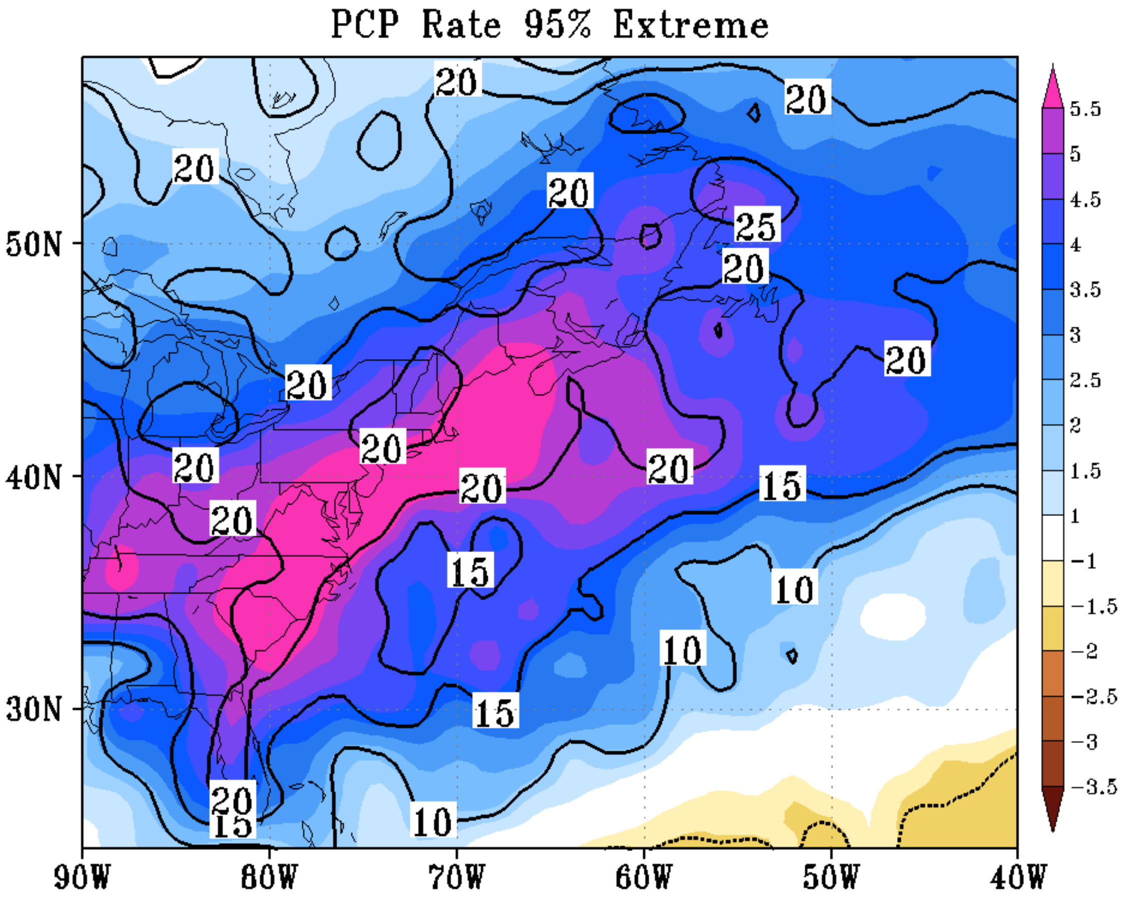

Fig. 4.10: The future changes of cyclone relative precipitation extreme (95% percentile) rate (colors, mm/day) and the percentage changes (contours) for the late 21st century (2069-2098 cool seasons) for the ensemble mean of the ten CMIP5 models.

The results using the 99% percentile to define the extreme events (not shown) are similar to using 95%, which suggests that the largest increase of precipitation extremes is just along the East Coast, but a slightly larger (20-25%) than the increase of 95% percentile (~20%).

4.3. Cyclone relative precipitation in the cyclone system

In addition to the earth-related cyclone relative precipitation, the future changes of cyclone relative precipitation within the synoptic-scale cyclone system were also investigated in the cyclone-related coordinate in this section. The related physical processes responsible to the future cyclone relative precipitation changes were also examined within the synoptic-scale cyclone system.

4.3.1 Future trend of cyclone relative precipitation

In order to examine the future trends of the precipitation around extratropical cyclone center over eastern North America and western Atlantic, two metrics were calculated for each cyclone center: the mean precipitation rate around the cyclone center and the maximum precipitation rate around the cyclone center within the small purple box in Fig. 2.4b, which covers the major part of the precipitation band.

Through the 21st century, there is a significant increase trend for the mean precipitation around the ECL cyclone centers (within the small purple box in Fig. 2.4b), not only for the ensemble mean but also for the individual models (Fig. 4.11a). The mean precipitation of ECL centers for ensemble mean increases by ~21% from 7.6-8.0 mm/day in the historical period (1979-2004 cool seasons) to 9.2-9.6 mm/day in the late 21st century (2069-2098 cool seasons). Meanwhile, the mean precipitation for the WA cyclone centers increases by ~10% from 6.8-7.1 mm/day in the historical period to 7.4-7.8 mm/day in the late 21st century (Fig. 4.11b). The increase (~14%) of mean precipitation for the ECW centers is just between the ECL and WA (not shown).

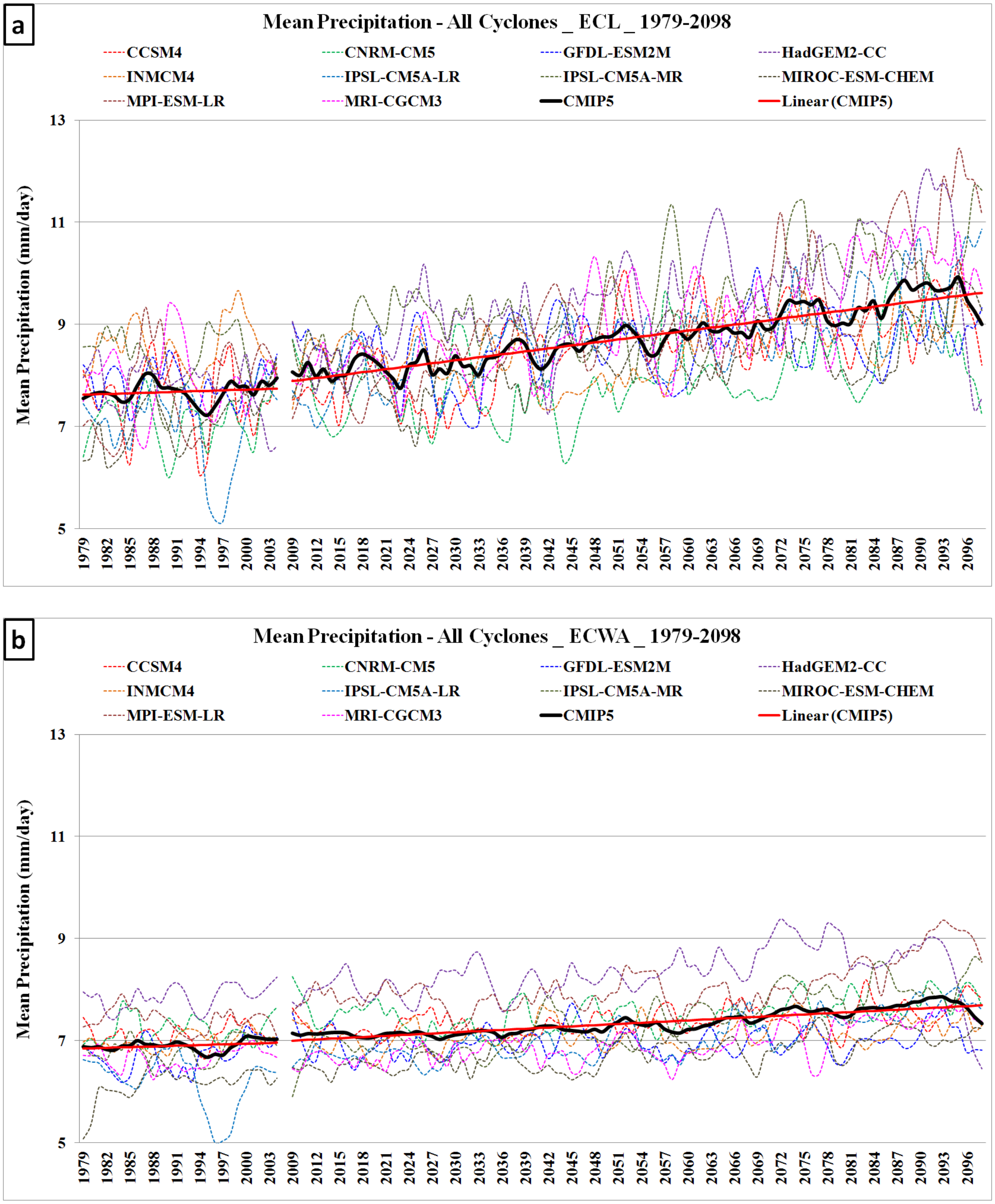

Fig. 4.11: The time series (3-year running mean) of mean precipitation around the cyclone center (within the small purple box in Fig. 2.4b) from 1979 to 2098 cool season for the cyclone centers within (a) the ECL region and (b) the WA regions. The black line is the ensemble mean of the 10 CMIP5 models, the red solid line is the linear trend of the CMIP5 mean, and the dashed lines are for the individual models.

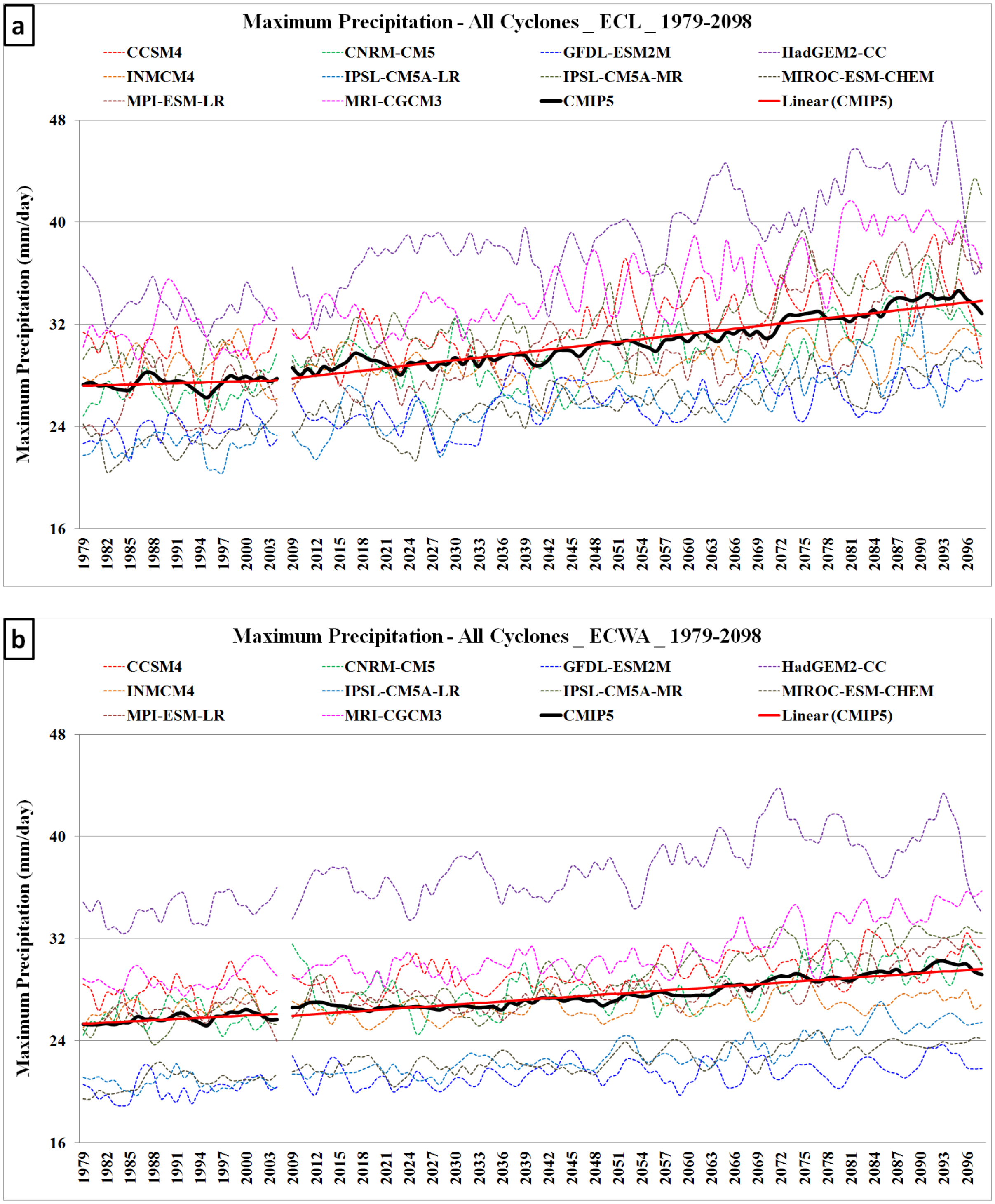

Fig. 4.12: Same as Fig. 4.11, but for the maximum precipitation.

The maximum precipitation around the ECL cyclone centers (within the small purple box in Fig. 2.4b) also has an increase trend, from ~27 mm/day in the historical period to ~34 mm/day by the end of 21st century, increasing about 26% (Fig. 4.12a). Similar to the results of mean precipitation, the increase of maximum precipitation for the WA centers is smaller (about 15%, Fig. 4.12b) than the ECL centers, and the increase for the ECW centers (about 20%, not shown) is just between the ECL and WA centers.

The variability among models for the maximum precipitation is very large, especially for the WA centers. For example, during historical period the maximum precipitation around WA cyclone centers is ~34 mm/day in HadGEM2-CC, but only ~20 mm/day in three low-resolution models, GFDL-ESM2M, IPSL-CM5A-LR, and MIROC-ESM-CHEM (Fig. 4.12b).

4.3.2 Distribution of cyclone relative precipitation intensity

In addition to the future trends of precipitation around extratropical cyclones, the intensity distributions of the precipitation were also examined. Similar with the approach for future trends of precipitation, two metrics, the mean precipitation rate and the maximum precipitation rate around the cyclone center (within the small purple box in Fig. 2.4b) were calculated for each cyclone center and used to examine the intensity distributions.

For the cyclone centers within ECL during historical period, the maximum precipitation is concentrated in 12-28 mm/day, and has a long tail to the heavy precipitation (Fig. 4.13a). The maximum precipitation of the WA cyclone centers is also concentrated in 12-28 mm/day (Fig. 4.13b). However, the overall distribution for the WA centers is narrower than the ECL centers, with fewer centers for the heavy precipitation part. For example, there are 18.3% ECL centers located in the bins > 40mm/day, while there are only 12.3% WA centers located in the same bins (Fig. 4.13b). The distribution of the ECW centers is very close to the distribution of the ECL (not shown).

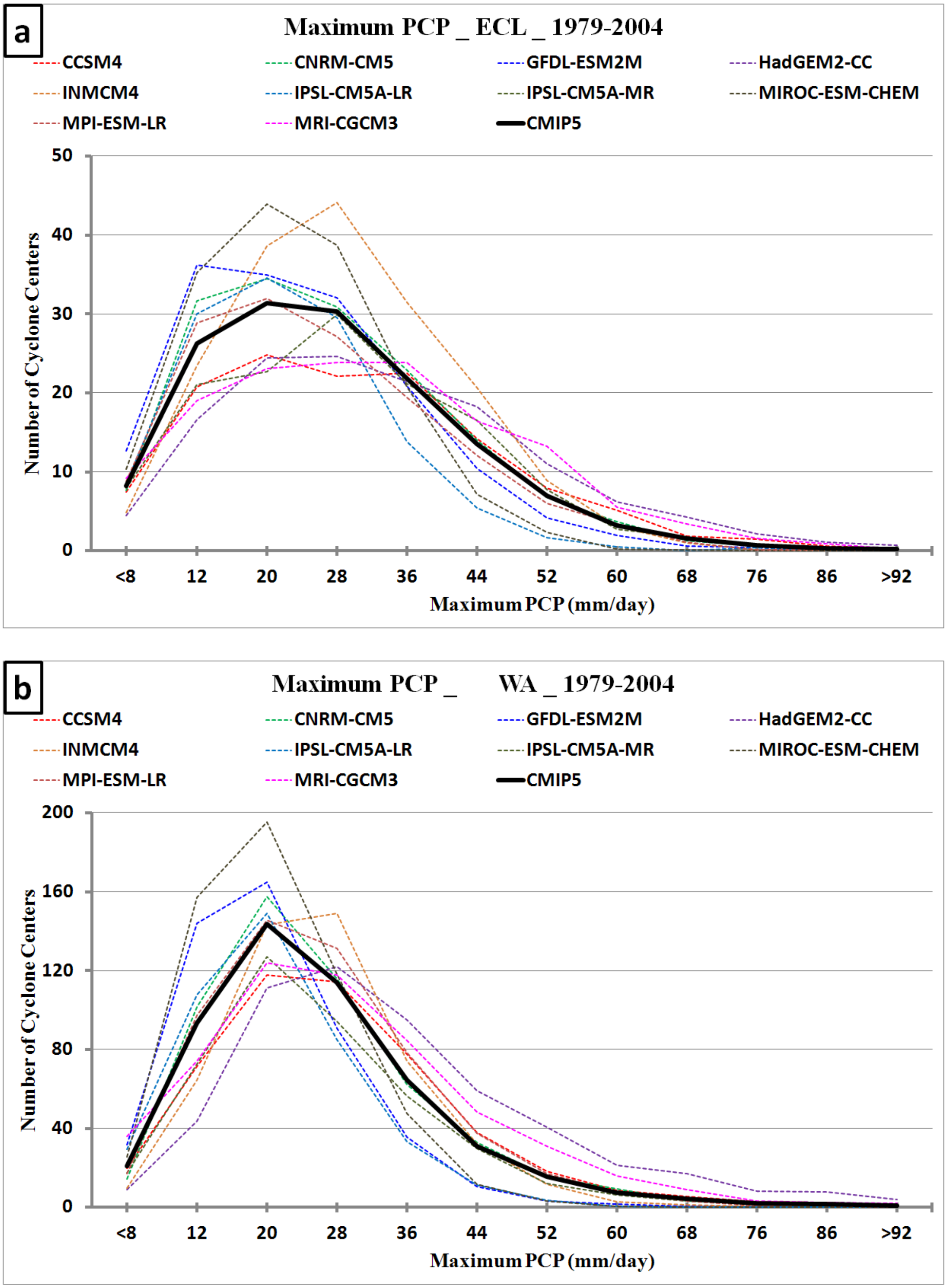

Fig. 4.13: The distribution of maximum precipitation around the cyclone centers (within the small purple box in Fig. 2.4b) for the mean of the 10 CMIP5 models (black line) and individual models (dashed lines) in historical period (1979-2004 cool seasons) for (a) the ECL region and (b) the WA region.

Through 21st century there is a significant shift towards the heavy precipitation part with high model agreement for all of the ECL, ECW and WA cyclone centers. For the ECL centers, all 10 CMIP5 models have an increase in maximum precipitation of > 48 mm/day (not shown); meanwhile, the ensemble mean has a significant increase for the maximum precipitation > 36 mm/day, and this increase become larger and larger from early to late 21st century (Fig. 4.14a).

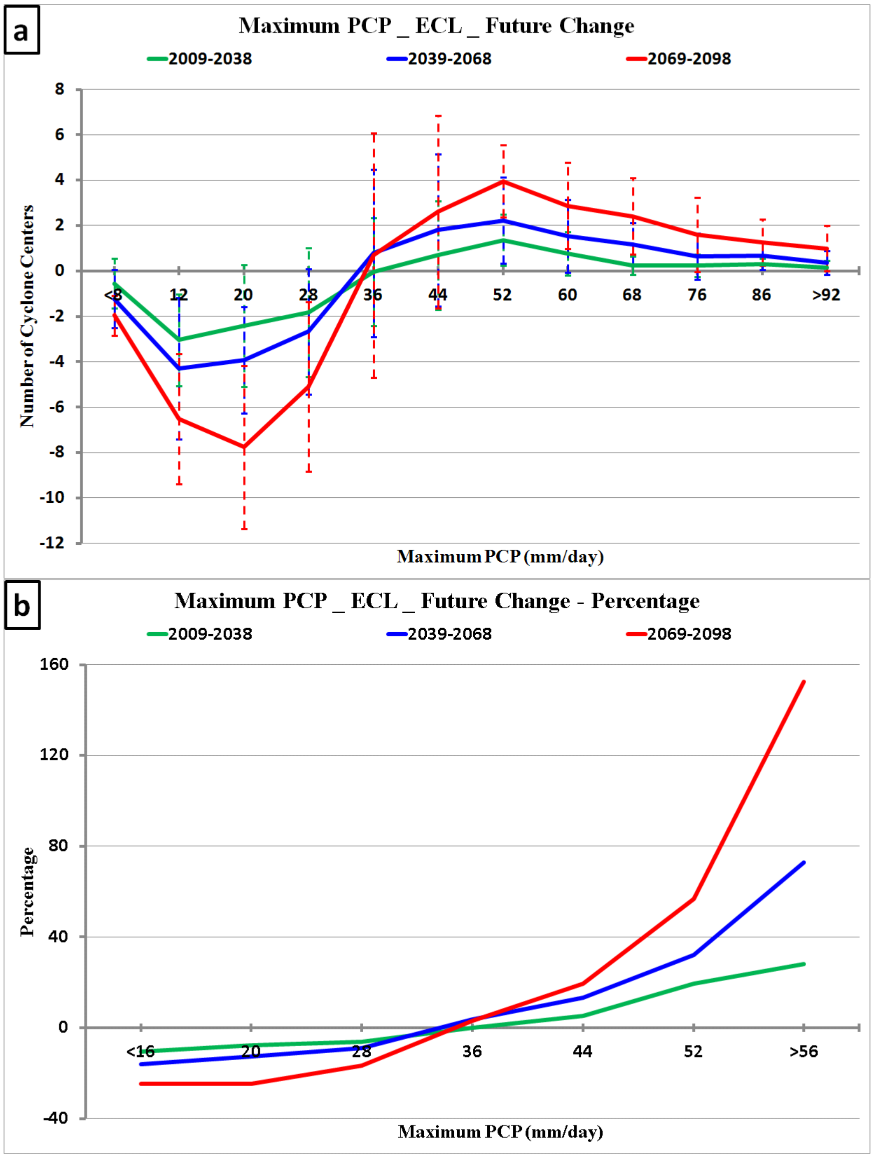

Fig. 4.14: (a) The future changes of the distribution in maximum precipitation around the ECL cyclone centers. (b) Same as (a), but for the percentage changes. The vertical bars in (a) are the spread (±1 standard deviation) of the models.

Although there is a relatively large uncertainty among the 10 CMIP5 model in the future change in precipitation (Fig. 4.14a), the uncertainty in the sign for the change in future precipitation amount is mainly concentrated at the 36 mm/day bin. The heaviest maximum precipitation around the ECL cyclone centers (>56mm/day, merged the bins of >56mm/day to get enough cases) has a significant (~150%) increase (Fig. 4.14b) in the late 21st century (2069-2098 cool seasons).

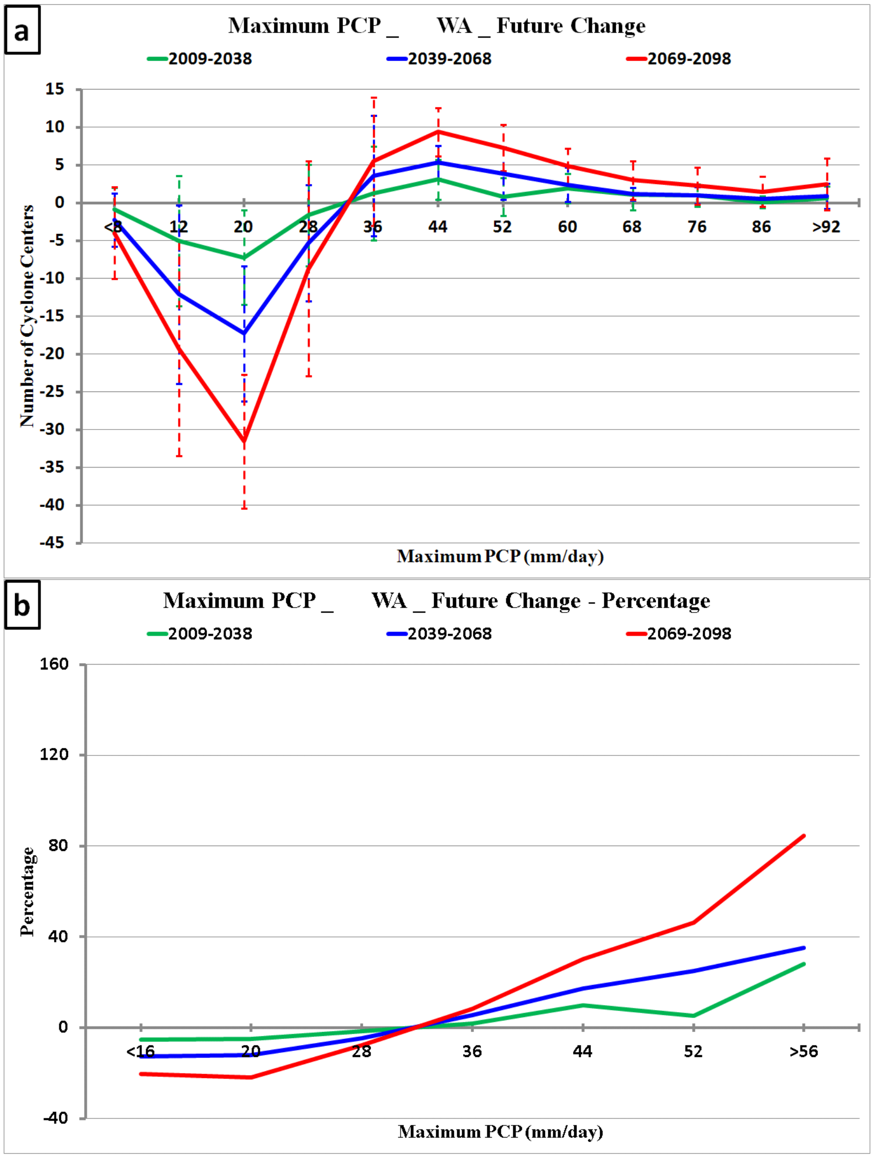

Fig. 4.15: Same as Fig. 4.14, but for the WA centers.

The WA also has a similar shift towards the heavy precipitation (Fig. 4.15a), but the increase for the heaviest maximum precipitation (>56mm/day) is about 85% (Fig. 4.15b), much smaller than the ECL. The changes for the ECW cyclone centers are between the ECL and WA centers (not shown).

The future change in the distribution of mean precipitation around the cyclone centers (within the small purple box in Fig. 2.4b) is similar to the results of maximum precipitation, in which there is a significant shift towards the heavy precipitation (not shown). However, the variability among models for the mean precipitation (Fig. 4.16) is much smaller than the maximum precipitation (Fig. 4.13). For example, the standard deviation at the frequency maximum bin is 3.1 (about 11% of the mean value 28.0) for the mean precipitation (2 mm/day bin, Fig. 4.16a) and it is 7.3 (about 23% of the mean value 31.4) for the maximum precipitation (20 mm/day bin, Fig. 4.13a). Overall, there is a significant shift towards the heavy precipitation through 21st century for the cyclone relative precipitation, and the ECL centers have the largest increase in the heaviest precipitation.

In order to focus on those ECL centers related to the heaviest precipitation and explore the future changes of those cases, the precipitation extreme cyclone cases were defined using the 95% percentile of the mean precipitation around cyclone centers. The extreme centers were defined for the historical and three future periods respectively: >18.4 mm/day for 1979-2004 cool seasons, > 19.2 mm/day for 2009-2038, > 20.6 mm/day for 2039-2068, and > 22.5 mm/day for 2069-2098. The mean precipitation around cyclone center was used rather than the maximum precipitation, since for the maximum precipitation the variability among models is too large as mentioned in early this section and Section 4.3.1.

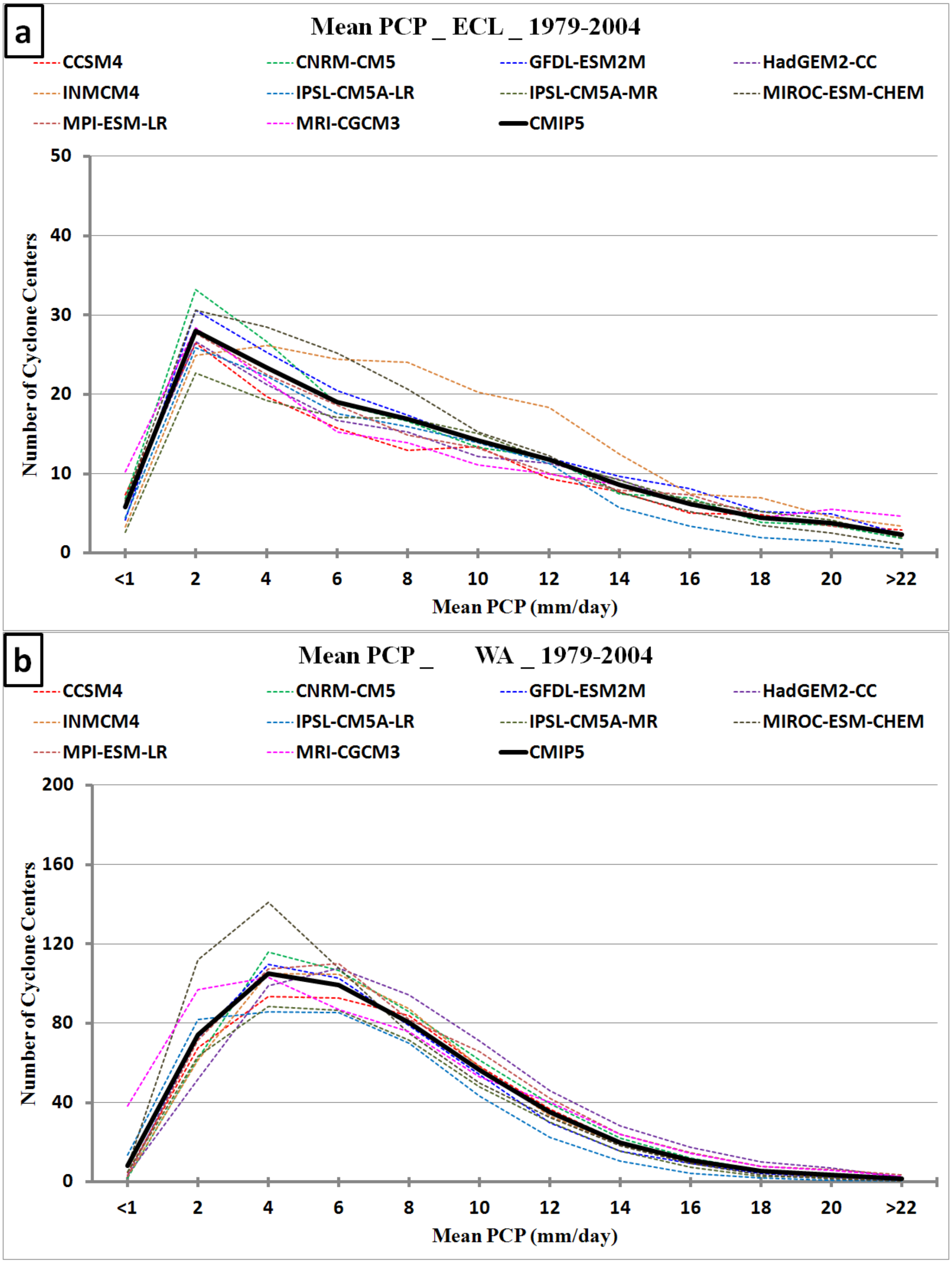

Fig. 4.16: Same as Fig. 4.13, but for the mean precipitation around the cyclone centers (within the small purple box in Fig. 2.4b).

Fig. 4.17 shows the distribution of those extreme precipitation events for the historical and three future periods. In the historical period (black histogram), over 90% of the extreme cases are concentrated at 18-26 mm/day; and during late 21st century (red histogram), over 90% of the extreme cases are concentrated at 22-32 mm/day, shifting to the heavier precipitation part significantly. Meanwhile, in late 21st century, it has a longer tail towards to the most extreme values. The 99% percentile was also used to define the extreme cases and the result is similar to the results using 95% percentile, the extreme cases shift towards to even heavier precipitation part significantly.

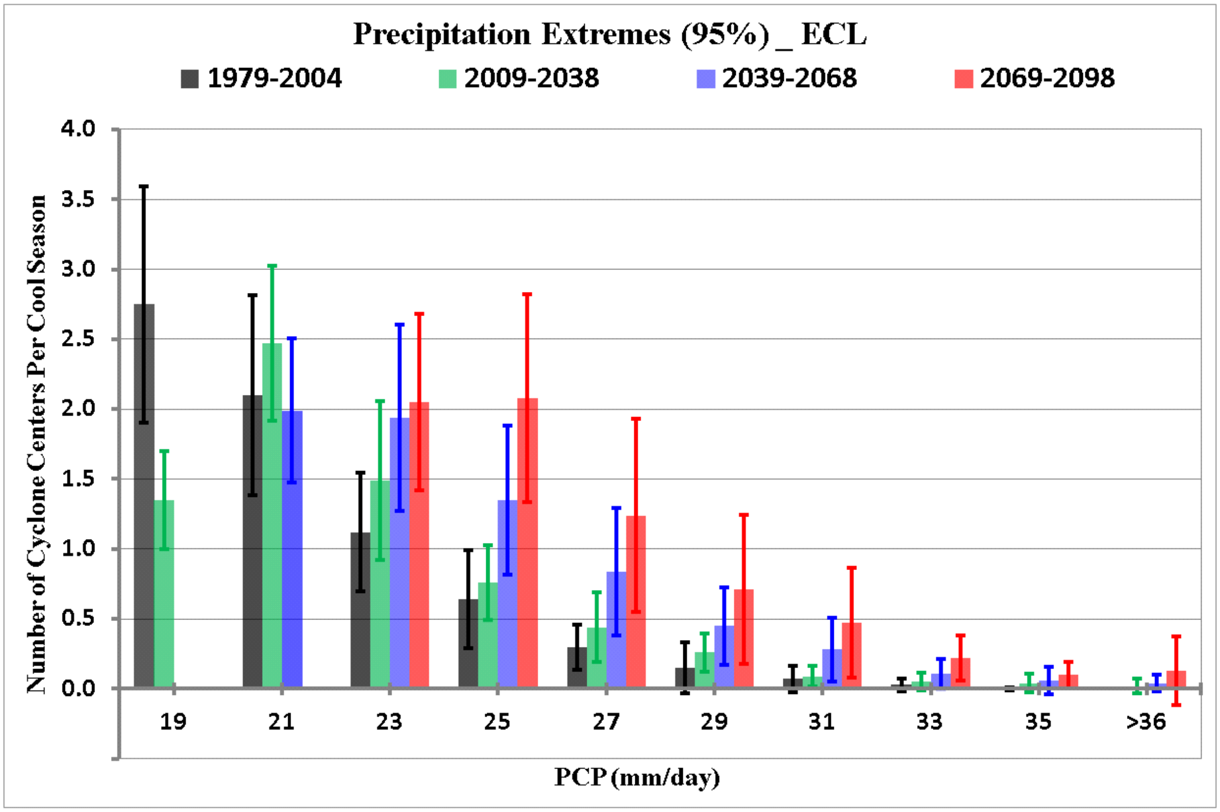

Fig. 4.17: The distribution of the extreme mean precipitation for the ECL cyclone centers for historical period (black), early (green), middle (blue) and late (red) 21st century. The vertical bars are the spread (±1 standard deviation) of the models.

4.3.3 Precipitation around cyclone center and the future changes

This section focuses on the spatial structure and intensity of the precipitation around cyclone centers in different regions and different intensity categories, and their future changes. Meanwhile, the related fields which have impacts on precipitation changes are also examined to better understand the precipitation changes in those different cyclones.

a. Structure and intensity of precipitation around cyclone center

The precipitation around the ECL, ECW and WA cyclone centers during historical period was compared to highlight the difference in precipitation structure and intensity around cyclone centers over different regions. Fig. 4.18 shows the CMIP5 models mean composite (average) SLP, surface precipitation, and 850-250 hPa moisture content for the cyclone centers within the ECL, ECW, and WA regions in Fig. 2.1 respectively. The precipitation maximum is located immediately to the northeast of cyclone center for all of these centers; and the precipitation maximum for the ECW centers (middle panel) is the largest (> 17 mm/day), while the maximum for the WA centers (bottom panel) is the smallest (~10 mm/day). The ECW centers, which are over and just east of the Gulf Stream, have the largest moisture content within the warm sector (Fig. 4.18d). Meanwhile there is much less moisture content for WA centers offshore (Fig. 4.18f), since most of the WA cyclone centers are further north over the relatively cool ocean. The difference in other factors that impact precipitation, such as vertical motion and stability, is smaller (not shown) than moisture content for the ECL, ECW, and WA cyclone centers. Thus, the mean precipitation for the ECL, ECW and WA centers depends more on the available moisture.

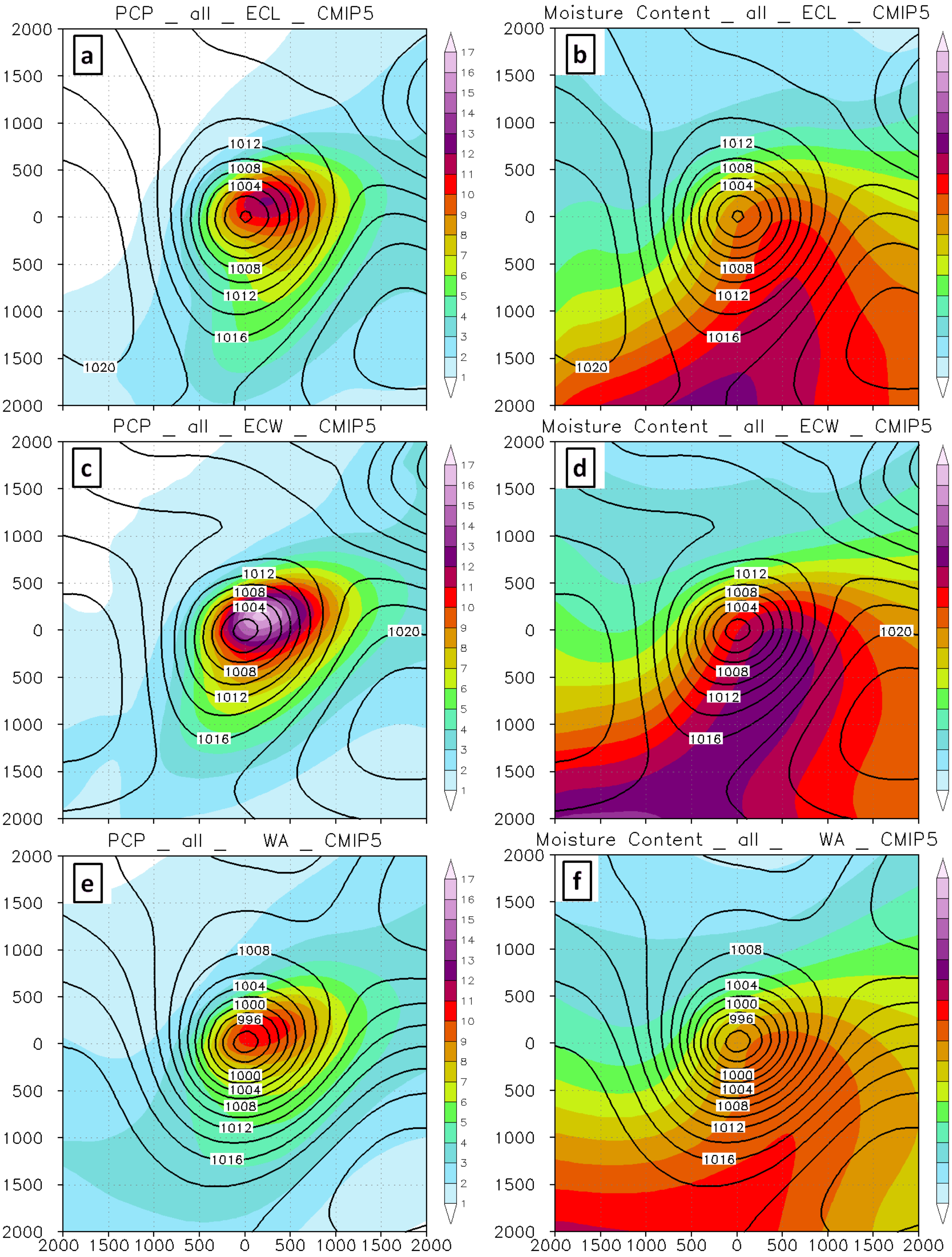

Fig. 4.18: The composite SLP (contours, hPa), precipitation (colors in left panel, mm/day) and 850-250hPa moisture content (colors in right panel, kg/m^2) for historical (1979-2004) mean of the 10 CMIP5 models for the cyclone centers within (a) (b) ECL, (c) (d) ECW, and (e) (f) WA. The X and Y axis shows the distance (km) from cyclone center.

Focusing on the ECL cyclone centers, which have the largest increase in precipitation (Section 4.3.1 and 4.3.2), the composite precipitation was also calculated for the S-Centers (< 990 hPa), M-Centers (990 – 1005 hPa), and W-Centers (>1005hPa) to explore the differences in cyclone systems of different intensity. There is a large well-defined comma-shaped precipitation region for the S-Centers, with the maximum around 14 mm/day over the comma head (Fig. 4.19a). The M-Centers have a smaller heavy precipitation area and a weaker precipitation maximum around 12 mm/day (Fig. 4.19c). The precipitation for W-Centers is concentrated just east and northeast of the cyclone center, with a maximum around 11 mm/day (Fig. 4.19e). There is a little more (~10%) moisture content over the warm side of the W-Centers than the M-Centers and S-Centers (not shown), since most of these systems are further south in the warmer air. However, the upward motion for S-Centers is significantly stronger, with a maximum of -0.24 Pa/s (700hPa level), and it covers much larger area than the W-Centers (Fig. 4.19bdf). The magnitude in upward motion for the M-Centers is between the S-Centers and W-Centers. As a result, the S-Centers have a much larger precipitation band and a stronger maximum than the M-Centers and W-Centers as mentioned above (Fig. 4.19a,c,e), which is mainly driven by the vertical motion while the differences of other factors, such as moisture content, are relatively small (not shown).

Through 21st century there is a significant increasing trends in the precipitation around extratropical cyclone centers over the eastern North America and western Atlantic (Section 4.3.1). The future changes of the composite precipitation around cyclone centers for the early, middle, and late 21st century were calculated. The precipitation increase in the late 21st century is the largest, thus only the future changes in late 21st century are shown and discussed in the following.

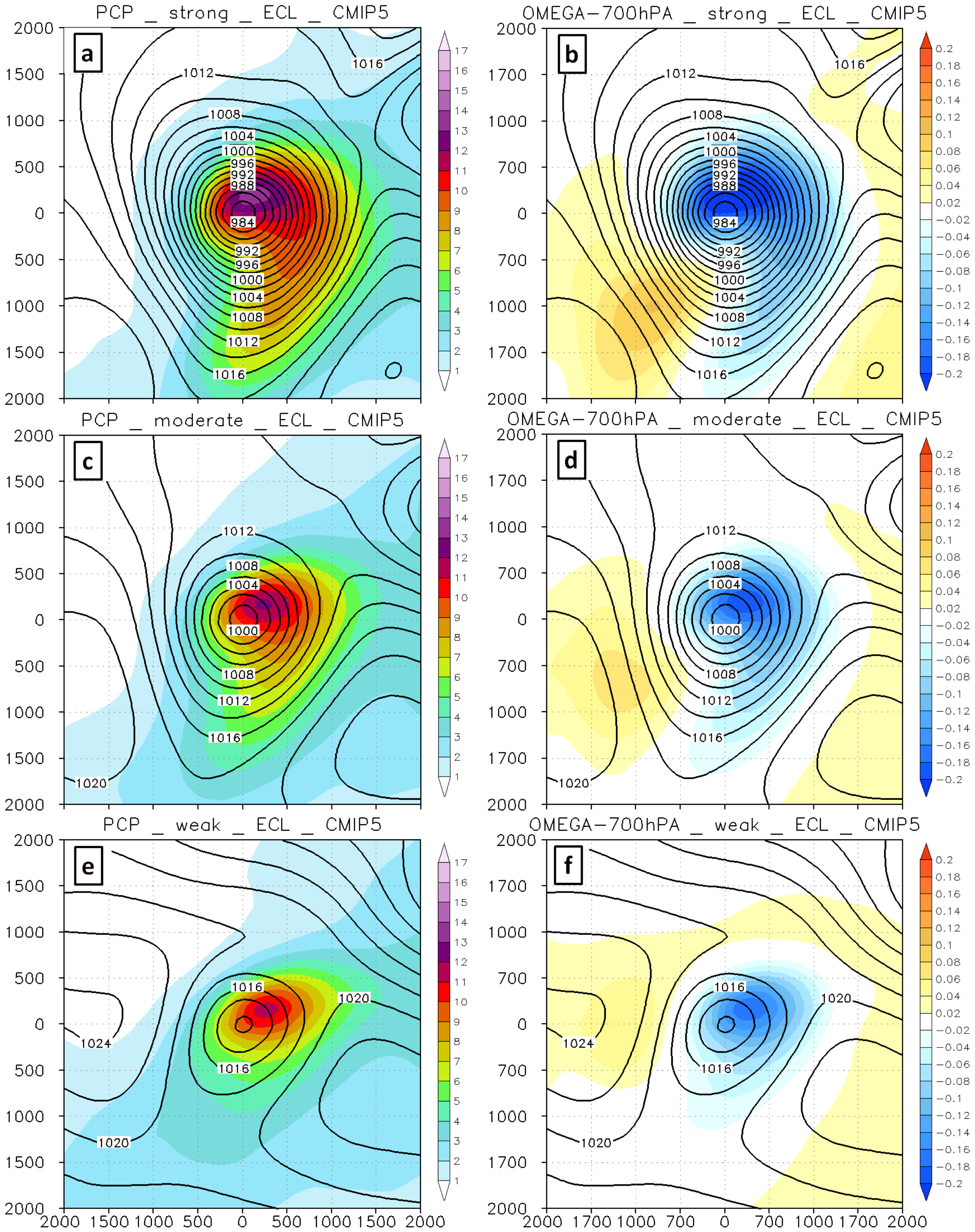

Fig. 4.19: The composite SLP (contours, hPa), precipitation (colors in left panel, mm/day) and 700hPa vertical motion (colors in right panel, Pa/s) for historical (1979-2004) mean of the 10 CMIP5 models for the (a) (b) S-Centers, (c) (d) M-Centers, and (e) (f) W-Centers within ECL region. The X and Y axis shows the distance (km) from cyclone center.

b. *Future precipitation changes for ECL, ECW and WA cyclone centers*

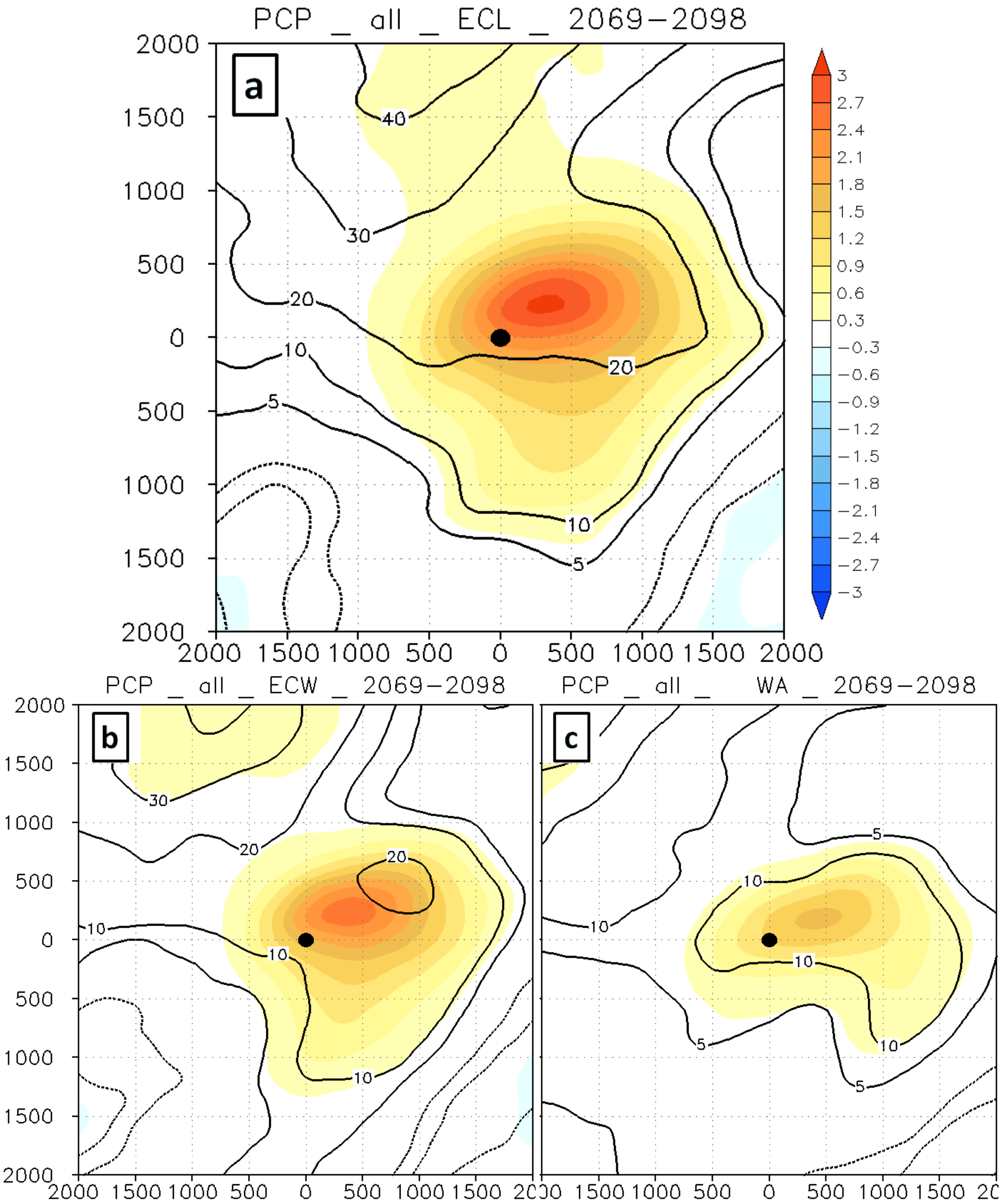

Fig. 4.20: The future precipitation changes (colors, mm/day) and the percentage changes (contours) for later 21st century (2069-3098 minus 1979-2004) for the (a) ECL, (b) ECW, and (c) WA cyclone centers.

Figure 4.20 shows the precipitation changes around cyclone centers within the ECL, ECW, and WA regions during late 21st century. As expected, the precipitation around cyclone centers increases with the climate warming (more water vapor). However, there is a relatively large difference in precipitation change for the ECL, ECW, and WA cyclone centers. The ECL centers have the largest increase in precipitation rate for both the absolute value and percentage, while the WA centers have the smallest increase. For example, the percentage increase of precipitation over the precipitation maximum region northeast of cyclone center (hereafter PMAX) is ~ 26% for the ECL, ~ 18% for the ECW, and ~13 % for the WA (Fig. 4.30).

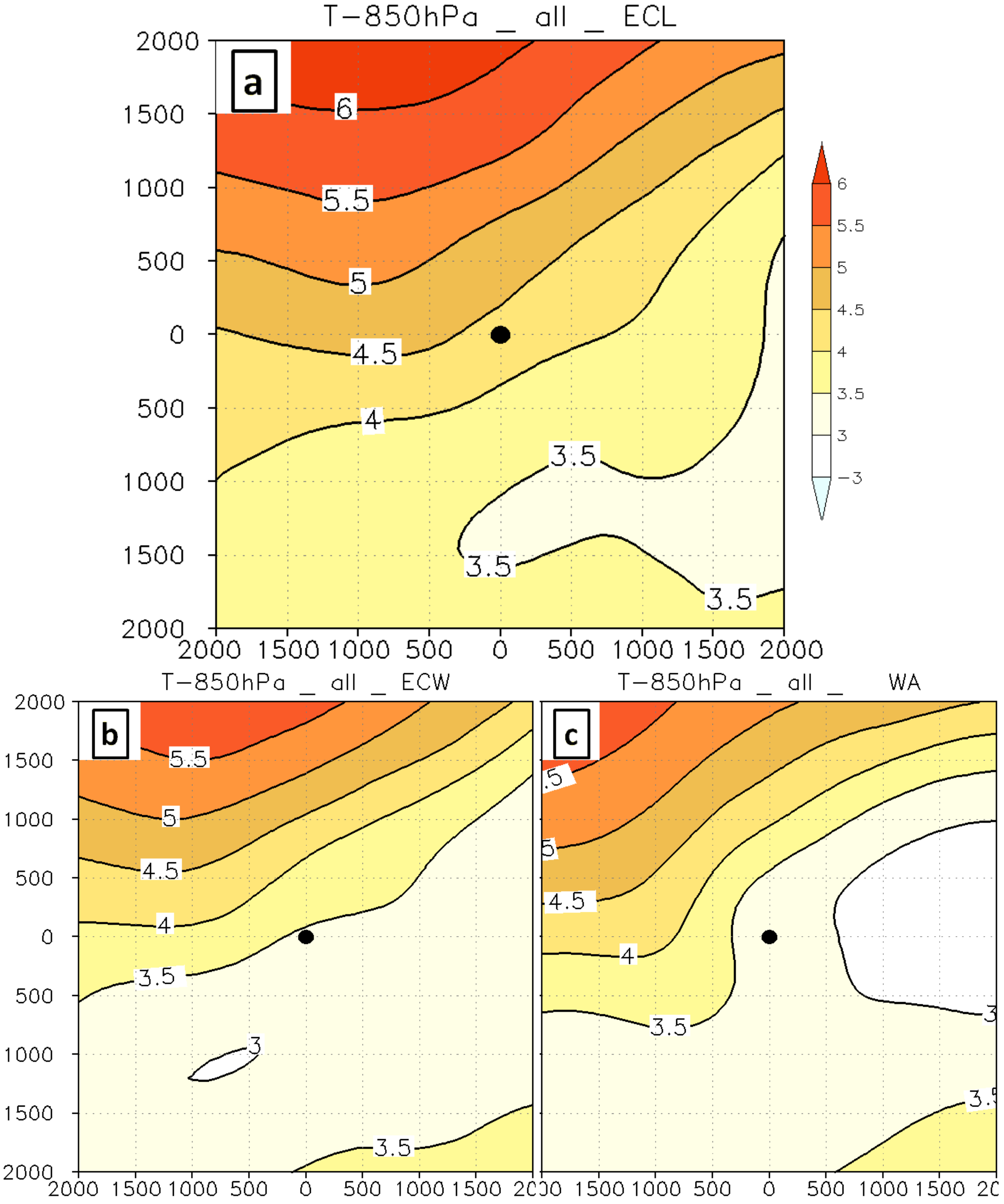

Fig. 4.21: Same as Fig. 4.20, but for the changes of 850hPa temperature (K).

In order to explore the reasons for the difference in precipitation increase, the future changes of surface and low troposphere temperature around those cyclone centers were calculated first. Overall, for all cyclone centers over the eastern North America and western Atlantic the surface and low troposphere temperature increase is relatively larger over the north-west side of the cyclone center (over or close to the North America continent) and it is smaller over the southeast side (over or close to the North Atlantic ocean). Meanwhile, the surface and low troposphere temperature increase around the ECL centers (over the continent) is larger than the WA centers (over the Atlantic). For example, the 850hPa temperature increases in Figure 4.21 represent these changes. This pattern is not surprising since the IPCC AR5 Chapter 12 shows that there is large spatial variability in the temperature changes, namely that the surface and low troposphere temperature increase over the Arctic and the North American continent is larger than the increase over North Atlantic in the CMIP5 RCP8.5 experiment. Over the PMAX of ECL cyclone centers, the 850hPa temperature increases by ~4.3 K, which is larger than the ECW (~3.5 K) and WA (~3.3 K) cyclone centers (Fig. 4.21).

The Clausius–Clapeyron relation suggests a ~7% increase in the moisture content when the temperature increases 1 K. The future increases of the moisture content at 850-250hPa (not including the lower level moisture because data is not available) for the ECL, ECW and WA cyclone centers (Fig. 4.22) and the temperature at that level (only 850hPa shown in Fig. 4.21) are consistent with the Clausius–Clapeyron relation, approximately 7% increase in moisture content per 1K increase in temperature. Thus, similar with the 850hPa temperature increases, the moisture increase at 850-250 hPa over the PMAX for the ECL cyclone centers (~30%) is larger than the ECW (~ 25%) and WA (~ 22%) centers (Fig. 4.22).

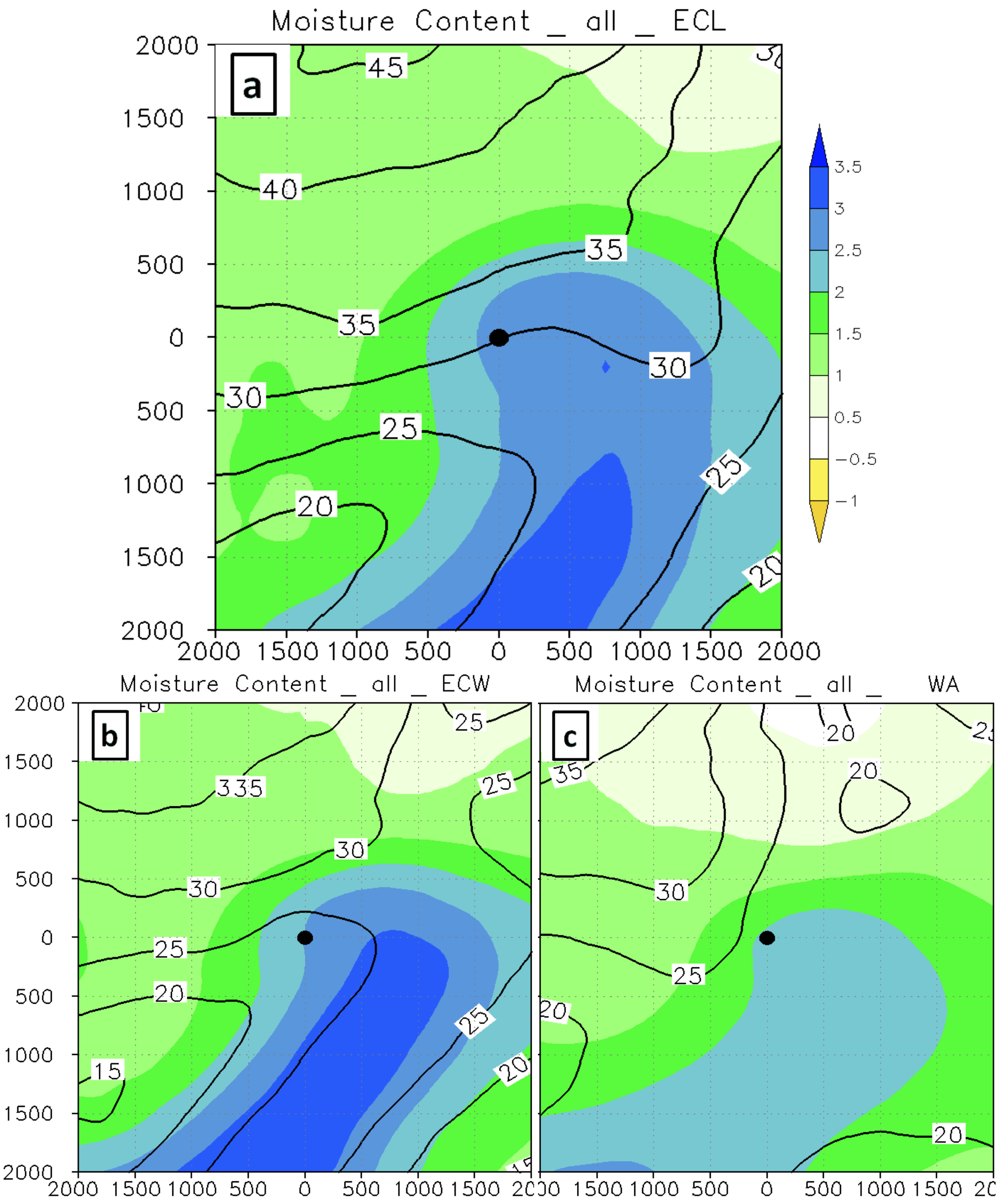

Fig. 4.22: Same as Fig. 4.20, but for the changes of 850-250hPa moisture content (kg/m^2).

Therefore, the differences in the surface and lower troposphere temperature increase (so the differences in the moisture increase) for the ECL, ECW and WA cyclone centers are important to the future precipitation increases. However, the precipitation responses (% per K) to the temperature increase are still different for the various regions. For example, over the PAMX, it is ~ 6.0% per K for the ECL, ~ 5.1% per K for the ECW and ~ 3.9% per K for the WA centers, indicating that there must be some other factors impacting the precipitation change. The low level wind speed, upper level jet, moist static stability, and warm advection were analyzed.

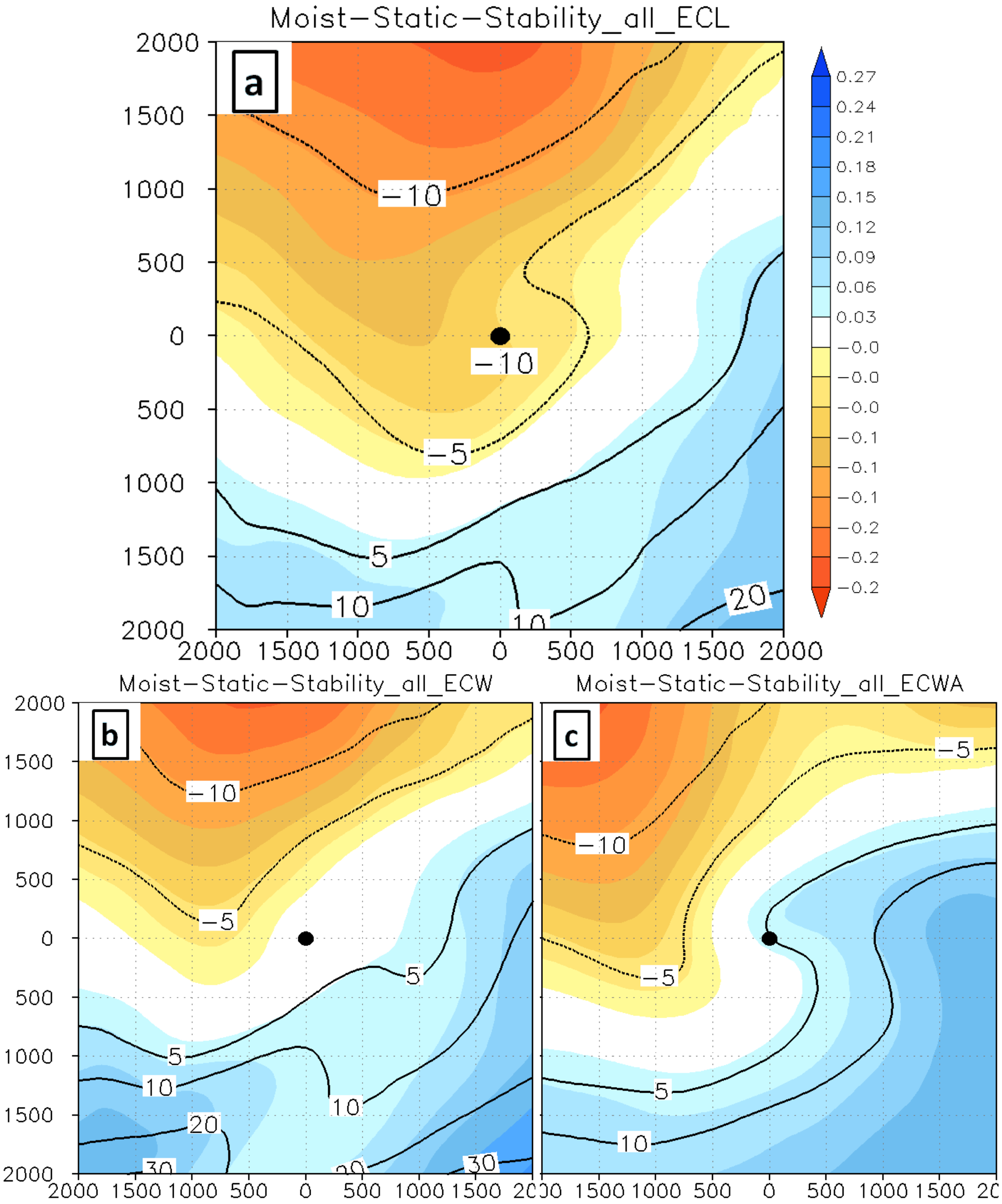

Fig. 4.23: Same as Fig. 4.20, but for the changes of 850-500hPa moist static stability ($N^2 \times 10^4$).

The field that has the largest difference in the future changes for the ECL, ECW, and WA cyclone centers is the moist static stability ($N^2 \times 10^4$, calculated following Durran and Klemp 1982; Jiang and Doyle 2009). Under climate change over North Hemisphere cool season the upper troposphere warms more quickly than the lower troposphere at low to middle latitudes (< 55°N). Meanwhile, at higher latitudes (>55°N) due to the amplification near the surface over continental regions at high latitudes, the low-level temperature increase is larger than at upper levels at high latitude (IPCC AR5 Chapter 12). As a result, the atmosphere becomes less stable at the high latitudes, especially over the land, while it becomes more stable over middle latitudes, especially over the Atlantic Ocean where the surface temperature increase is much smaller (Frierson 2006). The moist static stability changes at 850-500hPa (Fig. 4.23) around the ECL, ECW and WA cyclone centers over eastern North America and western Atlantic are consistent with that. Overall, the atmosphere becomes less stable in the northern and western side of the cyclone center and more stable in the south and east side. The boundary between the negative and positive change is close to or just over the cyclone center during late 21st century (Fig. 4.23). Around the ECL cyclone center and over the PMAX, the stability decreases by 5-10% which is more favorable for the precipitation increase. It is almost neutral for the ECW centers. However, the stability increases by 5-10% for the WA centers, which is one of the reasons responsible for the weaker precipitation response in this region.

The future change in some other factors is very similar for the ECL, ECW and WA cyclone centers, but may also contribute to the difference in precipitation response. For example, the upper level jet becomes slightly stronger (~5%) for all the ECL, ECW and WA cyclone centers and has similar positions (centers are located at the left side of the jet exit, not shown). The upward motion becomes slightly stronger (~ 5% over the PMAX by late 21st century) for the mean of all ECL cyclone centers, while it is near neutral for the WA centers.

c. *Future precipitation changes for S-Center, M-Center and W-Center*

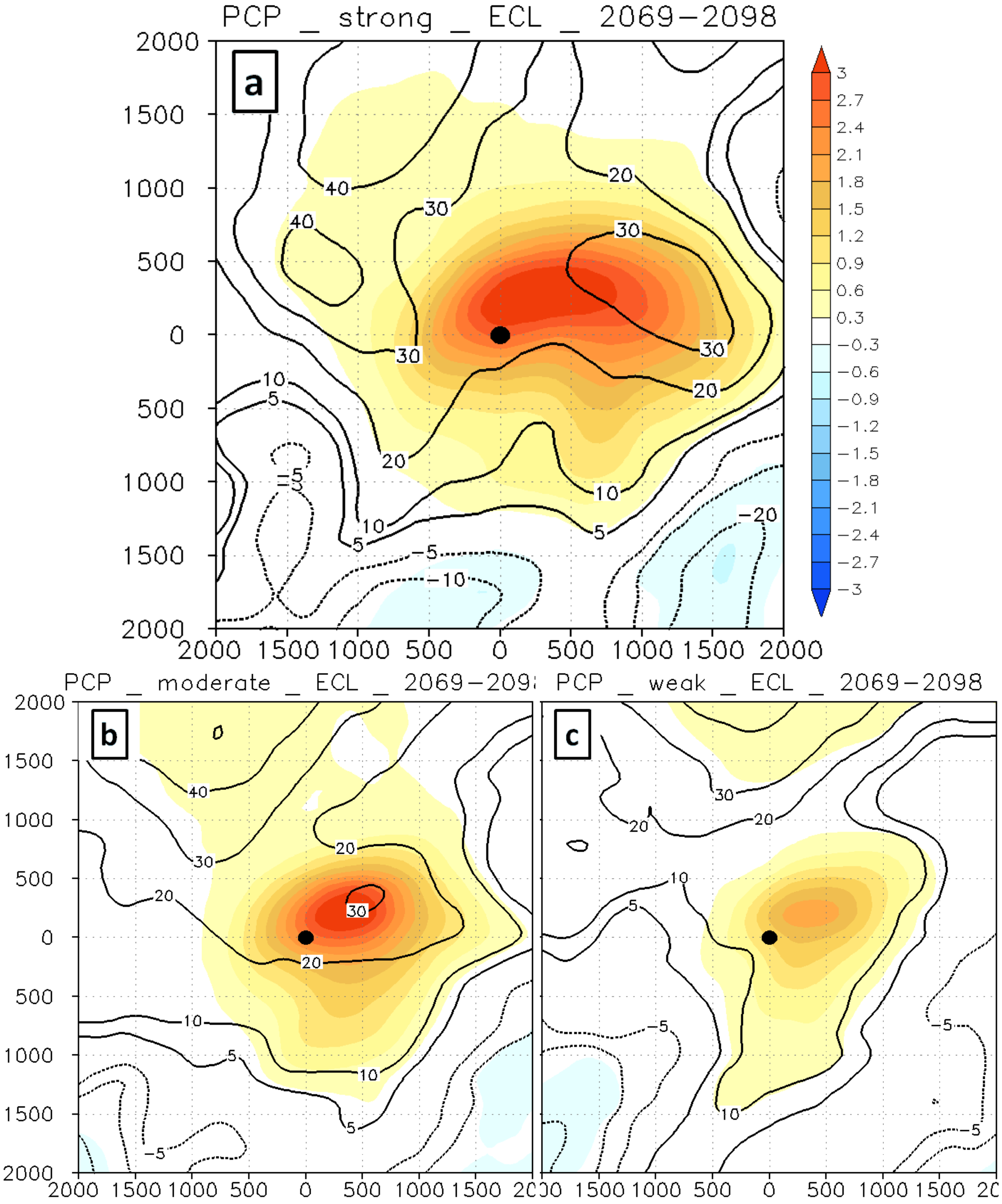

Fig. 4.24: The future precipitation changes (colors, mm/day) and the percentage changes (contours) for later 21st century (2069-3098 minus 1979-2004) for the (a) S-Centers, (b) M-Centers, and (c) W-Centers within the ECL region.

The precipitation around the ECL cyclone centers has the largest increase during late 21st century (Fig. 4.20). In historical period, the precipitation for the ECL S-Centers, M-Centers and W-Centers is quite different; the precipitation for the S-Centers is heavier and covers a much larger area than the W-Centers (Fig. 4.19). Thus, the future changes of precipitation for the S-Centers, M-Centers and W-Centers within the ECL regions were compared to highlight the difference in precipitation changes for the cyclones in different intensity.

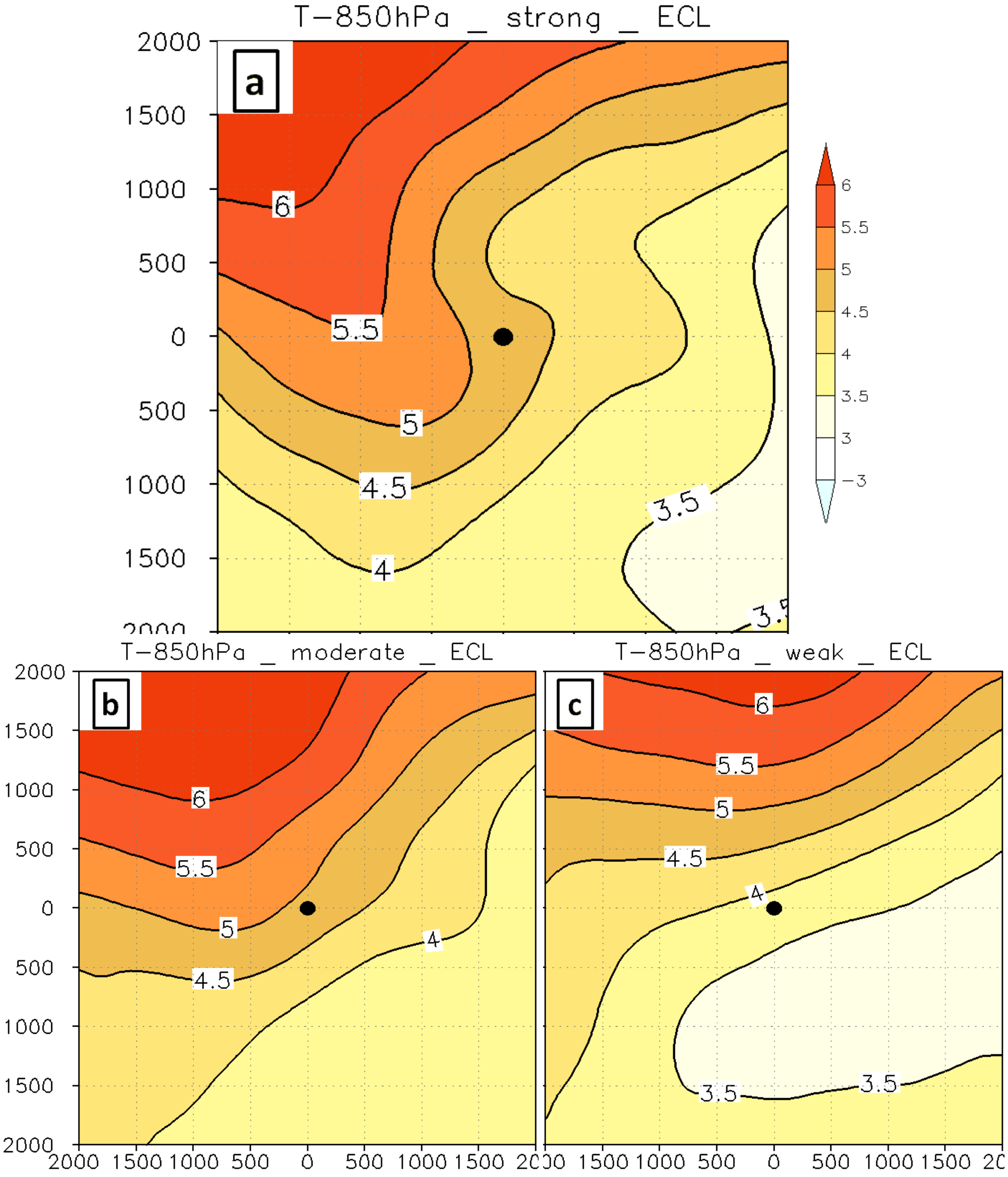

Fig. 4.25: Same as Fig. 4.24, but for the changes of 850hPa temperature (K).

The S-Centers have a pronounced increase (25-30%) just over the historical precipitation maximum in Fig. 4.19a, with the maximum increase of 3.3 mm/day (Fig. 4.24a). The precipitation increase of M-Centers has a similar pattern to the S-Centers, but the increase is a little smaller (Fig. 4.24b). Meanwhile, the increase for W-Centers is the smallest (~15%) and concentrated to a narrow region extending southward (Fig. 4.24c).

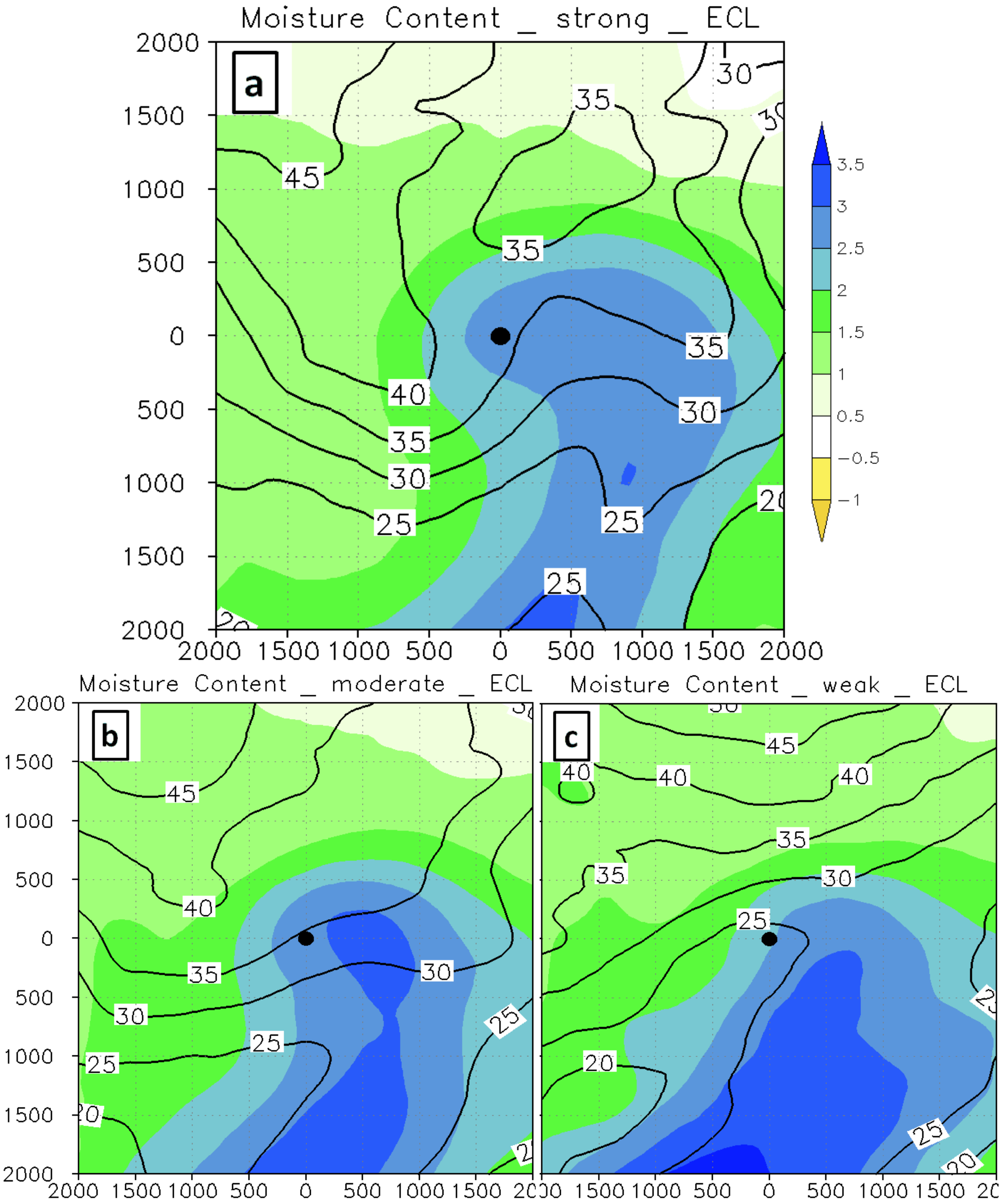

Fig. 4.26: Same as Fig. 4.24, but for the changes of 850-250hPa moisture content (kg/m^2).

The difference in the future changes of surface and low troposphere temperature for the S-Centers, M-Centers, and W-Centers within the ECL region is relatively small. For example, over PMAX, the increase of 850hPa temperature for the M-Centers (Fig. 4.25b) is very close to the S-Centers (Fig. 4.25a), with the difference < 0.5 K; and the increase of the W-Centers is slightly smaller (0.5-1.0 K) than the S-Centers (Fig. 4.25c).

The increase of moisture content (850-250hPa) is proportional to the increase of temperature, approximately following the Clausius–Clapeyron relation (~7% per K), for the S-Centers, M-Centers and W-Centers. Thus, the percentage increases of moisture content for the S-Centers and M-Centers are also very close, 33-35% over the PMAX (Fig. 4.26ab). Meanwhile, the moisture content increase for W-Centers (~ 28%) is a little smaller (Fig. 4.26c) than the S-Centers and M-Centers.

Besides the moisture content, there is a small increase (~5%) in the low-level wind speed (850 hPa) for over the warm side of S-Centers (Fig. 4.27a), which is favorable to the poleward moisture transport. There is little or no increase of 850hPa wind speed for the M-Centers (Fig. 4.27b), while there is a slight decrease (~5%) for the W-Centers (Fig. 4.27c).

In addition, another important factor with large differences for the S-Centers, M-Centers and W-Centers is the vertical motion. There is an increase in upward motion (~20% at 700hPa) with a maximum east of the S-Centers (Fig. 4.28a), which is at the same position of the precipitation percentage increase maximum (> 30%) in Fig. 4.24a. There is a smaller increase (10-12%) in upward motion for the M-Centers (Fig. 4.28b); but this increase in upward motion over the heavy precipitation region disappears for the W-Centers (Fig. 4.28c). The upper level jet (250 hPa wind speed) becomes slightly stronger (~5%) for all of the S-Centers, M-Centers, and W-Centers (not shown). However, the S-Centers are located just at the left side of the jet exit region, which is favorable to the upward motion, while the W-Centers are located close to the jet center (not shown).

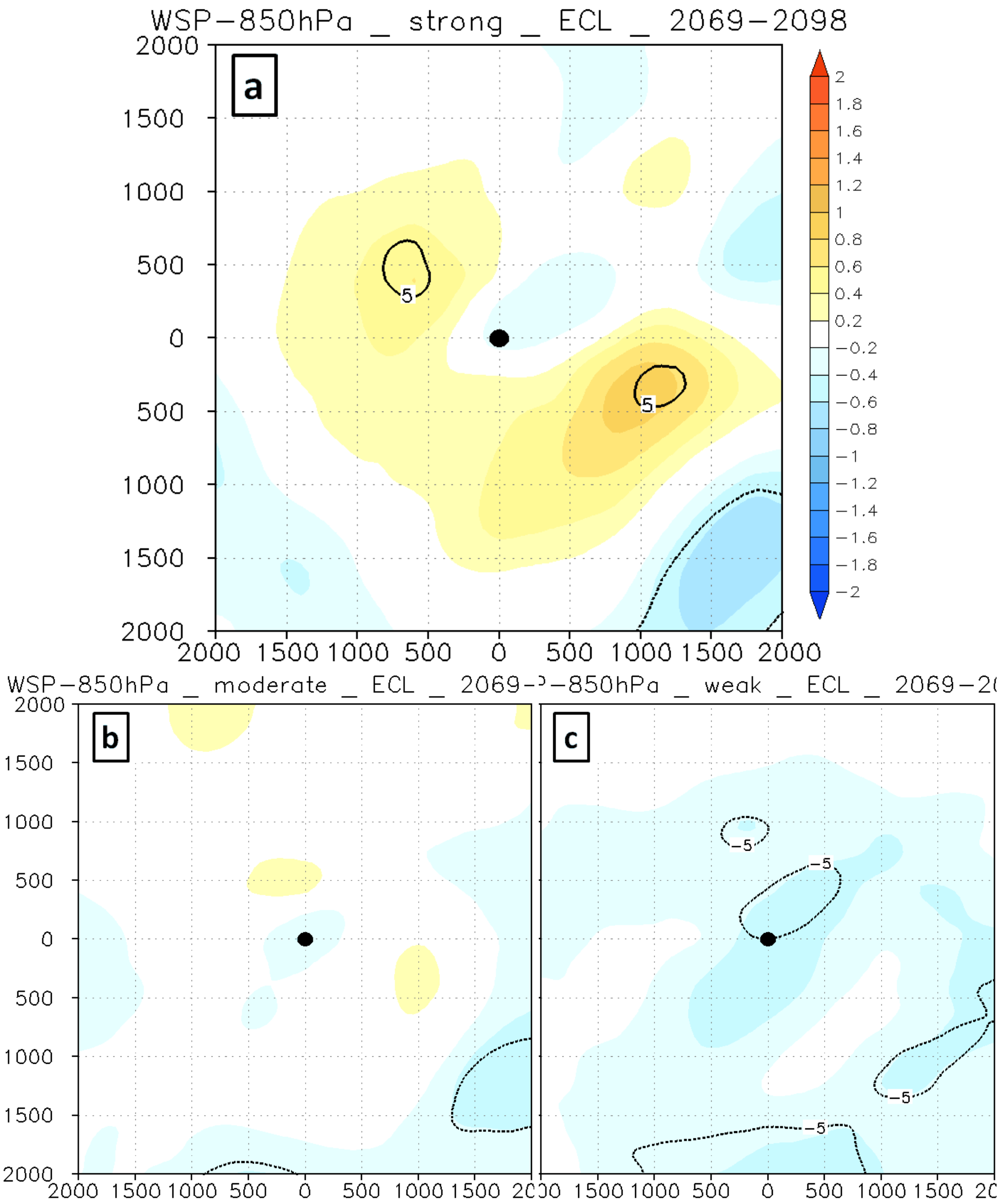

Fig. 4.27: Same as Fig. 4.24, but for the changes of 850hPa wind speed (m/s).

For the S-Centers, M-Centers and W-Centers within the ECL region, the difference in surface and low troposphere temperature (so the moisture content) is relatively small; but the different changes of vertical motion, upper level and low level wind speed in these systems of different intensity amplifies the precipitation differences. Meanwhile, the increase of 850 hPa wind speed and upward motion for the S-Centers and the larger increase in precipitation around the S-Centers indicate the positive feedback between the precipitation (latent heat release) and cyclone deepening.

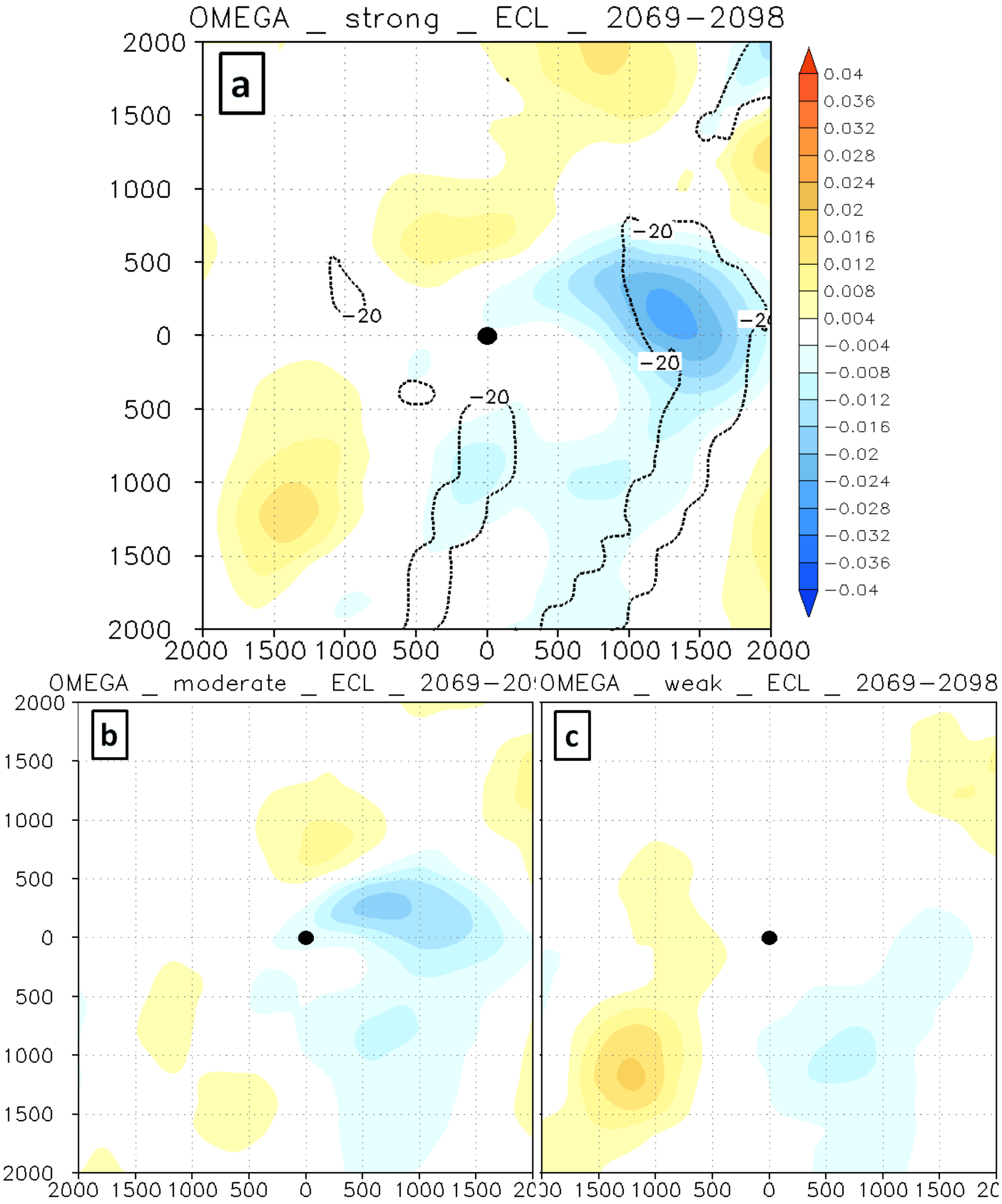

Fig. 4.28: Same as Fig. 4.24, but for the changes of vertical motion (Pa/s) at 700hPa.

4.4. The relation between the precipitation change and cyclone change

4.4.1 The future changes of extreme precipitation cyclones

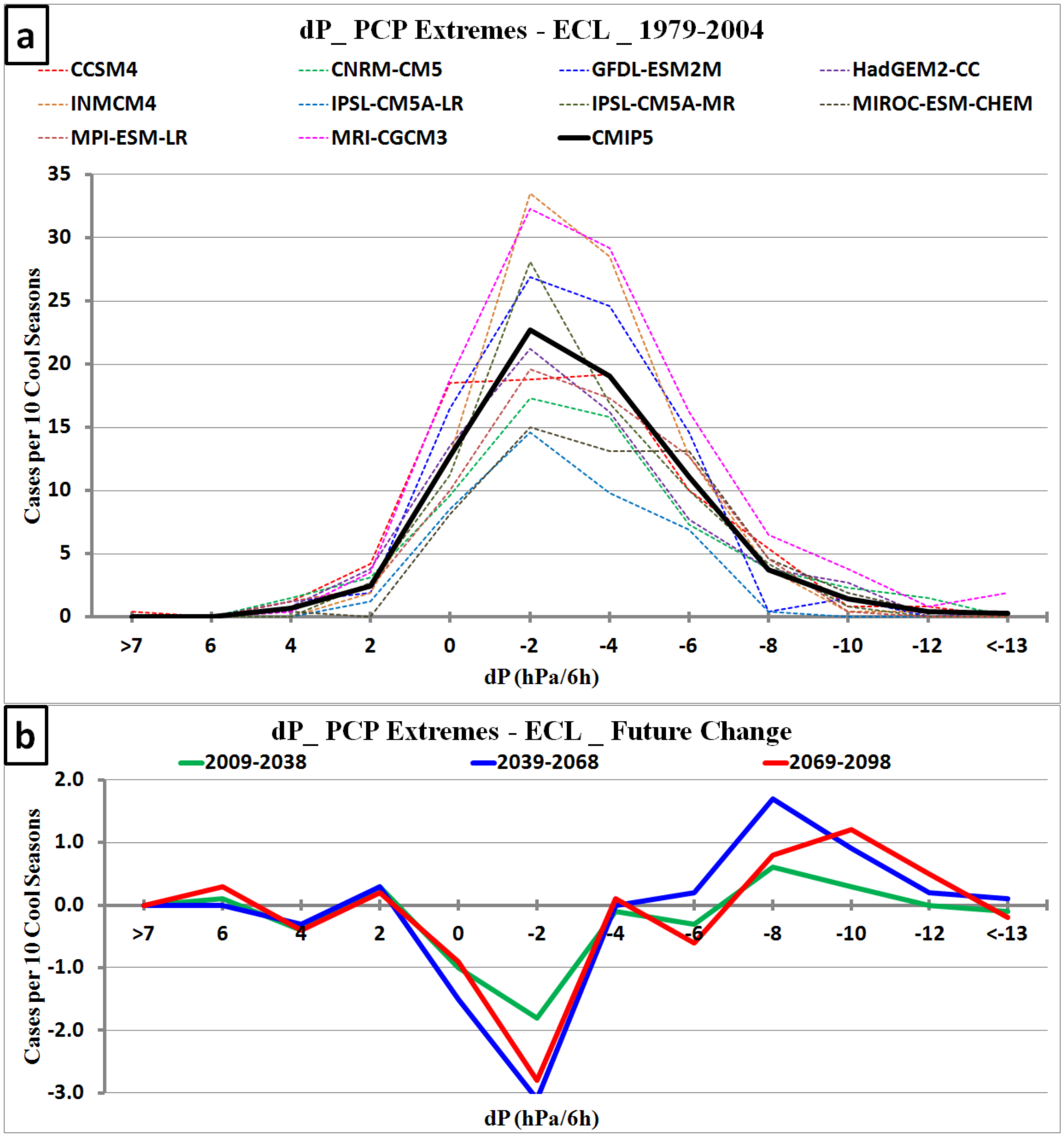

Fig. 4.29: (a) The distribution of cyclone deepening rate for precipitation extreme cyclone cases during historical period. (b) The future changes for the 3 future periods.

Under global warming, there are large increases in both mean precipitation and extreme precipitation associated with cyclones within the ECL region (Section 4.2 and 4.3). Meanwhile, there is an increase in the number of intense cyclones with more rapid deepening within the ECL region (Section 3.2). To explore the potential relationship between the heavier precipitation and the deeper cyclones within the ECL region, the related physical processes for precipitation extreme cyclone cases (cases in Fig. 4.17) defined in Section 4.3.2 were calculated and discussed in this section.

In the historical period, most of these cyclone cases deepen quickly, about 70% of these centers deepen over 2 hPa in 6 hours (Fig. 4.29a). During the middle and late 21st century, there are significant shifts towards the more rapid deepening rate, from around -2 hPa per 6 hours in historical period to -8 and -10 hPa per 6 hours in middle and late 21st century, respectively (Fig. 4.29b). This is similar to the future changes of cyclone deepening rate for the mean of Best7 models in Section 3.2.4. Meanwhile, the minimum central SLP of those cyclone centers associated with the precipitation extremes tends to be lower (not shown).

To explore the future changes in cyclone relative precipitation and the cyclone deepening for those extreme cases, the evolution of those cyclone cases were examined. Fig. 4.30 shows the ensemble mean evolution of those extreme cases. The deepest center within the ECL region of each cyclone track was defined as the reference point (time 0 at the right side of the x-axis in Fig. 4.30) and then moved backward to time -60 hours (60 hours before the deepest point).

The cyclone central SLP in the future periods is very close to or slightly higher (0.5hPa higher for 2069-2098) than the historical at 60 hours before the deepest center (Hour -60) within the ECL region (Fig. 4.30a). During the future periods, the center deepens more quickly for most time of the 60 hours, especially in middle and late 21st century (Fig. 4.30b). During the same time, the two important changes around the cyclone center through the century are the decrease of surface and 850hPa temperature gradient (surface temperature gradient in Fig. 4.30cd) and the increase of precipitation (Fig. 4.30ef). Although the baroclinicity is decreasing, those cyclone cases associated with the extreme precipitation within the ECL region are becoming deeper. Therefore, it is hypothesized that in those most extreme precipitation cases, the latent heat release from the precipitation compensates for the baroclinicity decrease and even enhances the cyclone deepening.

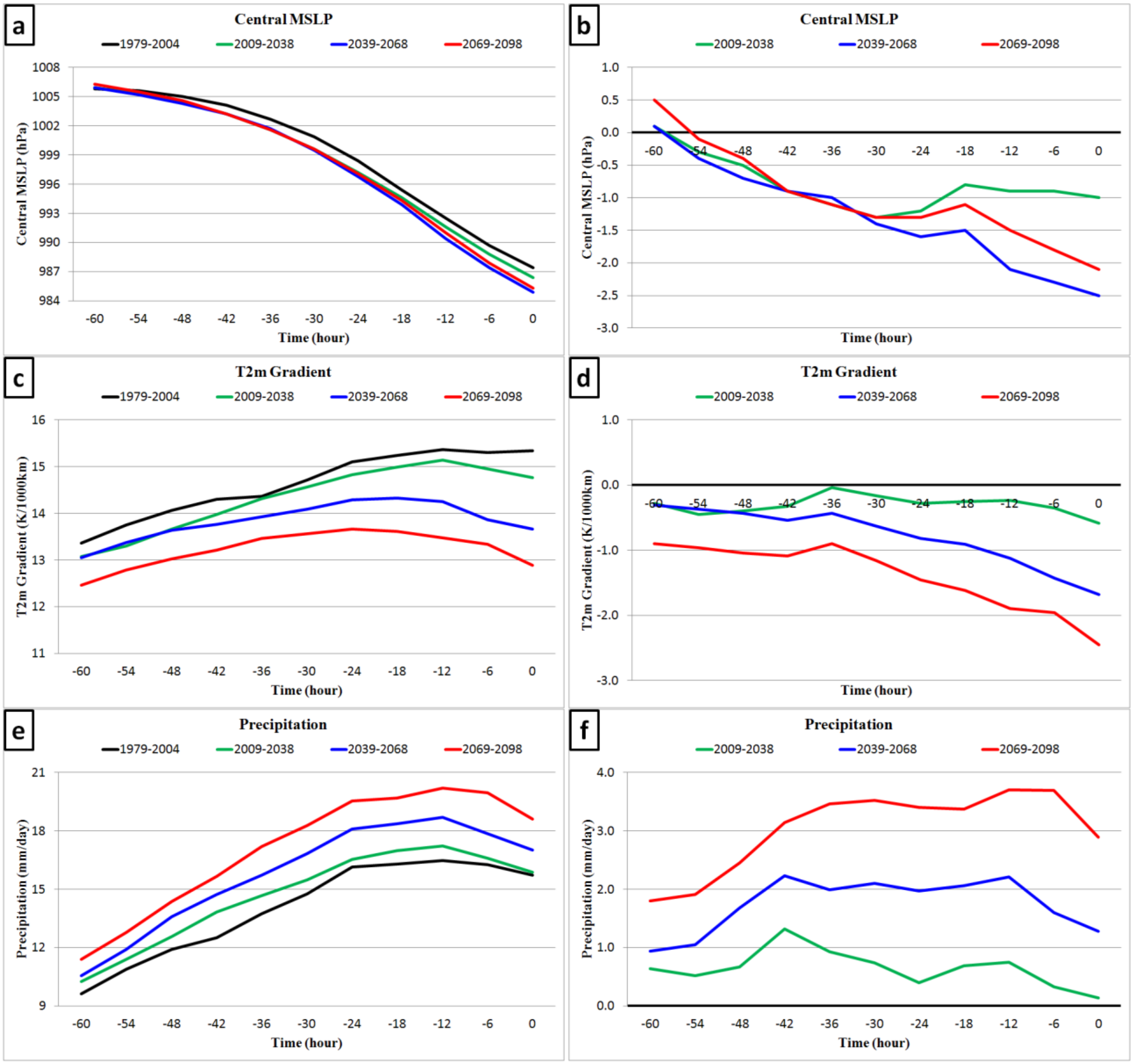

Fig. 4.30: The evolution of the cyclone cases associated with the precipitation extreme within ECL. The x-axis is the time (hour) before the deepest center within the ECL region. From top to bottom: cyclone central SLP (hPa), surface temperature gradient (K/1000km), and precipitation (mm/day). The left panel is the mean of the historical period (black) and the three future periods (green, blue and red); and the right panel is the future changes (future minus historical mean).

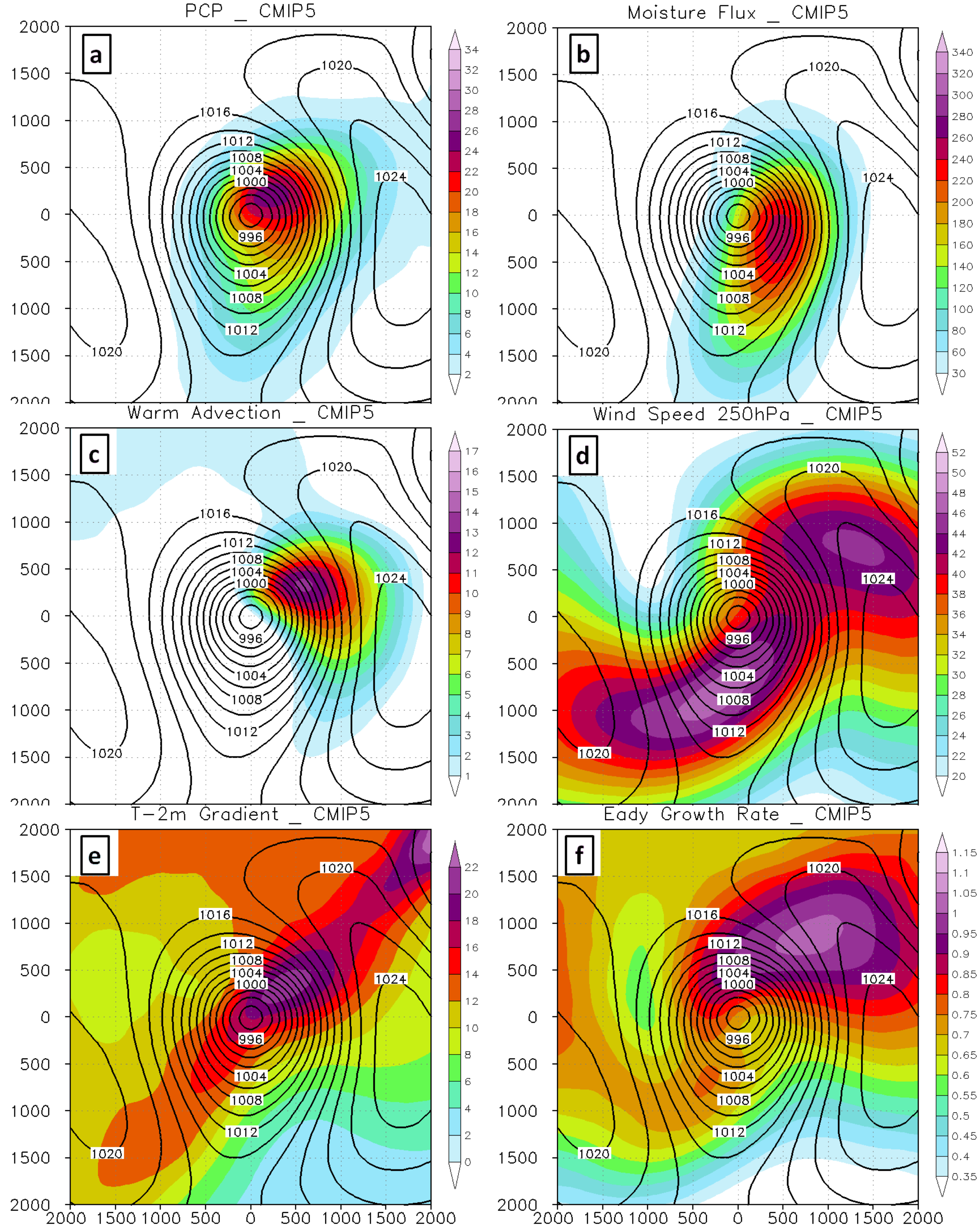

Fig. 4.31: The historical mean composite (a) precipitation (mm/day), (b) 850-250hPa moisture flux (kg/m*s), (c) 850hPa warm advection (K/s), (d) 250hPa wind speed (m/s), (e) surface temperature gradient (K/1000km), (f) 850-500hPa Eady growth rate (per day) for ECL cyclone center associated with precipitation extreme defined in Section 4.3.2.

In order to examine this hypothesis, the SLP, precipitation, meridional moisture flux (850-250hPa), warm advection (850hPa), surface temperature gradient, Eady growth rate (850-500hPa), and upper level jet (250hPa) for those cyclone cases through the cyclone developing were calculated. The fields for Hour -12, when the precipitation is heaviest, are discussed here.

Fig. 4.31 shows the historical mean fields at time Hour -12, when the precipitation rate is the largest. The cyclone center is relatively deep (993hPa) with the maximum precipitation > 24 mm/day over the northeast of the center (Fig. 4.31a). There is strong moisture flux at the warm side of the cyclone (Fig. 4.31b) and a prominent warm advection (850hPa) over northeast of the center (Fig. 4.31c). Meanwhile, the cyclone center is just located over the left side of cyclonic upper level jet exit region and close to the entrance of anti-cyclonic jet (Fig. 4.31d), where there is strong upper level divergence. The baroclinicity, both surface temperature gradient and Eady growth rate (850-500hPa) are strong over the north-east side of the center (Fig. 4.31ef). All of these conditions are conducive to the heavy precipitation and the cyclone developing.

During late 21st century, the baroclinicity is decreasing around the cyclone center (Fig. 4.32ef): surface temperature gradient decreases by 10-20%, but the 850-500hPa Eady growth rate has a smaller decrease (about 5%). There is no significant change for the warm advection around the cyclone center (Fig. 4.32c). Meanwhile, there is a large increase (around 30%) in the moisture flux over the warm side of the cyclone (Fig. 4.32b); and a small increase in upper level jet (~10 %) over the south side of the jet, a little far away from the center (Fig. 4.32d). Given these changes, the cyclone central SLP decrease by ~2 hPa (not shown) while the precipitation increases by 20-30% over the warm side of cyclone (Fig. 4.32a). Therefore, the increase of the latent heat release from heavier precipitation becomes more important to the cyclone developing, while the baroclinicity is decreasing and the other fields do not have significant changes.

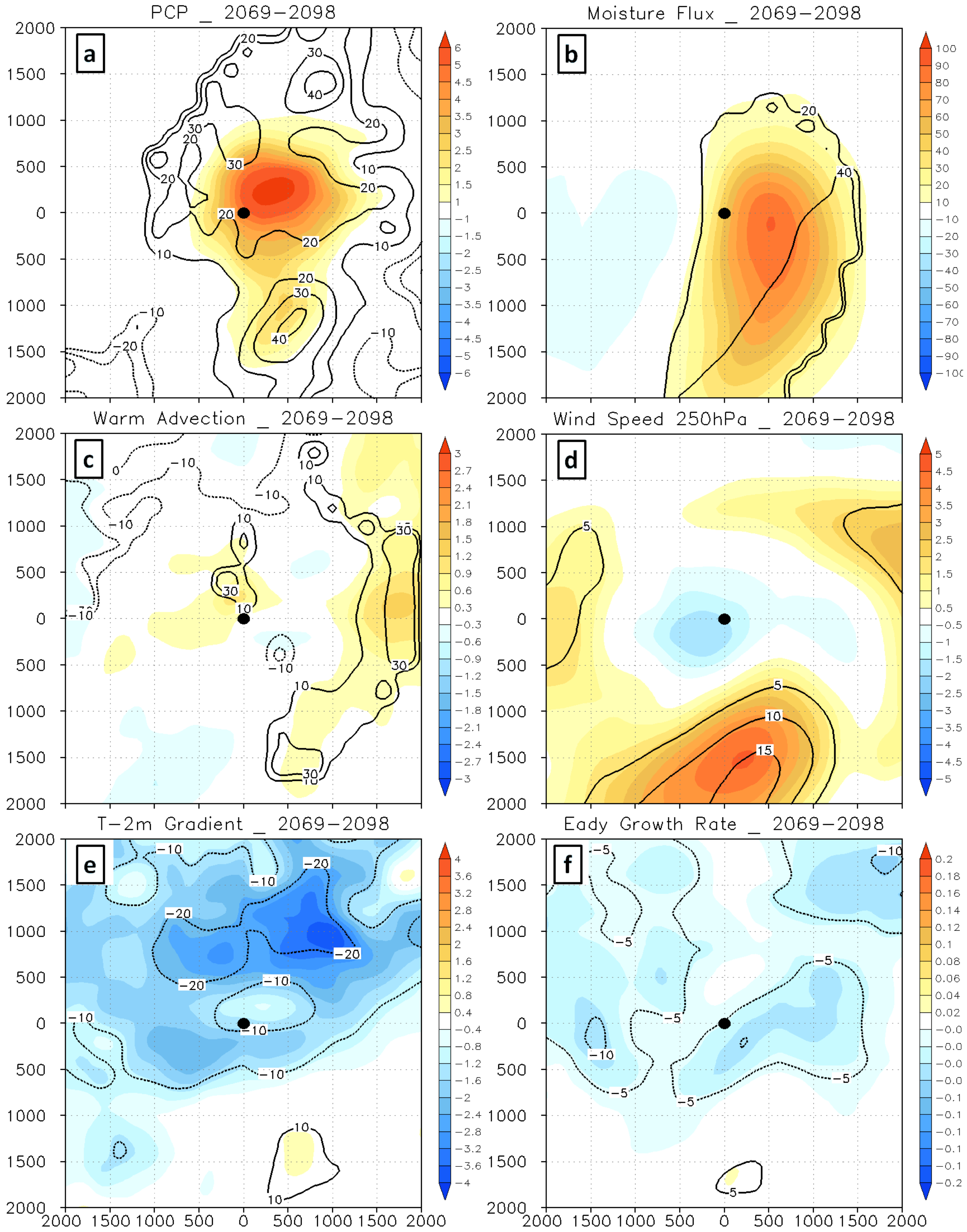

Fig. 4.32: Same as Fig. 4.31, but for the future changes during late 21st century (2069-2098 cool seasons), and the contours are the percentage changes.

4.4.2 The comparison between the Best and Worst models

In Chapter 3, the CMIP5 models are divided into two groups (Best7 and Worst7) based on their historical performance in cyclone simulation. There is an increase in the cyclone track density in the ECL region with more deep cyclones and more rapid deepening rate for the Best7 models, while those increases in ECL region become much weaker or close to neutral for the Worst7 models (Section 3.2). Therefore, the future changes of some related cyclone relative fields for the ECL cyclone centers were calculated and compared for the 5 BEST models (Best5, red in Table 4.1) and the 5 WORST models (Worst5, black in Table 4.1) in this Chapter.

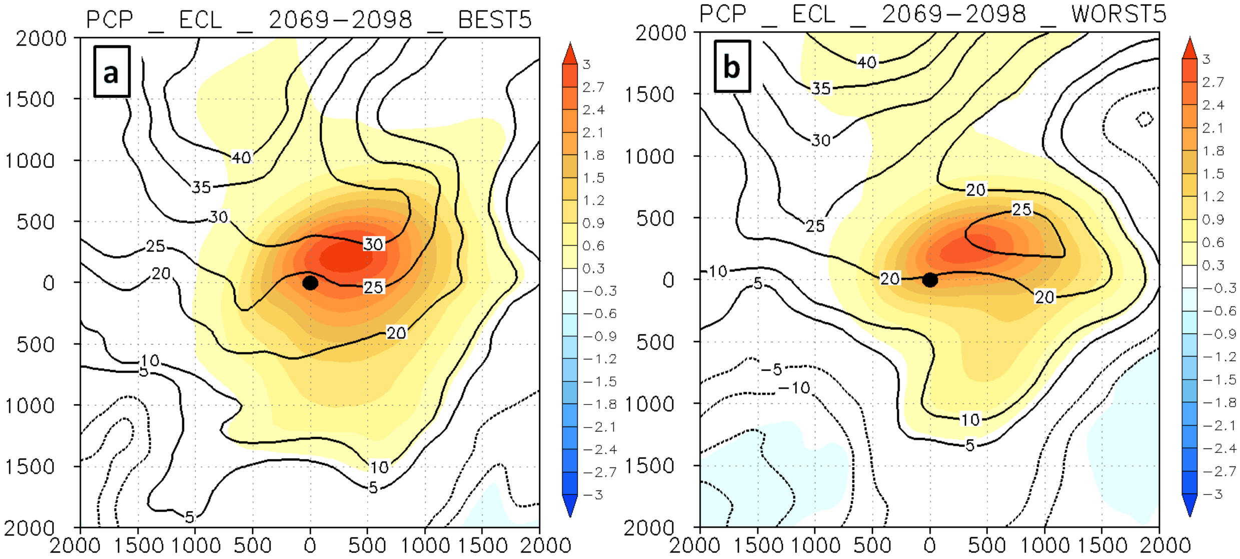

Fig. 4.33: The future changes of precipitation (mm/day, colors) and the percentage changes (%, contours) around the cyclone centers within the ECL region for 2069-2098 cool seasons. (a) The mean of the 5 models with better performance in cyclone simulation (red in Table 4.1). (b) The mean of the 5 models with worse performance in cyclone simulation (black in Table 4.1).

The precipitation of the ECL centers for the Best5 increases by 20-33% over the east and northeast of the center in late 21st century (Fig. 4.33a). Meanwhile, the increase for the Worst5 is 15-26% over the east and northeast of the center (Fig. 4.33b).

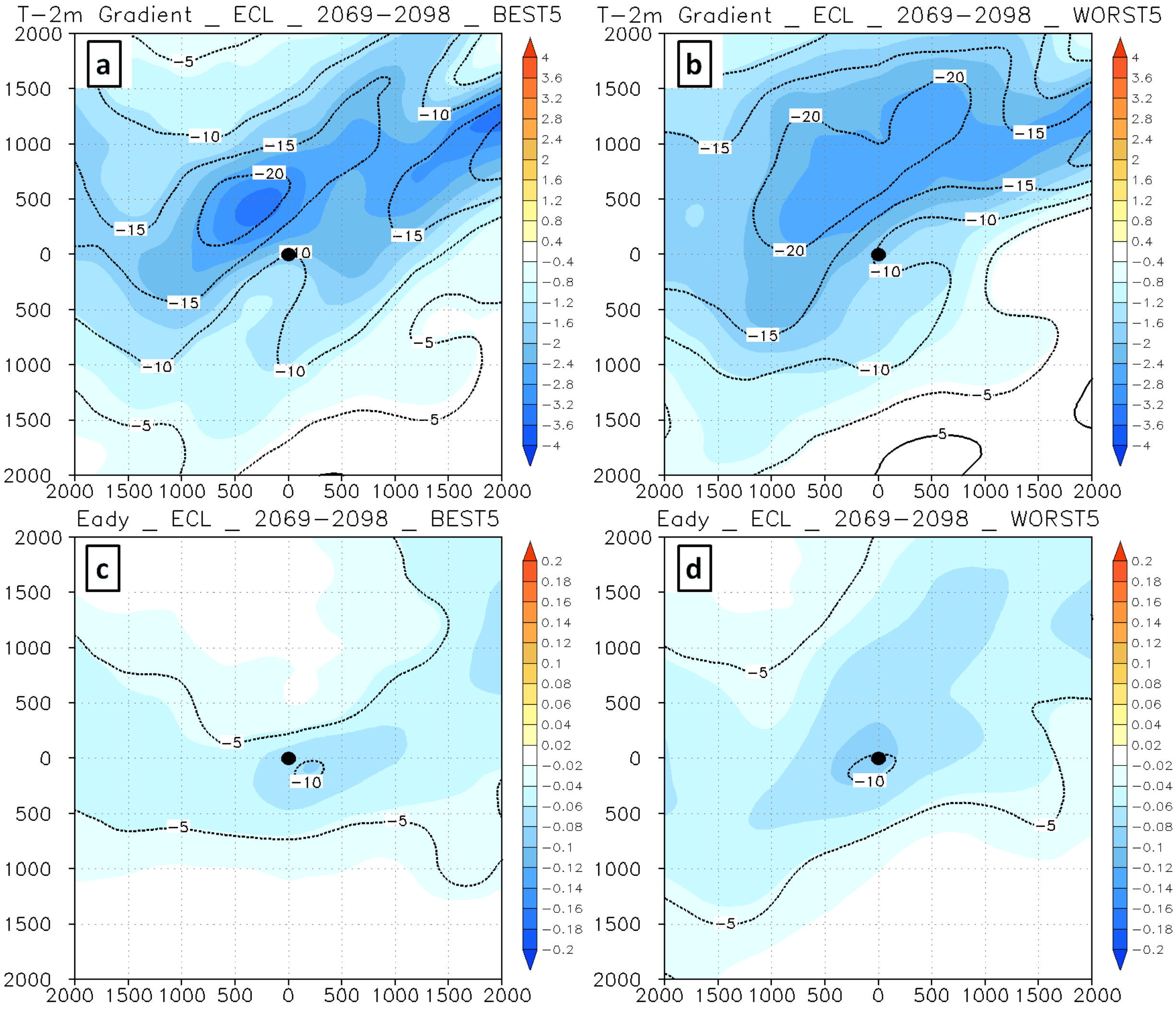

Fig. 4.34: Same as Fig. 4.33, but for the future changes of (a) (b) surface temperature gradient (K/1000km) and (c) (d) 850-500hPa Eady growth rate (day^{-1}).

The surface and low troposphere temperature increase (so the moisture content) in the Best5 is slightly larger (0.2-0.9 K) than the Worst5 around and over north of the cyclone center (not shown). Meanwhile, the wind speed at 850hPa has a ~5% increase over the warm side of cyclone for the Best5, which is favorable to the moisture transport, while there is no significant change for the Worst5 (not shown). The future changes of upper level forcing (~5% increase in 250hPa wind speed over south of cyclone center, not shown) are similar for the Best5 and the Worst5. As a result, the precipitation increase for the Best5 is larger (5-7%) than the Worst5

(Fig. 4.33), which indicates that there is a larger increase for the latent heat release from precipitation in the Best5 than the Worst5.

The baroclinicity decreases for the Best5 models are smaller than the Worst5 models. In the future changes of surface temperature gradient, the -15% and -20% areas for the Best5 are smaller than the Worst5 (Fig. 4.34a, b). The decrease of 850-500hPa Eady growth rate is similar, the Best5 is slightly smaller than the Worst5 (Fig.4.34c, d).

The comparisons of future changes in precipitation and baroclinicity between the Best5 models and the Worst5 models are consistent with the cyclone changes in Section 3.2. The BEST models have stronger increase in latent heat release from heavier precipitation and smaller decrease in baroclinicity than the WORST models when the changes of upper level jet (~5% increases) are close, so the BEST models tend to have increases in cyclone intensity and rapid deepening rate while the WORST models tend to be neutral in the ECL region.

4.5. Summary

Chapter 4 investigates the future changes of cyclone relative precipitation and the associated physical processes within the synoptic scale extratropical cyclone system over eastern North America and western Atlantic during cool season in CMIP5 Models. The cool season (November-March) precipitation over eastern North America and western Atlantic in CMIP5 models is evaluated with respect to the mean of two precipitation products (GPCP and CMAP). Most of the cyclones with better performance in cyclone simulation (red in Table 4.1) have smaller mean absolute error within the big ECWA region in Fig. 2.1. However, there are exceptions, such as HadGEM2-CC, which belongs to the Best7 in cyclone simulation in Section 3.1, overestimates the mean precipitation because it has too heavy precipitation for each cyclone center. The ensemble mean of the ten CMIP5 models have smaller mean error comparing to the individual models (Table 4.1), which provides confidence to explore the future changes of precipitation with the model mean.

The precipitation amount associated with those cyclone centers (the precipitation within the black box in Fig. 2.4b) contributes from 60% at relatively lower latitude (~25°N) to over 90% at relatively higher latitude (> 40°N) to the total cool season precipitation amount (contours in Fig. 4.4a) along the East Coast of North America. This is similar to the results form Hawcroft et al. (2012) using the GPCP and ERA-Interim data to estimate the contribution of extratropical cyclones to the total precipitation. By late 21st century, the relatively strong (<990 hPa) cyclone centers have the largest increase (20-30%) in precipitation rate along the East Coast (Fig. 4.7b), while the increase for the relatively weak (>1005 hPa) is only around 10% (Fig. 4.7d). In late 21st century, the cyclone relative precipitation amount increase by 10-20% along the East Coast, and most of the increase is from the cyclone centers <1005 hPa (Fig. 4.8), while the increase of precipitation rate for the relatively weak cyclone centers (>1005 hPa) is cancelled by the decrease of weak cyclone center frequency. Meanwhile, the local cyclone relative precipitation extreme (95% percentile at each grid) has a significant increase (10-25%) over eastern North America and western Atlantic, with an increase maximum (20-25%) just along the East Coast (Fig. 4.10).

The future changes of precipitation within the synoptic scale cyclone system are also investigated. Through 21st century, both of the mean and the maximum precipitation around the cyclone center (within the small purple in Fig. 2.4b) have significant increase trends (~21% and ~26% by the end of 21st century) for the ECL centers (Fig. 4.11a and Fig. 4.12a). The increase of the precipitation around WA centers (10-15%) is smaller. Meanwhile, the variability for the maximum precipitation amount models is large, especially for the WA cyclone centers (Fig. 4.12b); the difference among models can be as large as 70% of the maximum precipitation.

During 21st century there is a significant shift towards the heavy precipitation part for both of the mean and maximum precipitation around cyclone center within the eastern North America and western Atlantic (Fig. 4.14 and Fig. 4.15). The ECL cyclone centers have the largest increase (~150%) in the most extreme maximum precipitation (>56 mm/day). Meanwhile, the extreme (95% percentile) cyclone cases for the mean precipitation around the cyclone center within the ECL region have an increase from >18.4 mm/day in 1979-2004 cool seasons to >22.5 mm/day in 2069-2098 cool seasons (Fig. 4.17).

The precipitation increase for the ECL cyclone centers (> 20%) is larger than the ECW (14-20%) and WA (10-13%) cyclone centers (Fig. 4.20) during the late 21st century. One important reason is that comparing with the ECW and WA, the ECL cyclone centers has a larger increase in moisture content (Fig. 4.22), which is controlled by the surface and low troposphere temperature following the Clausius–Clapeyron relation. However, the moisture (Clausius–Clapeyron relation) is not the only factor controlling the precipitation change. The moist static stability is another reason responsible for the difference in precipitation changes for the ECL, ECW and WA centers, while the changes of other forcing (such as upper level jet) are similar between regions.

Within the ECL region the S-Centers have the largest increase in precipitation (25-30%, Fig. 4.24a) during late 21st century. The moisture content increase for the S-Centers (~35%) is slightly larger than W-Center (25-30%) (Fig. 4.26). There is a small increase (~5%) in 850 hPa wind speed for the S-Centers, which is favorable to the poleward moisture transport while there is a small decrease (~5%) for the W-Centers (Fig. 4.27). In addition, the upward motion over the northeast of cyclone center becomes stronger for the S-Centers (10-15%), but does not have changes for the W-Centers (Fig. 4.28). These conditions introduce a large difference in the precipitation changes for S-Centers, M-Centers and W-Centers. Meanwhile, the increase of 850hPa wind speed and upward motion for the S-Centers and its larger increase in precipitation indicate the potential feedback between the precipitation (latent heat release) and cyclone deepening.

The relationship between the heavier precipitation and deeper cyclone centers with more rapid deepening rate within the ECL region is also discussed through the evolution of the cyclone cases associated with the precipitation extremes in Section 4.4. While the baroclinicity is decreasing during 21st century under global warming, the latent heat release from heavier precipitation becomes more important to the cyclone developing, as it offsets the impacts of baroclinicity decrease and even enhances the cyclone deepening. Meanwhile, the slightly stronger upper level jet is also favorable to the deepening of the ECL cyclone centers, while the other factors (such as warm advection) don’t have significant changes (Fig. 4.32).

Chapter 5:
Extratropical Cyclones in Downscaled WRF

In this chapter, the eastern North American and western Atlantic extratropical cyclones in the CMIP5 general circulation models (GCMs) and the downscaled mesoscale model were compared to improve the understanding of the extratropical cyclone variations in the historical and future periods, and to determine the impact of model resolution on the results. The Weather Research and Forecasting model (WRF; Skamarock et al. 2008) was employed to dynamically downscale two CMIP5 models: CCSM4 (0.94°×1.25° resolution), which has relatively better performance in the extratropical cyclone simulation, and GFDL-ESM2M (2.0°×2.5° resolution), which underestimated the intensity and frequency of the extratropical cyclones significantly. Two sets of WRF runs using the same initial and boundary conditions from CMIP5 GCMs but different horizontal resolution: 0.2 degree (~20km, WRF-HR) and 1.0 degree (~100km, WRF-LR) were performed to demonstrate the impacts of model resolution on the simulation of extratropical cyclones during cool season. The 20 historical (1986-2005) winters (January-March) and 20 future (2080-2099) winters were compared to explore the future changes of extratropical cyclones.

5.1 Historical evaluation of extratropical cyclones in the downscaled WRF

Two CMIP5 models were dynamically downscaled (described in Section 2.5) using both the WRF-HR and the WRF-LR: CCSM4 (hereafter CCSM), WRF-HR forced by CCSM4 (hereafter C-WRF-HR), and WRF-LR forced by CCSM4 (hereafter C-WRF-LR); as well as GFDL-ESM2M (hereafter GFDL), G-WRF-HR and G-WRF-LR forced by GFDL-ESM2M. The extratropical cyclones and the associated precipitation during historical winters in these models were compared to evaluate the impacts of the WRF downscaling and the model resolution.

5.1.1 Cyclone track density, intensity, and deepening

a. Cyclone track density

The cyclone track density for the There are two cyclone track density maximum (> 3 cyclones per winter per 50,000 km^2) over eastern North America and the western Atlantic for the CFSR: one is over the Great Lakes and the other is along the East Coast of North America offshore (Fig. 5.1). The storm track along the East Coast is located over the U.S. Northeast offshore and extends northeastward.

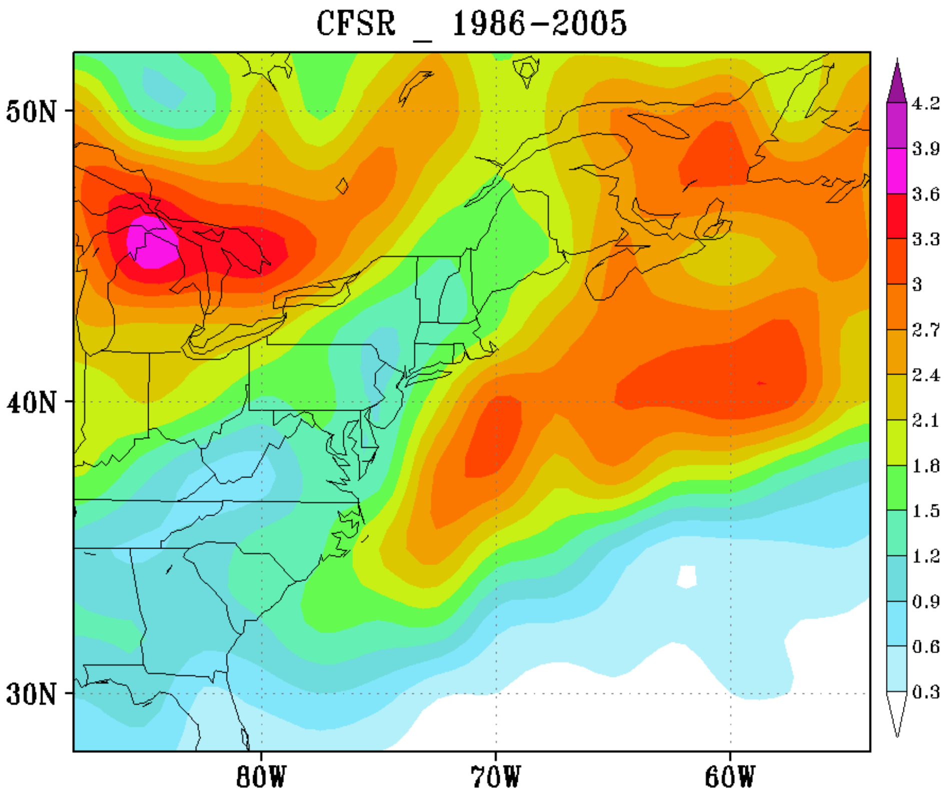

Fig. 5.1: Mean cyclone track density (cyclone per winter per 50,000 km^2) for the historical period (1986-2005 winters) for CFSR.

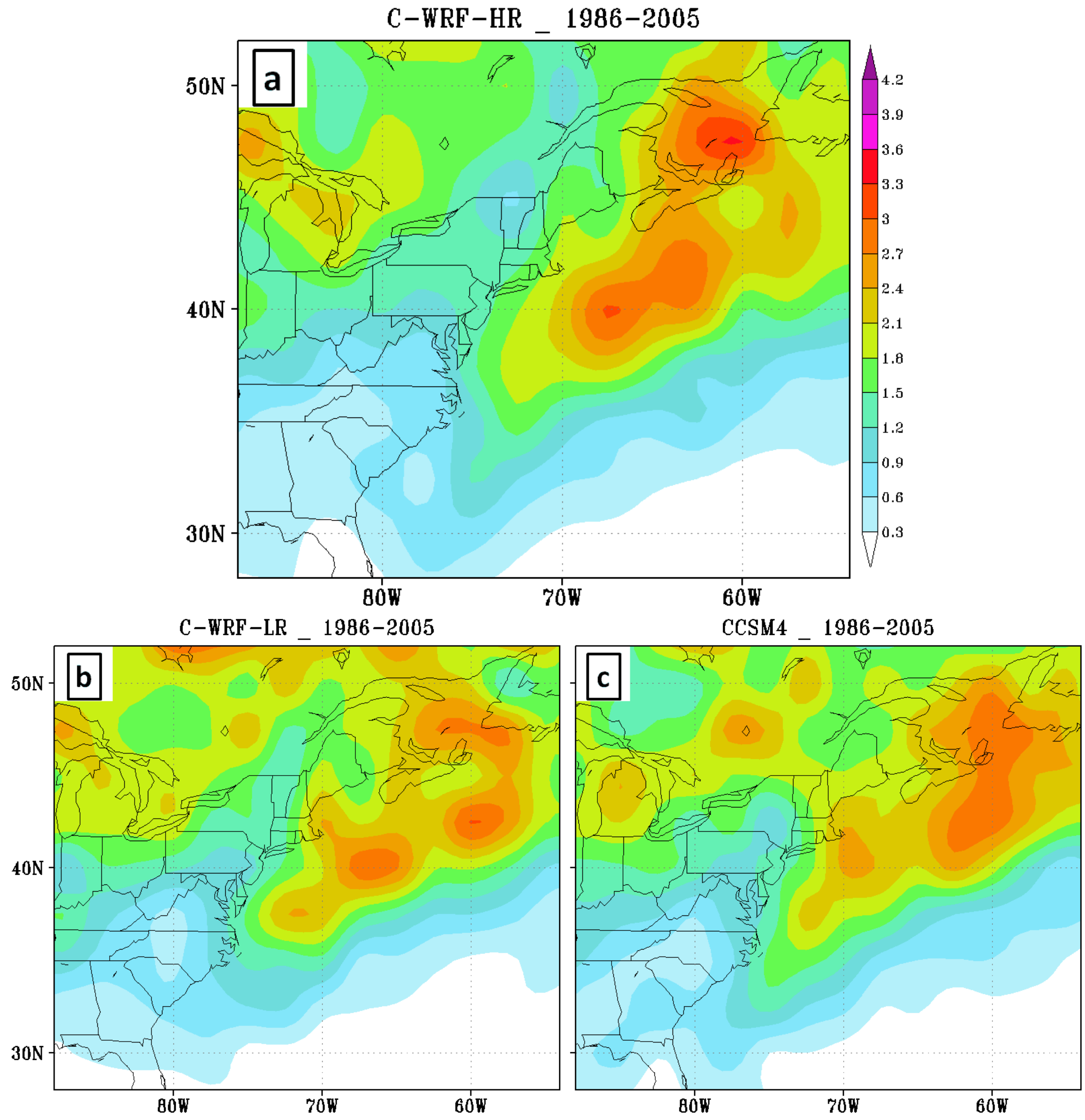

Fig. 5.2: Same with Fig. 5.1, but for (a) C-WRF-HR, (b) C-WRF-LR, and (c) CCSM.

The CCSM is able to reproduce the track density maximum along the East Coast, but underestimates the density by ~ 20% (Fig. 5.2c). The track density over the Great Lakes in CCSM is much smaller (~35%) than the CFSR. The C-WRF-LR (1°×1°), which is in a similar resolution with CCSM (0.94°×1.25°), has the track density similar to the CCSM (Fig. 5.2b). Meanwhile, the cyclone track density for the C-WRF-HR (0.2°×0.2°) has more well-defined maxima over both of the Great Lakes and East Coast, but it still underestimates the track density (15-30%) over the East Coast and the Great Lakes (Fig. 5.2a).

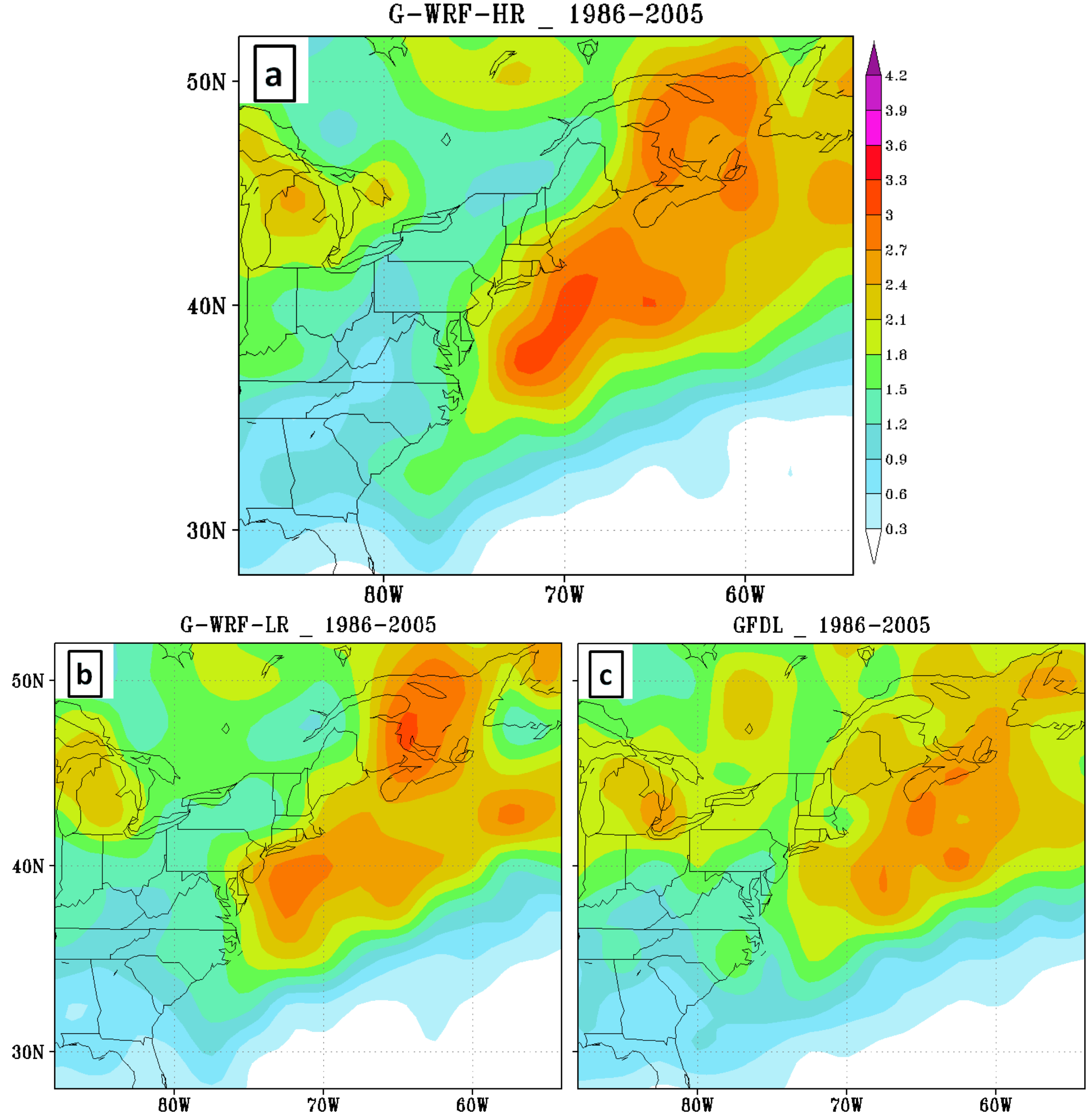

Fig. 5.3: Same with Fig. 5.1, but for (a) G-WRF-HR, (b) G-WRF-LR, and (c) GFDL.

As compared with the GFDL (2.0°×2.5°), the track density along the East Coast for both of the G-WRF-LR (1°×1°) and the G-WRF-HR (0.2°×0.2°) are more concentrated (Fig. 5.3) and closer to the CFSR (Fig. 5.1), while the G-WRF-HR has a slightly larger (10-15%) track density along the storm track (Fig. 5.3). However, the storm track for the GFDL, the G-WRF-LR, and the G-WRF-HR is too close to the East Coast (Fig. 5.3), while the storm track in the CCSM, the C-WRF-LR, and the C-WRF-HR is more offshore (Fig. 5.2), since the resolution of the CCSM SST is finer than the GFDL SST. This is consistent with the results in Section 3.1.1, which indicates that the coarse resolution CMIP5 models have the storm track too close to the East Coast.

Overall, the amplitude and the spatial distribution of cyclone track density in the low resolution WRF is close to the corresponding GCM, while the high resolution WRF has a better spatial pattern, closer to the CFSR, although it still underestimates the track density.

In addition to the cyclone track density, the cyclone moving speed was also calculated for all of those models (Table 5.1). The mean cyclone moving speed within the ECWA region is 55.6 km/h for the CFSR. The moving speed for the CCSM is 55.5 km/h, almost the same as the CFSR; while the speed of GFDL is much slower, 44.8 km/h. The cyclone moving speed in the downscaled WRF runs is similar to the corresponding GCM (Table 5.1), controlled by the propagation of the large scale circulation (such as upper level trough) from the GCM.

Table 5.1: The mean cyclone moving speed (km/h) within the ECWA region for the historical (1986-2005) winters.

CFSR	CCSM	C-WRF-HR	C-WRF-LR	GFDL	G-WRF-HR	G-WRF-LR
55.6	55.5	52.8	54.6	44.8	44.8	43.9

b. *Cyclone intensity*

The intensity distributions for the cyclones within the ECWA region were compared for the GCMs and WRF runs. Unlike the ECWA region (Fig. 2.1) used for the CMIP5 models in

Chapter 3, the ECWA region in this chapter is a little smaller, since the WRF domain (black in Fig. 5.4) only covers part of the WA region (Fig. 5.4).

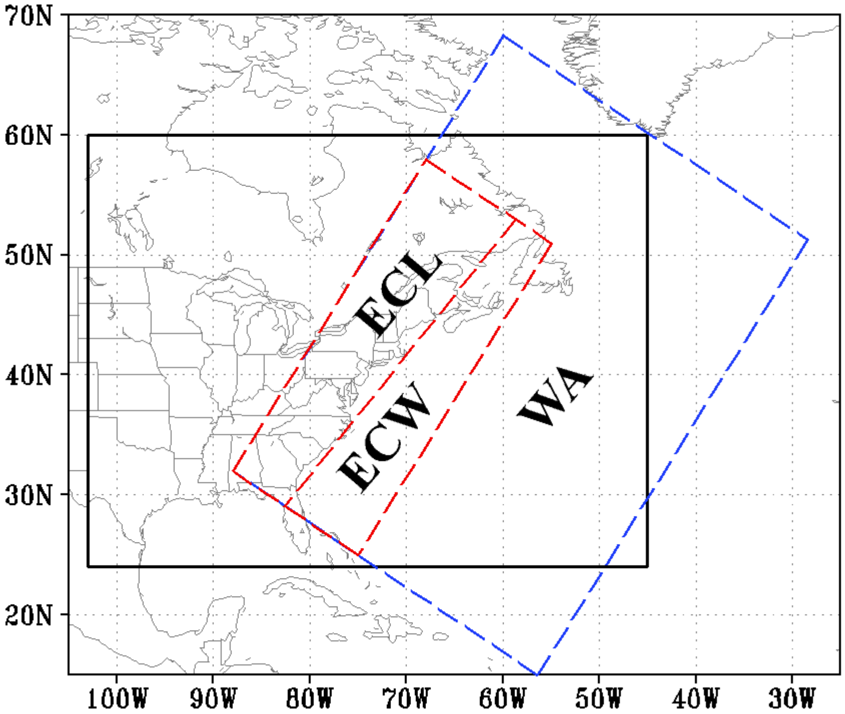

Fig. 5.4: The WRF domain (black box) and the other domains (ECL, ECW and WA).

In the CFSR, there are 44.5 extratropical cyclones per winter within the ECWA region during historical period, with a maximum frequency in the 1004hPa and 996hPa bins (black line in Fig. 5.5). The CCSM (38.3 cyclones per winter) underestimates the total number of cyclones within ECWA region, especially for the cyclones < 988 hPa (green line in Fig. 5.5). The intensity distribution for the C-WRF-LR is very close to the CCSM (blue line in Fig. 5.5), but with slightly fewer (~ 5%) cyclones. However, the intensity distribution of C-WRF-HR is shifted towards the more intense part of the distribution (red line in Fig. 5.5), with more deep cyclones than the CCSM and closer to the CFSR for storms < 988hPa, although the total number of cyclones (37.4) is almost the same with the CCSM (38.3)

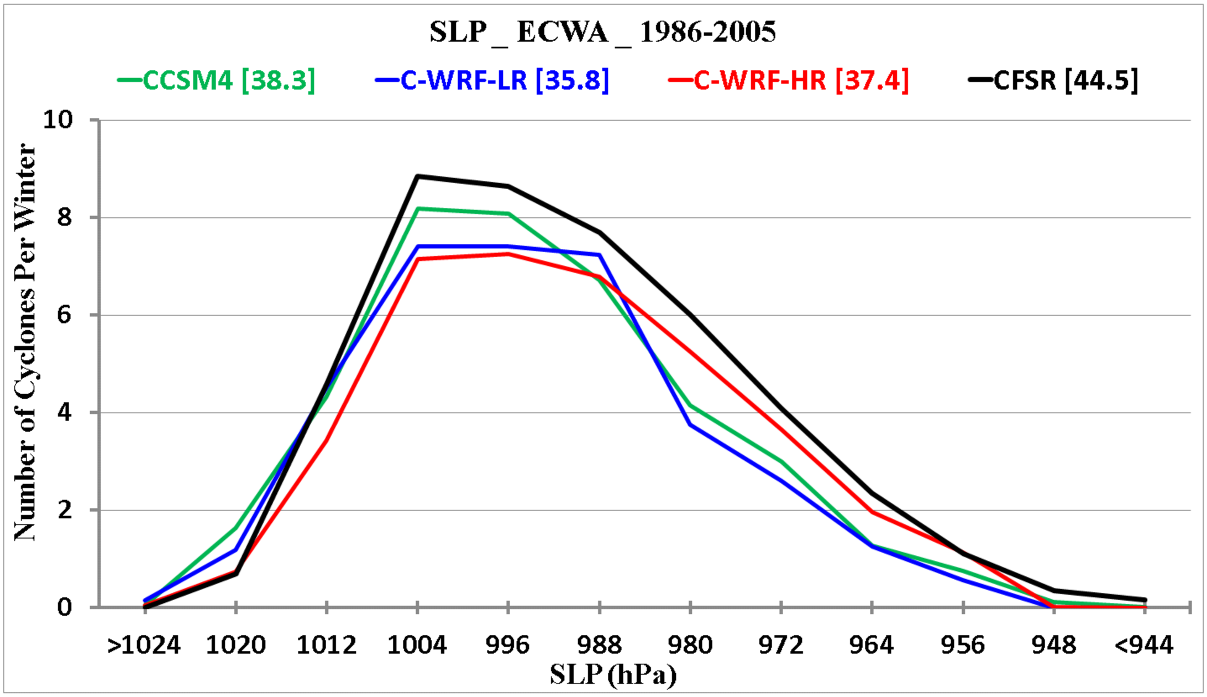

Fig. 5.5: The mean intensity distribution of cyclones within the ECWA region for the historical (1986-2005) winters. The black line is for the CFSR, green is for the CCSM4, blue is for the C-WRF-LR, and red is for the C-WRF-HR.

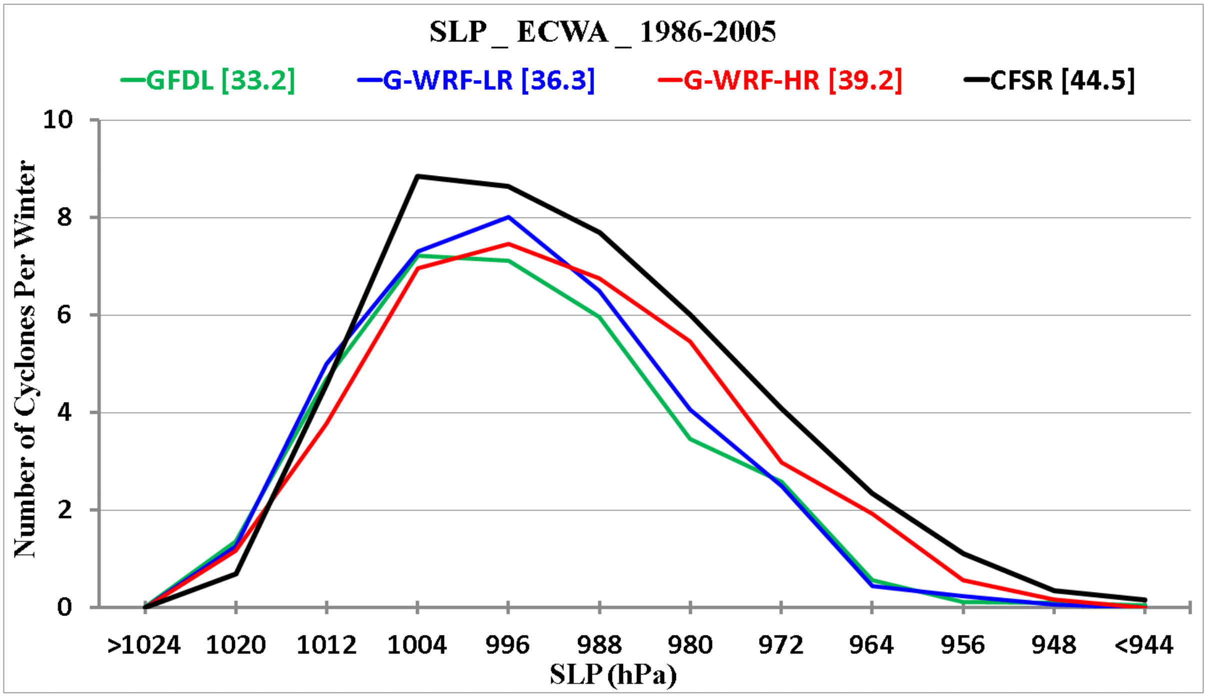

Fig. 5.6: Same as Fig. 5.5, but for the GFDL, G-WRF-LR, and G-WRF-HR.

The comparison of intensity distributions for GFDL and the corresponding downscaled WRF (Fig. 5.6) is similar to the CCSM and its WRF. The GFDL underestimates the relatively intense cyclones (< 988hPa) significantly (30%). The G-WRF-LR has a similar intensity distribution with the GFDL, but with ~ 3 more cyclones per winter from 1004 hPa to 972 hPa. The intensity distribution of the G-WRF-HR is shifted towards the intense direction, closer to the CFSR; and G-WRF-HR (39.2) has ~18% more cyclones than the GFDL (33.2).

c. *Cyclone deepening*

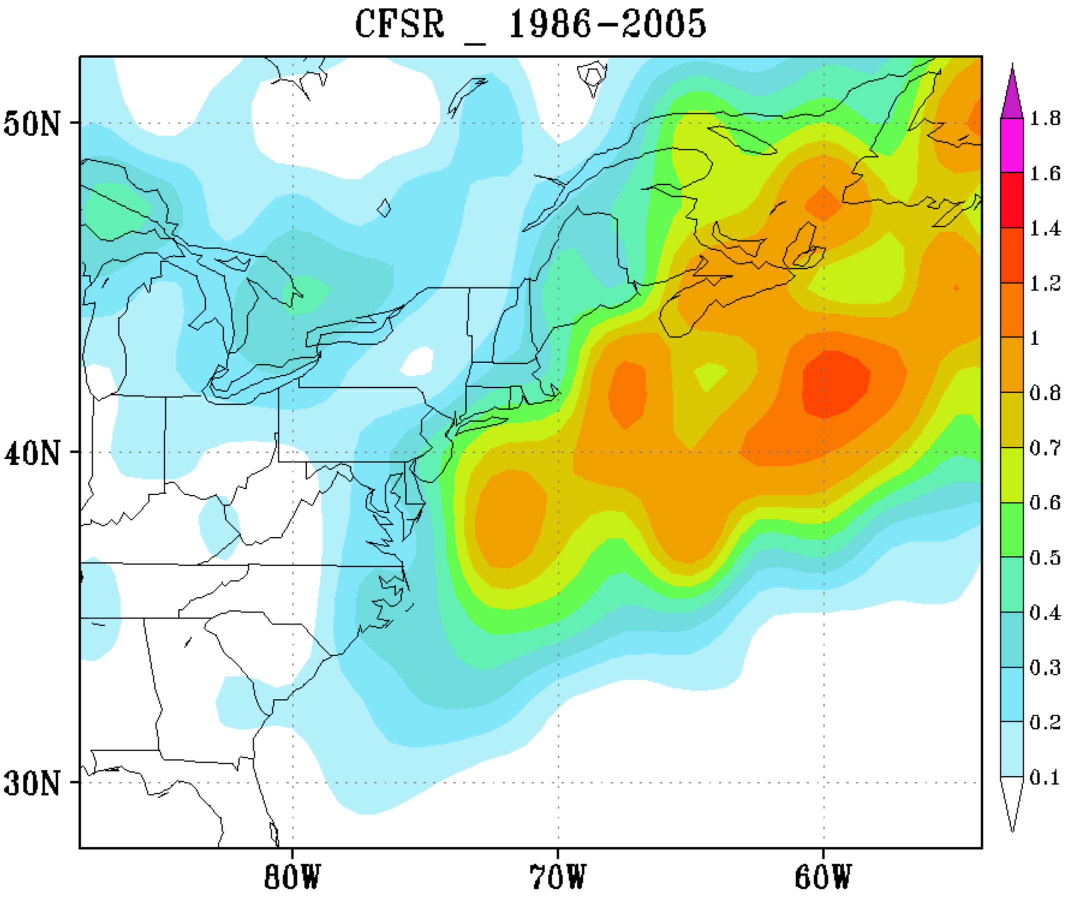

Fig. 5.7: The mean spatial density (cases per winter per 50,000 km^2) for the rapid deepening (> 4 hPa/6h) cases for the historical period (1986-2005 winters) for CFSR.

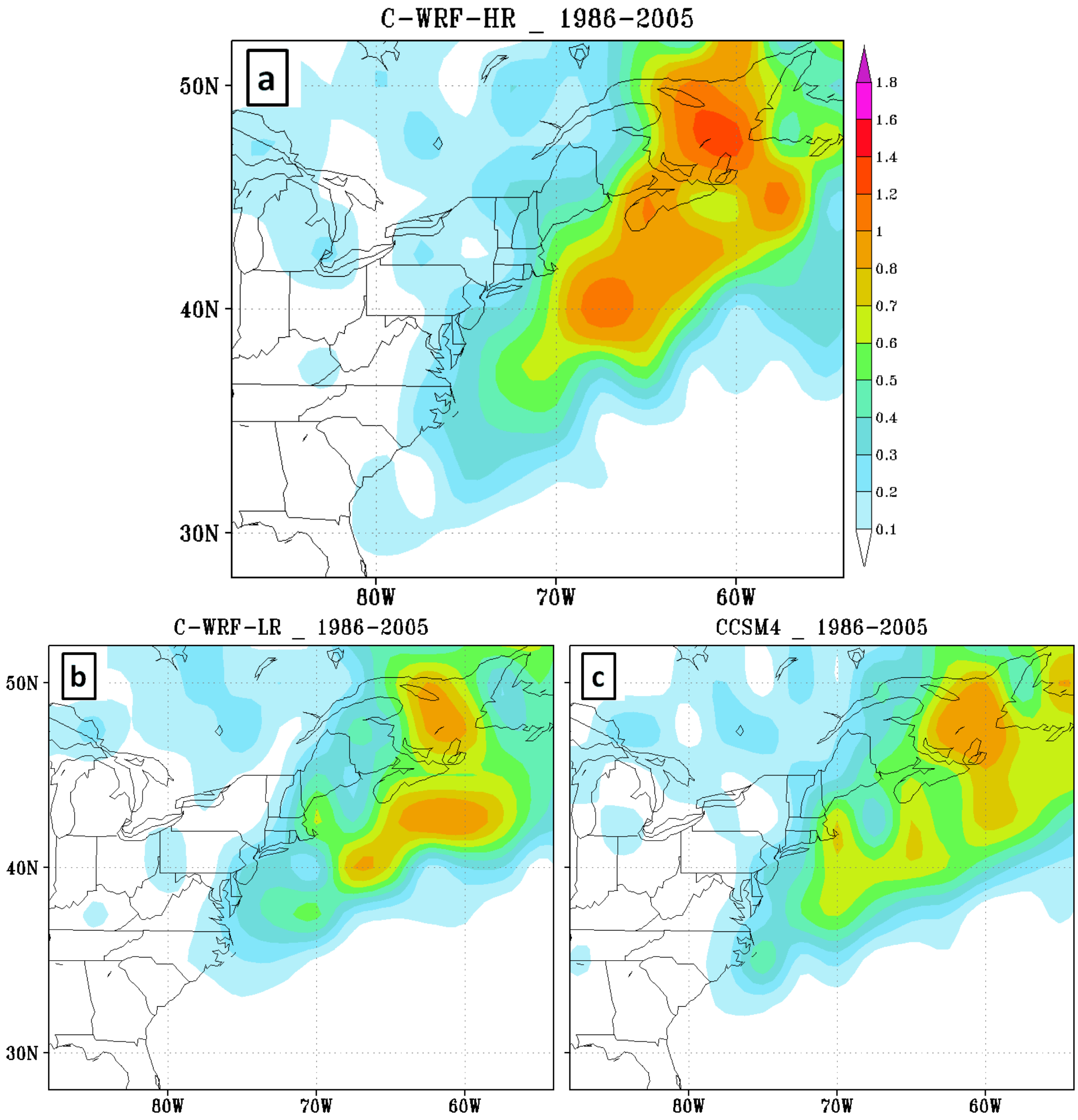

Fig. 5.8: Same as Fig. 5.7, but for the (a) C-WRF-HR, (b) C-WRF-LR, and (c) CCSM.

The spatial density of rapid deepening rate (deepening > 4 hPa/6h) was calculated for all of these models. In order to include enough cases, the 4 hPa/6h threshold for the rapid deepening is used in this chapter instead of the 5 hPa/6h in Chapter 3, since it only has 3 months for each winter in this chapter, but there are 5 months for CMIP5 models in Chapter 3. The CCSM and the GFDL will have too few cases for the spatial density of rapid deepening rate using the 5 hPa/6h. For the CFSR, most of the rapid deepening occurs over the storm track along the East Coast with the frequency around 1 case per 50,000 km^2 per winter (Fig. 5.7).

The CCSM4 (Fig. 5.7c) and the C-WRF-LR (Fig. 5.7b) also have most of the rapid deepening cases over the storm track along the East Coast, but they underestimate the frequency by 20-40%. Meanwhile, the C-WRF-HR has more rapid deepening cases than the CCSM and the C-WRF-LR, close to the CFSR; but the maximum in rapid deepening (> 0.6 case per 50,000 km^2 per winter) storms is shifted to north slightly (Fig. 5.7a) as compared with the CFSR.

The distribution of cyclone deepening rate within the ECWA region (Fig. 5.9) is consistent with the results of rapid deepening density (> 4 hPa/6h): the CCSM and C-WRF-LR underestimate the rapid deepening rate, while the C-WRF-HR is closer to the CFSR.

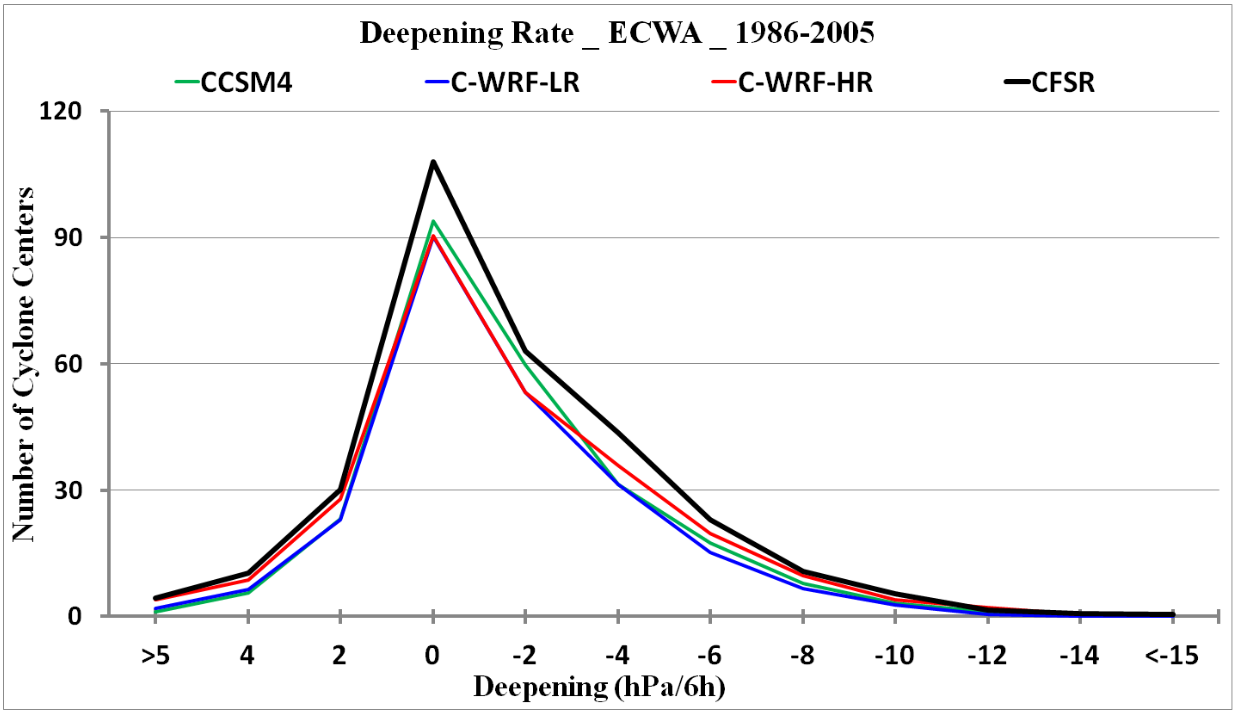

Fig. 5.9: The mean distribution of deepening rate of the cyclones within the ECWA region during the historical (1986-2005) winters. The black line is for the CFSR, green is for the CCSM4, blue is for the C-WRF-LR, and red is for the C-WRF-HR.

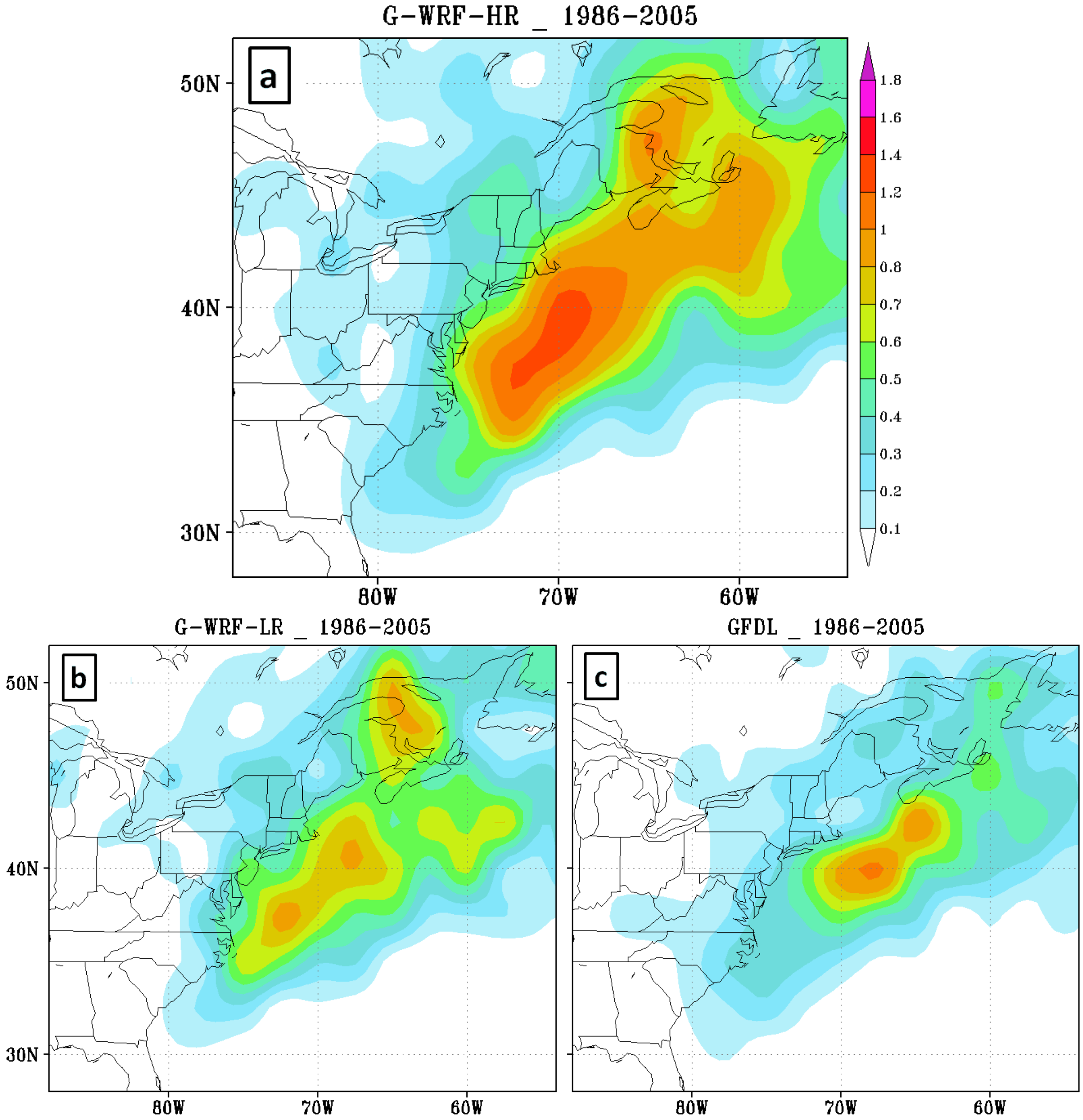

Fig. 5.10: Same as Fig. 5.7, but for the (a) G-WRF-HR, (b) G-WRF-LR, and (c) GFDL.

The amplitude of cyclone rapid deepening density for the GFDL and its associated WRF runs has similar results; the density of rapid deepening cases for the GFDL (Fig. 5.10c) and G-WRF-LR (Fig. 5.10b) is much smaller (20-40%) than the CFSR, while the G-WRF-HR (Fig. 5.10a) is closer to the CFSR. However, comparing with the CCSM and its WRF runs, the GFDL, G-WRF-LR, and G-WRF-HR have the rapid deepening density maximum shifted to south.

The distribution of cyclone deepening rate for the GFDL and its downscaled WRF runs is shown in Figure.5.11. The total number of the cyclone centers for the GFDL, G-WRF-LR and G-WRF-HR is close to the CFSR, but this was likely the result of underestimating the number of cyclone tracks (Fig. 5.5) and cyclones in the GFDL and its WRF runs moving more slowly (by ~20%) than the CFSR (Table 5.1). However, the GFDL and G-WRF-LR still underestimate the rapid deepening rate (deepening > 4 hPa/6h), while the G-WRF-HR is close to the CFSR.

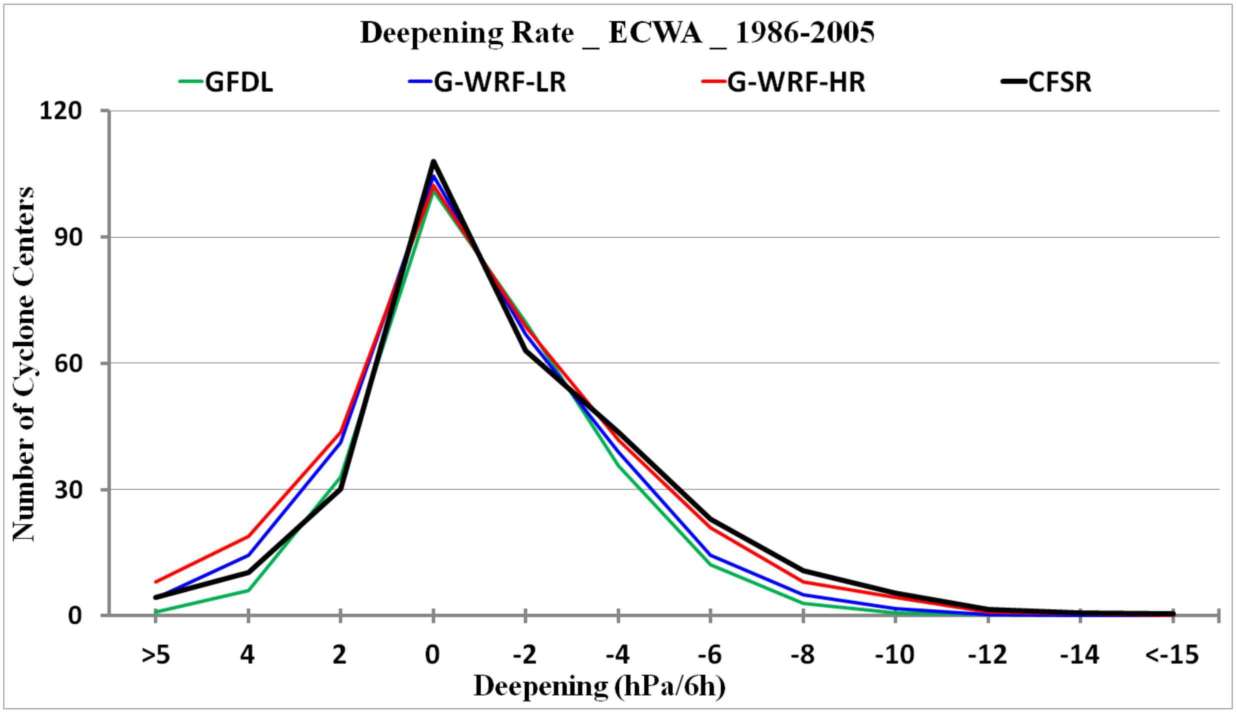

Fig. 5.11: Same as Fig. 5.9, but for the GFDL, G-WRF-LR, and G-WRF-HR.

d. <u>*Verification metrics*</u>

Similar with Section 3.1.5, a quantitative comparison performed to evaluate the model performance using four indices for the cyclones within ECWA region with respect to the CFSR: the spatial correlation of cyclone track density (TR), the absolute difference of the cyclone track density (TD), the correction for the distribution of cyclone minimum SLP (PR), and the absolute difference for the distribution of cyclone minimum SLP (PD).

Table 5.2: Verification of the models for TR, TD, PR and PD. The member ranking is presented for each of these verification metrics, and the models are ordered according to their final ranking. The RK_TR, RK_TD, RK_PR and RK_PD are the ranking for TR, TD, PR and PD respectively.

Model	TR	TD	PR	PD	RK_TR	RK_TD	RK_PR	RK_PD
G-WRF-HR	0.927	0.27	0.993	0.69	1	1	2	3
C-WRF-HR	0.906	0.42	0.997	0.61	3	5	1	1
CCSM4	0.905	0.39	0.982	0.68	4	4	3	2
GFDL	0.909	0.34	0.966	1.07	2	3	6	6
G-WRF-LR	0.890	0.33	0.969	0.92	5	2	5	5
C-WRF-LR	0.885	0.49	0.978	0.81	6	6	4	4

The WRF-HR runs have better overall performance, but the WRF-LR runs have worse performance than the original GCMs (Table 5.1). The G-WRF-HR has the best overall performance and cyclone track density, while the C-WRF-HR has the best cyclone intensity distribution. The CCSM has better track density and intensity distribution than the C-WRF-LR, while the G-WRF-LR improves the intensity distribution comparing with the GFDL.

5.1.2 Cyclone relative precipitation

The mean precipitation amount for the historical (1986-2005) winters was calculated for the CCSM, GFDL, and their corresponding downscaled WRF runs, and the results were compared with the mean of the GPCP and CMAP (GPCP_CMAP). The winter precipitation amount maximum (> 660 mm per winter) for the GPCP_CMAP is located over the storm track along the East Coast at middle latitudes (35-40°N), and the winter precipitation amount of the GPCP_CMAP along the coastline is around 300 mm (Fig. 5.12).

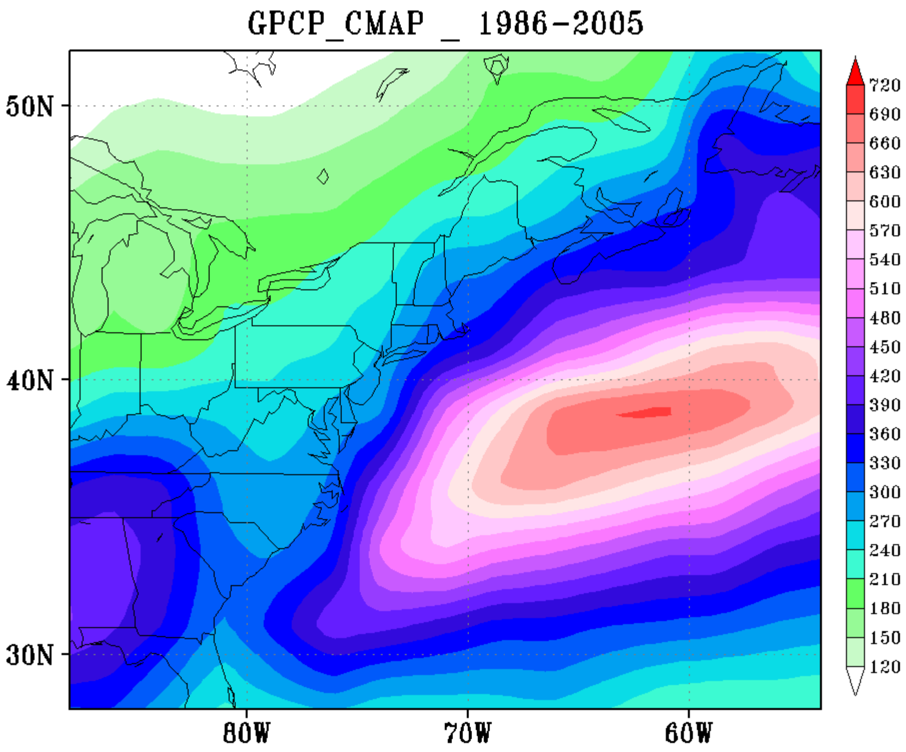

Fig. 5.12: The mean precipitation amount (mm per winter) of the historical (1986-2005) winters for the mean of GPCP and CMAP (GPCP_CMAP).

The precipitation amount maximum in the CCSM is shifted north (~40°N), but the amount is close to the GPCP_CMAP (Fig. 5.13c). The precipitation associated with extratropical cyclones (within the black box in Fig. 2.4b) contributes from 50% (contours in Fig. 5.13c) around 30°N to >80% over >45°N of the East Coast to the total precipitation (colors, Fig. 5.13c), which is similar to the results of the 10 CMIP5 models in Chapter 4 (Fig. 4.4a). The precipitation amount maxima in the C-WRF-LR and the C-WRF-HR are located almost the same position as the CCSM (Fig. 5.13a, b). The C-WRF-HR overestimated the precipitation maximum along the storm track by 10-15% as compared to the GPCP_CMAP. However, both of the C-WRF-LR and C-WRF-HR has 10-20% less precipitation just inland of the East Coast than the GPCP_CMAP. The contribution of cyclone relative precipitation to the total precipitation in the WRF (contours in Fig. 5.13a, b) runs is higher (~10%) than the CCSM.

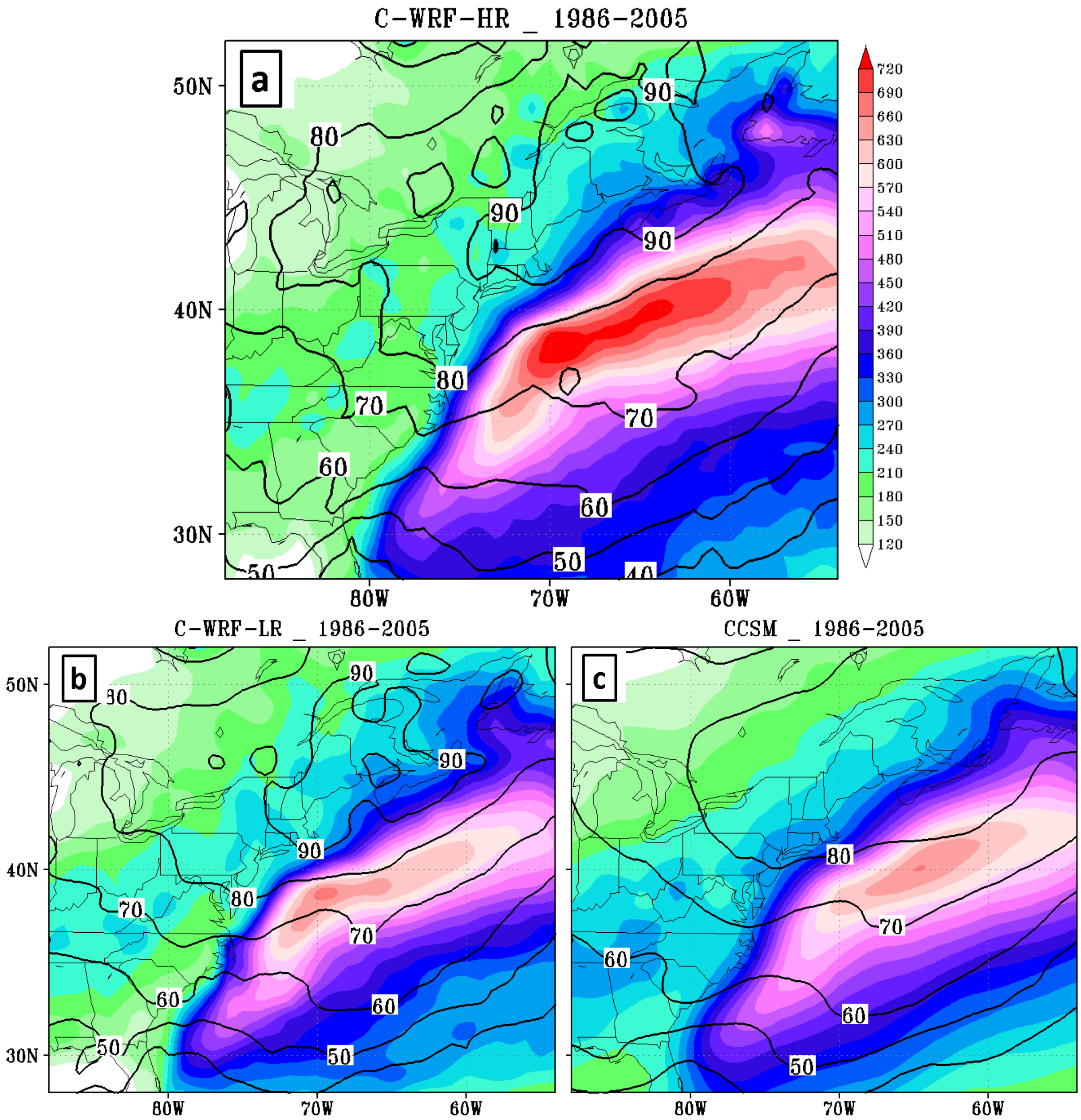

Fig. 5.13: Same as Fig. 5.12, but for the (a) C-WRF-HR, (b) C-WRF-LR, and (c) CCSM, with the contribution (%, contours) of cyclone relative precipitation (within the black box in Fig. 2.4b) to the total precipitation amount.

The maxima of winter precipitation amount in the GFDL and its downscaled WRF runs are located at nearly the same position with the GPCP_CMAP (Fig. 5.14). However, the maximum precipitation amount at the east side of the storm track in the G-WRF-HR is ~20% larger (Fig. 5.14a) than in the GPCP_CMAP. Given the slower propagating speed (Table 5.1), although the GFDL has fewer cyclone tracks, the maximum precipitation is almost the same as the GPCP_CMAP. The contributions of cyclone relative precipitation for the GFDL and its WRF runs are almost the same, from ~55% at the south of the East Coast to ~95% at the north of the East Coast.

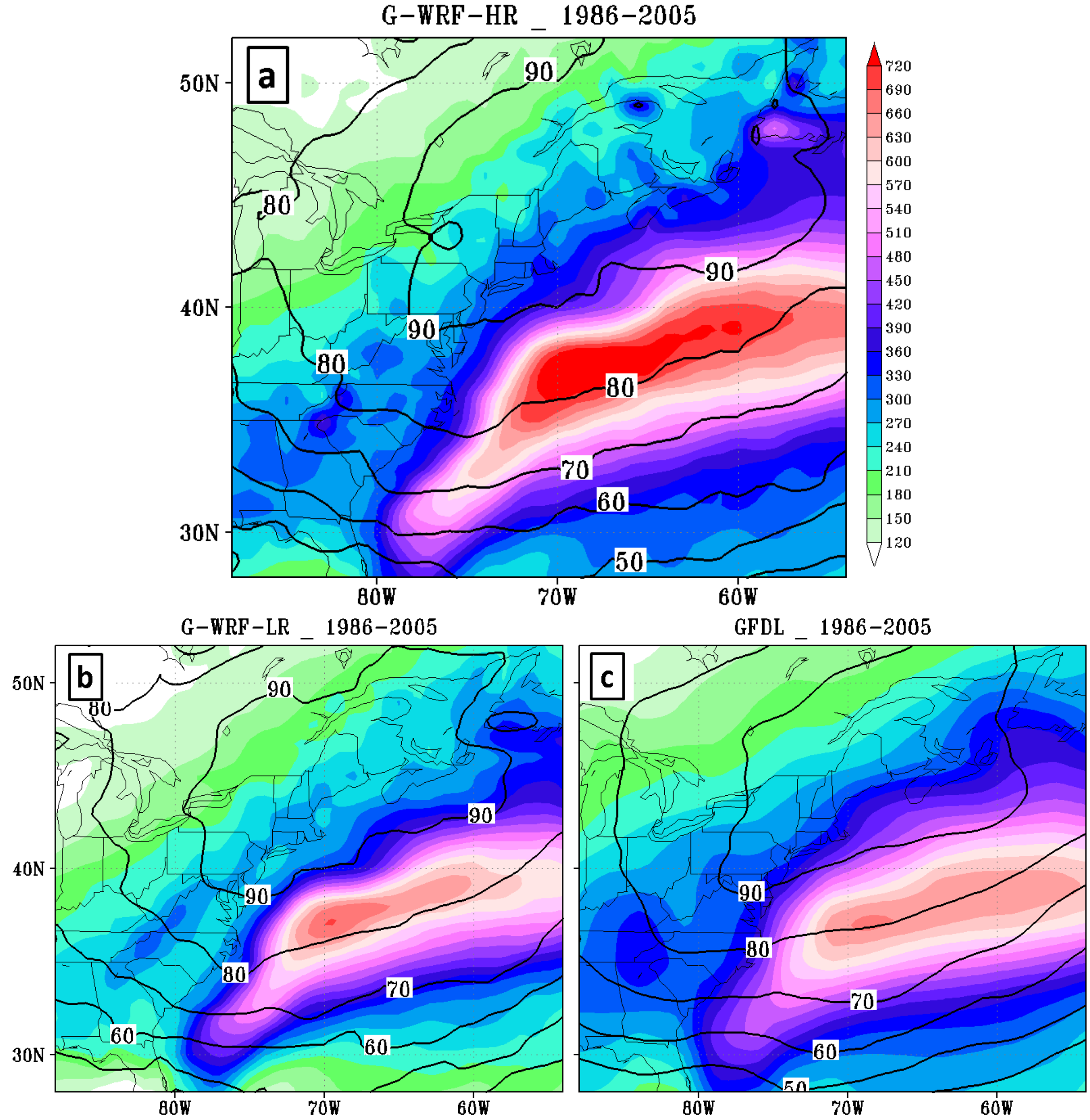

Fig. 5.14: Same as Fig. 5.13, but for the (a) G-WRF-HR, (b) G-WRF-LR, and (c) GFDL.

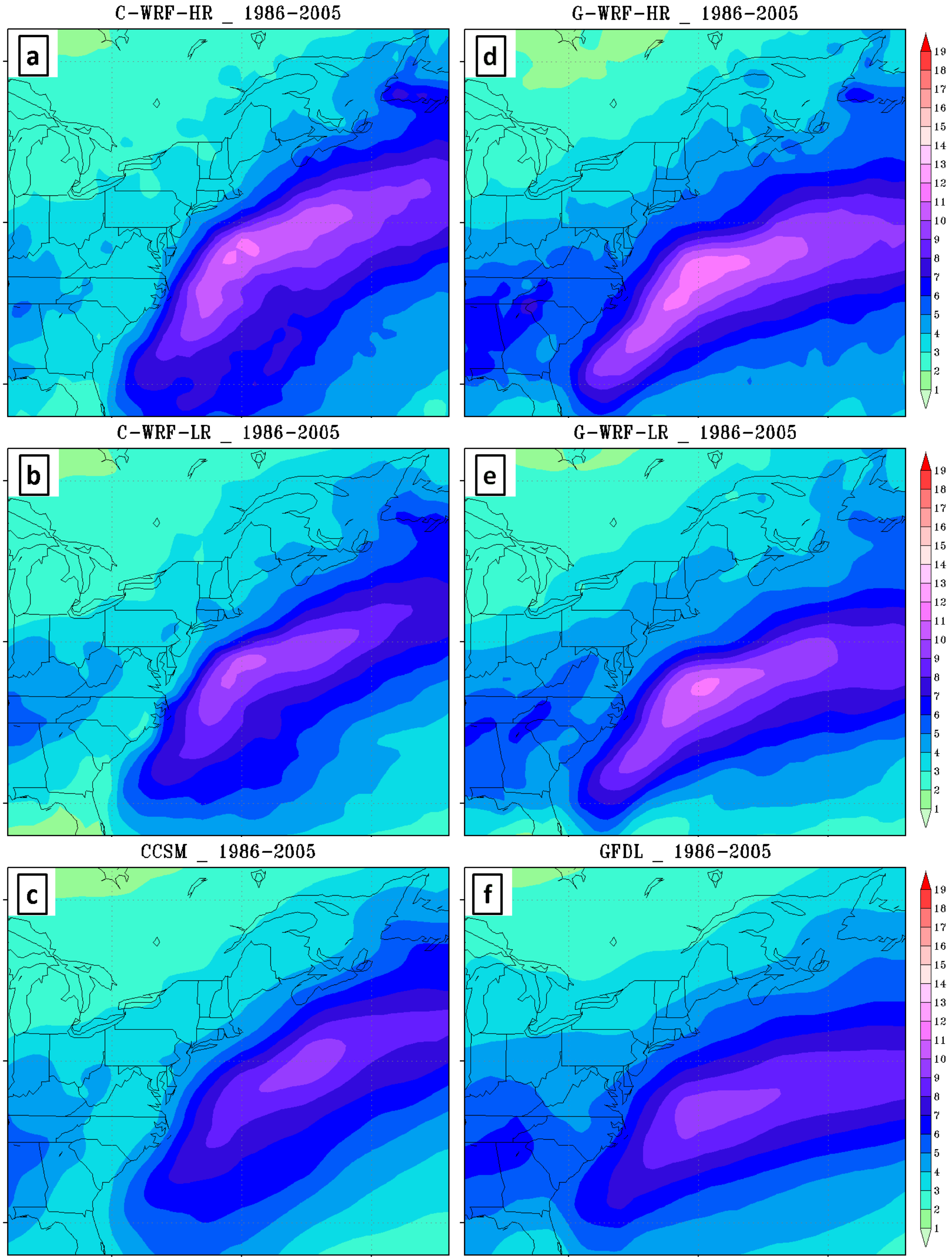

Fig. 5.15: The normalized cyclone relative precipitation rate (mm/day per cyclone) for the historical winter mean for the (a) C-WRF-HR, (b) C-WRF-LR, (c) CCSM, (d) G-WRF-HR, (e) G-WRF-LR, and (f) GFDL.

The normalized cyclone relative precipitation rate maximum is strongly related to model resolution (Fig. 5.15). The WRF-HR has the largest precipitation maximum (~12 mm/day), the WRF-LR is smaller, and the GCMs have the smallest precipitation rate maximum; and the difference between the CCSM (0.94°×1.25°) and the C-WRF-LR (1°×1°) is smaller than the difference between the GFDL (2.0°×2.5°) and the G-WRF-LR (1°×1°). However, the resolution is not the only factor controlling the precipitation intensity; other factors (such as model parameterization, large scale circulation) may also have large impact.

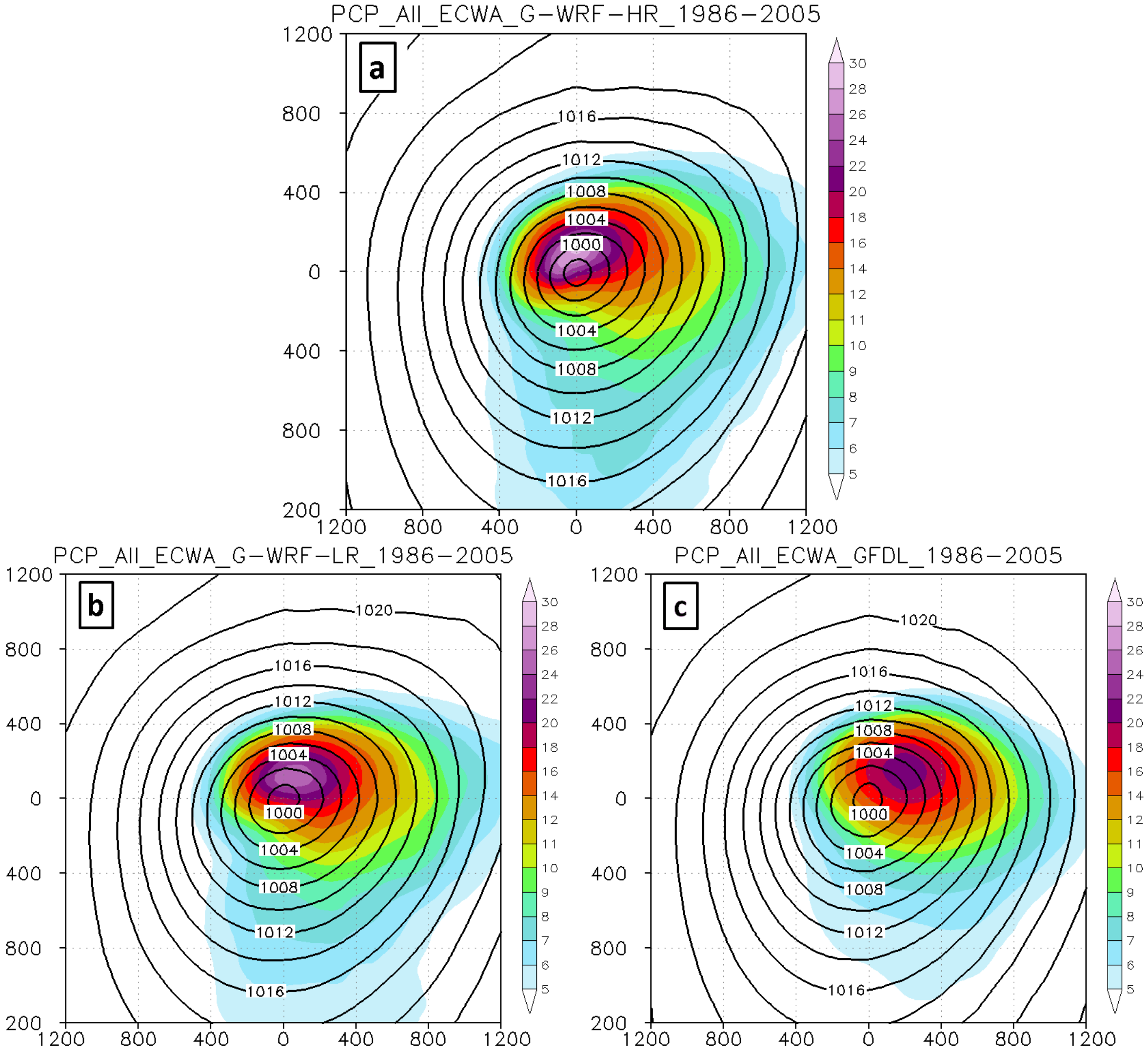

Fig. 5.16: Composite precipitation (colors, mm/day) and SLP (contours, hPa) for cyclone centers within the ECWA during historical winters, (a) G-WRF-HR, (b) G-WRF-LR, and (c) GFDL.

Within the synoptic scale cyclone system, the composite precipitation maximum for the cyclone centers within the ECWA region is 29 mm/day for the G-WRF-HR with a mean cyclone central SLP ~996.9 hPa, while the G-WRF-LR has 25 mm/day with a mean central SLP ~999.2 hPa, and 23 mm/day for the GFDL with the central SLP ~999.4 hPa (Fig. 5.16). The composite precipitation for the CCSM and its WRF runs is similar, with the C-WRF-HR having the largest maximum precipitation (not shown).

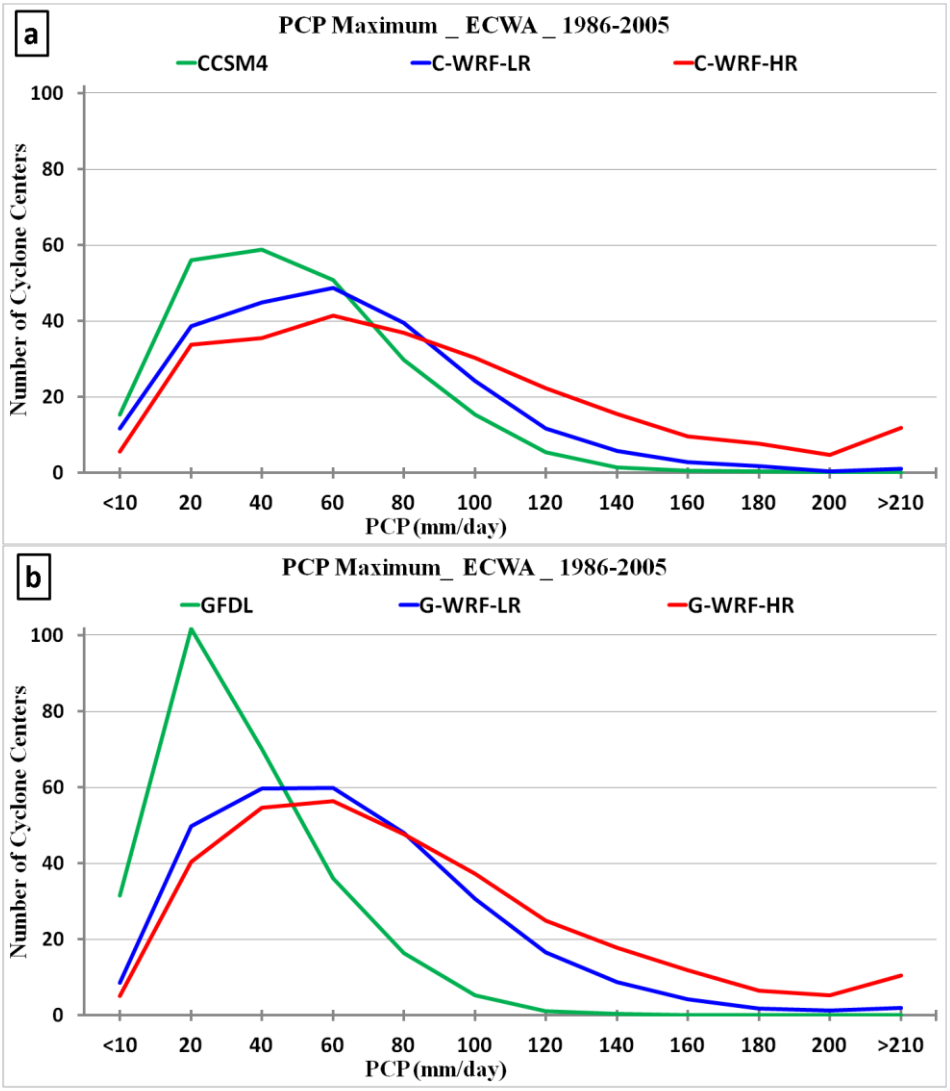

Fig. 5.17: The distribution of maximum precipitation around cyclone center (within the small purple box in Fig. 2.4b) within the ECWA during the historical (1986-2005) winters: (a) the green line is CCSM, the blue line is C-WRF-LR, and the red line is C-WRF-HR; (b) the green line is GFDL, the blue line is G-WRF-LR, and the red line is G-WRF-HR.

In addition to the mean precipitation fields, the distributions of maximum precipitation around cyclone center (within the small purple box in Fig. 2.4b) within the ECWA region during the historical (1986-2005) winters were compared (Fig. 5.17). The CCSM has a maximum at the 40 mm/day bin (Fig. 5.17a), while WRF runs have the maximum at 60 mm/day and a significant shift towards heavier precipitation; and the C-WRF-HR has a longer tail extending to extremely heavy precipitation (> 200 mm/day). The distributions for the G-WRF-LR and the G-WRF-HR are similar to the WRF forced by CCSM. However, the maximum precipitation distribution for the coarse resolution GFDL is much narrower, most (~90%) of the cases are concentrated at < 70 mm/day.

5.1.3 Physical processes responsible for the differences among models

As described in Section 5.1.1 and 5.1.2, the downscaled WRF runs are highly influenced by the original GCM, since the CMIP boundary conditions and SST are used. For example, the position of the storm track (more onshore or offshore) and the cyclone moving speed in both WRF-HR and WRF-LR are similar to the corresponding GCM. However, the WRF-HR has larger difference from the original GCM than the WRF-LR run, with the WRF-HR having a smaller bias for cyclone intensity and deepening rate, and it has more precipitation. The results of the WRF-HR are quite different from the WRF-LR, suggesting that the model resolution plays an important role in the cyclone simulation. In this section, the baroclinicity (surface and 850hPa temperature gradient, and 850-500 hPa Eady growth rate), upper level forcing (250hPa wind speed), and diabatic contribution (diabatic PV at 900-750 hPa level) are examined to explore the reasons for the differences among models for the historical period.

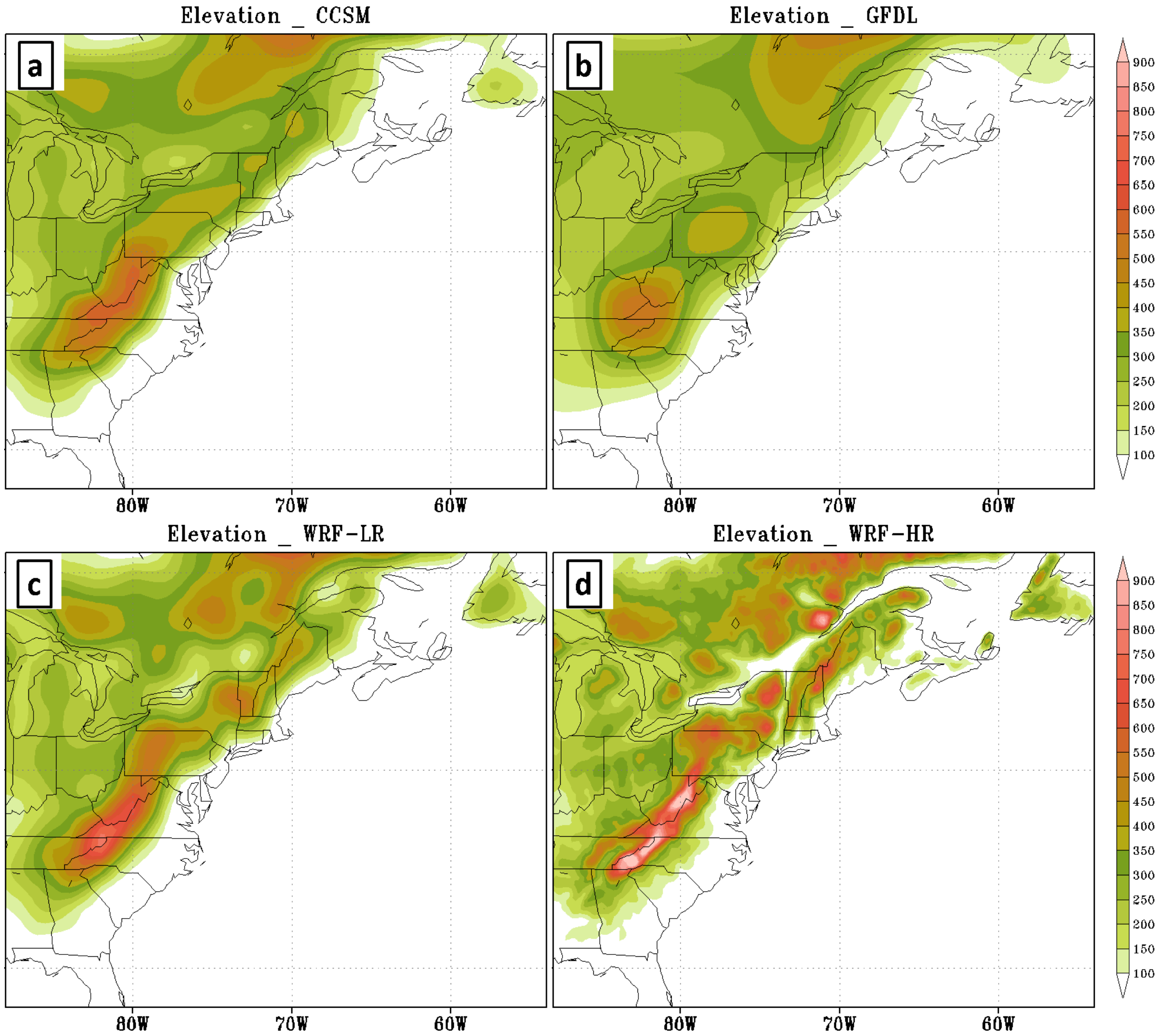

Fig. 5.18: The elevation (m) in the (a) CCSM, (b) GFDL, (c) WRF-LR, and (d) WRF-HR.

First of all, the terrain in WRF-HR and WRF-LR is more realistic than in the coarse resolution GCMs, especially GFDL-ESM2M. The elevation of the Appalachian Mountains in the downscaled WRF is higher than in the GCMs. For example, in WRF-HR the highest elevation of the Appalachian Mountains in Pennsylvania, Virginia and West Virginia is 600-950 m (Fig. 5.18d), which is almost the same with the real elevation. In the WRF-LR (Fig. 5.18c), the elevation of the Appalachian Mountains is smoother and 100-200 m lower than in the WRF-HR. The elevation in the CCSM (Fig. 5.18a) is close to the WRF-LR given the comparable model resolution. However, in the GFDL (Fig. 5.18b) the elevation of the Appalachian Mountains is much lower; the highest elevation is 350-550 m in Pennsylvania, Virginia and West Virginia, which is 250-400 m lower than in the WRF-HR.

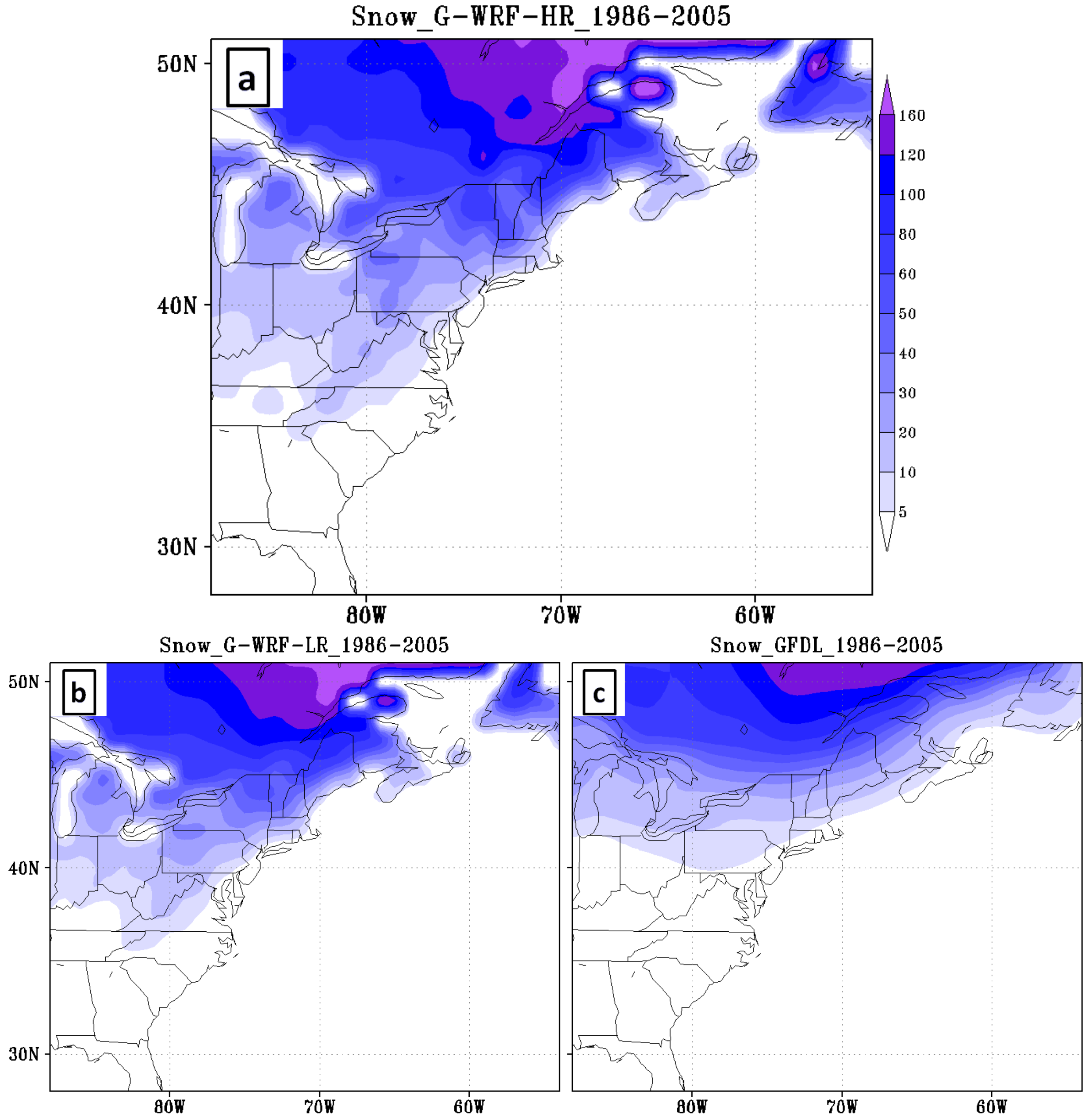

Fig. 5.19: The mean surface snow amount (kg/m^2) during the historical (1986-2005) winters for (a) G-WRF-HR, (b) G-WRF-LR, and (c) GFDL.

Given the higher elevation of the Appalachian Mountains in the WRF, especially in the WRF-HR, the snow extends further south over the eastern U.S. comparing with the GFDL (Fig. 5.19). Meanwhile, the higher and more realistic elevation of the Appalachian Mountains in the WRF allows the Appalachian cold-air damming to be better represented.

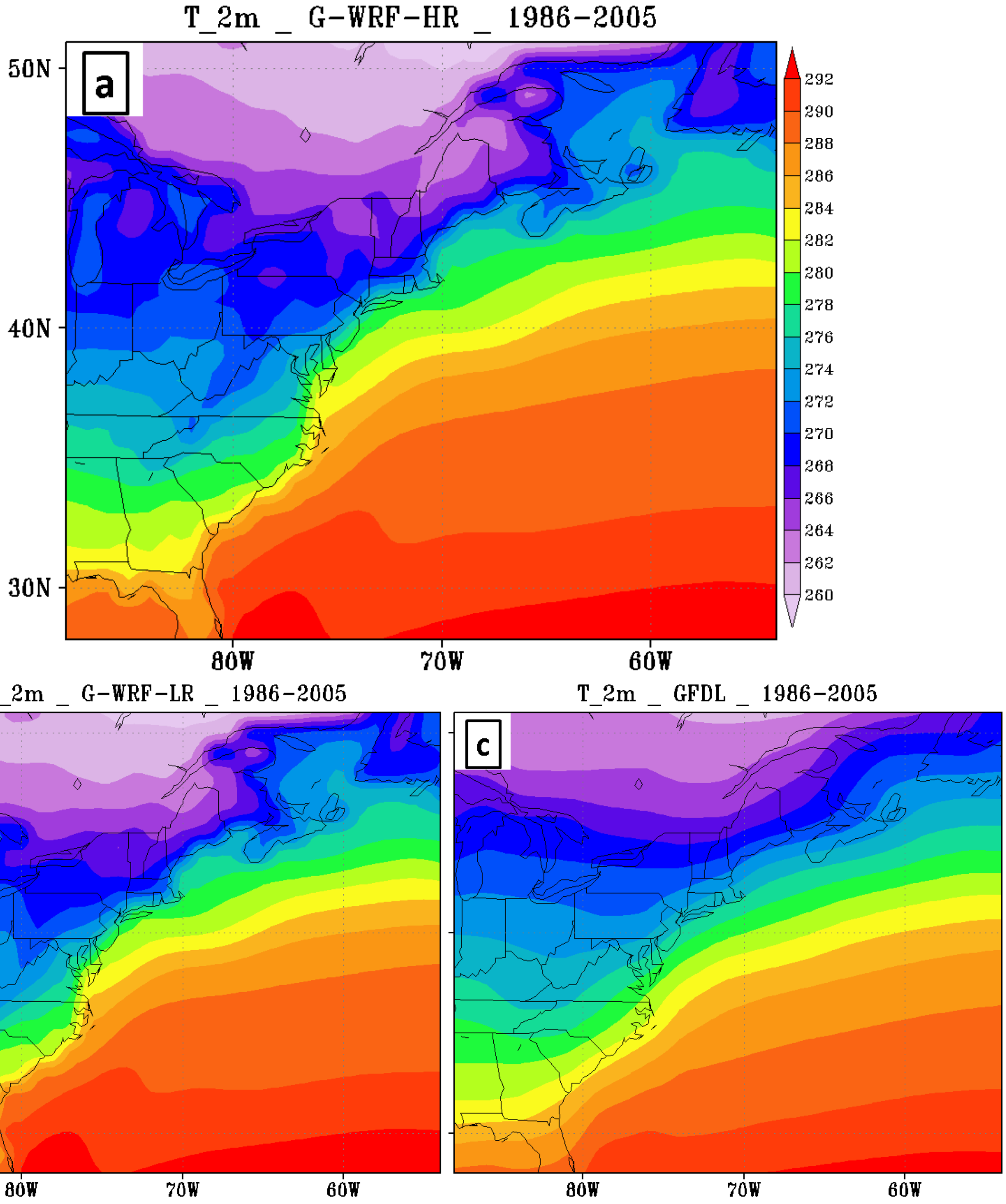

Fig. 5.20: The mean surface temperature (K) during the historical (1986-2005) winters for (a) G-WRF-HR, (b) G-WRF-LR, and (c) GFDL.

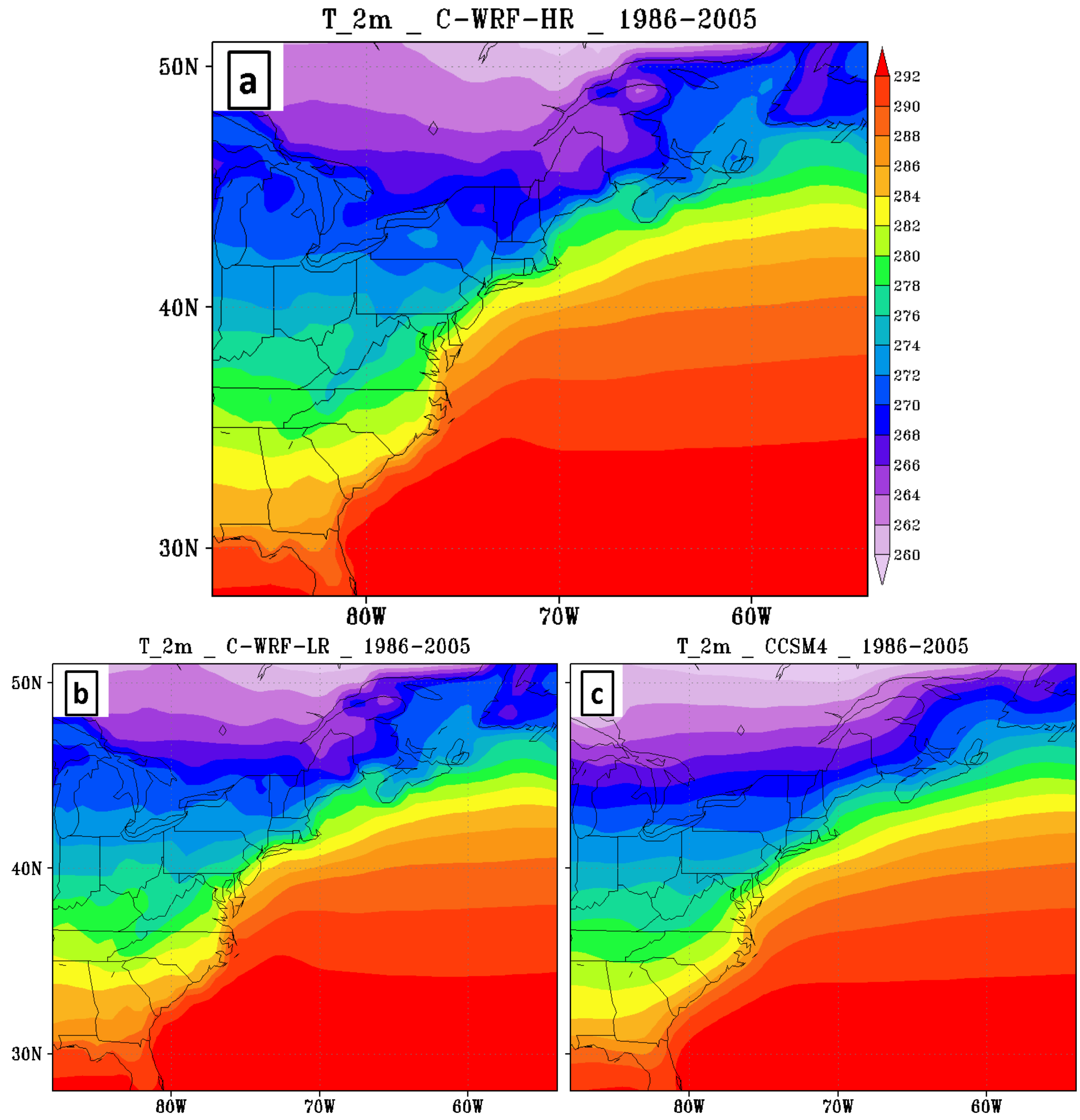

Fig. 5.21: Same as Fig. 5.20, but for the (a) C-WRF-HR, (b) C-WRF-LR, and (c) CCSM.

As a result, the differences in surface temperature for the GFDL and corresponding WRF are large (Fig. 5.20) over eastern U.S. at relatively high latitude (> 40°N). The surface temperature over this region is 1-2.5 K colder in the G-WRF-LR and 1-3.5 K colder in the G-WRF-HR than in the GFDL (Fig. 5.20). Over the ocean, the difference of surface temperature between the WRF and the GFDL is smaller: it is 0.5-1.5 K warmer in the WRF than the GFDL.

Therefore, the surface temperature gradient in WRF is much stronger than the GFDL. For example, for the ECL cyclone centers, the surface temperature gradient in the G-WRF-HR is 20-50% stronger than the GFDL while the G-WRF-LR is 20-40% stronger than the GFDL over the northeast side of cyclone center (Fig. 5.22). The difference in temperature gradient at low troposphere (such as 850hPa) is 10-20% (not shown) between the GFDL and the WRF runs, which is smaller than the surface.

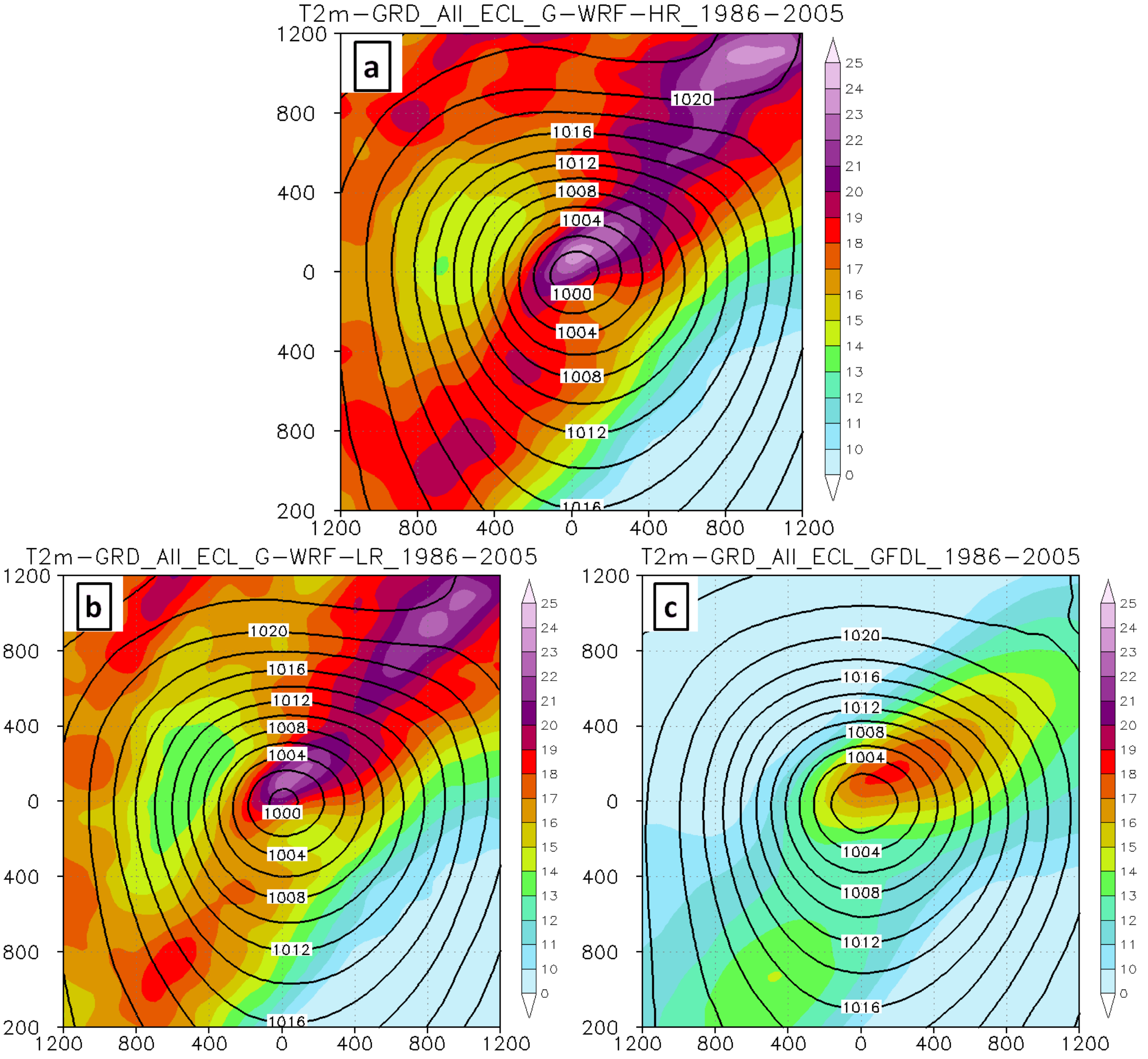

Fig. 5.22: Composite surface temperature gradient (colors, K/1000km) and SLP (contours, hPa) for cyclone centers within the ECL during historical winters, (a) G-WRF-HR, (b) G-WRF-LR, and (c) GFDL.

Comparing the surface (2m) temperature for the CCSM, C-WRF-LR and C-WRF-HR (Fig. 5.21), the difference over the ocean is relatively small (< 1 K), since the SST for WRF is the same as the CCSM, while the difference over land along the East Coast is also not large (< 2 K) for most of the region. Thus although the C-WRF-LR and the C-WRF-HR have a stronger surface temperature gradient than the CCSM, the difference is only 10-15% (not shown) which is smaller than the GFDL group. Meanwhile, the difference (~10%) of temperature gradient at 850hPa (not shown) is smaller than the surface.

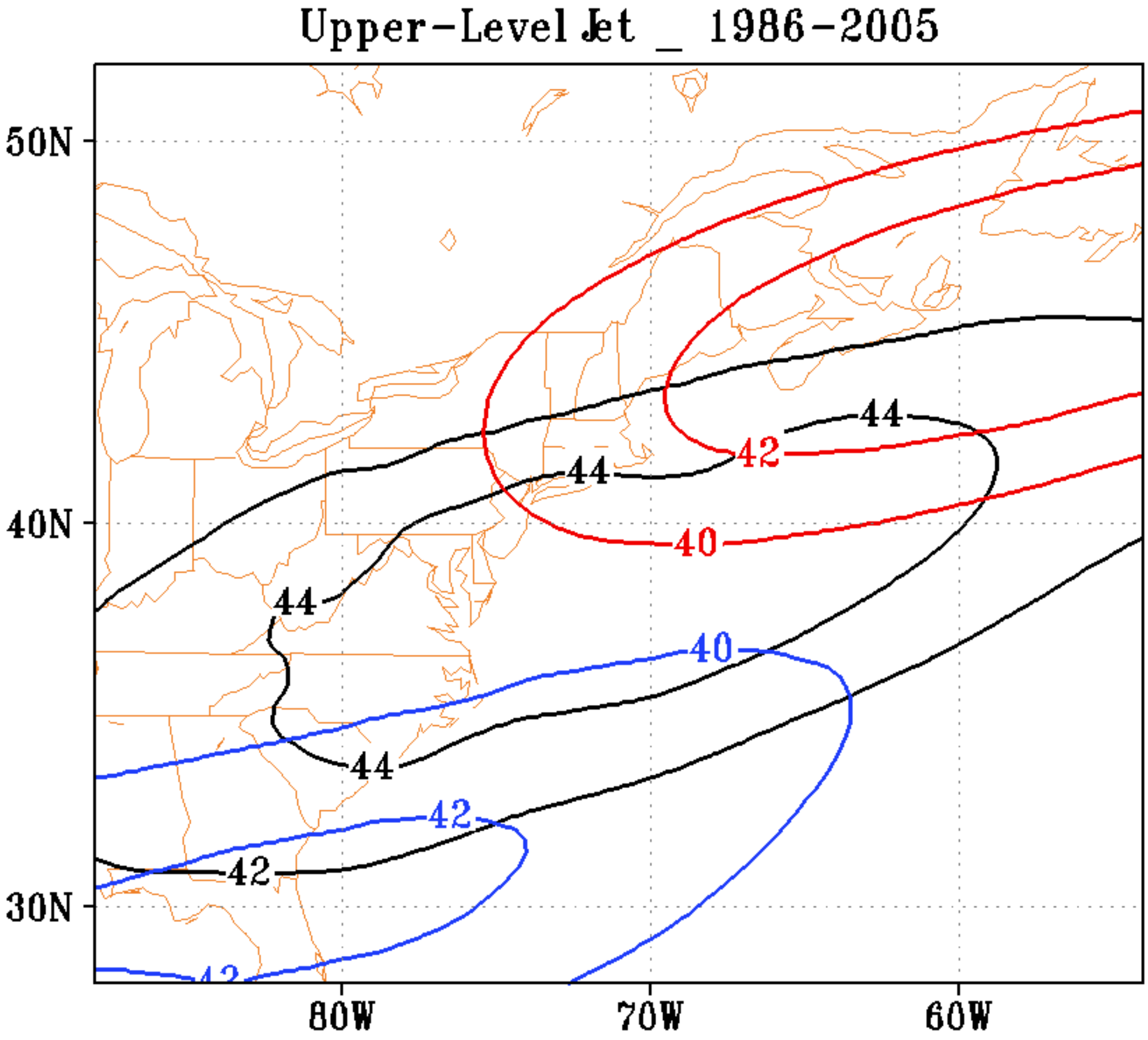

Fig. 5.23: The upper level jet (250hPa wind speed, m/s), the black contours are the CFSR, the red contours are the CCSM, and the blue contours are the GFDL.

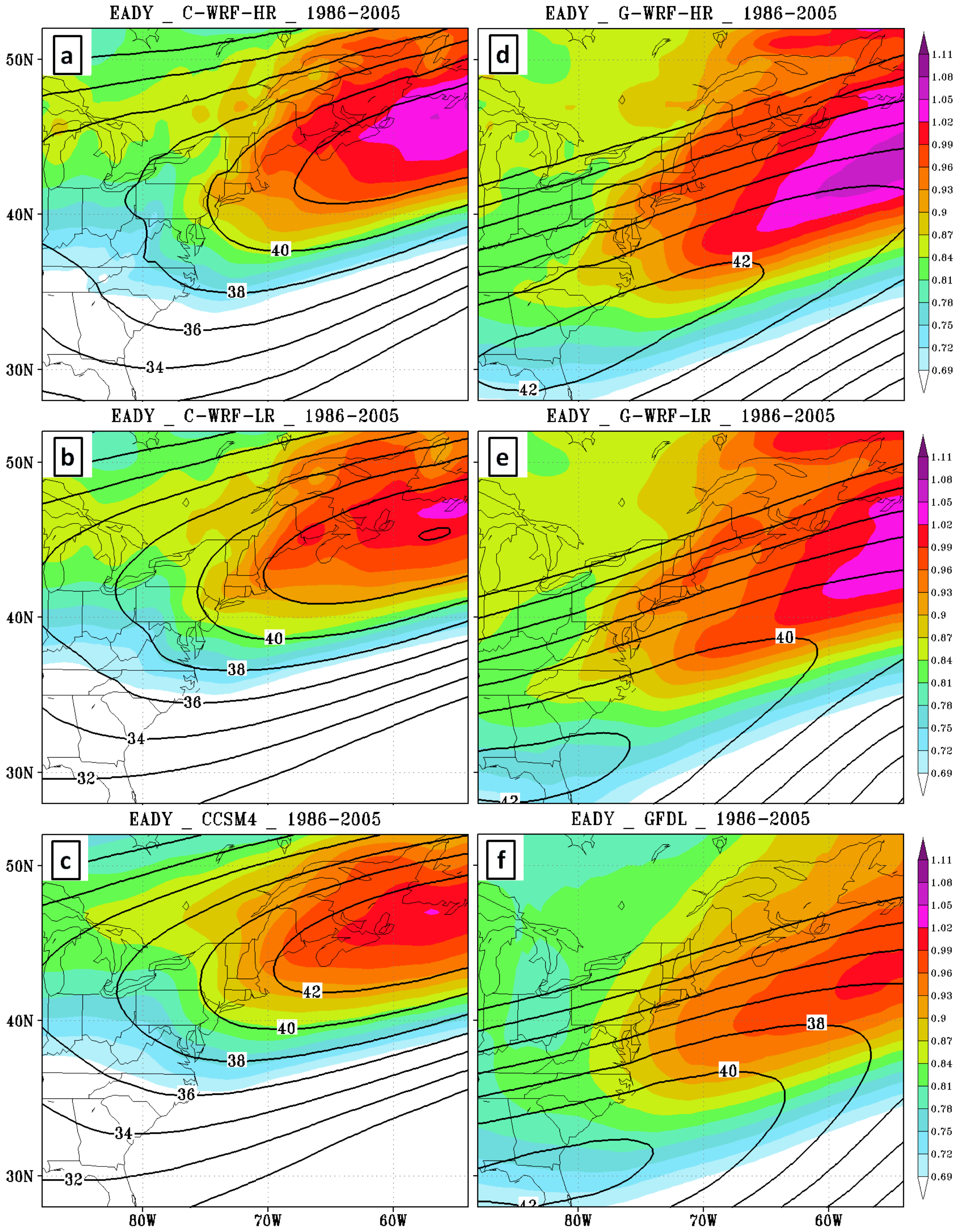

Fig. 5.24: The wind speed (contours, m/s) at 250hPa and the 850-500hPa Eady growth rate (colors, per day) for the historical winter mean for (a) C-WRF-HR, (b) C-WRF-LR, (c) CCSM, (d) G-WRF-HR, (e) G-WRF-LR, and (f) GFDL.

The Eady growth rate (850-500 hPa) maximum (>1per day) in the CCSM and its WRF runs is located over the east of the southeast Canada (colors in Fig. 5.24a-c). The maximum in the C-WRF-HR is ~5% stronger than the CCSM, while the maximum in the C-WRF-LR is almost the same as the CCSM. In the GFDL and its WRF runs, the Eady growth rate maximum is close to the CCSM runs, but extends southwestward to the east of U.S. Northeast (colors in Fig. 5.24d-f). The Eady growth rate maximum in the G-WRF-HR is ~10% stronger than the GFDL, and the G-WRF-LR is ~5% stronger than the GFDL.

The upper level jet (250 hPa) in the CFSR is located at middle latitudes (35-40°N) of the U.S. East Coast with a maximum of ~45 mm/s; meanwhile, the positions of the upper level jets in the CCSM and the GFDL are quite different (Fig. 5.23). The jet is shifted to northeast in the CCSM, but shifted to southwest in the GFDL. The positions of the jet in the C-WRF-LR and C-WRF-HR are similar to the CCSM, shifted to the east of U.S. Northeast and southeast Canada with a maximum of ~43 m/s (contours in Fig. 5.24a-c), which is slightly weaker (5%) than the CFSR. The upper level jet in the WRF runs forced by the GFDL is located over the southeast U.S., shifted to the southwest comparing with the CFSR. In the G-WRF-HR, the upper level jet is slightly stronger than the GFDL and G-WRF-LR (contours in Fig. 5.24d-f). Overall, the difference of the upper level jet intensity is relatively small (~5%), but the positions of the jet in the CCSM runs and the GFDL runs is quite different (Fig. 5.24).

Comparing the precipitation around cyclone centers, the G-WRF-HR has ~10% more mean precipitation over the comma head than the G-WRF-LR and the GFDL, with a 20-30% stronger precipitation maximum than the G-WRF-LR and GFDL (Fig. 5.16). The precipitation differences for the CCSM group are similar to the GFDL group. Thus the stronger latent heat release from the heavier precipitation in WRF-HR may enhance the cyclone deepening.

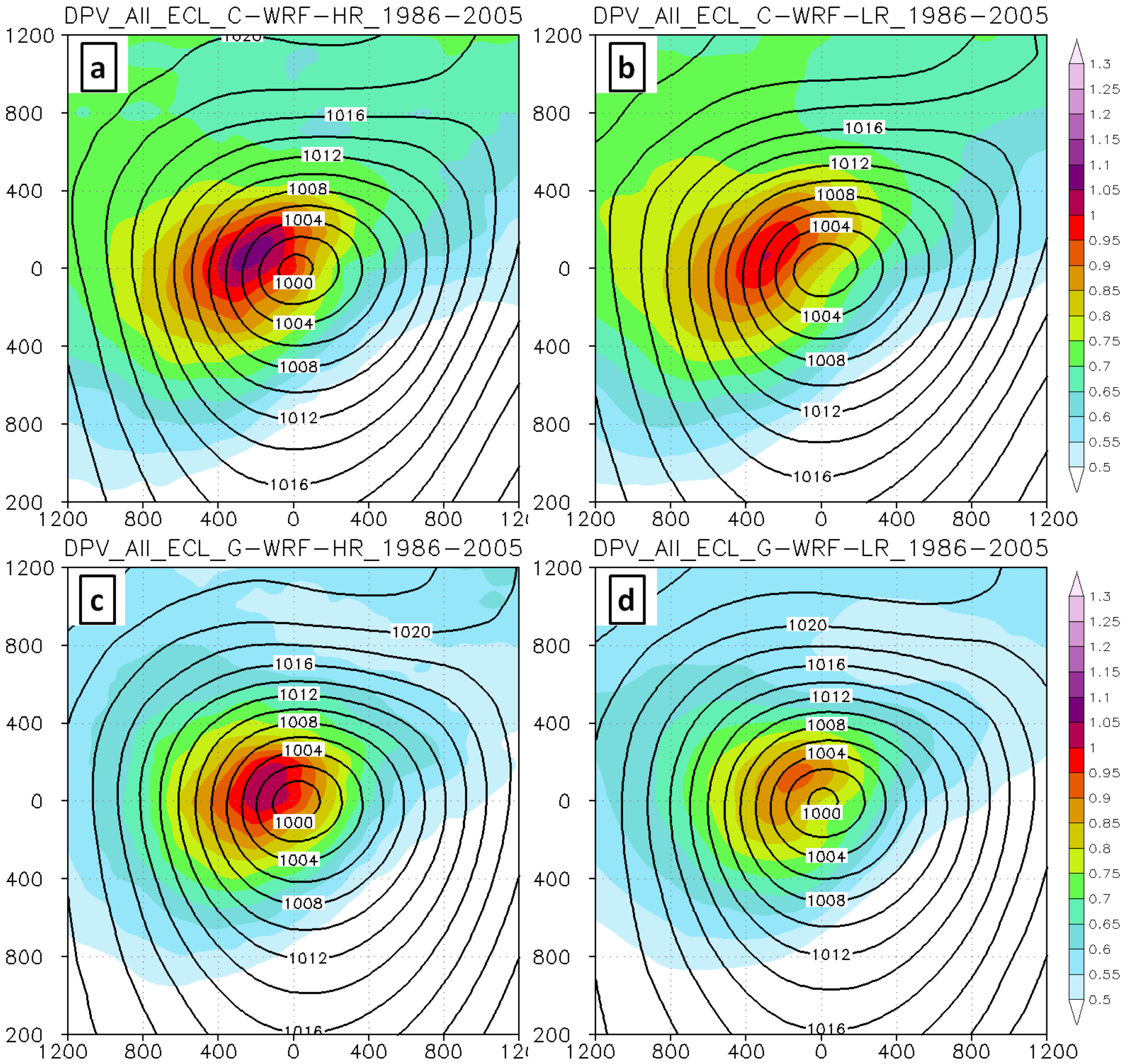

Fig. 5.25: The composite DPV (colors, PVU) and SLP (contours, hPa) for the cyclones within the ECL region during historical (1986-2005) winters, for (a) C-WRF-HR, (b) C-WRF-LR, (c) G-WRF-HR, and (d) G-WRF-LR.

In order to quantitatively estimate the impact of latent heat release, the diabatic potential vorticity (DPV) was calculated as the 900-750 hPa Ertel PV (following the study of Marciano et al. 2015) for the WRF runs (it is not calculated for the GCMs due to the lack of the data). The DPV maxima (~ 1 PVU) are located at the west of cyclone center for all of these models (Fig. 5.25), which is similar to the result in Marciano et al. (2015). However, the DPV is 10-15% stronger in the WRF-HR than the WRF-LR for the mean of all cyclone centers within the ECL region (Fig. 5.25). It indicates that the amount of latent heat release is very sensitive to the horizontal resolution, which is consistent with the conclusion from Willison et al. (2013), who found an enhanced positive feedback between cyclone intensification and latent heat release from precipitation in the higher resolution (20km) WRF runs relative to the coarser (120km) resolution WRF runs.

Overall, although the G-WRF-LR and HG-WRF-HR are forced by the GFDL, the surface baroclinicity (surface temperature gradient) in the G-WRF-LR and G-WRF-HR is much stronger (20-40%). The difference in the upper level baroclinicity is smaller; the 850hPa temperature is 10-20% stronger and 850-500 hPa Eady growth rate is 5-10% stronger in the G-WRF-LR and G-WRF-HR than the GFDL. The stronger baroclinicity and the stronger (~5%) upper level jet in the WRF runs yields ~3 more cyclones per winter in the G-WRF-LR, ~6 more cyclones and a more realistic track density distribution in the G-WRF-HR over the ECWA region. Meanwhile, the cyclones in the G-WRF-HR are significantly deeper than not only the GFDL, but also the G-WRF-LR. When the surface temperature, Eady growth rate, and upper level jet in the G-WRF-HR is slightly stronger (~5%) than the G-WRF-LR, the significant stronger (15%) DPV in the G-WRF-HR plays a more important role in the more intense cyclones (Fig. 5.6) and more rapid deepening rate (Fig. 5.9 and Fig. 5.10).

The result of the CCSM runs is similar with the GFDL runs, the 10-15% stronger mean DPV in the C-WRF-HR enhances the cyclone deepening, while the difference in the other factors is relatively small (~5%). Meanwhile, the northeastward shift of the upper level jet in the CCSM4 runs (Fig. 5.24) yields a northeastward shift of the rapid deepening cases (Fig. 5.8) comparing to the CFSR (Fig. 5.7).

5.2 Future changes of the cyclones in downscaled WRF

In this section, the future changes of extratropical cyclones and the associated precipitation are examined for the CCSM group, including both the GCM and the downscaled WRF runs (Section 5.2.1), and the GFDL group (Section 5.2.2). The future changes in the CCSM group and the GFDL group are compared; and the physical processes responsible for those changes are explored. The future changes are also compared among the GCM, the WRF-LR, and the WRF-HR to investigate the impacts of dynamical downscaling and model resolution.

5.2.1 Future changes of cyclones in The CCSM and the downscaled WRF

In the CCSM, the cyclone track density decreases up to ~ 20% over the western Atlantic, while it increases 10-30% along the East Coast with a maximum (~ 1 cyclone track per winter) over the east of U.S. Northeast and southeast of Canada (Fig. 5.26c). The spatial pattern of the track density changes for the C-WRF-LR is similar to the CCSM, and most of the increase (10-40%) is concentrated along the East Coast (Fig. 5.26b). Meanwhile, in the C-WRF-HR there is also a 10-40% increase along the East Coast and smaller increase over some inland regions of eastern North America (Fig. 5.26a); but the decrease of track density over the western Atlantic is somewhat smaller (~10%) as compared with the CCSM and the C-WRF-LR.

The future change in the cyclone intensity distribution within the ECL regions is similar to the track density changes. Within the ECL region, there are increases in the numbers of cyclone centers for most intensity bins (Fig. 5.27). The increase (5-10%) for the CCSM is concentrated within the 1010-990 hPa bins, but there is a ~20% decrease in the extremely weak (> 1005 hPa) cyclone centers. There is an increase in both the C-WRF-LR (~10%) and C-WRF-HR (10-20%) cyclone centers > 995 hPa. However, only the C-WRF-HR has an increase (~20%) in the extremely deep (< 975hPa) cyclone centers (Fig. 5.27b); and it also has a ~20% increase for the extremely strong (> 40 m/s) 850hPa wind speed cases (not shown), which is consistent with the increase of extremely deep (SLP) centers.

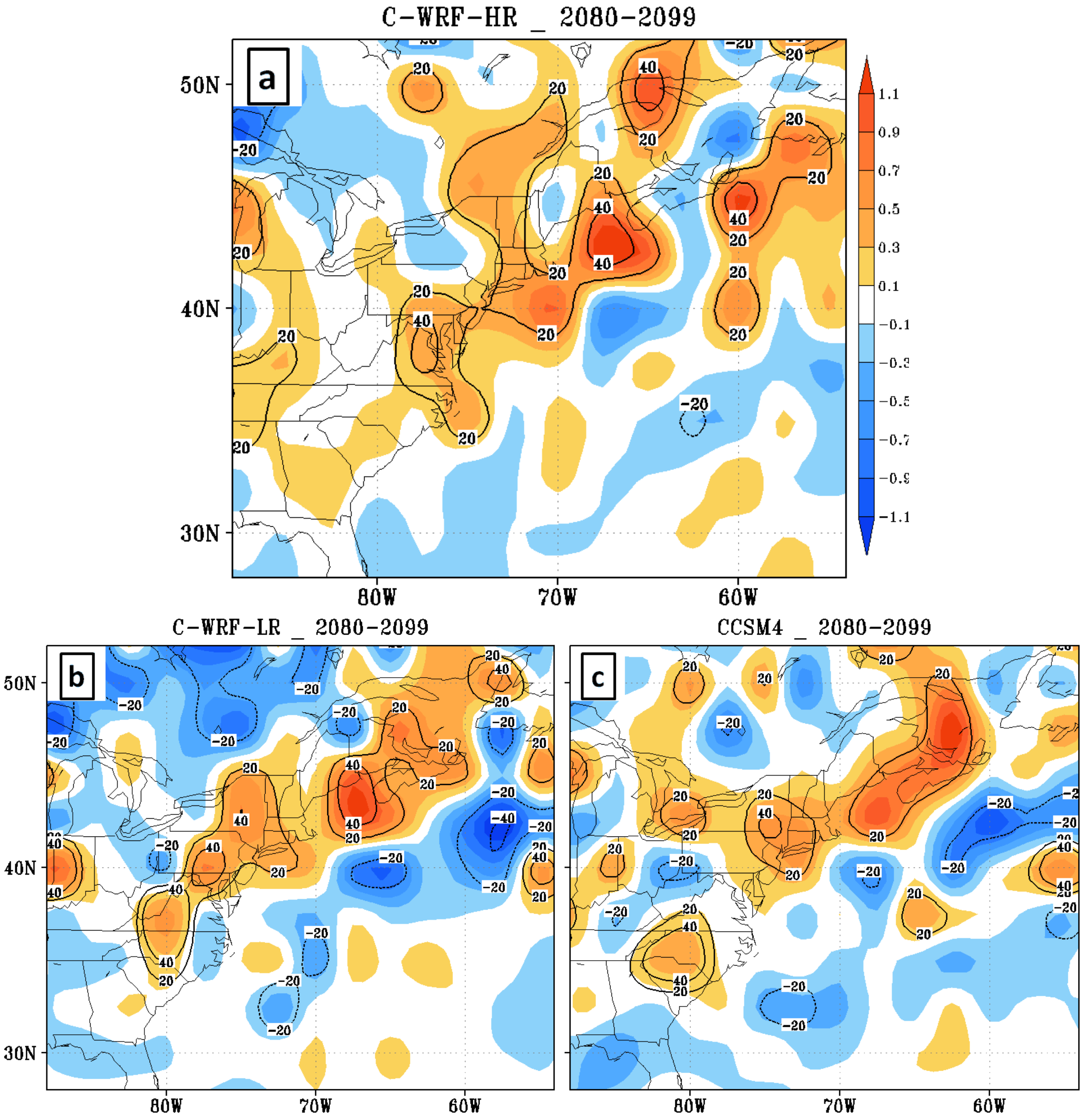

Fig. 5.26: The changes of cyclone track density (colors, per winter per 50,000km^2) and the percentage (contours) in the future (2080-2099) winters for the (a) C-WRF-HR, (b) C-WRF-LR, and (c) CCSM.

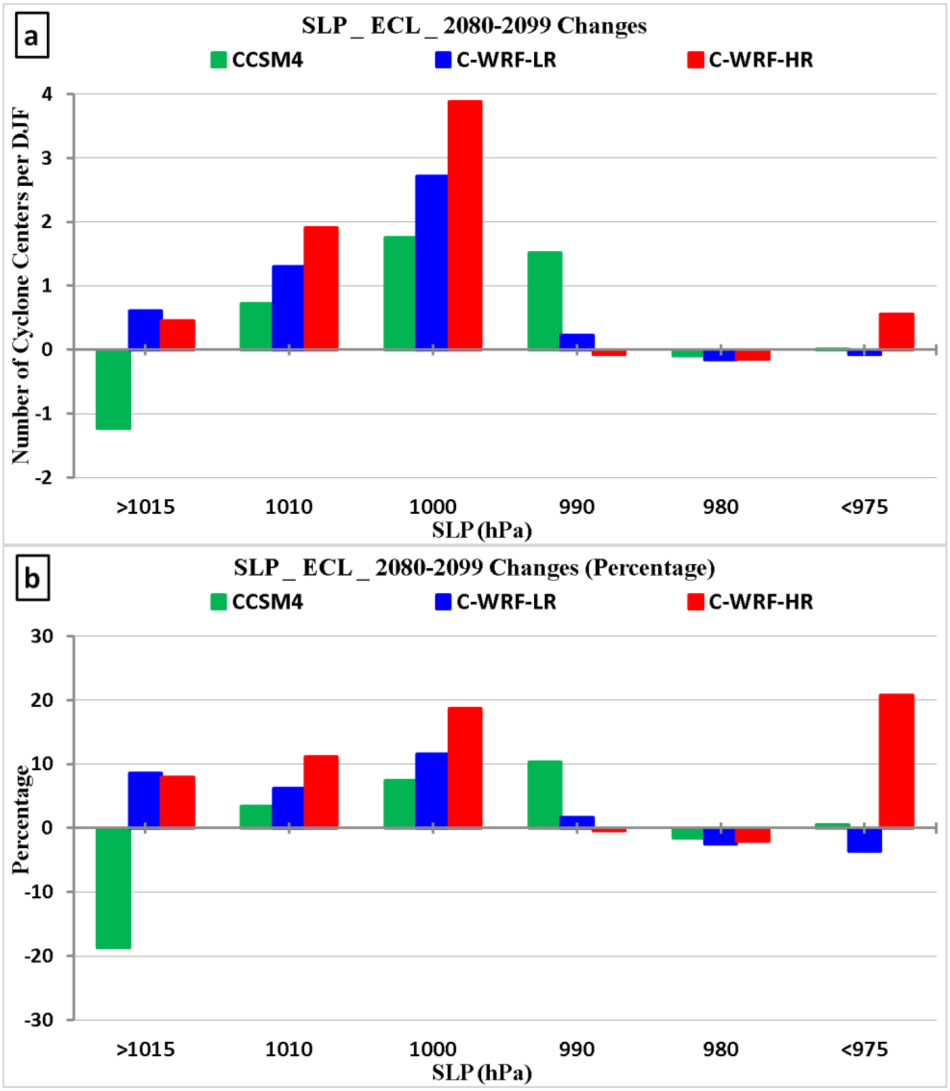

Fig. 5.27: (a) The changes of cyclone intensity distribution in the future (2080-2099) winters for the cyclone centers within the ECL region. Green is the CCSM; blue is the C-WRF-LR, and red is the C-WRF-HR. (b) same as (a), but for the percentage change.

Within the WA region there is a ~25% decrease in the number of cyclone centers around 1010 hPa for the CCSM and the C-WRF-LR, while the C-WRF-HR increases by ~30% at the > 1015 hPa bin and ~10% for 990 hPa bin (Fig. 5.28). Overall, the number of cyclone centers within the WA region is decreasing for the CCSM and the C-WRF-LR, while there is no significant change for the C-WRF-HR.

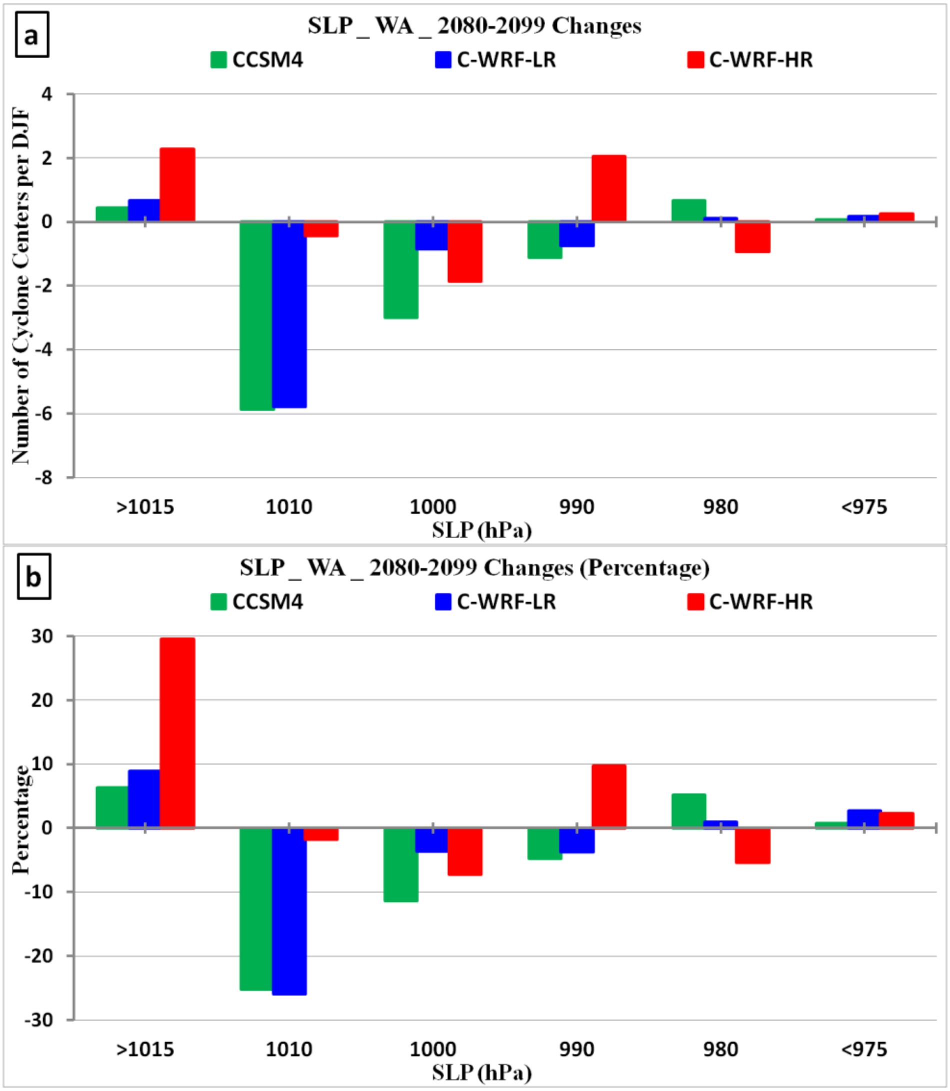

Fig. 5.28: Same as Fig. 5.27, but for the cyclone centers within the WA region.

Accompanied with the increase in the cyclone frequency along the East Coast, the density of rapid deepening rate (4 hPa/6h) also increases by 10-40% over northeast of U.S. Northeast in the CCSM (Fig. 5.29c). There is a similar increase in the density of rapid deepening rate over the same region for the C-WRF-LR (Fig. 5.29b). Meanwhile, the increase in the C-WRF-HR is stronger (20-50%) and expands to the western Atlantic and further south along the East Coast (Fig. 5.29c).

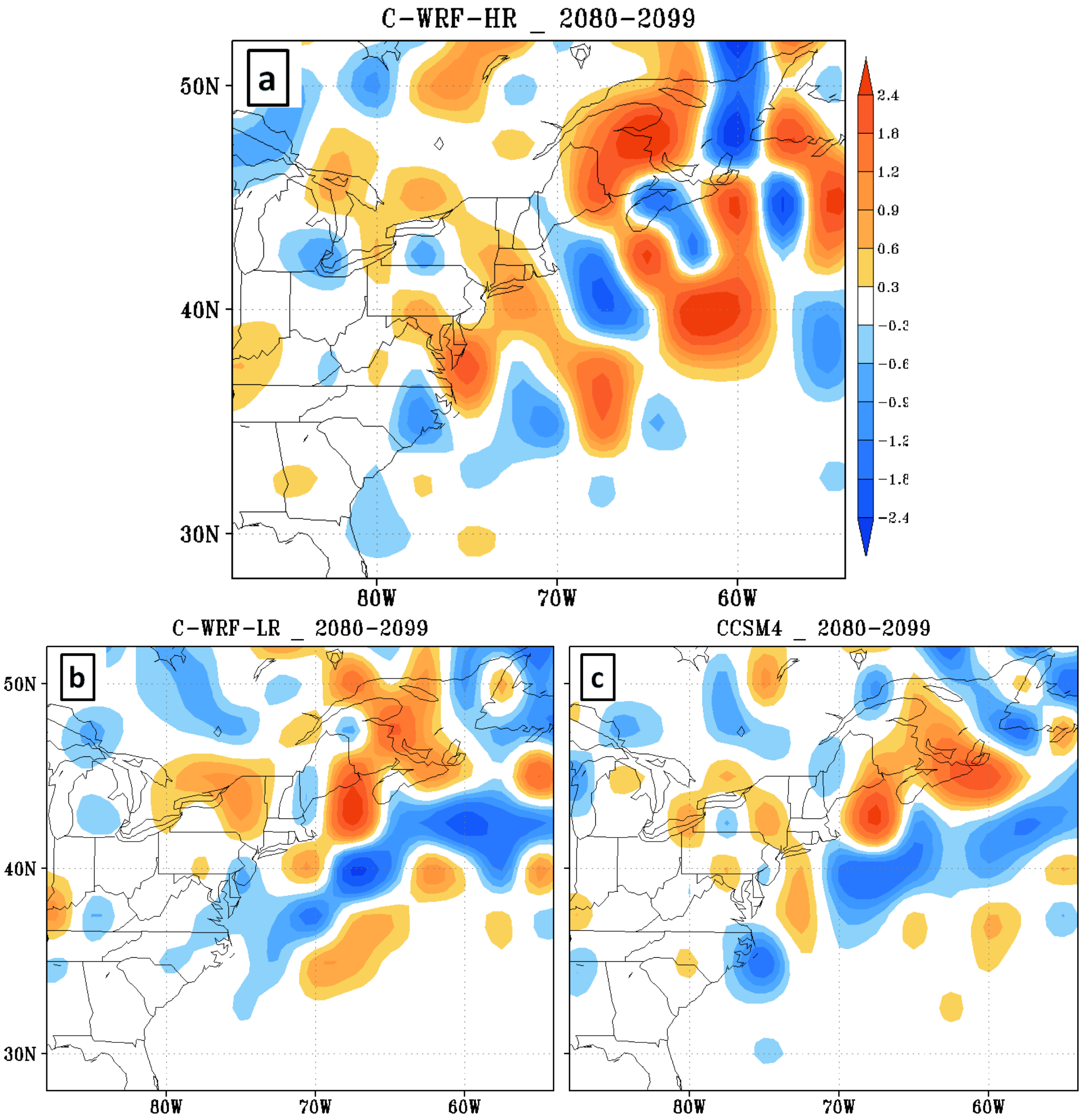

Fig. 5.29: Same as Fig. 5.28, but for the rapid deepening rate (> 4 hPa/6h, cases per 5 winters per 50,000km^2).

In the distribution of cyclone deepening rate for the cyclones within the ECL region (Fig. 5.30), there are increases in both of the -2 and -4 hPa/6h bins, and the increase for the C-WRF-LR (20-40%) is slightly larger than the CCSM4 (15-35%) but smaller than the C-WRF-HR (25-

55%). For the deepening more than -5hPa/6h bin, the C-WRF-HR has a ~20% increase, while the increase for the CCSM (~4%) and the C-WRF-LR (~9%) is much smaller.

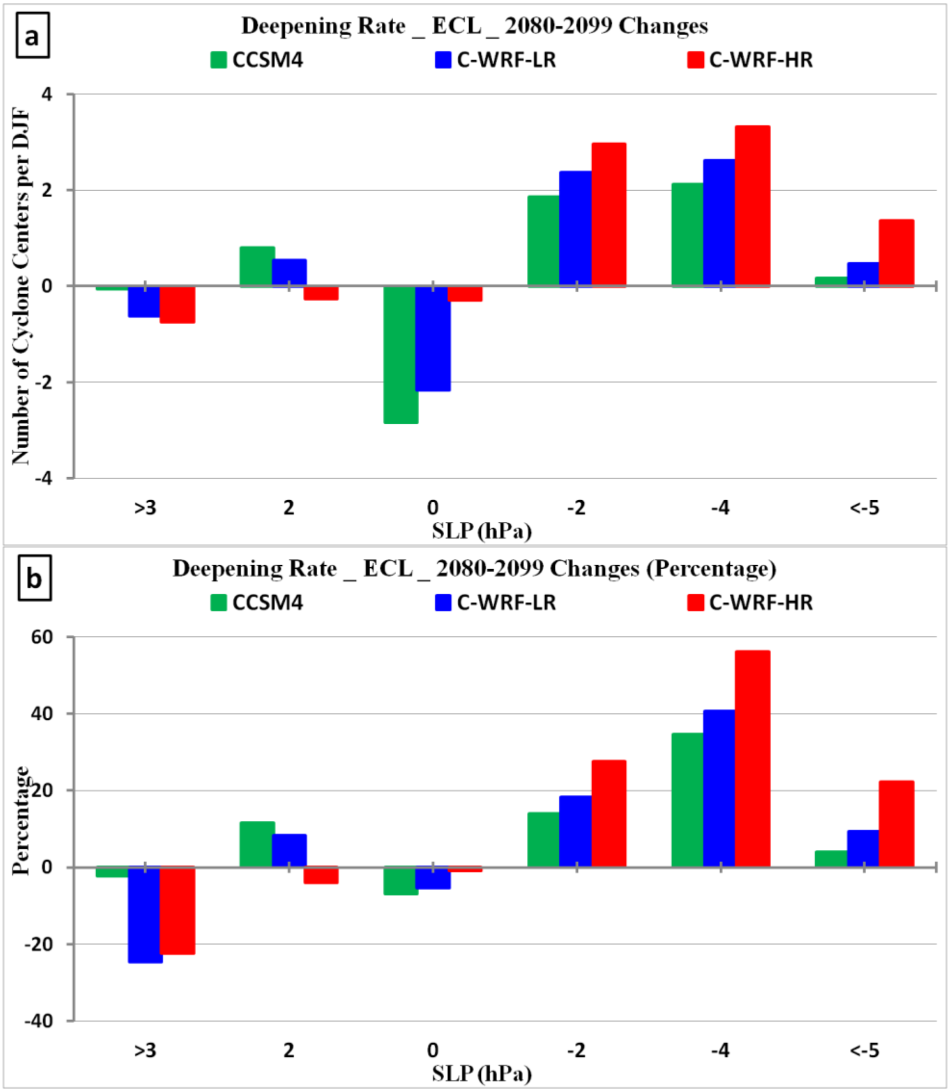

Fig. 5.30: Same as Fig. 5.27, but for the deepening rate.

In addition to the cyclone frequency, intensity distribution and deepening rate, the future changes of cyclone relative precipitation were also calculated and compared. The cyclone relative precipitation amount increases almost everywhere for all of the CCSM, C-WRF-LR and C-WRF-HR over eastern North America and the western Atlantic (Fig. 5.31). The increase over the continent (20-40%) is larger than the increase over the ocean (5-20%) in the CCSM and C-WRF-HR. The pattern of the future changes in the C-WRF-LR is similar to the CCSM and C-WRF-HR, but the increase of the mean cyclone relative precipitation is slightly smaller (5-10%).

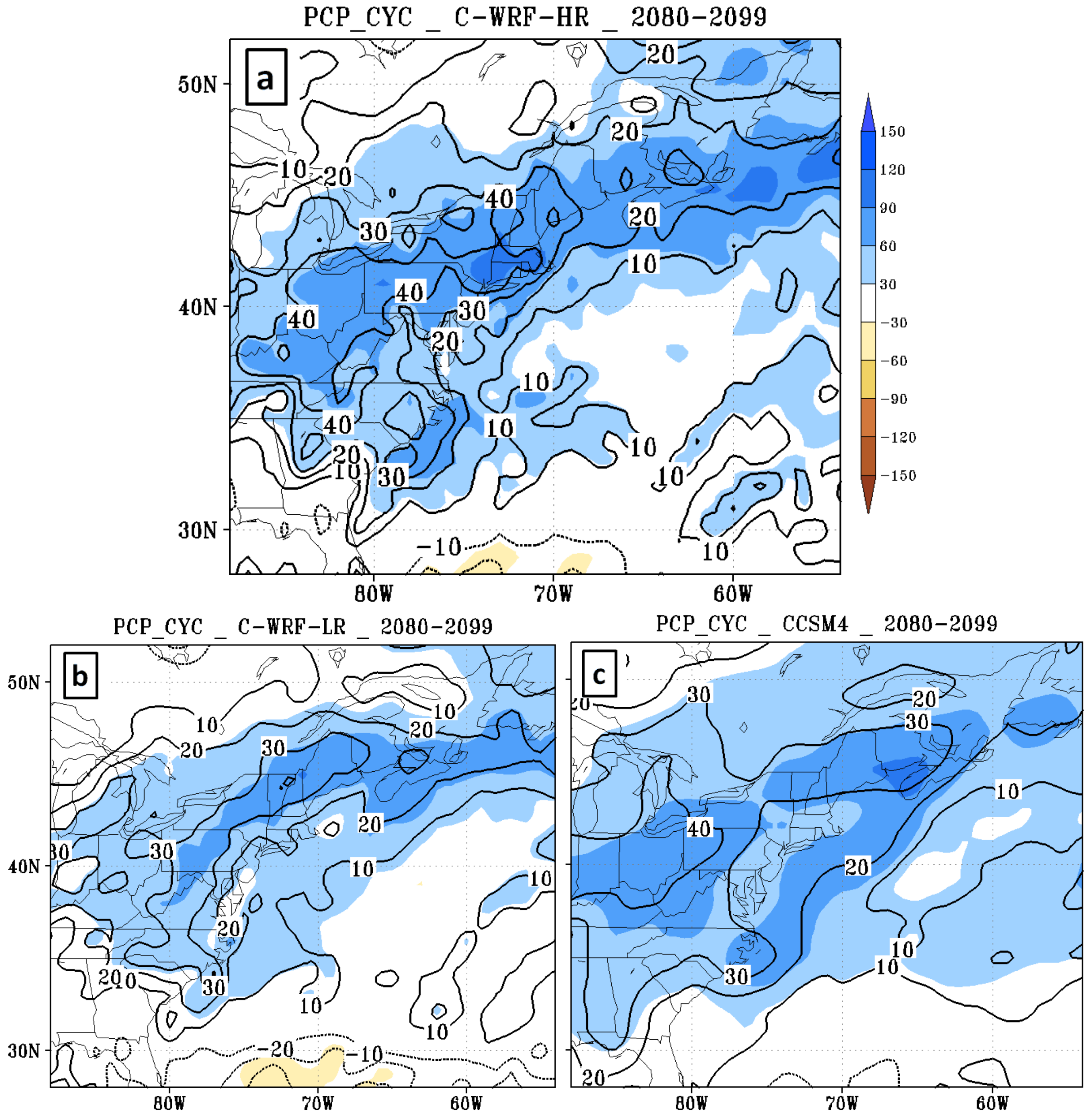

Fig. 5.31: The changes of mean cyclone relative precipitation amount (colors, mm per winter) and the percentage changes (contours, %) in the future (2080-2099) winters, for the (a) C-WRF-HR, (b) C-WRF-LR, and (c) CCSM.

Within the synoptic scale cyclone systems for the ECL region, the precipitation increase maximum (5mm/day, ~30%) for the CCSM is located over the northeast of the cyclone center, while the increase maximum in the WRF is shifted closer to the cyclone center (Fig. 5.32). The precipitation increase in C-WRF-LR is slightly smaller (~5%) than the increase in the C-WRF-HR. The precipitation increases for the cyclone centers within the ECW and WA is smaller than the ECL, especially for the cyclone centers within the WA region (~10%).

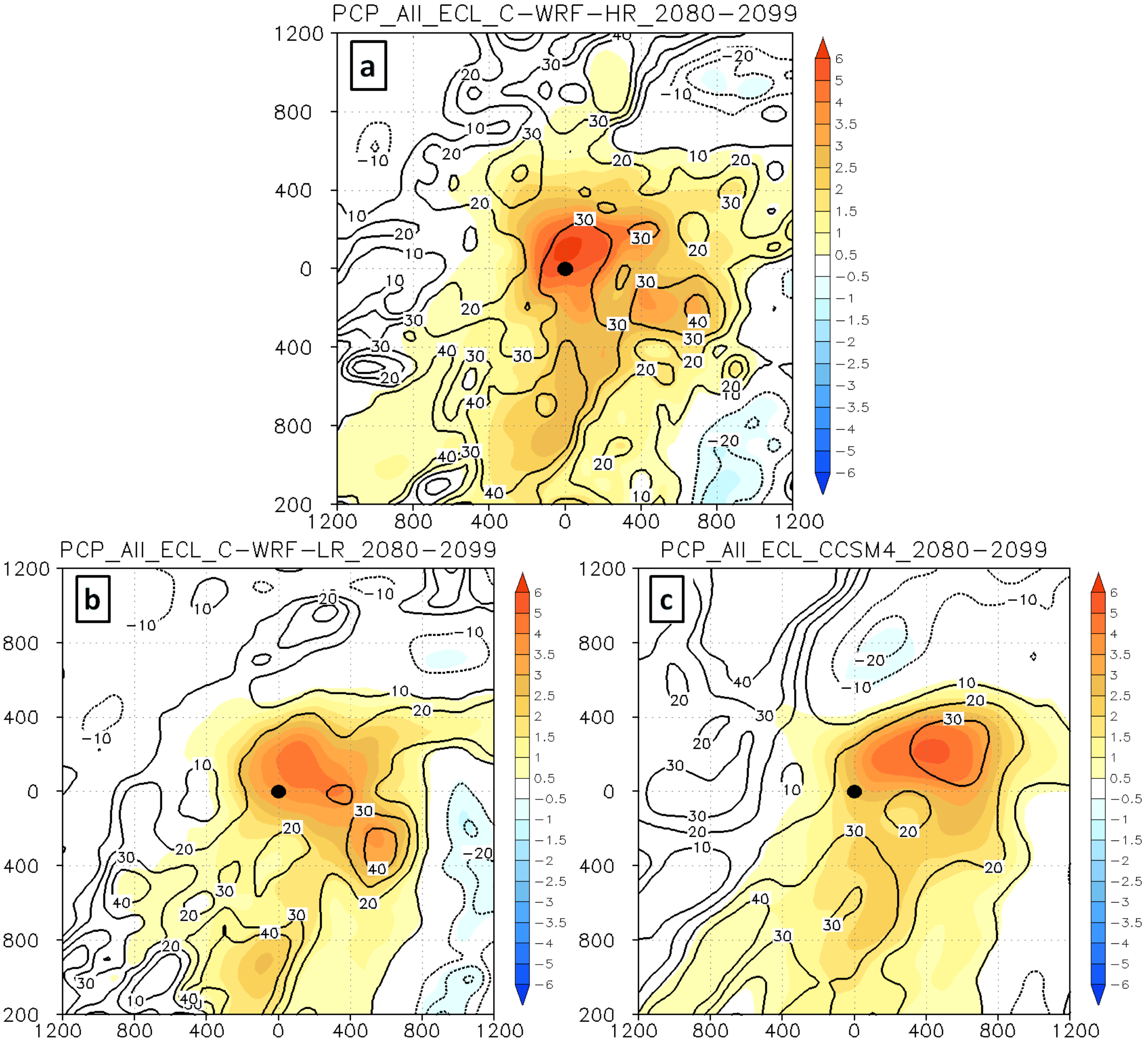

Fig. 5.32: The changes of precipitation (colors, mm/day) and the percentage (contours, %) around the cyclone centers within the ECL region in the future (2080-2099) winters for the (a) C-WRF-HR, (b) C-WRF-LR, and (c) CCSM. The black dot is the cyclone center.

The future changes of cyclone relative precipitation intensity for the ECL and the WA regions are compared (Fig. 5.33) since the precipitation changes for the cyclone centers within the ECL region are much larger than the WA region (Fig. 5.31).

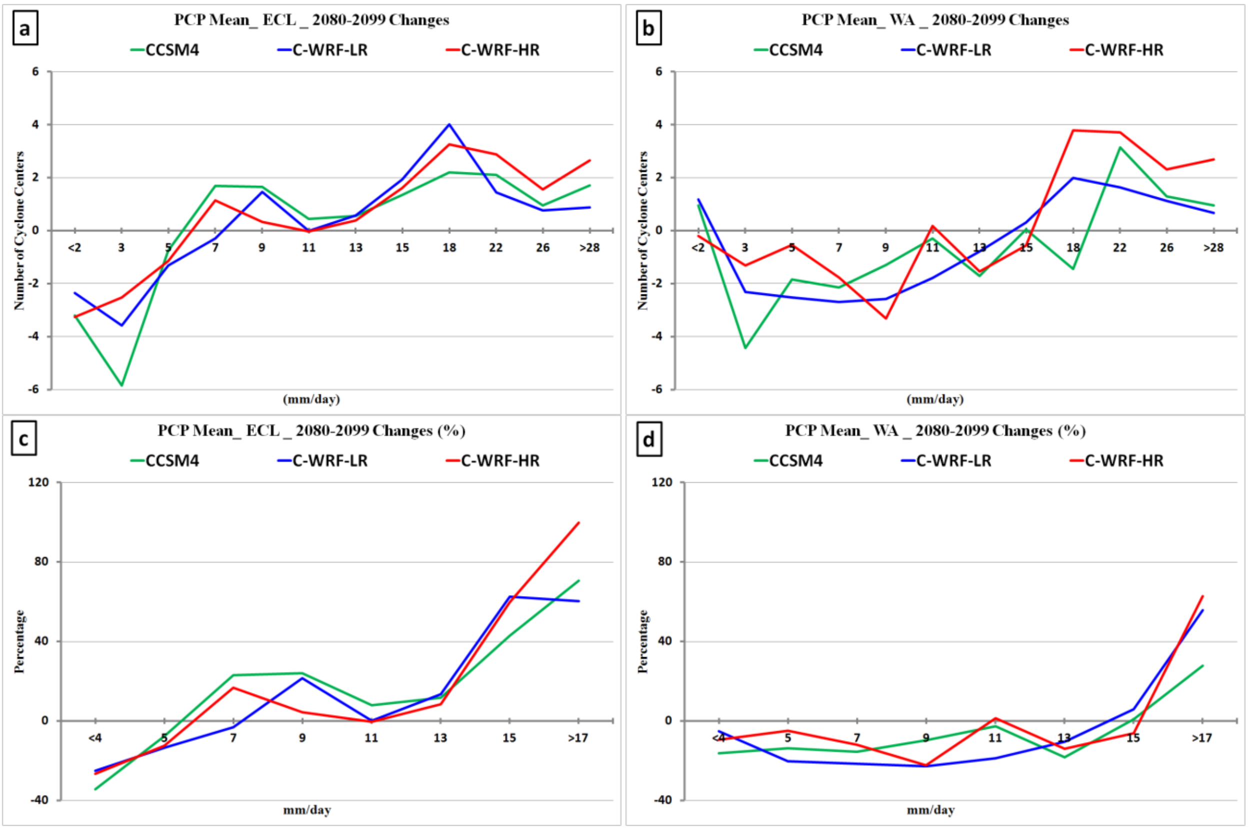

Fig. 5.33: (a) The changes of the distribution for the mean precipitation around cyclone centers (within the purple box in Fig. 2.4b) for the cyclone centers within ECL for the CCSM (green), C-WRF-LR (blue), and C-WRF-HR (red); (c) same as (a), but for the percentage changes. (b) and (d) are the same as (a) and (c), but for the cyclone centers within the WA region.

For the mean precipitation around the cyclone centers (within the purple box in Fig. 2.4b), there is a significant shift towards the heavier precipitation for the cyclone centers within the ECL region in all of the CCSM, the C-WRF-LR, and the C-WRF-HR (Fig. 5.33). There is a 10-30% decrease in the frequency of cyclone centers with the mean precipitation < 6 mm/day, while the cyclone frequency with mean precipitation > 6mm/day increases (Fig. 5.33.a). The increases for the heaviest mean precipitation (> 17 mm/day) is 60-70% for the CCSM and the C-

WRF-LR and ~100% for the C-WRF-HR (Fig. 5.33c), which indicates that there will be a large increase in the extreme precipitation events. For the cyclone centers within the WA region, the cyclone frequency for the mean precipitation > 17 mm/day increases by ~60% for the C-WRF-HR and C-WRF-LR runs and ~30% for the CCSM, while it decreases by 5-20% for the precipitation < 15 mm/day. Although the mean cyclone relative precipitation increase over the WA (~10%) region is much smaller than the East Coast region (20-40%, Fig. 5.31), there is also a significant increase in the heaviest cyclone relative precipitation (Fig. 5.33b, d) indicating more extreme precipitation events in the future.

5.2.2 Future changes of cyclones in the GFDL and the downscaled WRF

The future cyclone changes in the GFDL and its WRF runs are quite different from the CCSM and its WRF runs. In all of the GFDL, the G-WRF-LR, and the G-WRF-HR, the cyclone track density has a 10-40% decrease from the north of Gulf coast to the western Atlantic (Fig. 5.34). The decrease over the western Atlantic is slightly larger in the G-WRF-LR and the G-WRF-HR than in the GFDL. Along the East Coast and over the inland continent of eastern North America, there are some increases in the cyclone track density, but only the increase over the east of southeast Canada is statistical significant. Over most of the ECL region, the future changes are noisy and not significant in the GFDL, the G-WRF-LR and the G-WRF-HR, which is different from the track density changes in the CCSM and its WRF runs.

Although the future changes in cyclone track density along the East Coast is noisy, which is different from the significant decrease over the western Atlantic, the number of cyclone centers over the ECL region decrease (10-30%) in most of these intensity categories and slightly increase (5-10%) in the relatively weak (> 1005 hPa) cyclone centers in the G-WRF-HR and the

G-WRF-LR (Fig. 5.35). The future changes of cyclone intensity distribution for the ECW and the WA regions in the GFDL, G-WRF-LR and G-WRF-HR are similar to the changes in the ECL region, but with larger decreases (20-35%) in most of the intensity categories (not shown).

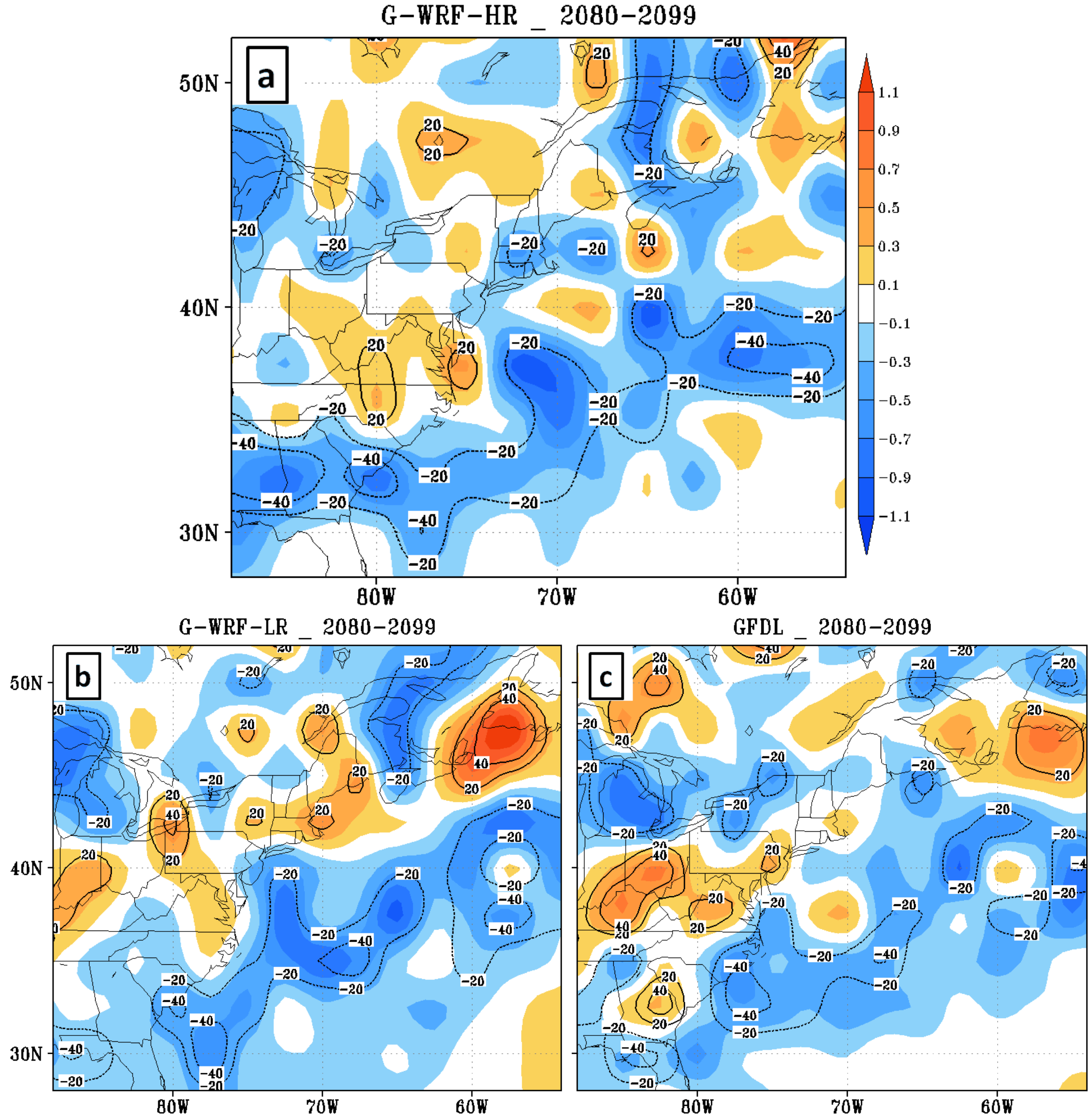

Fig. 5.34: The changes of cyclone track density (colors, per winter per 50,000km^2) and the percentage (contours) in the future (2080-2099) winters for the (a) G-WRF-HR, (b) G-WRF-LR, and (c) GFDL.

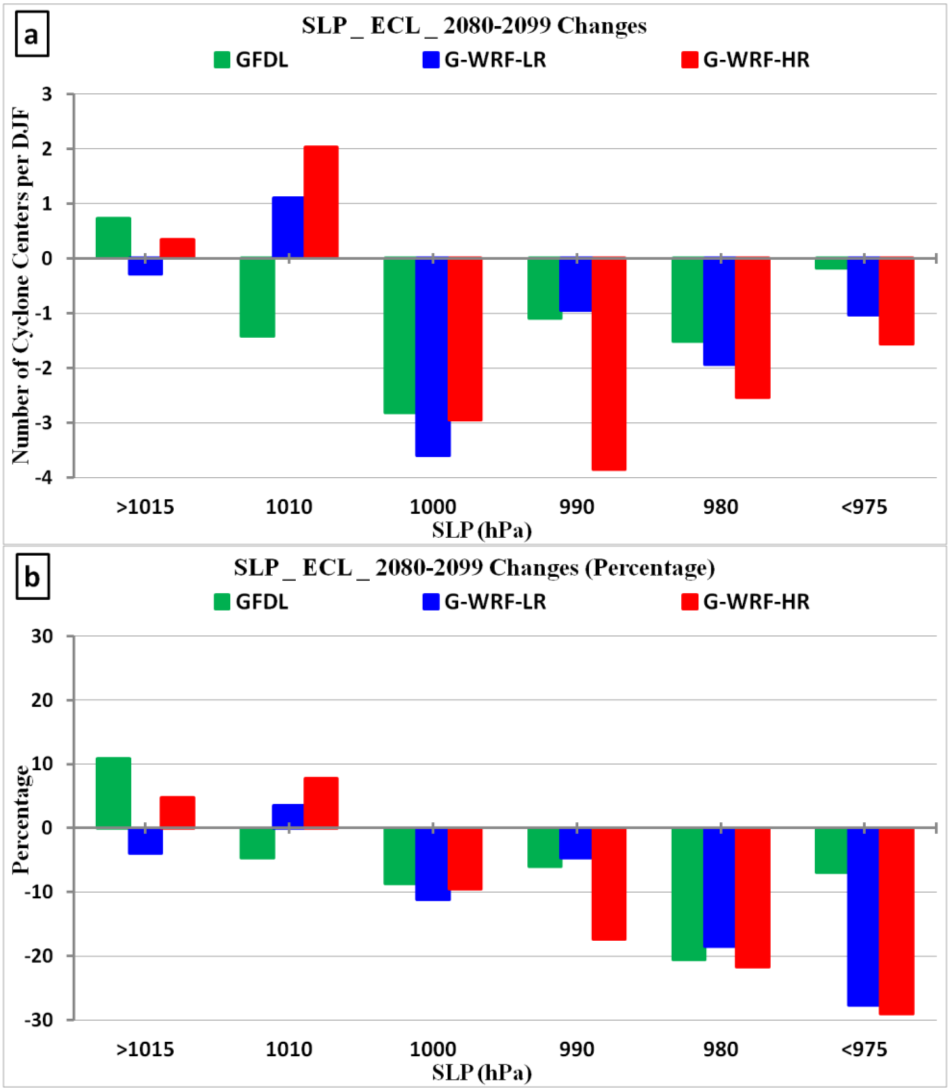

Fig. 5.35: (a) The changes of cyclone intensity distribution in the future (2080-2099) winters for the cyclone centers within the ECL region. Green is the GFDL; blue is the G-WRF-LR, and red is the G-WRF-HR. (b) same as (a), but for the percentage change.

The density of cyclone rapid deepening rate has a large decrease (10-50%) over the western Atlantic in the GFDL and the G-WRF-HR; and a relatively smaller decrease (10-40%) in the G-WRF-LR (Fig. 5.36). Over the East Coast, the change of rapid deepening rate is nearly neutral for the GFDL, and noisy for the WRF runs, with an increase (10-25%) over some small regions within the ECL for the G-WRF-HR and an increase (10-30%) over the east of U.S. Northeast and the east of southeast of Canada (Fig. 5.36).

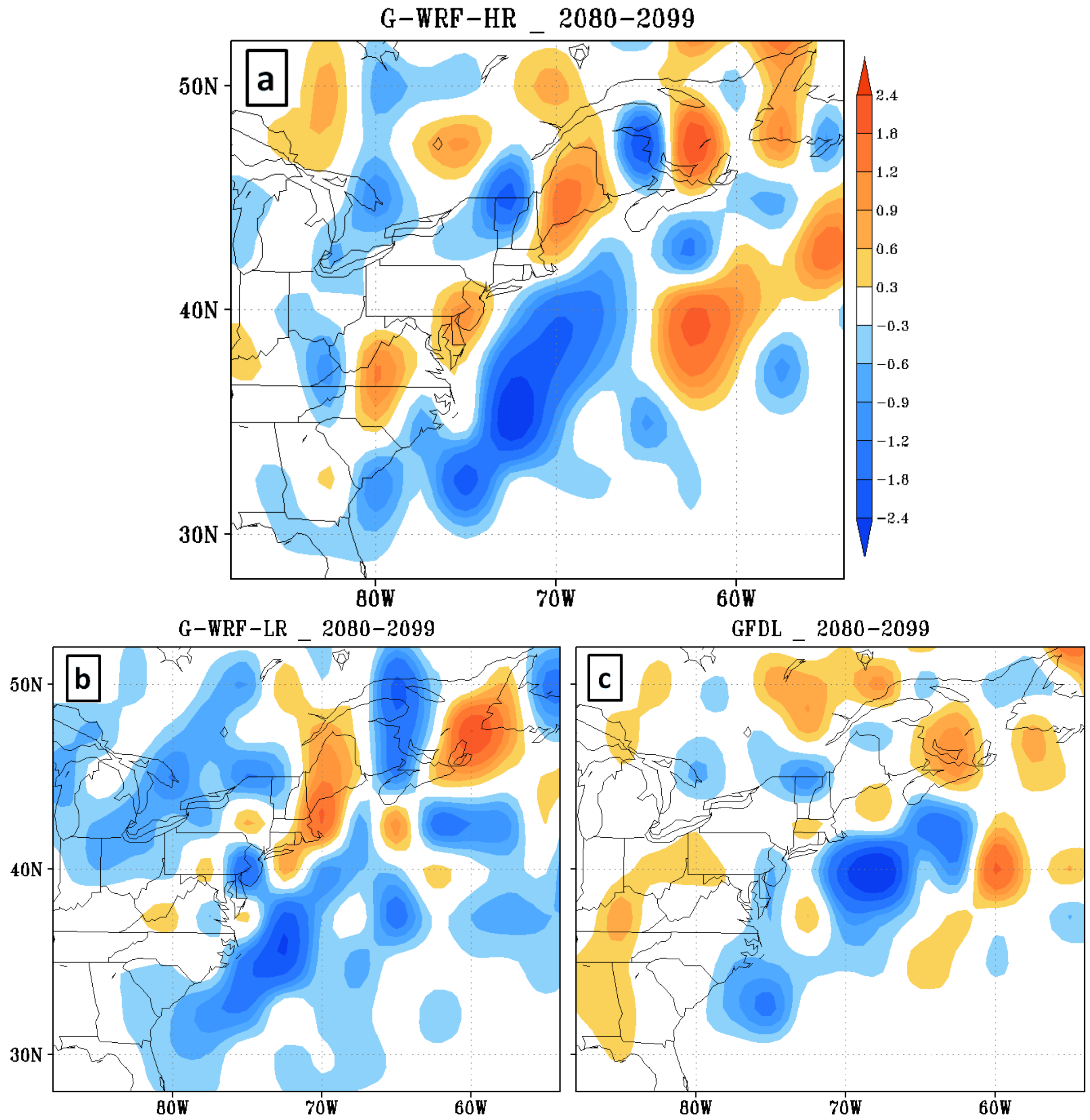

Fig. 5.36: Same as Fig. 5.34, but for the rapid deepening rate (> 4 hPa/6h, cases per 5 winters per 50,000km^2).

The distribution of the cyclone deepening rate for the GFDL and the downscaled WRF runs decreases (10-30%) at most of those deepening rate bins. However, there is a small increase (5-10%) in the -5 hPa/6h bin in both of the GFDL and its WRF runs (Fig. 5.37).

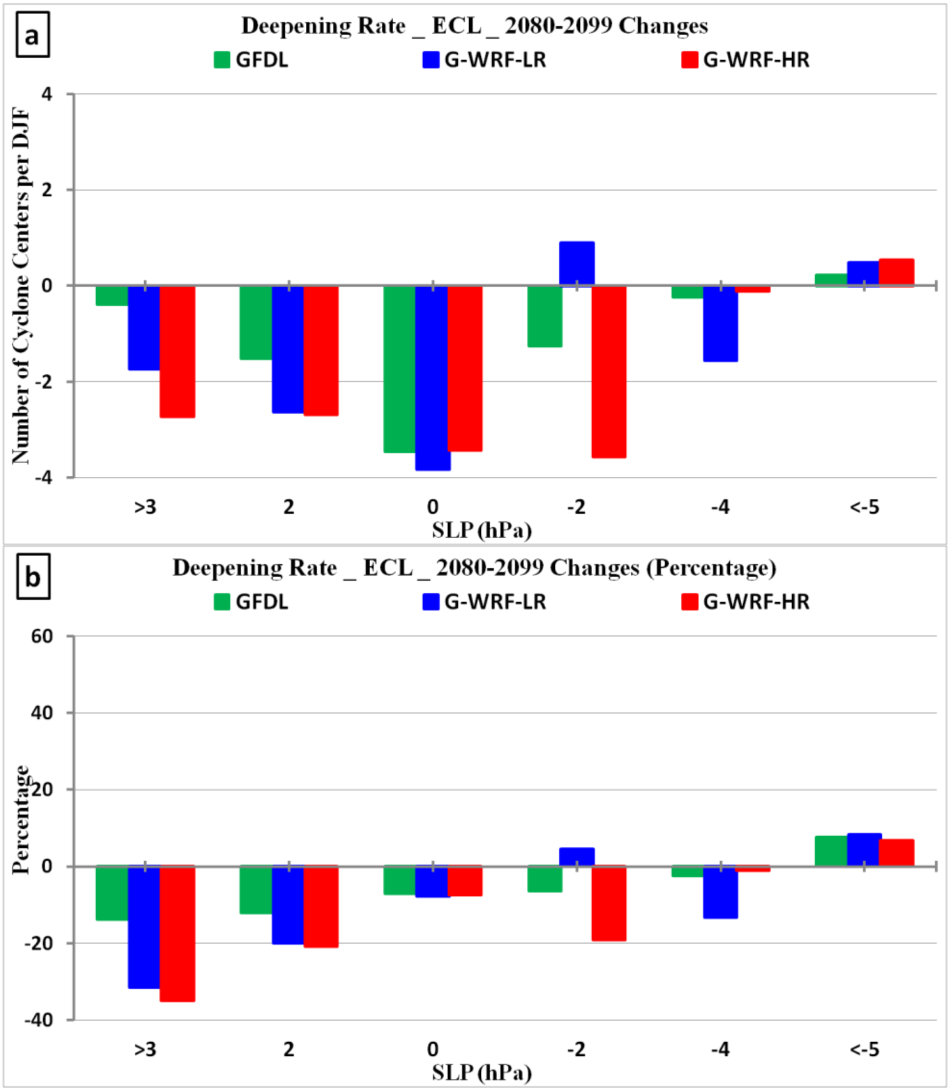

Fig. 5.37: Same as Fig. 5.35, but for the cyclone deepening rate.

The cyclone relatively precipitation rate around the cyclone center for the GFDL and the corresponding WRF runs also increases (Fig. 5.38), but much smaller than the CCSM and its WRF runs (Fig. 5.32). The precipitation increases over the precipitation maximum region (northeast of the cyclone center) are only 10-15% for the GFDL and the WRF runs. In the GFDL, the maximum of precipitation rate increase (~3.5 mm/day) is located over the northeast of the cyclone center (east of the historical precipitation maximum), and it also has a smaller increase extending to the southwest of the cyclone center (Fig. 5.38c). In the downscaled WRF (Fig.

5.38a, b), the increase amount maximum (2-3 mm/day, 20-35% over that region) is shifted to the southwest of the cyclone center, close to the southwest boundary of the historical precipitation (Fig. 5.16a, b).

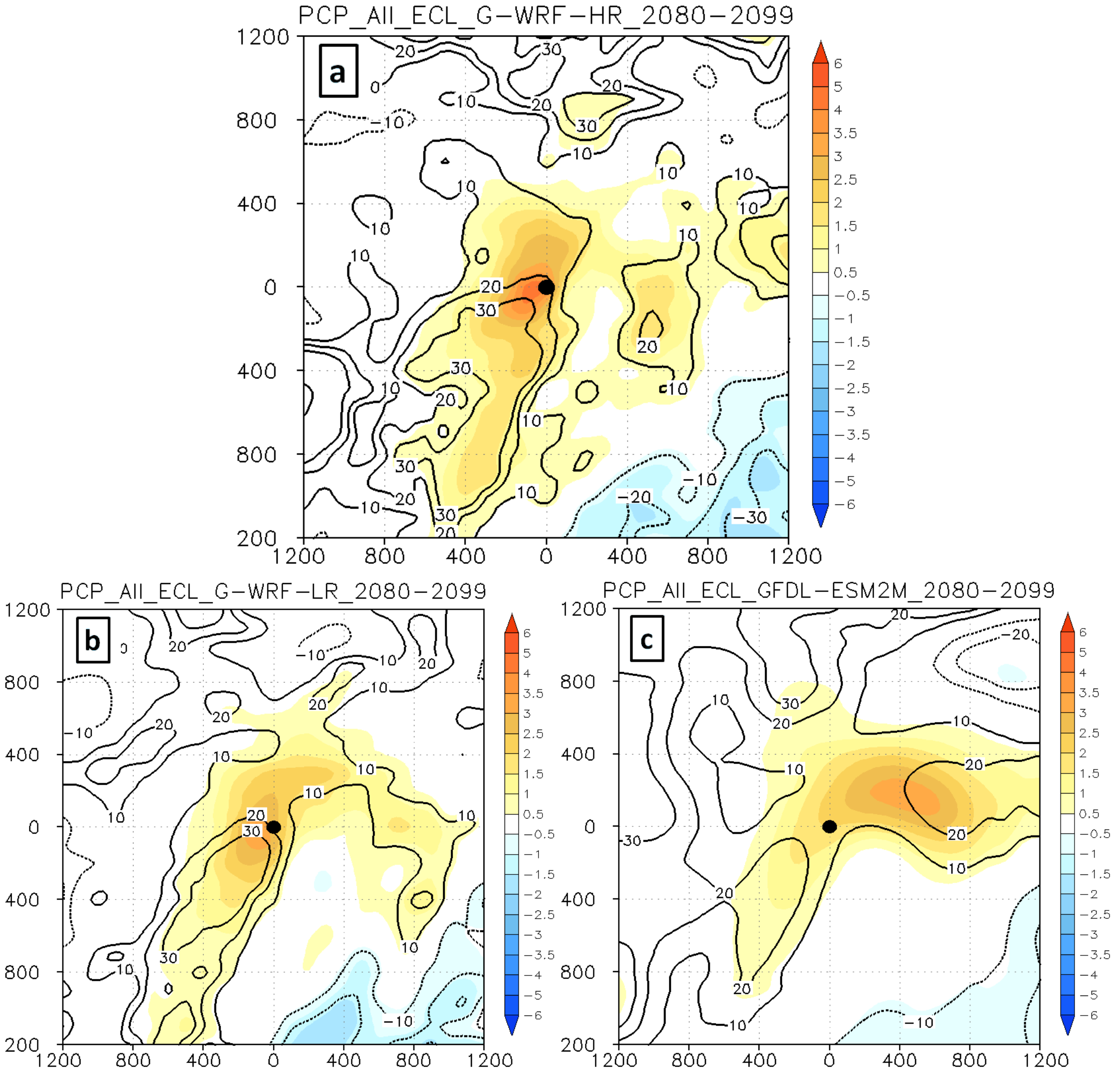

Fig. 5.38: The changes of precipitation (colors, mm/day) and the percentage (contours, %) around the cyclone centers within the ECL region in the future (2080-2099) winters for the (a) G-WRF-HR, (b) G-WRF-LR, and (c) GFDL. The black dot is the cyclone center.

Figure 5.39 shows the cyclone relative precipitation rate (normalized to each cyclone center) over the earth-related map. There are 10-35% increases in the cyclone relative precipitation rate over the North America continent > 35°N and over the East Coast in the GFDL and the G-WRF-HR, while the increase in the G-WRF-LR (10-25%) is a little smaller over those regions (Fig. 5.39). Meanwhile, there are 10-25% decreases in the precipitation rate from the Gulf of Mexico to the western Atlantic; and the decrease in the WRF runs is slightly larger (~5%) than in the GFDL.

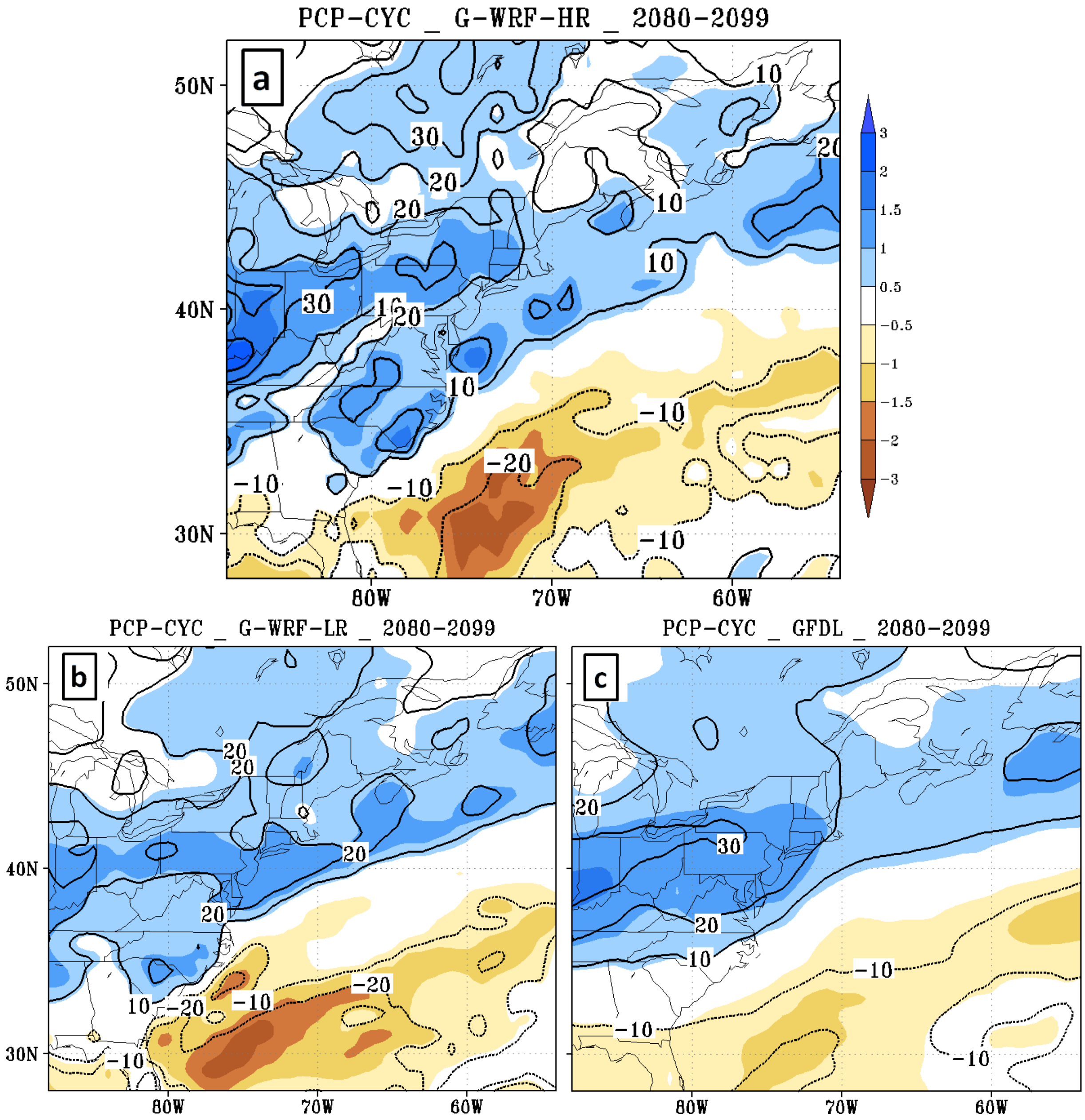

Fig. 5.39: The changes of mean cyclone relative precipitation rate (colors, mm/day, normalized to each cyclone) and the percentage changes (contours, %) in the future (2080-2099) winters, for the (a) G-WRF-HR, (b) G-WRF-LR, and (c) GFDL.

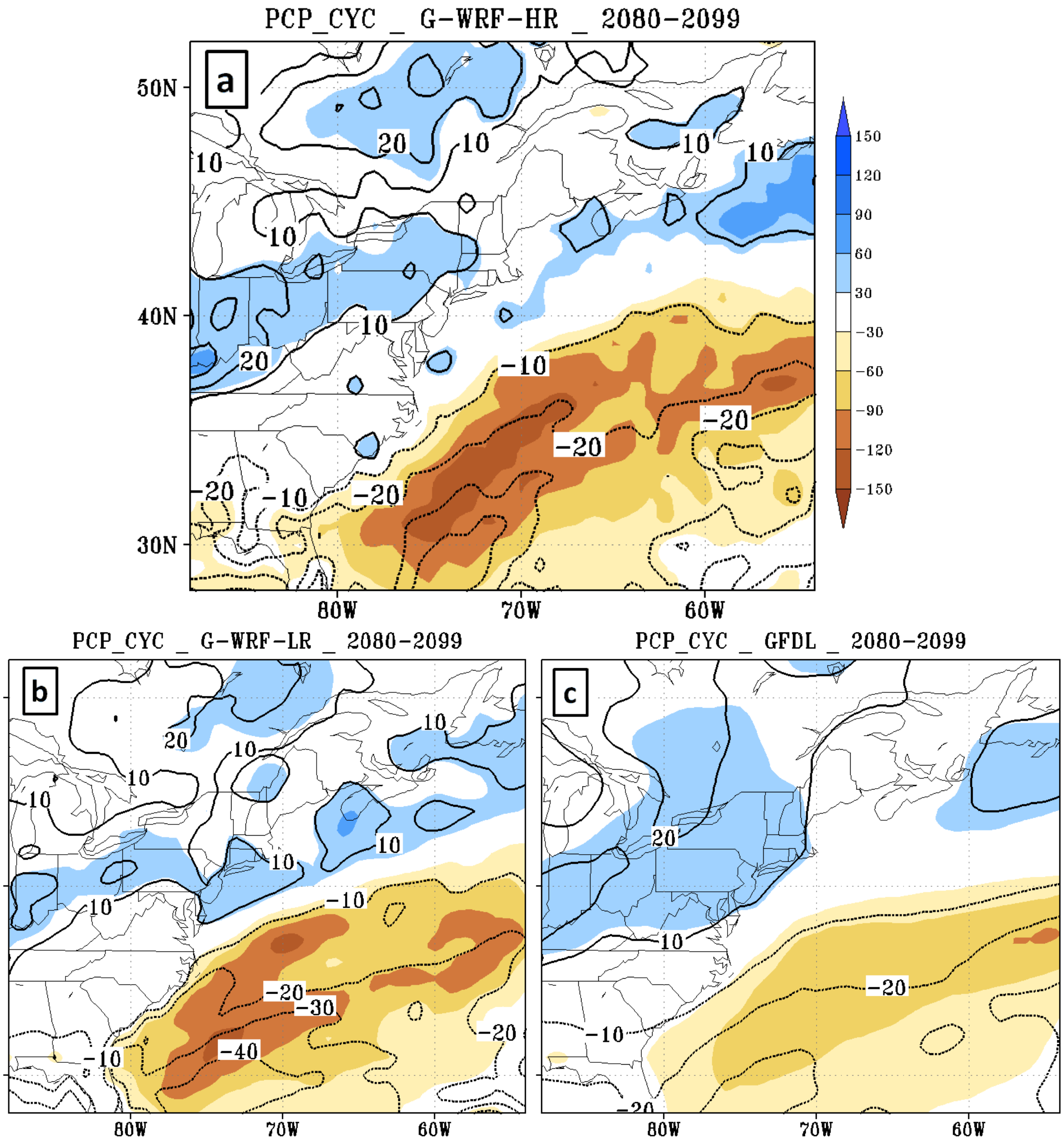

Fig. 5.40: The changes of mean cyclone relative precipitation amount (colors, mm per winter) and the percentage changes (contours, %) in the future (2080-2099) winters, for the (a) G-WRF-HR, (b) G-WRF-LR, and (c) GFDL.

The winter mean cyclone relative precipitation amount increases 10-20% over North America continent > 40°N; but over the Gulf of Mexico and the western Atlantic it decreases 10-40% in the WRF runs, and 10-30% in the GFDL (Fig. 5.40). The future percentage increase in cyclone relative precipitation amount over the continent and the East Coast is smaller than the precipitation rate increase since it is inhibited by the decrease of cyclone frequency. Meanwhile, the decrease of precipitation over the ocean is enhanced by the cyclone decrease.

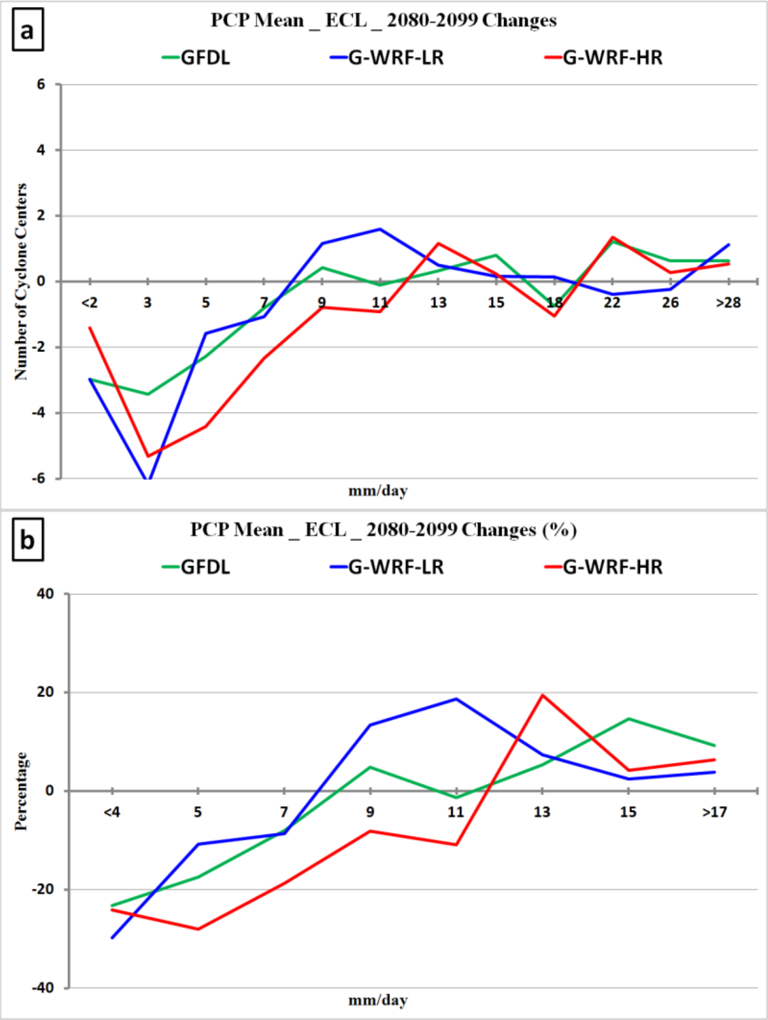

Fig. 5.41: (a) The changes of the distribution for the mean precipitation around cyclone centers (within the purple box in Fig. 2.4b) for the cyclone centers within ECL for the GFDL (green), G-WRF-LR (blue), and G-WRF-HR (red); (b) same as (a), but for the percentage changes.

In addition to the mean spatial precipitation fields, the mean precipitation rate around the cyclone centers was also calculated. There is a shift towards the heavy precipitation similar in the CCSM and its WRF runs, but the increase for the relative heavy precipitation (> 10mm/day) is small (5-20%) for the GFDL and the corresponding WRF runs (Fig. 5.41).

5.2.3 Physical processes responsible for the different future changes

There are many differences for the future changes of extratropical cyclones over eastern North America and the western Atlantic in those model projections described in Section 5.2.1 and 5.2.2. Along the East Coast, the cyclone frequency and deepening rate increase in the CCSM, C-WRF-LR, and C-WRF-HR, but do not have significant change or even decrease in the GFDL, G-WRF-LR, and G-WRF-HR. Meanwhile, the cyclone frequency and deepening rate decreases in all models for the WA region. Comparing the CCSM and the WRF runs forced by the CCSM, the C-WRF-HR has larger increase in the cyclone frequency, deepening rate, extremely heavy precipitation (Fig. 5.33a, c), and extremely deep cyclones (Fig. 5.27) over the East Coast. This section focuses on the physical process responsible for those differences.

a. *The different future changes in the C-WRF-HR and G-WRF-HR*

In the C-WRF-HR, the cyclogenesis increases 1.7 (~11%) cyclones per winter within the EC (ECL+ECW) region and does not have significant change within the WA, while the number of cyclones from the west, especially from the Alberta Clipper, decreases by 1.3 cyclones (~10%). Meanwhile, the total number of cyclones within the ECWA region only has a small increase (~0.5 cyclone per winter). Therefore, the cyclone frequency increase over the EC region is mainly from the increase in the cyclogenesis over the EC and the shift of the cyclone tracks from the WA to the EC, since the cyclone frequency over the WA decreases while the total cyclone numbers within the ECWA doesn't have significant change.

In the G-WRF-HR, the cyclogenesis decreases 1.1 (~10%) cyclones per winter within the EC region and decreases 0.5 within the WA, while the cyclones from the west also decreases by 1.2 (~10%) cyclones per winter. The total cyclone numbers within the ECWA region decreases by 2.9 (~8%) cyclones per winter. Meanwhile, the cyclone tracks are also shifted from the western Atlantic to the EC slightly.

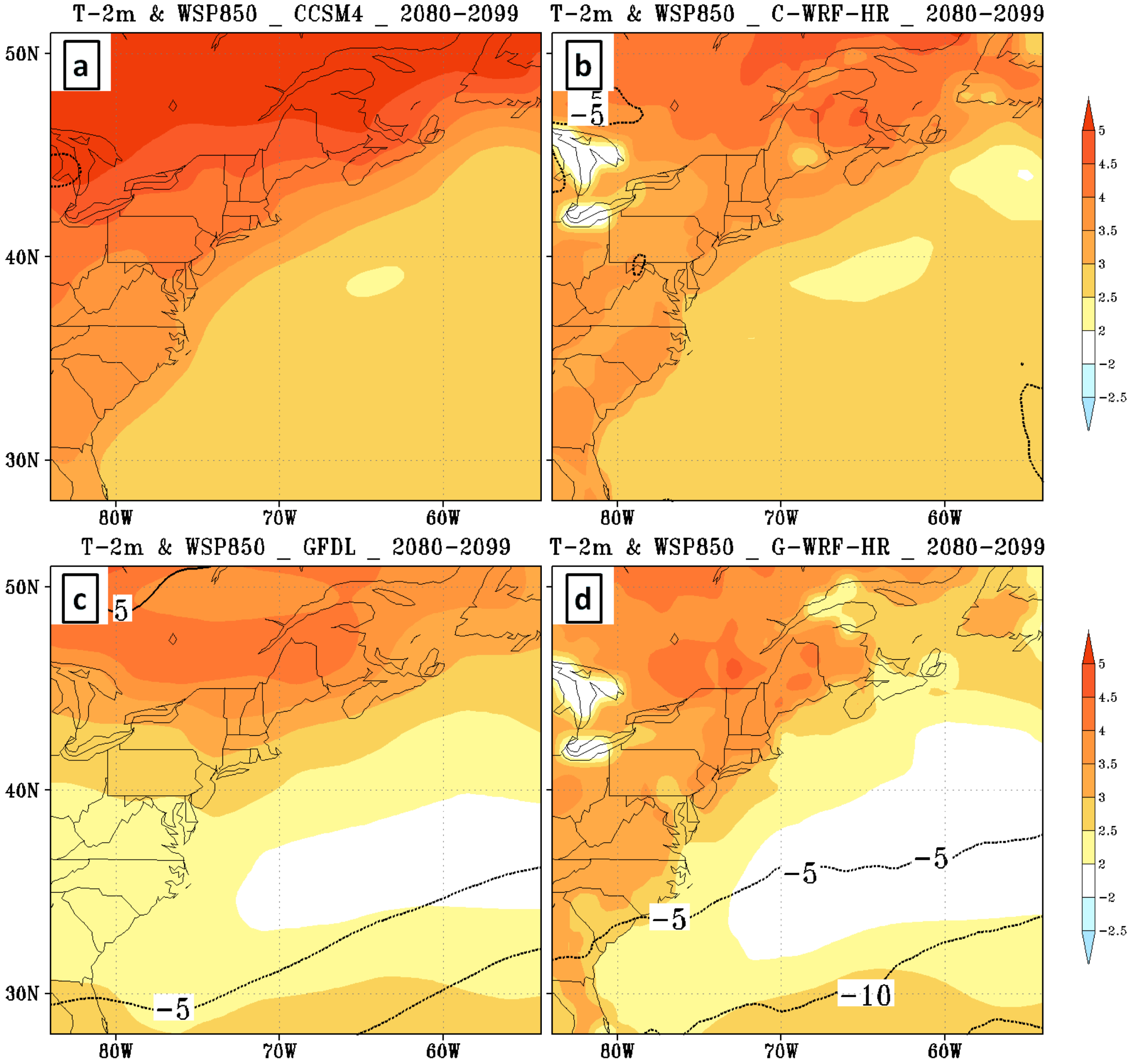

Fig. 5.42: The changes of surface temperature (colors, K) and the percentage changes of 850hPa wind speed (contours, %) in the future (2080-2099) winters, for the (a) CCSM, (b) C-WRF-HT, (c) GFDL, and (d) G-WRF-HR.

In order to investigate the reasons for those cyclone changes, the future changes of the baroclinicity, upper level jet, upper level PV, and the diabatic contribution are compared between the C-WRF-HR and G-WRF-HR, as well as the ECL and the WA regions.

First of all, the future changes of the surface (2m) temperature in the CCSM and the GFDL are compared. The surface temperature increase in the CCSM is 1-2 K larger over the eastern North America and ~1 K larger over the western Atlantic than the GFDL (Fig. 5.42). The surface temperature increase over the ocean in the downscaled WRF is dominated by the original GCM since the WRF are forced by the SST from the corresponding GCM. Comparing the future changes of the surface temperature in the C-WRF-HR and the G-WRF-HR, the increase in the C-WRF-HR is 0.8-1.4 K larger over the ocean and 0.6-1.2 K larger over the continent than the G-WRF-HR. The 850hPa temperature changes are similar to the surface, but the increase is slightly smaller (not shown).

Because the surface temperature increase over the land is larger than over the ocean, the surface temperature gradient along the East Coast decreases in all model runs. For example, the surface temperature gradient decreases ~1 K/1000km (5-10%) in the C-WRF-HR, and it decreases 1.5-2.5 K/1000km (~10%) in the G-WRF-HR over the East Coast (Fig. 5.43). However, in the C-WRF-HR the decrease maximum over the coast of U.S. Northeast is more offshore and located over the southeast of the historical surface temperature gradient maximum region (> 15 K/1000km, red contour in Fig. 5.43). In the G-WRF-HR, the decrease maximum over the U.S. Northeast is just along the coastline, over the same region as the historical surface temperature gradient maximum (red contour in Fig. 5.43). Meanwhile, the decrease in the G-WRF-HR (1.5-2.5 K/1000km) is larger than the C-WRF-HR (~1 K/1000km). The distribution of future changes in the 850hPa temperature gradient is similar with the surface changes, but the decrease (5-10%) at 850hPa is smaller than the surface temperature gradient decrease in both the C-WRF-HR and the G-WRF-HR.

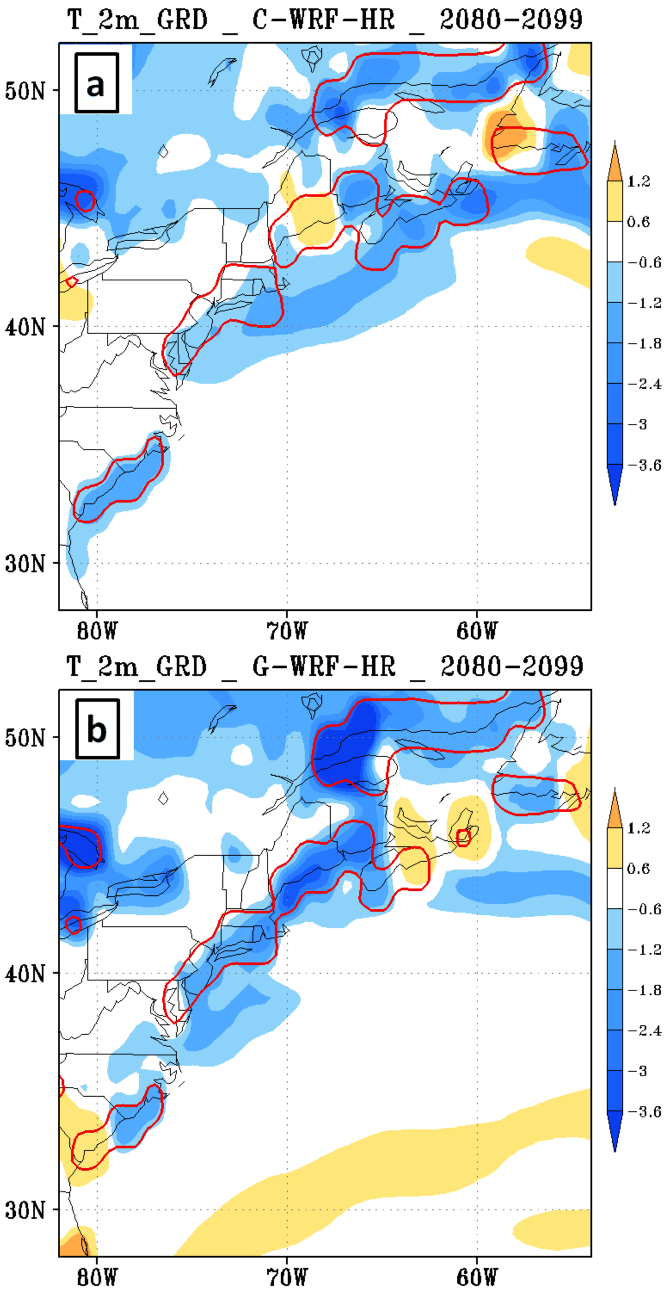

Fig. 5.43: The changes of mean surface (2m) temperature gradient (colors, K/1000km) for the future winters, the red contours are the maximum of surface temperature gradient (> 15 K/1000km) in historical winters.

In addition to the surface and low level temperature gradient, the 850-500 hPa Eady growth rate is also calculated to examine the baroclinicity at that level. For the ECL cyclone centers, the Eady growth rate decreases by 5-10% over the north and the southwest of the cyclone center for both the C-WRF-HR and G-WRF-HR (Fig. 5.44a, b); and the decreases are far away from the cyclone center in the C-WRF-HR. However, for the WA cyclone centers, the Eady growth rate decreases by 5-15% around the cyclone center and the northeast of the center in both of the C-WRF-HR and G-WRF-HR (Fig. 5.44c, d).

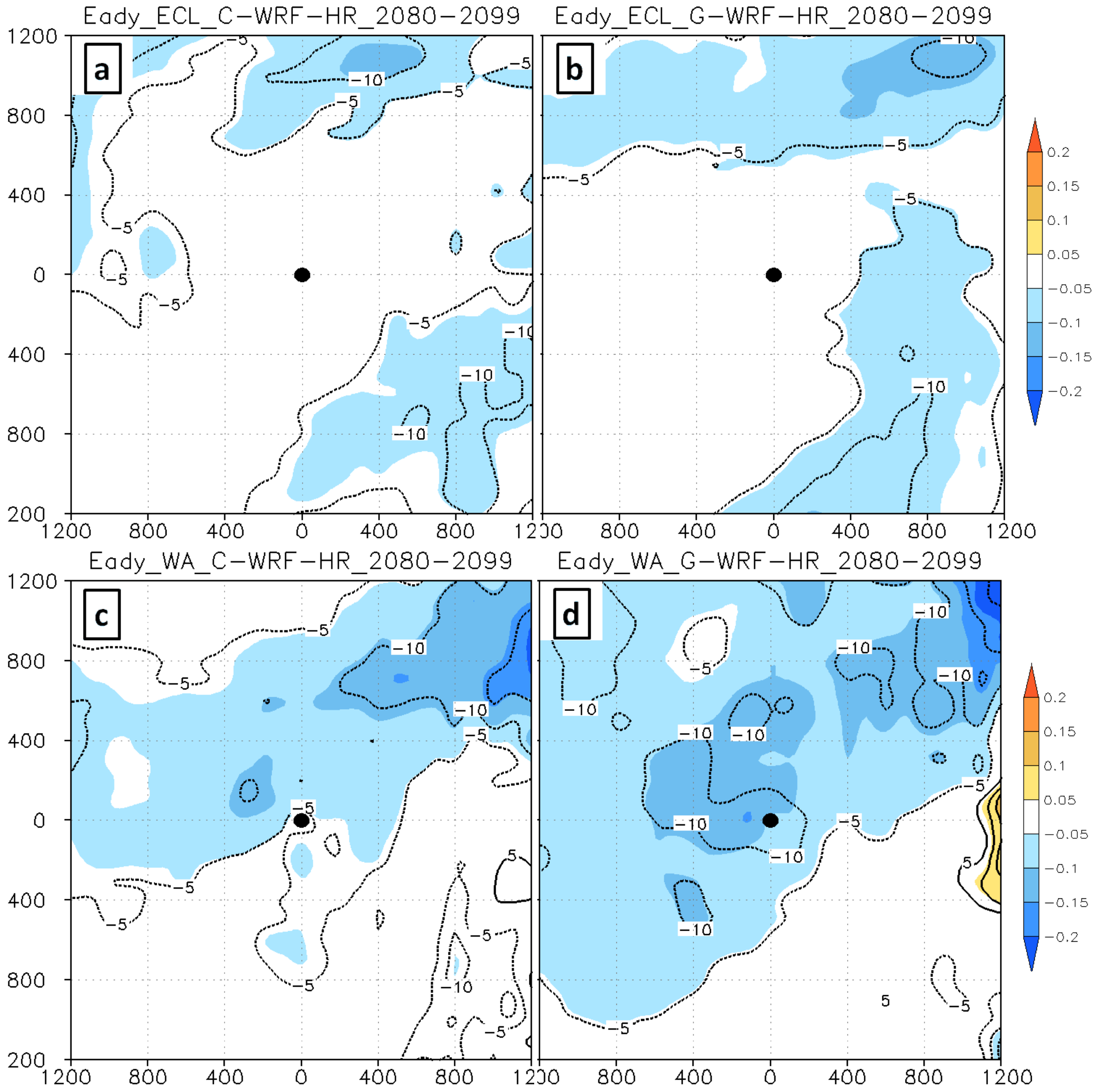

Fig. 5.44: The future changes of composite Eady growth rate (colors, per day) at 850-500hPa and the percentage changes (contours) for the cyclone centers within the (a) ECL and (c) WA region in the C-WRF-HR; (b) and (d) are the same as (a) and (c) but for the G-WRF-HR.

The future changes of upper level jet are also examined since it has impacts to the storm track as the baroclinicity. In the C-WRF-HR, the future winter mean 250hPa wind speed has a significant shift towards the north (Fig. 5.45a). The wind speed becomes weaker over most of the WA region, while the jet becomes stronger (0.5-2.0 m/s) along the East Cost. However, in the G-WRF-HR, the 250hPa wind speed increases (~0.5 m/s) almost everywhere over this region; and the increase maximum (> 1m/s) is located at the U.S. Northeast, which is far away from the jet in this model (Fig. 5.45.b).

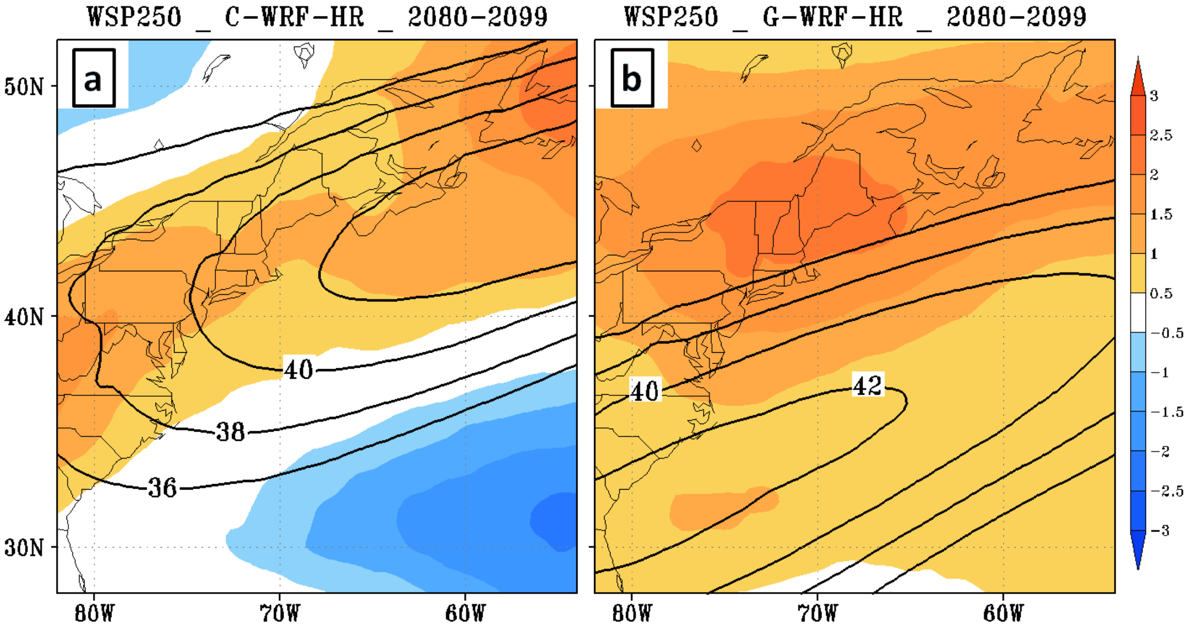

Fig. 5.45: The changes of 250 hPa wind speed (colors, m/s) for the future winters and the historical mean 250 hPa wind speed (contours, m/s) for the (a) C-WRF-HR and (b) G-WRF-HR.

The future changes of the winter mean upper level (200-300 hPa) PV decreases over the western Atlantic by 5-15% (0.3-0.6 PVU) for the C-WRF-HR and 5-10% (~0.4 PVU) for the G-WRF-HR (Fig. 5.46). That decrease is related to the decrease of static stability at the tropopause and the lower stratosphere since the mean temperature increase maximum is at 200-300 hPa over the low latitudes, while the temperature increase maximum over the North Hemisphere high latitudes is over the continent and Arctic region at surface (IPCC Report 5).

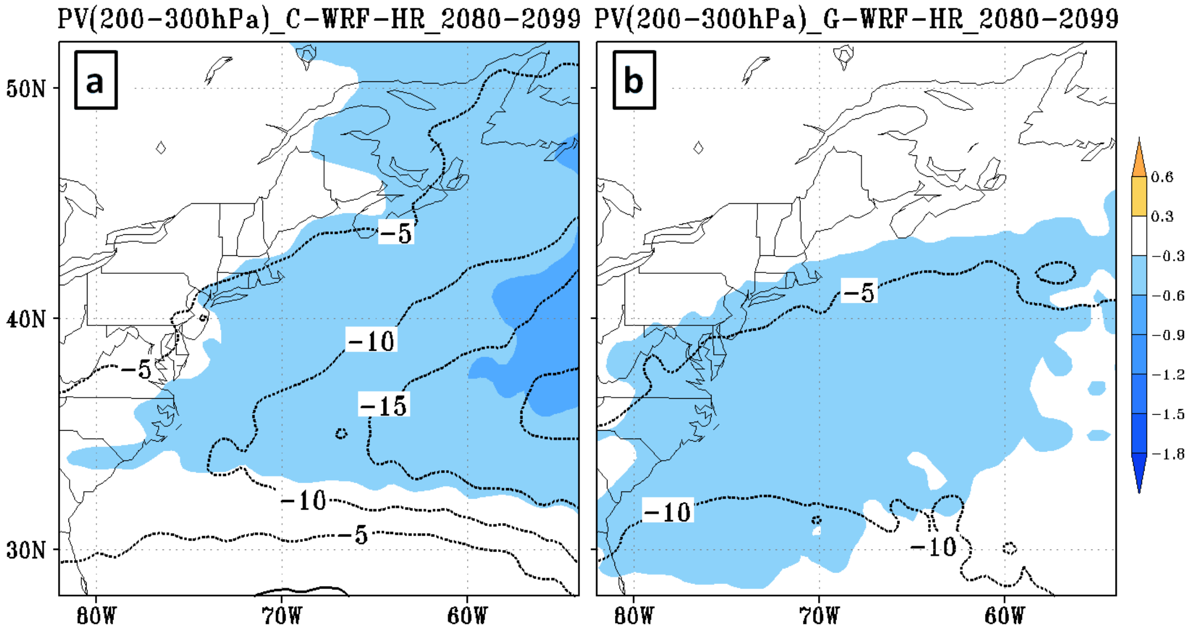

Fig. 5.46: The changes of 200-300 hPa PV (colors, PVU) in the future winters and the percentage changes (contours) for the (a) C-WRF-HR and (b) G-WRF-HR.

In addition to the baroclinicity, upper level jet, and upper level PV, the increasing latent heat release from heavier precipitation becomes more important to the cyclogenesis and developing. The cyclone relative precipitation change in the C-WRF-HR (10-25%) is larger than the G-WRF-HR (~10%) around the cyclone centers within the EC region (Fig. 5.47). The moisture content (950-250hPa) percentage increase in the C-WRF-HR is 5-10% larger than the G-WRF-HR (not shown) over the EC region while the increase of the surface temperature in the C-WRF-HR is 0.6-1.5K larger, which is consistent with the Clausius–Clapeyron relation (~7% increase in moisture per K temperature increase). The moisture percentage increase over the continent is larger (5~25%) than over the ocean since the temperature increase over the land is larger than over the ocean for both the C-WRF-HR and G-WRF-HR. Meanwhile, similar with the moist static stability (850-500hPa) changes in CMIP5 models described in Section 4.3.3, the stability increases over the western Atlantic and decrease over the North America at relatively high latitudes. The difference is that the stability decreases over most regions of eastern North

America slightly (~5%) in C-WRF-HR, and decrease only over the continent > 45°N in G-WRF-HR (not shown). As a result, the future stability changes are favorable to the precipitation increase over most of the EC region and unfavorable to the precipitation increase over the WA region in C-WRF-HR, while the stability increase inhibit the precipitation increase over most region of the ECWA in the G-WRF-HR. The stronger upper level jet (Fig. 5.45) in both models is favorable to the upward motion over the EC region (so precipitation), especially in the C-WRF-HR. Therefore, the cyclone relative precipitation increase for the EC cyclones in the C-WRF-HR (10-25%) is larger than the G-WRF-HR (~10%) (Fig. 5.47); and the precipitation increase over the EC region (10-25% in C-WRF-HR) is larger than the WA region (~10% in C-WRF-HR) (not shown).

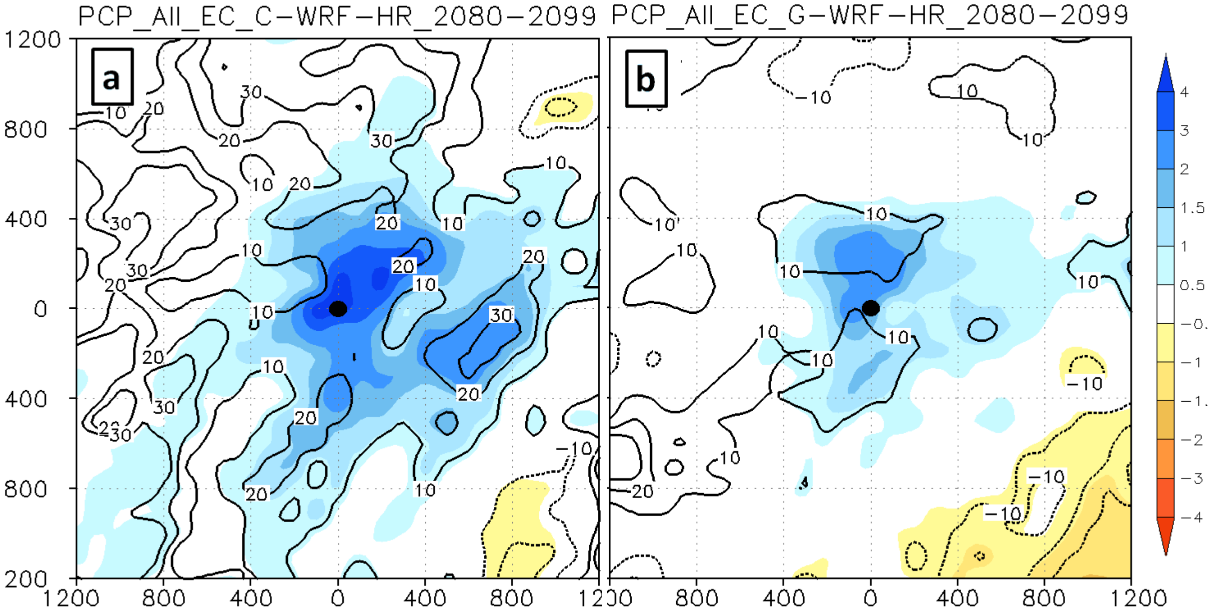

Fig. 5.47: Same as Fig. 5.44, but for the precipitation (mm/day) around the EC cyclone centers.

The larger increases in precipitation around the EC cyclone centers in the C-WRF-HR bring more latent heat release than the G-WRF-HR. The DPV around the EC cyclone centers increases by 5-15% in the C-WRF-HR, and only ~5% in the G-WRF-HR (Fig. 5.48).

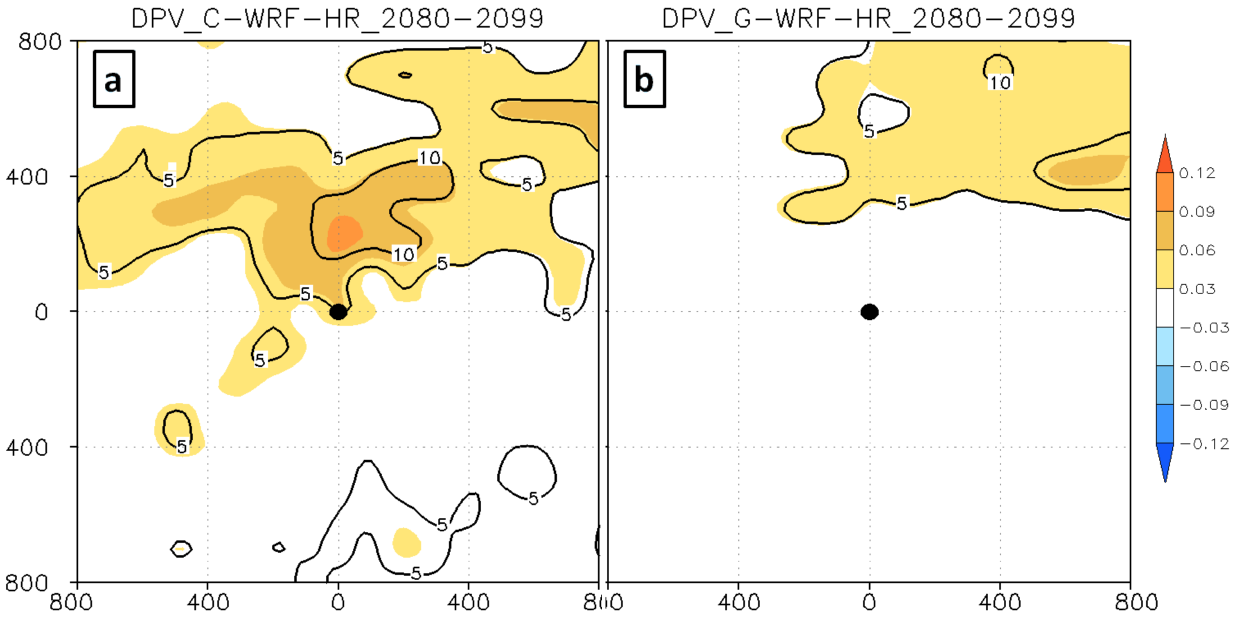

Fig. 5.48: Same as Fig. 5.47, but for the DPV (PVU).

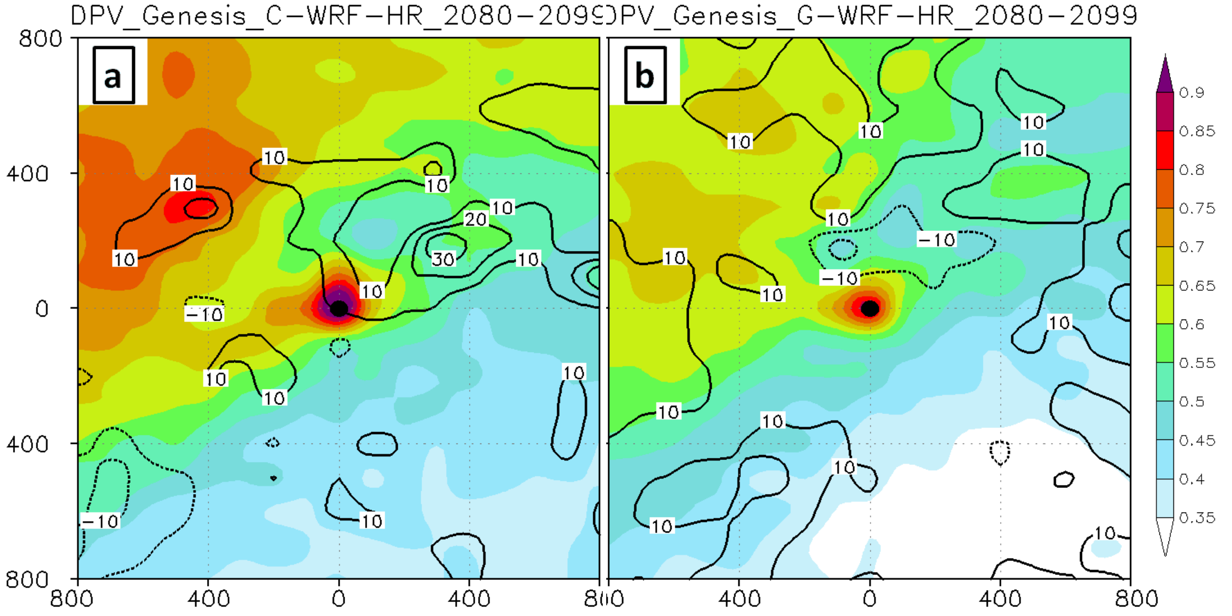

Fig. 5.49: Same as Fig. 5.43, but for the DPV at 900-750 hPa (colors, PVU) and the changes (contours, %) around the cyclogenesis point within the EC (ECL+ECW) region.

Not just for the mean of all cyclone centers, at the cyclogenesis point within the EC region, the DPV maximum in the C-WRF-HR (1.0 PVU) is much stronger than the G-WRF-HR (0.8 PVU) around the cyclone center (Fig. 5.49), which is similar with the precipitation. Since the precipitation increase in the WA region is much smaller than the EC region as described above, the latent heat release in the WA region is also smaller (not shown) in both the C-WRF-HR and the G-WRF-HR.

Overall, in the C-WRF-HR, although the surface and 850hPa temperature gradient decreases (~1K/1000km) over the East Coast (Fig. 5.43a), most of the decrease along the coast of U.S. Northeast is more offshore and the temperature gradient over the ECL region decreases slightly (~5%). The Eady growth rate does not have significant changes around the ECL cyclone centers, and it decreases by 5-15% for the WA centers (Fig. 5.44a, c). Meanwhile, the upper level jet is shifted to the north, and become stronger (0.5-2.0 m/s) along the ECL region (Fig. 5.45a). The upper level (200-300 hPa) PV decreases by 5-15% over the western Atlantic while it does not have significant changes over the ECL region. However, the increase of latent heat release around the ECL cyclone centers (5-13%) is much stronger than the WA centers while the precipitation increases is 10-25% for the ECL cyclone centers and only ~10% for the WA centers. That stronger latent heat release (DPV) exists as early as the cyclogenesis point within the EC region. Therefore, there is an increase (~11%) in the cyclogenesis as well as rapid deepening rate over the EC region, and the cyclone tracks are shifted towards to the ECL region where the upper level jet and latent heat release become stronger and there is no significant decrease in the baroclinicity and upper level PV in the C-WRF-HR. In the G-WRF-HR, given the larger baroclinicity (temperature gradient and Eady growth rate) decrease and the weaker latent heat release increase comparing to the C-WRF-HR, and similar changes for the upper level jet and upper level PV with the C-WRF-HR, the cyclone frequency decrease significantly, especially over the WA region.

b. *The difference between the C-WRF-LR and the C-WRF-HR*

The future changes of cyclones in the CCSM, C-WRF-LR, and C-WRF-HR are similar, but the major difference is that the C-WRF-HR has larger increase in the extreme events, especially within the ECL region, while the C-WRF-LR is closer to the CCSM as described in Section 5.2.1. For example, the C-WRF-HR has significant larger increase in the extremely deep cyclones (< 975 hPa, Fig. 5.27), rapid deepening rate (> 5 hPa/6h, Fig. 5.30), and heavy precipitation (mean precipitation > 17 mm/day, Fig. 5.33) within the ECL region. Although the number of extremely deeper cyclone centers within the WA region (~11.4 centers per winter) is still much more than the ECL region (~3.4 centers per winter) in the future winters under global warming, the significant future increase of these extremely deep cyclone centers occurs within the ECL region.

The future changes of baroclinicity, upper level jet, upper level PV and latent heat release over the ECL regions is investigated in Section 5.2.3 a. In order to explore the physical processes through the evolution of the cyclone associated with the extreme events within the ECL region in the WRF runs forced by the CCSM, the extremely deep cyclones (defined as 95% percentile) for the historical and future winters are compared for the C-WRF-LR and the C-WRF-HR. The thresholds of the extreme cyclones in the C-WRF-LR is 979.3 hPa for the historical winters and 980.4 hPa for the future winters; and in the C-WRF-HR it is 976.9 hPa for the historical winters and 976.2 hPa for the future winters. The time series of the related variables were calculated from the deepest center within the ECL region (defined as Hour_0) backwards to 42 hours before that deepest point (Hour_-42).

First of all, for both of the C-WRF-HR and the C-WRF-LR, the baroclinicity for those cyclones are significant weaker in the future winters. For example, the surface temperature gradient in the future winters is 10-20% weaker than the historical winters (Fig. 5.50b); the 850-500 hPa Eady growth rate has a similar decrease (5-15%) in the future winters (not shown).

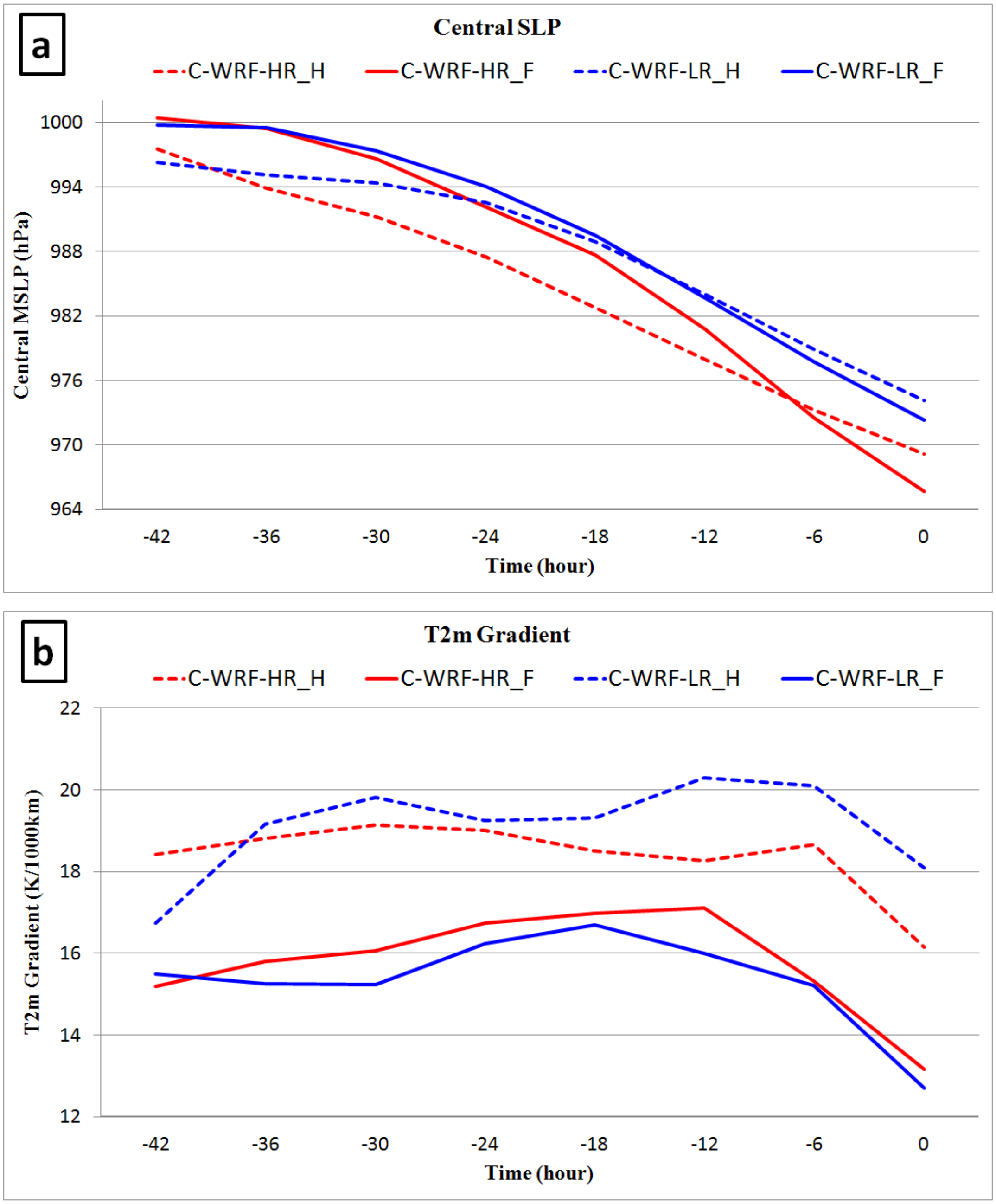

Fig. 5.50: The time series of (a) cyclone central SLP (hPa) and (b) mean surface temperature gradient (K/1000km) around cyclone center for the extreme cyclones within the ECL region, from the deepest center within the ECL region (defined as Hour_0) backwards to 42 hours before that deepest point (Hour_-42). The red lines are the C-WRF-HR and the blue lines are the C-WRF-LR. The dashed lines are for the historical winters and the solid are for the future winters.

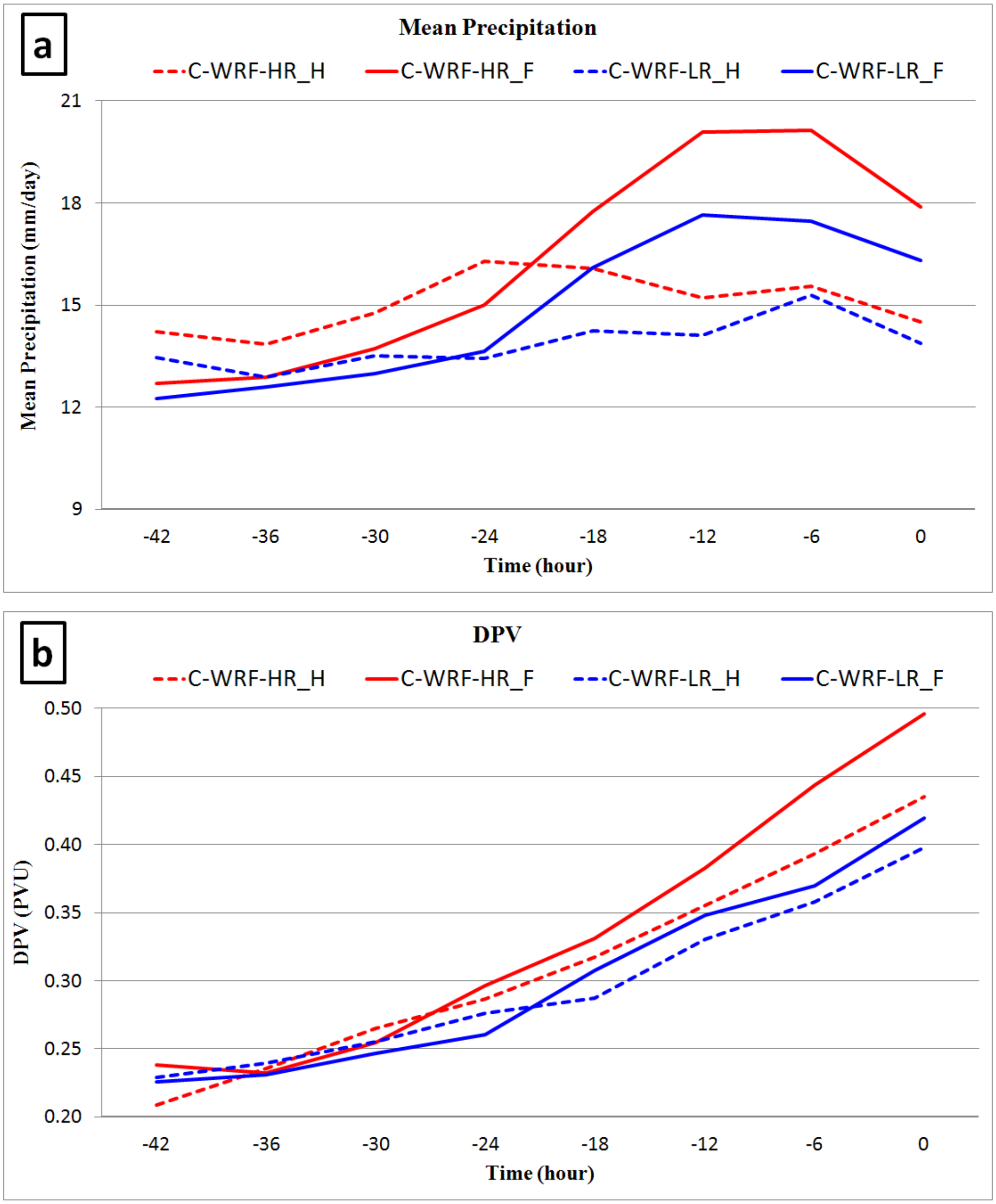

Fig. 5.51: Same as Fig. 5.50, but for (a) the mean precipitation (mm/day) around cyclone center and (b) mean DPV (PVU) around the cyclone center.

The central SLP for the C-WRF-HR in the future winters is 1000.5 hPa, which is 3.0 hPa higher than the historical winters (997.5 hPa) at Hour_-42 (red lines in Fig. 5.50.a). Then the cyclone in the future maintains 3-4 hPa weaker than the historical one until Hour_-18, and both of the cyclones are becoming deeper with time. Meanwhile, with 5-10% more moisture (950-250 hPa, not shown) the mean precipitation around the weaker future cyclone center (so weaker upward motion) is still 1-2 mm/day weaker than the historical one until Hour_-24 (red lines in Fig. 5.51a). However, from Hour_-24 to Hour_-18, the precipitation for the future cyclone becomes heavier than the historical one since there is ~20% more moisture content at this time point in the future and the cyclone is relatively strong (~990hPa). Starting from Hour_-18, the future cyclone deepens rapidly at a 4-5 hPa/6h rate (red solid line in Fig. 5.50a) with the significantly heavier (25-30%) precipitation (red solid line in Fig. 5.51a) and stronger (10-15%) DPV (red solid line in Fig. 5.51b); meanwhile, the baroclinicity is still weaker than the historical cyclone (Fig. 5.50b) and the differences of upper level jet and PV are small (~5%, not shown). At Hour_0 (the deepest cyclone center within the ECL), the future cyclone is ~3.5 hPa deeper than the historical one (Fig. 5.50a). The strong feedback between the cyclone deepening and latent heat release (so DPV) from heavier precipitation plays a dominant role in those increases of extremely deep cyclones and rapid deepening rate in the future winters, while the baroclinicity becomes weaker and the other factors (such as upper level jet) do not have large changes within the ECL region in the C-WRF-HR.

That kind of future increase in extremely deep cyclone centers does not occur within the WA region. Because the future increase of latent heat release around the cyclone centers within the WA region is much smaller than the ECL due to the much weaker increase in the precipitation, since the percentage increase of moisture content is smaller (smaller temperature increase) within the WA than the ECL and the static stability is increasing within the WA while the stability does not have much change or even slightly decreases within the ECL.

In the C-WRF-LR, the future extreme cyclone also deepens more rapidly than the historical one (blue lines in Fig. 5.50a), and has similar increases for the precipitation and DPV with the C-WRF-HR, but they are much weaker comparing with the C-WRF-HR, although the C-WRF-LR is forced by the same CCSM and has a similar increase in moisture content within the C-WRF-HR (difference < 5%). Therefore, the cyclone deepening and latent heat release are very sensitive to the horizontal resolution of the model, which is consistent with the results in Willison et al. (2013), showing an enhanced positive feedback between cyclone intensification and latent in their 20km WRF simulations.

5.3 Summary

In Chapter 5, the CMIP5 CCSM4 and GFDL-ESM2M are dynamically downscaled with the low resolution (1.0°, LR) and high resolution (0.2°, HR) WRF for 20 historical (1986-2005) winters and 20 future (2080-2099) winters.

In C-WRF-HR and C-WRF-LR (forced by CCSM4), the cyclone frequency and the spatial distribution of cyclone track density are dominated by the original CCSM4 (Fig. 5.2). However, the C-WRF-HR has a better intensity distribution with more intense (< 988hPa) cyclones, closer to the distribution of the CFSR (Fig. 5.5). The intensity distribution of the C-WRF-LR is similar to the CCSM, underestimating the number of intense cyclones (Fig. 5.5). Meanwhile, there are more rapid deepening (> 4 hPa/6h in Chapter 5) cases in the C-WRF-HR than the C-WRF-LR and the CCSM (Fig. 5.8 and Fig. 5.9), while those two underestimate the cyclone rapid deepening cases significantly (20-40%).

The C-WRF-HR overestimates the mean winter precipitation amount by 10-15% with respect to the mean of GPCP and CMAP, while the C-WRF-LR and CCSM have less (5-10%) precipitation than the GPCP_CMAP. The C-WRF-HR also has a stronger (20-25%) precipitation maximum around the cyclone center within the synoptic cyclone system than the CCSM. The distribution of the maximum precipitation around the cyclone center in the C-WRF-HR is shifted towards the heavier precipitation part significantly (Fig. 5.17a). The precipitation intensity in the C-WRF-LR is between the CCSM and the C-WRF-HR.

The general results for the GFDL, G-WRF-LR and G-WRF-HR are similar with the CCSM group. The G-WRF-HR has a better performance in the cyclone intensity and cyclone deepening rate distribution (Fig. 5.6, Fig. 5.10, and Fig. 5.11). Different from the WRF forced by the CCSM, the G-WRF-HR has 6 (~18%) more and the G-WRF-LR has 3 (~9%) more cyclones per winter within the ECWA region than the GFDL (Fig. 5.10). The maximum precipitation in the GFDL is significantly weaker than the other members, with 90% cases < 70 mm/day (Fig. 5.17b).

There are more cyclones in the WRF forced by GFDL than the original GFDL, because in the G-WRF-LR and G-WRF-HR has much stronger baroclinicity: the surface temperature gradient is 20-40% stronger (Fig. 5.22), the 850hPa temperature is 10-20% stronger, and the 850-500 hPa Eady growth rate is 5-10% larger (Fig. 5.24) than the GFDL. In addition to the baroclinicity, the ~5% increase of upper level jet (Fig. 5.24) and 5-15% increase of DPV (Fig. 5.25) in the WRF runs yields ~3 more cyclones per winter in the G-WRF-LR, ~6 more cyclones and more intense cyclones. The differences among the CCSM, C-WRF-HR and C-WRF-LR are smaller than the GFDL runs.

In the future (2080-2099) winters, there are 1.7 (11%) more cyclogenesis, 10-40% more track density and rapid deepening cases within the EC region in the C-WRF-HR than the historical (1986-2005) winters (Fig. 5.26, Fig. 5.27a, Fig. 5.29, and Fig. 5.30a). In the C-WRF-HR, the upper level jet becomes stronger (0.5-2.0 m/s) and is shifted to the north just along the ECL region (Fig. 5.45); and there is a significant increase in the latent heat release over the ECL region (5-15%) from the heavier precipitation (Fig. 5.47 and Fig. 5.48) from the cyclogenesis through the evolution of cyclone along the East Coast. Meanwhile, the surface temperature gradient decrease maximum is more offshore (Fig. 5.43), and the decrease of Eady growth rate (Fig. 5.44) and upper level PV (Fig. 5.46) is relatively small (~5%) over the ECL region. Therefore, there is a slight increase in the cyclogenesis and the cyclone tracks are shifted towards the ECL region from the western Atlantic.

In the G-WRF-HR, the increases of cyclone frequency and rapid deepening rate over the ECL region disappear, and the decrease over the WA regions is stronger than the C-WRF-HR (Fig. 5.34, Fig. 5.35, Fig. 5.36 and Fig. 5.37). Because the baroclinicity decreases are stronger (10-15%, Fig. 5.43), while the increase of latent heat release is weaker (~5%, Fig. 5.48) due to the weaker precipitation increase than the C-WRF-HR.

There are also significant increases in the extremely deep cyclones (Fig. 5.30) and extremely heavy precipitation (Fig. 5.33) over the ECL region in the C-WRF-HR. The strong feedback between the increased latent heat release from much heavier precipitation and the cyclone deepening plays a more important role (Fig. 5.50 and 5.51) in those extreme events, while upper level jet increase by ~5% and the baroclinicity and upper level PV are decreasing in the C-WRF-HR.

Chapter 6:
Conclusions and Future Work

6.1 Summary

This dissertation provides a unique comprehensive study in the ability of climate and mesoscale models in simulating the variability of extratropical cyclones, the regional future changes of the extratropical cyclones, and their associated regional climate and extreme weather during cool season over eastern North America and western Atlantic. The extratropical cyclones in 26 historical and 90 future cool seasons in 15 CMIP5 models are identified and analyzed to evaluate the model's historical performance and predict the future changes through 21st century under global warming. A cyclone relative approach is developed to investigate the extratropical cyclone characteristics and the associated physical processes for different kinds of cyclone systems, through the life cycle of extratropical cyclone. The future changes of cyclone relative precipitation over eastern North America and western Atlantic are investigated on the geophysical map and in the mesoscale cyclone system. Two CMIP5 models are dynamically downscaled using WRF to provide the high resolution regional climate projections over eastern North American and western Atlantic and improve the understanding to the future changes of extratropical cyclones.

The key results of this dissertation are summarized below:

1. Most of the CMIP5 models underpredict the cyclone numbers over the eastern North America and western Atlantic with respect to the CFSR, especially for the intense cyclones. The relatively high resolution models tend to have better performance than those coarse resolution models.

2. There is a decrease in the cyclone track density over western Atlantic during the 21st century in CMIP5 RCP8.5 experiment. However, over inland along the East Coast of North America there are increases in the number of intense cyclones and rapid deepening cases in the Best7 models.
3. Most of the increase in cool season precipitation amount comes from the strong and moderate cyclones, while the increase of weak cyclone precipitation is inhibited by the large decrease in cyclone frequency. Meanwhile, the ECL cyclones have larger increase in precipitation rate and extreme precipitation events than the WA cyclones.
4. There are strong positive feedback between the precipitation increase and cyclone deepening for those ECL intense cyclones associated with extreme precipitation. During the extreme precipitation, the strong latent heat release enhances the rapid deepening of the cyclones. Meanwhile, the more rapid deepening will strengthen the upward motion, which is favorable to the precipitation increase.
5. In the CCSM and its downscaled WRF, there are 10-40% increases in cyclone track density and rapid deepening cases over the ECL region. Because over the ECL region, the baroclinicity decrease is weak and more offshore, the upper level jet is shifted to north and more onshore, and there is a large increase in the latent heat release from heavier precipitation. In addition, the strong positive feedback between the heavier precipitation and cyclone rapid deepening in the high resolution WRF leads to a 20% increase of extremely deep cyclones in the ECL region. In the WRF runs forced by the GFDL, those increases over the ECL region become much weaker and close to neutral.

6.2 Conclusions

6.2.1 The ability of GCM and WRF in simulating extratropical cyclones

This dissertation evaluates the performance of 15 CMIP5 models and 2 downscaled WRF in the simulation of the cool-season extratropical cyclone over eastern North America and western Atlantic. This work aims to inspect the ability and the deficiency of the models to increase the confidence of future projections and inform the future model development.

The unprecedented CMIP5 high-frequency (6-hourly) model output provides a unique opportunity to evaluate the frequency, intensity, and spatial distribution of extratropical cyclones in a multi-model framework. All of the 15 CMIP5 models are able to produce a cyclone track density maximum over eastern North America and western Atlantic, as well as a reasonable distribution for cyclone intensity and deepening rate. However, most of these CMIP5 models underestimate the total number of cyclones in this region, which is consistent with the results from Zappa et al. (2013). One important factor for cyclogenesis is the near surface temperature gradient, which is highly related to the model resolution and impacted by the SST. In some coarse resolution (> 2°) CMIP5 models, the features of Gulf Stream and the terrains of Appalachian Mountains (so snow cover and surface temperature) are not well represented. As a result, in those models the surface temperature gradient at north side of the Gulf Stream is too weak (~50% of the CFSR), and the relatively strong surface temperature gradient over the East Coast is too concentrated along the coast of Northeast U.S. Those models underestimate the total number of cyclones by 20-30% comparing to the CFSR. The cyclone track density maximum tends to be too onshore and concentrated at the coast of Northeast U.S. Meanwhile, the cyclogenesis density maximum is shifted to north in those coarse resolution models due to the absence of the surface baroclinicity (temperature gradient) at the southeastern of eastern U.S.

This is similar to the results in Woollings et al. (2010), which shows that a higher SST resolution tends to shift the storm track southward toward the Gulf Stream. The relatively high resolution models with better represented surface temperature tend to have better performance in the magnitude and spatial distribution of cyclone track and genesis density. It indicates that the model resolution is one of the most important factors for cyclone simulation.

The resolution is not the only thing controlling the cyclone simulation. The coarse resolution MPI-ESM-LR (~ 1.8°) has a realistic coastline and a better presented surface temperature gradient than the other coarse resolution models, and also has a good final ranking for the cyclone simulation. Some other factors which are important to the cyclogenesis and developing, such as the tropospheric baroclinicity and upper level jet, are more independent of the model resolution. For example, IPSL-CM5A-LR (3.7°×1.8°) has a stronger upper level jet (~48 m/s) and larger Eady growth rate area of > 0.9 day^{-1} comparing with the CFSR and most of other models. It implies that the poor performance of IPSL-CM5A-LR is not a result of lack of tropospheric or upper level forcing comparing with the other models. With a higher resolution than IPSL-CM5A-LR, INMCM4 has very weak upper level jet (~38 m/s) and Eady growth rate (< 0.83 day^{-1}). Further studies are needed to investigate the related factors which have impacts on the cyclone simulation in GCM. For example, the upper level jet has large impact on the cyclone activities, but there are large uncertainties for the position and intensity of the upper level jet which suggests that there are vertical levels with different horizontal temperature gradients among these GCMs. A further study investigating the bias of upper level jet is important to understand the cyclone simulation, and sheds new light on improving the simulation of extratropical cyclones in GCMs in addition to higher resolution.

The cyclone simulation in the downscaled WRF is also evaluated. The initial and boundary conditions including the SST for WRF are from the CMIP5 GCM. Therefore, the baroclinic disturbances entering the WRF are from the GCM and the surface temperature over ocean in WRF is highly controlled by the same coarse resolution SST with the GCM. As a result, the cyclone frequency and the spatial distribution of cyclone track density in WRF are dominated by the original GCM. However, the more realistic terrains in high resolution WRF (so the snow cover, surface temperature, cold-air damming, etc.) over the eastern North America allow the re-building of a stronger surface baroclinicity zone than the GCM, especially the coarse resolution GCM. As a result, the WRF-HR forced by GFDL-ESM2M has ~18% more cyclones and has a cyclone track density maximum extending further south than GFDL-ESM2M.

The WRF-HR has more intense cyclones, so smaller negative bias for the number of deep cyclones due to the stronger latent heat release from better resolved diabatic processes. Given the similar other conditions, the WRF-HR has stronger latent heat release and then deeper cyclones than the WRF-LR, which indicates that the latent heat release is very sensitive to the horizontal resolution. This is consistent with the conclusion from Willison et al. (2013), who found an enhanced positive feedback between cyclone intensification and latent heat release in the higher resolution (20km) WRF relative to the coarser (120km) resolution WRF.

Many studies (Wills et al. 2016; Jacobs et al. 2004; Czaja and Frankignoul, 2002) suggested the strong influences of SST over the western boundary currents on the atmospheric circulation over the North Atlantic, including the storm track. Hirata et al. (2016) demonstrated that the SST variations have strong influence in the latent heat release related to the moisture supply from the ocean and then impact the cyclone intensification in a rapidly developing extratropical cyclone case. The WRF downscaling in this dissertation used the coarse resolution

(1.0°-1.5°) SST from the CMIP5 GCM to keep consistency. An additional experiment using high resolution SST is needed to investigate the influence of SST horizontal resolution on the extratropical cyclone simulation in the WRF-HR.

6.2.2 The future changes of extratropical cyclones over the East Coast

The future changes of extratropical cyclones were investigated using the CMIP5 RCP8.5 experiment, as well as the downscaled WRF runs. This dissertation focuses on future changes over eastern North America and western Atlantic and emphasizes the regional nature of the future changes over the East Coast of North America through 21st century. The future changes in the mean of 7 CMIP5 models with better historical performance (Best7) are highlighted, and compared with the changes in the ensemble mean of the 7 models with relatively worse performance (Worst7).

There is a significant decrease in cyclone track density over western Atlantic in late 21st century in the ensemble mean of the Best7 (10-30%) and the Worst7 (10-20%). This decrease of cool-season extratropical cyclone due to the decrease of baroclinicity under global warming was found in many studies (Geng and Sugi 2003; Lambert and Fyfe 2006; Bengtsson et al. 2009; Chang 2013, Zappa et al. 2013).

Different from those studies, this dissertation found a 10-20% increase in cyclone track density, including 10-40% more intense (<980hPa) cyclones and 20-40% more rapid deepening rate (> 5 hPa/6h) in the Best7 models over the ECL in late 21st century. In the Worst7 models these increases become much weaker and close to neutral. Some previous studies suggested that the central pressure of the more extreme extratropical cyclones may intensify under global warming (Mizuta et al. 2011; Long et al. 2009). However, there are uncertainties in the future changes in cyclone intensity (Geng and Sugi 2003; Lambert and Fyfe 2006; Catto et al. 2011). This dissertation highlights those increases of cyclones over the ECL in the Best7, which will be easily smoothed out in the ensemble mean of all the 15 models. The concern is that current GCMs, especially those very coarse resolution GCMs, represent moist processes poorly, which will introduce large uncertainties for the contribution of diabatic processes to the cyclone intensification with more moisture available in the air under global warming.

The dynamically downscaled WRF is utilized to determine the robustness of those results from CMIP5 models and explore the related physical processes. Two CMIP5 models (CCSM4 and GFDL-ESM2M) with different resolutions and different future projections are selected to be downscaled. The future projections in both of the high resolution and low resolution WRF are highly impacted by the original GCMs, meanwhile the high resolution WRF provides more details for the future changes. In the WRF-HR forced by CCSM4 there are 10-40% increase in cyclone track density over the East Coast region, which is from a slight increase in cyclogenesis over this region and a northward shift of cyclone track density maximum from western Atlantic. Meanwhile, over the ECL region there is a ~20% increase in extremely deep cyclones (< 975 hPa) with more rapid deepening cases due to the stronger latent heat release from much heavier precipitation in the C-WRF-HR. This result is consistent with Marciano et al. (2015), who found that enhanced latent heat release is responsible for this regional increase in future cyclone intensity in their simulations of 10 major extratropical cyclones over the East Coast. However, the G-WRF-HR does not have that kind of increase in deep cyclones and only has some weak increase or no significant changes over the East Coast. Comparing to the C-WRF-HR, in the G-WRF-HR the baroclinicity decrease is larger; the precipitation (so latent heat release) increase is much smaller; and there is not a northward shift of upper level jet.

6.2.3 The future changes of precipitation over the East Coast

There are significant increase trends for the magnitude and frequency of future precipitation over the eastern North America under global warming (Semenov and Bengtsson, 2002; Hayhoe et al. 2007; Kharin et al. 2007; Kunkel et al. 2013a; Scoccimarro et al. 2013; Maloney et al. 2014). This dissertation investigates the future changes of cyclone relative precipitation, which contributes >80% of the total precipitation at middle and high (>35°N) latitudes of eastern North America, and explored the physical processes responsible to the precipitation increase in the mesoscale cyclone systems.

The cool-season precipitation amount associated with the extratropical cyclones increases by 10-30% in late 21st century over the East Coast of North America, which is similar to previous studies (Zappa et al. 2013; Lombardo et al. 2014; Marciano et al. 2015). This dissertation also found that most of the precipitation amount increase is from the moderate and strong cyclones (<1005hPa), while the relatively small increase of precipitation rate for the weak cyclones is inhibited by the decrease of weak cyclone frequency.

There is a significant shift towards the heavy precipitation part for both of the mean and maximum precipitation around cyclone center over the East Coast region. The largest increase of precipitation intensity is associated with the relatively deep cyclones (< 990hPa) over the ECL region. Given the great increase of moisture and the small decrease of moist static stability over the East Coast land, and the strong poleward moisture transport over the warm side of the deep cyclone, the positive feedback between the latent heat release from heavy precipitation and the cyclone deepening is much stronger in those ECL strong cyclone systems in middle and late 21st century. This positive feedback becomes more important to cyclone developing and precipitation increase when the baroclinicity is decreasing under global warming and the upper level forcing does not have significant changes.

6.3 Future work

1. Downscale more CMIP5 models to investigate the probabilistic robustness of future climate change and extreme weather events on regional scales in WRF.

There is a high confidence for the decrease of extratropical cyclone during cool season over the western Atlantic based on the previous studies and the results in this dissertation. However, there are large uncertainties for the future changes of cyclones over the East Coast of North America among the CMIP5 models. In the downscaled WRF-HR forced by CCSM4, there are increases for the cyclone frequency, rapid deepening cases, and extremely deep cyclones. Meanwhile, those increases become much weaker in the WRF-HR forced by GFDL-ESM2M. Given the large difference in the low troposphere temperature, precipitation, upper level jet, etc, the difference between the two WRF-HR projections is expected. However, more downscaled projections are needed to get a full picture of the physical processes controlling those future changes and increase the confidence of the future changes on regional scale.

In order to insure the variety of the ensemble members, the CMIP5 models with different future projections, historical performance and resolutions will be selected. Meanwhile, in order to increase the confidence to the increase of intense cyclones over East Coast, at least one more CMIP5 model with that increase will be downscaled to validate the relationship between the latent heat release and cyclone intensification.

2. Create an ensemble of high-resolution simulations for eastern North America and western Atlantic to understand future changes of extreme weather on regional scale associated with extratropical cyclones, including precipitation, strong winds and extreme cold events.

The high resolution downscaled WRF provides a more realistic cyclone intensity distribution, as well as more regional details for the extreme weather than the GCMs. Using the ensemble of high-resolution WRF simulations described in future work (1), the future changes of those extreme precipitation, strong wind, and extreme cold events associated with the extratropical cyclones over eastern North America and western Atlantic will be investigated on the geographic map and in the mesoscale cyclone systems using the cyclone relative approach. The future changes of the related physical processes will also be examined to explore the relationship between the future changes of extratropical cyclones and the future changes of extreme weather.

3. Extend the analysis and modeling on extratropical cyclones over the U.S. east coast to other highly populated regions, such as the U.S. west coast.

Apply the extratropical cyclone dataset (CFSR and CMIP5) and the cyclone relative approach to study the extratropical cyclones in the Northeast Pacific, including their frequency, intensity, tracks, and the associated extreme weather. For example, investigate the extreme precipitation associated with atmospheric river and extratropical cyclone, which has great impacts on the U.S. west coast. The WRF downscaling approach can also be similarly used to better resolve the terrains and the coastal features over the west coast, and create the high resolution regional simulations to study the regional climate and extreme weather.

4. Extend the analysis and modeling on extratropical cyclones over the U.S. east coast to other large-scale atmospheric circulation systems such as anticyclone to study heat waves.

In this dissertation, the cool season extratropical cyclones over U.S. east coast are investigated. The tracking approach can be similarly used to identify the anticyclones systems to study heat waves associated with atmospheric ridges and blocking highs in summer over North America.

References

Adler, Robert F., et al. "The version-2 global precipitation climatology project (GPCP) monthly precipitation analysis (1979-present)." *Journal of hydrometeorology* 4.6 (2003): 1147-1167.

Agel, Laurie, et al. "Climatology of daily precipitation and extreme precipitation events in the northeast United States." *Journal of Hydrometeorology* 16.6 (2015): 2537-2557.

Ashley, Walker S., and Alan W. Black. "Fatalities associated with nonconvective high-wind events in the United States." *Journal of Applied Meteorology and Climatology* 47.2 (2008): 717-725.

Bauer, Mike, and Anthony D. Del Genio. "Composite analysis of winter cyclones in a GCM: Influence on climatological humidity." *Journal of climate* 19.9 (2006): 1652-1672.

Bengtsson, Lennart, Kevin I. Hodges, and Noel Keenlyside. "Will extratropical storms intensify in a warmer climate?." *Journal of Climate* 22.9 (2009): 2276-2301.

Black, Robert X. "The maintenance of extratropical intraseasonal transient eddy activity in the GEOS-1 assimilated dataset." *Journal of the atmospheric sciences* 55.20 (1998): 3159-3175.

Catto, Jennifer L., Len C. Shaffrey, and Kevin I. Hodges. "Can climate models capture the structure of extratropical cyclones?." *Journal of Climate* 23.7 (2010): 1621-1635.

Catto, Jennifer L., Len C. Shaffrey, and Kevin I. Hodges. "Northern Hemisphere extratropical cyclones in a warming climate in the HiGEM high-resolution climate model." *Journal of Climate* 24.20 (2011): 5336-5352.

Chang, Edmund KM, Sukyoung Lee, and Kyle L. Swanson. "Storm track dynamics." *Journal of Climate* 15.16 (2002): 2163-2183.

Chang, Edmund KM, and Siwon Song. "The seasonal cycles in the distribution of precipitation around cyclones in the western North Pacific and Atlantic." *Journal of the atmospheric sciences* 63.3 (2006): 815-839.

Chang, Edmund KM. "Diabatic and orographic forcing of northern winter stationary waves and storm tracks." *Journal of Climate* 22.3 (2009): 670-688.

Chang, Edmund KM, et al. "Storm-track activity in IPCC AR4/CMIP3 model simulations." *Journal of Climate* 26.1 (2013): 246-260.

Chang, Edmund KM. "CMIP5 projection of significant reduction in extratropical cyclone activity over North America." *Journal of Climate* 26.24 (2013): 9903-9922.

Colle, Brian A., et al. "New York City's vulnerability to coastal flooding." *Bulletin of the American Meteorological Society* 89.6 (2008): 829.

Colle, Brian A., Katherine Rojowsky, and Frank Buonaito. "New York City storm surges: Climatology and an analysis of the wind and cyclone evolution." *Journal of Applied Meteorology and Climatology* 49.1 (2010): 85-100.

Colle, Brian A., et al. "Historical evaluation and future prediction of eastern North American and western Atlantic extratropical cyclones in the CMIP5 models during the cool season." *Journal of Climate* 26.18 (2013): 6882-6903.

Colle, Brian A., James F. Booth, and Edmund KM Chang. "A review of historical and future changes of extratropical cyclones and associated impacts along the US east coast." *Current Climate Change Reports* 1.3 (2015): 125-143.

Czaja, Arnaud, and Claude Frankignoul. "Observed impact of Atlantic SST anomalies on the North Atlantic Oscillation." *Journal of Climate* 15.6 (2002): 606-623.

Dee, D. P., et al. "The ERA-Interim reanalysis: Configuration and performance of the data assimilation system." *Quarterly Journal of the royal meteorological society* 137.656 (2011): 553-597.

Di Liberto, Tom, et al. "Verification of a multimodel storm surge ensemble around New York City and Long Island for the cool season." *Weather and Forecasting* 26.6 (2011): 922-939.

Feser, Frauke, et al. "Storminess over the North Atlantic and northwestern Europe—A review." *Quarterly Journal of the Royal Meteorological Society* 141.687 (2015): 350-382.

Field, Paul R., and Robert Wood. "Precipitation and cloud structure in midlatitude cyclones." *Journal of climate* 20.2 (2007): 233-254.

Geng, Quanzhen, and Masato Sugi. "Variability of the North Atlantic cyclone activity in winter analyzed from NCEP-NCAR reanalysis data." *Journal of Climate* 14.18 (2001): 3863-3873.

Geng, Quanzhen, and Masato Sugi. "Possible change of extratropical cyclone activity due to enhanced greenhouse gases and sulfate aerosols-Study with a high-resolution AGCM." *Journal of Climate* 16.13 (2003): 2262-2274.

Hawcroft, M. K., et al. "How much Northern Hemisphere precipitation is associated with extratropical cyclones?." *Geophysical Research Letters* 39.24 (2012).

Hayhoe, Katharine, et al. "Past and future changes in climate and hydrological indicators in the US Northeast." *Climate Dynamics* 28.4 (2007): 381-407.

He, Juanxiong, et al. "The WRF nested within the CESM: Simulations of a midlatitude cyclone over the Southern Great Plains." *Journal of Advances in Modeling Earth Systems* 5.3 (2013): 611-622.

Hirata, Hidetaka, et al. "Response of rapidly developing extratropical cyclones to sea surface temperature variations over the western Kuroshio–Oyashio confluence region." *Journal of Geophysical Research: Atmospheres* 121.8 (2016): 3843-3858.

Hirsch, Matthew E., Arthur T. DeGaetano, and Stephen J. Colucci. "An East Coast winter storm climatology." *Journal of Climate* 14.5 (2001): 882-899.

Hodges, K. I. "A general method for tracking analysis and its application to meteorological data." *Monthly Weather Review* 122.11 (1994): 2573-2586.

Hodges, K. I. "Feature tracking on the unit-sphere." *Monthly Weather Review* 123.12 (1995): 3458-3465.

Hodges, Kevin Ivan, et al. "A comparison of recent reanalysis datasets using objective feature tracking: Storm tracks and tropical easterly waves." *Monthly Weather Review* 131.9 (2003): 2012-2037.

Hodges, Kevin I., R. W. Lee, and Lennart Bengtsson. "A comparison of extratropical cyclones in recent reanalyses ERA-Interim, NASA MERRA, NCEP CFSR, and JRA-25." *Journal of Climate* 24.18 (2011): 4888-4906.

Hoskins, Brian J., and Paul J. Valdes. "On the existence of storm-tracks." *Journal of the atmospheric sciences* 47.15 (1990): 1854-1864.

Hoskins, Brian J., and Kevin I. Hodges. "New perspectives on the Northern Hemisphere winter storm tracks." *Journal of the Atmospheric Sciences* 59.6 (2002): 1041-1061.

Hoskins, Brian John, and Kevin Ivan Hodges. "A new perspective on Southern Hemisphere storm tracks." *Journal of Climate* 18.20 (2005): 4108-4129.

Jacobs, Neil A., et al. "Role of the Gulf Stream on extratropical cyclogenesis." *20th Conference on Weather Analysis and Forecasting/16th Conference on Numerical Weather Prediction*. 2004.

Jung, Thomas, et al. "Sensitivity of extratropical cyclone characteristics to horizontal resolution in the ECMWF model." *Quarterly Journal of the Royal Meteorological Society* 132.619 (2006): 1839-1857.

Knox, John A., et al. "Non-Convective High Winds Associated with Extratropical Cyclones." *Geography Compass* 5.2 (2011): 63-89.

Kunkel, Kenneth E., et al. "Monitoring and understanding trends in extreme storms: State of knowledge." *Bulletin of the American Meteorological Society* 94.4 (2013): 499-514.

Lackmann, Gary M. "The South-Central US Flood of May 2010: Present and Future*." *Journal of Climate* 26.13 (2013): 4688-4709.

Lambert, Steven J., and John C. Fyfe. "Changes in winter cyclone frequencies and strengths simulated in enhanced greenhouse warming experiments: results from the models participating in the IPCC diagnostic exercise." *Climate Dynamics* 26.7-8 (2006): 713-728.

Lombardo, Kelly, Brian A. Colle, and Zhenhai Zhang. "Evaluation of historical and future cool season precipitation over the eastern United States and western Atlantic storm track using CMIP5 models." *Journal of Climate* 28.2 (2015): 451-467.

Maloney, Eric D., et al. "North American climate in cmip5 experiments: part iii: assessment of twenty-first-century projections*." *Journal of Climate* 27.6 (2014): 2230-2270.

Marciano, Christopher G., Gary M. Lackmann, and Walter A. Robinson. "Changes in US East Coast cyclone dynamics with climate change." *Journal of Climate* 28.2 (2015): 468-484.

Nakamura, Hisashi. "Midwinter suppression of baroclinic wave activity in the Pacific." *Journal of the atmospheric sciences* 49.17 (1992): 1629-1642.

Naud, Catherine M., Derek J. Posselt, and Susan C. Van Den Heever. "Observational analysis of cloud and precipitation in midlatitude cyclones: Northern versus Southern Hemisphere warm fronts." *Journal of Climate* 25.14 (2012): 5135-5151.

Naud, Catherine M., et al. "Multiple satellite observations of cloud cover in extratropical cyclones." *Journal of Geophysical Research: Atmospheres* 118.17 (2013): 9982-9996.

Neu, Urs, et al. "IMILAST: a community effort to intercompare extratropical cyclone detection and tracking algorithms." *Bulletin of the American Meteorological Society* 94.4 (2013): 529-547.

Novak, David R., Brian A. Colle, and Sandra E. Yuter. "High-resolution observations and model simulations of the life cycle of an intense mesoscale snowband over the northeastern United States." *Monthly Weather Review* 136.4 (2008): 1433-1456.

Paciorek, Christopher J., et al. "Multiple indices of Northern Hemisphere cyclone activity, winters 1949-99." *Journal of Climate* 15.13 (2002): 1573-1590.

Picca, Joseph C., et al. "The value of dual-polarization radar in diagnosing the complex microphysical evolution of an intense snowband." *Bulletin of the American Meteorological Society* 95.12 (2014): 1825-1834.

Pinto, Joaquim G., et al. "Changes in storm track and cyclone activity in three SRES ensemble experiments with the ECHAM5/MPI-OM1 GCM." *Climate Dynamics* 29.2-3 (2007): 195-210.

Rasmussen, Roy, et al. "High-resolution coupled climate runoff simulations of seasonal snowfall over Colorado: a process study of current and warmer climate." *Journal of Climate* 24.12 (2011): 3015-3048.

Saha, Suranjana, et al. "The NCEP climate forecast system reanalysis." *Bulletin of the American Meteorological Society* 91.8 (2010): 1015.

Salari, V., and Ishwar K. Sethi. "Feature point correspondence in the presence of occlusion." *IEEE Transactions on Pattern Analysis and Machine Intelligence* 12.1 (1990): 87-91.

Sato, Tomonori, Fujio Kimura, and Akio Kitoh. "Projection of global warming onto regional precipitation over Mongolia using a regional climate model." *Journal of Hydrology* 333.1 (2007): 144-154.

Scoccimarro, Enrico, et al. "Heavy precipitation events in a warmer climate: results from CMIP5 models." *Journal of climate* 26.20 (2013): 7902-7911.

Semenov, Vladimir, and Lennart Bengtsson. "Secular trends in daily precipitation characteristics: greenhouse gas simulation with a coupled AOGCM." *Climate Dynamics* 19.2 (2002): 123-140.

Skamarock, W. C., et al. *A description of the advanced research WRF Ver. 30. NCAR Technical Note*. NCAR/TN-475, 2008.

Straus, David M., and J. Shukla. "Variations of midlatitude transient dynamics associated with ENSO." *Journal of the atmospheric sciences* 54.7 (1997): 777-790.

Sweet, William V., and Chris Zervas. "Cool-season sea level anomalies and storm surges along the US East Coast: Climatology and comparison with the 2009/10 El Niño." *Monthly Weather Review* 139.7 (2011): 2290-2299.

Taylor, Karl E., Ronald J. Stouffer, and Gerald A. Meehl. "An overview of CMIP5 and the experiment design." *Bulletin of the American Meteorological Society* 93.4 (2012): 485.

Wang, Xiaolan L., Val R. Swail, and Francis W. Zwiers. "Climatology and changes of extratropical cyclone activity: Comparison of ERA-40 with NCEP-NCAR reanalysis for 1958-2001." *Journal of Climate* 19.13 (2006): 3145-3166.

Wang, Xiaolan L., et al. "Inter-comparison of extra-tropical cyclone activity in nine reanalysis datasets." *Atmospheric Research* 181 (2016): 133-153.

Wernli, Heini, and Michael Sprenger. "Identification and ERA-15 climatology of potential vorticity streamers and cutoffs near the extratropical tropopause." *Journal of the atmospheric sciences* 64.5 (2007): 1569-1586.

Willison, Jeff, Walter A. Robinson, and Gary M. Lackmann. "The importance of resolving mesoscale latent heating in the North Atlantic storm track." *Journal of the Atmospheric Sciences* 70.7 (2013): 2234-2250.

Wills, Samantha M., David WJ Thompson, and Laura M. Ciasto. "On the Observed Relationships between Variability in Gulf Stream Sea Surface Temperatures and the Atmospheric Circulation over the North Atlantic." *Journal of Climate* 29.10 (2016): 3719-3730.

Woollings, Tim, et al. "Storm track sensitivity to sea surface temperature resolution in a regional atmosphere model." *Climate dynamics* 35.2-3 (2010): 341-353.

Xie, Pingping, and Phillip A. Arkin. "Global precipitation: A 17-year monthly analysis based on gauge observations, satellite estimates, and numerical model outputs." *Bulletin of the American Meteorological Society* 78.11 (1997): 2539.

Zappa, Giuseppe, Len C. Shaffrey, and Kevin I. Hodges. "The ability of CMIP5 models to simulate north atlantic extratropical cyclones*." *Journal of Climate* 26.15 (2013): 5379-5396.

Zappa, Giuseppe, et al. "A multimodel assessment of future projections of north atlantic and european extratropical cyclones in the cmip5 climate models*." *Journal of Climate* 26.16 (2013): 5846-5862.

Zappa, Giuseppe, et al. "Extratropical cyclones and the projected decline of winter Mediterranean precipitation in the CMIP5 models." *Climate Dynamics* 45.7-8 (2015): 1727-1738.